

Development of new approaches for
characterising DNA origami-based nanostructures
with atomic force microscopy and super-resolution microscopy

DISSERTATION

zur Erlangung des akademischen Grades

Doctor rerum naturalium
(Dr. rer. nat.)

vorgelegt

dem Bereich Mathematik und Naturwissenschaften
der Technischen Universität Dresden

von

M.Sc. Franziska Elisabeth Fischer
geboren am 16. Dezember 1987 in Dresden, Deutschland

eingereicht am 09.08.2018

Gutachter

Prof. Dr. rer. nat. et Ing. habil. Michael Mertig
Prof. em. Dr. rer. nat. Manfred Stamm

verteidigt am 09.01.2019

Die Dissertation wurde in der Zeit von Januar 2013 bis August 2018 an der
Professur für Physikalische Chemie, Mess- und Sensortechnik und am
cfaed - Center for Advancing Electronics Dresden, TU Dresden - angefertigt.

For Mom. For Dad.

*“When morning comes, you would better find yourself saying:
'I have so many choices of what to do or what to leave - every morning, every day.
I better judge for myself, and - go ahead and do it.'”*

Stefan Hell

Contents

Abstract	3
1 Introduction	5
1.1 Objective and thesis outline	5
1.2 DNA nanotechnology: structure assembly and current research areas	8
1.2.1 Structure assembly	8
1.2.2 Current fields of research	14
1.3 Overview over the current techniques for the structural characterisation of DNA origami .	16
1.3.1 Gel electrophoresis	17
1.3.2 Atomic force microscopy	17
1.3.3 Fluorescence techniques	19
1.3.4 Super-resolution microscopy	20
1.4 Precision and trueness in SRM and multicolour co-localisation approaches	23
1.5 Towards the assembly of CP molecules with DNA origami and possible applications . . .	26
1.5.1 Conjugated polymers	26
1.5.2 Polythiophene and water-soluble, regioregular, end-functionalised derivatives via state-of-the-art synthesis	29
1.5.3 Nanopatterning of conjugated polymers for single-molecule studies	30
1.5.4 Nanopatterning of conjugated polymers with DNA	32
1.5.5 State-of-the-art polymer-DNA origami hybrids	33
2 Materials and Methods	37
2.1 Chemicals	37
2.2 DNA origami synthesis	37
2.3 AuNP and AuNR attachment to the pads and tPads	38
2.4 Formation of P3(EO)₃T-b-ODN BCPs and hybrids of BCPs and origami pads	39
2.5 Methods used on multiple occasions	40
2.6 Atomic force microscopy	42
2.6.1 Sample preparation for scanning in air and high-resolution scanning in liquid . . .	42
2.6.2 Melting studies	42
2.6.3 Locating of the BCP in hybrids in high-resolution liquid AFM images using the FindFoci algorithm	42
2.7 Super-resolution fluorescence microscopy	45
2.7.1 Protocols	45
2.7.2 Error propagation	49
3 Construction and characterisation of two 2D DNA origami structures with emphasis on AFM-based investigations	51
3.1 Design, synthesis and characterisation of pad and tPad	51

3.1.1	Design and synthesis	51
3.1.2	Structure evaluation	53
3.1.3	Yield determination and synthesis variations to improve the yield	56
3.1.4	Thermal and mechanical stability	60
3.1.5	Stacking	65
3.2	Towards decorating DNA origami	66
3.2.1	Design of the link sequences	66
3.2.2	Testing the binding capabilities of the links	67
3.2.3	Testing the pegboard qualities of tPads and pads by arranging nanoscale gold	68
3.3	Summary	70
4	Qualitative and quantitative characterisation of polymer-DNA origami hybrids with AFM	73
4.1	Three step hybrid fabrication	73
4.2	Results of the quantitative analysis of high-resolution AFM images of polyhiophene-DNA origami hybrids	80
4.2.1	Object size	83
4.2.2	Number of objects and object positions on the different pad types	84
4.3	Influence of the scanning on the samples and limitations of AFM	93
4.4	Summary and outlook	95
5	Characterisation of surface-deposited 2D DNA origami with multicolour super-resolution microscopy	97
5.1	Basic principles, origami under test and method procedure	97
5.1.1	Basic principles and labelling	98
5.1.2	The two tPad designs	99
5.1.3	Method procedure	100
5.2	Results	104
5.2.1	Colour offset after mapping	105
5.2.2	Characterising the structural integrity of origami samples	110
5.2.3	Reliability and robustness of the multicolour method	124
5.3	Summary	128
6	Summary and Outlook	131
6.1	Thesis summary	131
6.2	Discussion and future tasks	133
	Appendix	137
	A Additional images	139
	B EGNAS	151
	C DNA sequences	153
	D List of abbreviations	165
	List of Figures	199
	List of Tables	201

Abstract

DNA nanotechnology has developed a versatile set of methods to utilise DNA self-assembly for the bottom-up construction of arbitrary two- and three-dimensional DNA objects in the nanometre size range, and to functionalise the structures with unprecedented site-specificity with nanoscale objects such as metallic and semiconductor nanoparticles, proteins, fluorescent dyes, or synthetic polymers. The advances in structure assembly have resulted in the application of functional DNA-based nanostructures in a gamut of fields from nanoelectronic circuitry, nanophotonics, sensing, drug delivery, to the use as host structure or calibration standard for different types of microscopy. However, the analytical means for characterising DNA-based nanostructures drag behind these advances. Open questions remain, amongst others in quantitative single-structure evaluation. While techniques such as atomic force microscopy (AFM) or transmission electron microscopy (TEM) offer feature resolution in the range of few nanometres, the number of evaluated structures is often limited by the time-consuming manual data analysis.

This thesis has introduced two new approaches to quantitative structure evaluation using AFM and super-resolution fluorescence microscopy (SRM). To obtain quantitative data, semi-automated computational image analysis routines were tailored in both approaches.

AFM was used to quantify the attachment yield and placement accuracy of poly(3-tri(ethylene glycol)thiophene)-b-oligodeoxynucleotide diblock copolymers on a rectangular DNA origami. This work has also introduced the first hybrid of DNA origami and a conjugated polymer that uses a highly defined polythiophene derivative synthesised via state-of-the-art Kumada catalyst-transfer polycondensation. Among the AFM-based studies on polymer-origami-hybrids, this was the first to attempt near-single molecule resolution, and the first to introduce computational image analysis. Using the FindFoci tool of the software ImageJ revealed attachment yields per handle between 26-33%, and determined a single block copolymer position with a precision of 80-90%. The analysis has pointed out parameters that potentially influence the attachment yield such as the handle density and already attached objects. Furthermore, it has suggested interactions between the attached polymer molecules.

The multicolour SRM approach used the principles of single-molecule high-resolution co-localisation (SHREC) to evaluate the structural integrity and the deposition side of the DNA origami frame “tPad” based on target distances and angles in a chiral fluorophore pattern the tPads were labelled with. The computational routine that was developed for image analysis utilised clustering to identify the patterns in a sample’s signals and to determine their characteristic distances and angles for hundreds of tPads simultaneously. The method excluded noise robustly, and depicted the moderate proportion of intact tPads in the samples correctly. With a registration error in the range of 10-15 nm after mapping of the colour channels, the precision of a single distance measurements on the origami appeared in the range of 20-30 nm.

By broadening the scope of computational AFM image analysis and taking on a new SRM approach for structure analysis, this work has presented working approaches towards new tools for quantitative analysis in DNA nanotechnology. Furthermore, the work has presented a new approach to constructing hybrid structures from DNA origami and conjugated polymers, which will open up new possibilities in the construction of nanoelectronic and nanophotonic structures.

Chapter 1

Introduction

1.1 Objective and thesis outline

Entering the nanoscale in science and technology has shaped the world we live in today. It is accountable for the remarkable progress in information technology (with the 10 nm node currently being introduced^[1]), has led to new kinds of functional materials in construction, clothing, or coatings and created new, interdisciplinary fields in physics, chemistry, medicine, and other sciences. Currently, nanofabrication relies on top-down methods. These methods, e.g., lithography, use large devices to carve smaller structures from bulk material, which reaches its limits as the structure sizes reach the molecular, or eventually the atomic level. Bottom-up processes build nanostructures from sub-nanometre precursors. Currently, they offer a strategy to augment the top-down methods, but hold the potential to replace it. Some bottom-up methods like dip-pen lithography, electron beam lithography or focused ion beam lithography use technically advanced, macroscopic instruments to manipulate individual molecules or atoms. Using controlled particle self-assemblies, however, requires less expensive equipment and promises a higher throughput.

Outstanding self-assembled structures occur in nature. Biological molecules like proteins, RNA, carbohydrates, lipids and DNA form target structures with sub-nanometre precision, for example, protein capsules of viruses, motor proteins that conduct linear or rotary movements, or lipid membranes. The self-assembly of a DNA double strand from two single strands is the most understood of the aforementioned processes to date. The field of DNA nanotechnology has developed routines to build artificial nanosized structures from DNA, and hybrids of those and various other nanomaterials. For the formation of such DNA-based nanostructures, robust and efficient protocols have been established in the past 30 years. As a result of its maturing, the field is moving on to exploring functionality and the application of DNA-based nanostructures in a gamut of fields such as nanomedicine, fluorescence microscopy, molecular scaffolding in nuclear magnetic resonance (NMR) spectroscopy or protein cryogenic electron microscopy (cryo-EM), structural biophysics, biosensing or plasmonics and photonics.

With this new focus, the demand for structure analysis beyond proof-of-principle structure formation, yield determination and standardized high-performance analysis routines will play an increasing role.

However, the analytical means for characterising DNA-based nanostructures drag behind the advances in other parts of the field^[2]. Characterisation usually relies on a small number of techniques that can provide the means and the resolution to probe thin layers of delicate biological nanoscale material. Gel electrophoresis and fluorescence techniques, for example, are suited for bulk characterisation. For resolving single structures and their features, atomic force microscopy (AFM) and transition electron microscopy (TEM) are the most common techniques, while super-resolution fluorescence microscopy (SRM) has also been used in combination with DNA nanotechnology.

Open questions remain regarding both the choice of methods as well as the type of analyses performed. Furthermore, if DNA templates shall eventually be used at industrial scale, suitable quality control methods have to account for both the bulk and the single structure, while being robust, scalable, and preferably feasible and low-tech. The current methods for bulk characterisation can possibly meet these demands with few adjustments. However, automating the most common single-molecule techniques to date, AFM and TEM, has still to overcome challenges, of which the automated image analysis and data processing is one of the most formidable. In order to achieve that, both methods would have to resolve the structural details of DNA templates at a higher resolution and contrast than they routinely do. Furthermore, origami analysis has often remained qualitative, proofing, for example, that a structure or functionality can be acquired in principle. Quantitative analyses, such as a yield determination for every step of forming particle-functionalised DNA nanostructures, or detailed comparisons of a structure design and assembled origami, are not routinely provided. For these tasks, protocols and methods need to be established that survey statistically relevant numbers of single origami structures.

This thesis seeks to promote quantitative structure evaluation in DNA origami-based nanofabrication. Objects under study are two two-dimensional (2D) origami structures. One is a cavity-bearing DNA frame referred to as tPad in the following. The other is a novel hybrid structure of a polythiophene derivative and a rectangular DNA origami named pad.

2D DNA origami objects were chosen here because such objects are the basis in numerous state-of-the-art studies, which utilise their uniquely addressable surfaces. 2D origami has served as pegboard for various nanomaterials. Cavity-bearing structures such as the tPad are attractive, because they can, on top of that, arrange objects precisely within the confined space, e.g., for single-molecule studies, or serve as lithography substrates^[3-5].

This work focuses on the two characterisation methods AFM and super-resolution microscopy as the most suitable for DNA-based 2D structures. Super-resolution microscopy has been used with DNA origami before, but only rarely for the structural characterisation of DNA origami templates. The presented SRM method explores a multicolour labelling strategy in order to extract nm-precise structural information together with positioning information for single DNA nanostructures. Unlike AFM, the SRM approach easily processes a statistically relevant number of specimen to characterise an entire sample. Thus, it is one of the few methods that combine single structure and bulk evaluation.

AFM is used in a first set of studies to quantify the assembly yield and thermal stability of the tPads. The characterisation of the frames provides new structural data for cavity-bearing DNA nanostructures using known AFM techniques. A second set of studies investigates the hybrid of the semiconducting polythiophene derivative and the origami pad. For that purpose, the particle analysis tool FindFoci^[6] was introduced to AFM images of these DNA-based nanostructures. This approach allows for collecting structural information such as object heights and positions semi-automatically.

The latter set of studies attempts semi-automatic quantitative structure analysis in a relatively young branch of DNA nanotechnology. Hybrids of DNA and metallic or semiconducting nanoparticles (NP) are part of one heavily studied field of DNA nanotechnology, which is creating nanoscale electronic, plasmonic and optoelectronic devices and circuits. Conjugated polymers (CPs), such as polythiophenes, have entered the field only recently. In contrast to the majority of polymers, CPs are intrinsically semiconducting due to the extended π -system along their polymer backbone; and through a process called doping, they can obtain almost metallic conductivity. CPs are assumed to play a key role in next-generation electronics^[7], because they combine electric and photonic properties with the promise of mechanical flexibility, low-cost, green, on-demand printing, scalability, low-power operation, and intelligence in signal processing^[8,9]. On the one hand, templating CPs with DNA origami has the potential to augment DNA-based systems. Unlike inorganic nanoparticles, single CP molecules can act as flexible nanoscale conductor, and offer a broad range to customise their properties via synthesis. On the other hand, DNA origami can

template useful structures for basic research in conjugated polymers. Studying single or few CP molecules has reportedly promoted the understanding of basic physical mechanisms behind electronic and photonic material performance^[10]. Furthermore, the assembly of CP molecules, for example, guided by π - π -stacking, greatly influences the optical and electronic properties of the material, and in the end the device performance^[11]. Numerous studies have reported on the assembly behaviour in thin films, however, few studies address this topic at the nanoscale with few molecules involved. Furthermore, single CP molecules are considered promising candidates for single-molecule electronics. However, the lack of reproducibility and the technical difficulty of constructing single-molecule junctions or assemble few CP molecules in a controlled fashion has greatly inhibited the research in these fields. DNA nanotechnology provides means to place single CP molecules with a precision and spatial control similar to or beyond that of current techniques for constructing single-molecule junctions, while being reproducible and straightforward in use at the same time. Despite this broad field of potential applications, examples of the incorporation of CPs into nanoscale DNA origami-based structures remain scarce in the literature^[12–14]. Only one of these approaches^[13,14] reports on the placement of single or few polymer molecules of polyphenylene vinylene (PPV) obtained via oxidative polymerisation.

The challenge going hand in hand with constructing such hybrids of DNA origami and single CP molecules is characterising them. Polymer molecules neither possess a fixed shape nor include strongly electron-scattering elements. Thus, they will not provide characteristic shapes in electron microscopy images, which is the technique of choice for metallic nanoparticles on DNA nanostructures. Due to their extended conjugated π -systems and the inevitable dispersity of their molecular weights, the optical properties of CPs are not as defined as, for example, those of a quantum dot or a small organic dye molecule either. Together with the structural flexibility of CP molecules, this renders super-resolution-based approaches unsuitable as well. While AFM was used before to characterise CPs on DNA origami^[12–14], this work presents the first attempt to determine the attachment yield and the accuracy of the positioning of the CPs on the near-single molecule level. Using the aforementioned computational particle analysis tool FindFoci for that purpose will both reduce human bias and provide quantitative data instead of just qualitative results.

This first chapter will introduce the field of DNA nanotechnology with emphasis on 2D origami and selected aspects under research in DNA origami. Furthermore, it will introduce DNA origami characterisation methods with focus on the application of AFM and super-resolution microscopy in DNA nanotechnology. As last field, conjugated polymers and DNA-polymer hybrids will be introduced.

Chapter 2 summarises the materials and methods used.

Chapter 3 reports on the design and synthesis of the 2D origami templates that will be used to construct the objects under study in the Chapters 4 and 5. Furthermore, Chapter 3 reports on the versatile use of liquid AFM for the quantitative evaluation of the DNA nanostructures. For the first time, this data is reported for a 2D origami structure with a cavity.

Chapter 4 presents a new method to place molecules of a water-soluble P3RT-type polythiophene derivative site-specifically on a 2D origami template. It focuses on the characterisation of the polymer-origami hybrids with high-resolution AFM using the FindFoci^[6] plugin of ImageJ^[15] for the semi-automated particle analysis.

Chapter 5 introduces a characterisation method that uses multicolour super-resolution microscopy and the principles of single-molecule high-resolution co-localisation (SHREC) to evaluate simultaneously the structural integrity, placement, orientation and deposition site of surface-bound origami structures.

Chapter 6 summarises the work.

1.2 DNA nanotechnology: structure assembly and current research areas

1.2.1 Structure assembly

Basic terminology in bottom-up assembly with DNA

Structural DNA nanotechnology, which includes DNA origami, has developed a number of methods to construct artificial, geometrically and topologically complex 2D and 3D DNA nanoobjects using the natural DNA self-assembly. The self-assembly of a DNA double strand from two single strands is called hybridisation. It relies on few basic principles that can be utilised easily for nanofabrication. Two important basics are the Watson-Crick base pairing between complementary bases^[16] and the fact that DNA double strands assume in principle one secondary structure.

Single-stranded DNA (ssDNA) is a biopolymer made of nucleotides comprising of a deoxy ribose unit, a phosphate unit and one of the four bases (b) adenine (A), thymine (T), cytosine (C) or guanine (G). During the hybridisation, each base forms hydrogen bonds with a base from the second single strand (Figure 1.1 a). Watson and Crick have discovered a specificity in this base pairing^[16], according to which adenine binds thymine with two hydrogen bonds and cytosine binds guanine with three hydrogen bonds under physiological conditions. Hence, the base sequences of the hybridising strands have to be complementary. Under physiological conditions, the resulting double strands always assume the so-called B-DNA conformation, a right-handed helix with a diameter of approximately 2 nm and a pitch of about 10.4 base pairs (bp), with a step of 0.34 nm per base pair (Figure 1.1 b).

The dissociation of a DNA double helix due to thermal denaturation is called melting. The temperature, at which 50 % of a DNA single strand is duplexed with its complementary strand, while the other 50 % are free in solution, is referred to as melting temperature T_M of that DNA single strand. T_M depends, amongst others, on the sequence, the concentration of the ssDNA and the monovalent and divalent ions in the DNA solution^[17].

While the Watson-Crick base pairing largely determines the formed structure, the hydrogen bonds in the base pairs are not the major stabilising force in a DNA double helix. One major contributor are stacking interactions^[18-21] (Figure 1.1 a). These are complex, non-covalent interactions between parallel layers of hydrogen-bonded base pairs with energy contributions from, for example, electrostatic (Coulomb energies), induction or dispersion (atom-atom potentials) energies^[19,22]. Stacking interactions do not just take place within a DNA double helix but also between terminal base pairs of two helices.

If at the end of a DNA double helix a terminal base pair occurs, it is referred to as a blunt end. Helix termini with single-stranded overhangs are referred to as sticky ends.

DNA nanotechnology's basic construction elements are such sticky ends, and the immobile, branched four-arm Holliday junction^[23] (Figure 1.1 c). This motif consisting of four arms joined at a central node occurs in the otherwise linear DNA double helices during DNA recombination. It can be constructed artificially from four oligodeoxynucleotides (ODNs) incorporating sequences that can hybridise to form the arms. To create an immobile junction, the ODN sequences on either side of the node must be non-complementary.

The sticky ends utilised in DNA nanotechnology are typically 6 - 20 b long. When a second DNA molecule carries a complementary sticky end, they hybridise and connect the two molecules (see also Section 1.2.1). The first immobile junction was proposed and constructed in 1982^[24] and 1983^[25], respectively, and the first artificial DNA nanoobject, a cube^[26] made of four junctions joined by sticky ends, in 1991.

Non-templated assembly: tile-based lattices, polyhedra, bricks and canvases

The first method to construct artificial DNA nanoobjects has been the tile-based assembly, which builds 2D and 3D¹ structures from short ODNs (20–60 b). The resulting structures can be roughly classified into wireframe structures and lattices.

Among the wireframe structures, which were reviewed by Simmel *et al.*^[27], are platonic solids like the aforementioned cube, tetrahedra, buckyballs, icosahedra or tubes. The cube was the first attempt of Nadrian C. Seeman *et al.* towards 3D DNA crystals that can co-localise proteins and other guest molecules, which Seeman proposed as the original goal behind DNA nanotechnology^[24,28]. Moving towards this goal, 2D lattice assembly with a predefined periodicity from a variety of DNA motifs was investigated as well (Figure 1.1 d). As a lattice building block, few strands were assembled into tiles with double crossover (DX)^[29] or triple crossover (TX)^[30] motifs, while the paranemic crossover (PX) motif has been used to build covalently linked 1D arrays^[31–33]. 2D lattices from one or several types of tiles as well as the organisation of nanoparticles or biomolecules on such lattices have been demonstrated. A recent review of lattice design, construction and applications was published by Chandransekaran *et al.*^[34].

A milestone towards the fulfilment of Seeman’s vision was the creation of a 3D lattice from DNA tensegrity triangular motifs^[35] that grow into macroscopic crystals^[36]. Following variations in the cavity size and using different asymmetric units, recent advances in stabilising the crystals^[37,38] have led to first applications of 3D crystals as hosts, for example, for polyaniline molecules^[39].

Among the drawbacks of tile-based assembly is the demand for a high control of the stoichiometry of the staple strands in the assembly solutions. Apart from the 3D crystals, the wireframe structures are comparably labile. Due to this, the first structure, an octahedron, could only be visualised by cryo-EM^[40] 13 years after introducing the first cube structure.

The 2D and 3D lattices have also long lacked size control. Finite 2D and 3D arrays have only emerged recently using the canvas^[41] and the brick approach^[42].

Templated assembly: DNA origami

Finite 2D DNA nanoobjects have been produced first in 2006 with a different method that has shaped the field: DNA origami^[45]. In contrast to the aforementioned approaches, DNA origami uses a long DNA single strand (template, scaffold strand) and folds and fixes it into the desired shape with custom-synthesised ODNs (staple strands) that are two orders of magnitude shorter than the template (Figure 1.1 e). The structure folds from the DNA single strands due to hybridisation in an annealing process that usually involves heating the strand solution above the melting temperature and a subsequent cooling procedure. The folding proceeds in near-quantitative yield without the need for purified staples. Besides the most common thermal annealing, annealing procedures at lower or at room temperature have been investigated that rely on chemicals^[46] or removing the secondary structures in the scaffold strand through mechanically manipulating single scaffold molecules^[47].

2D origami has been constructed in an abundance of shapes from simple geometrical figures to smiley faces^[45] or a map of China^[48]. Since the method’s invention, the structural complexity has evolved far beyond the initial 2D single layers. 3D structures were first fabricated by folding 2D origami into a hollow container^[49] and multilayer bricks^[50] followed by twisted bundles^[51] and hollow curved objects like spheres and flasks^[52]. Wireframe^[53] and mesh-like^[54–56] DNA origami structures have been reported as well.

Basic construction principles of DNA origami will be discussed in Chapter 3 using the examples of the rectangular pad and the frame-like tPad structures, which are both 2D origami. For the construction and structure prediction, different user-friendly software tools have been developed, which has been discussed in different reviews^[57,58]. The program caDNA^[59] is routinely used for DNA origami structure design

¹3D: three-dimensional

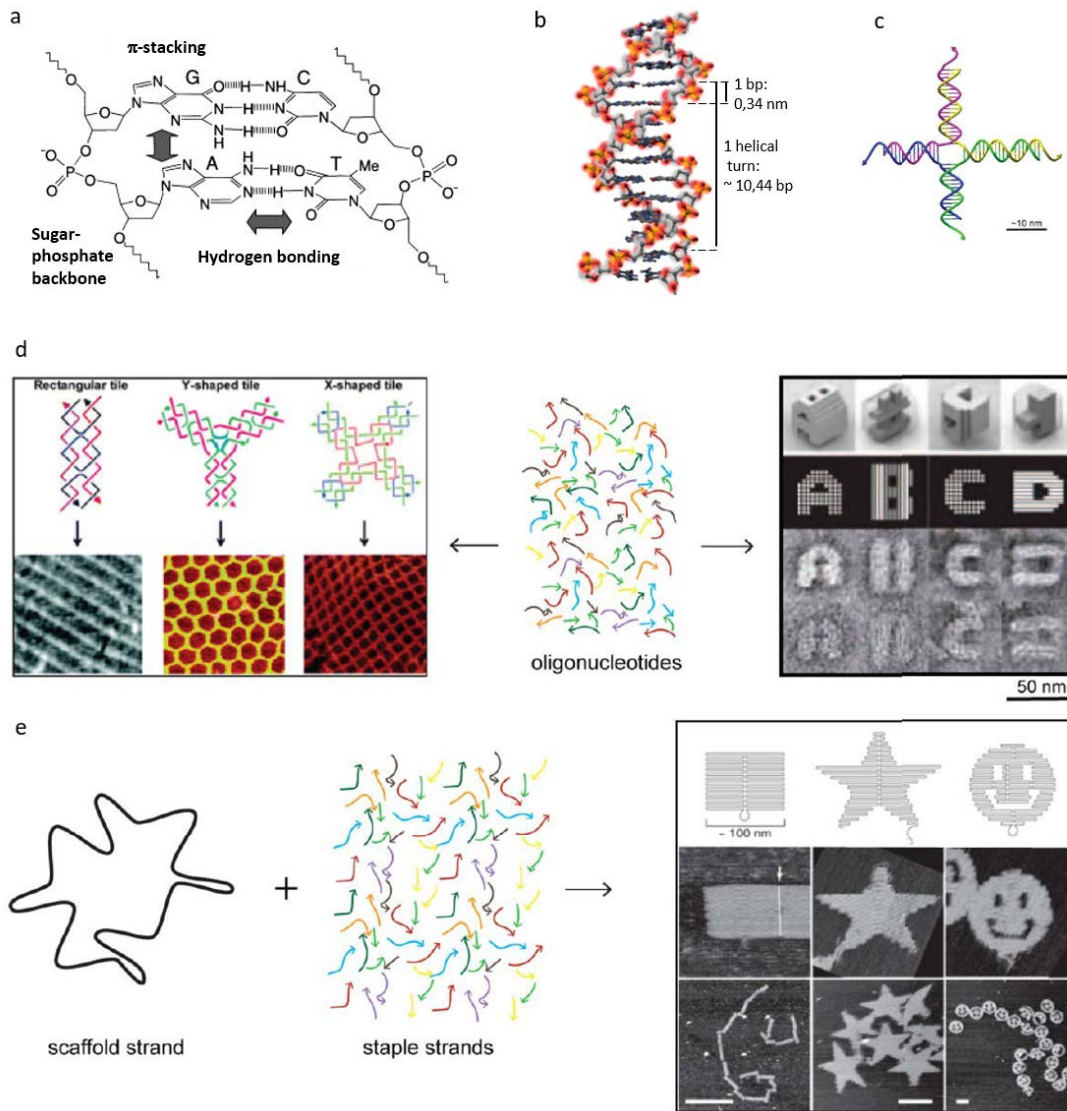


Figure 1.1: Structure formation in DNA nanotechnology. a) Detail of two hybridised single strands made of deoxy ribose and phosphate (sugar-phosphate backbone), and one of the four nucleobases adenine (A), guanine (G), cytosine (C) and thymine (T). It displays the Watson-Crick base pairs adenine-thymine with two hydrogen bonds and cytosine-guanine with three hydrogen bonds, and highlights π -stacking interactions between the nucleobases. Adapted with permission from^[43]. Copyright 2002 Japanese Photochemistry Association. b) Double-stranded DNA helix. Adapted from^[44]. c) Holliday junction with sticky ends. d) Non-templated assembly of DNA nanostructures: tiles, bricks. e) Templated assembly: DNA origami. Parts c), d) and e) adapted with permission from^[2]. Copyright 2017 American Chemical Society.

based on a square or a honeycomb lattice. The program CanDo^[60,61] allows predicting the shape and structure of designed DNA nanostructures, as they would occur in solution. For wireframe structures, the program vHelix^[54] has been introduced. The interface DAEDALUS^[62] takes design automation one step further, as it automatically converts any 3D solid object (in the form of CAD files) into the sequences from which the object can be assembled².

More detailed overviews over DNA origami structure formation and applications have been published recently by Hong *et al.*^[69] and Xavier and Chandrasekaran^[58].

Pinning on the pegboards: attaching nanomaterials to DNA origami

A unique strength of DNA origami is the capability of its surfaces to serve as pegboards for various nanomaterials, for which examples are listed in Section 1.2.2. On such a surface made of B-DNA helices, each base can be an attachment point, which translates into a surface addressability of 0.34 nm. For adjacent objects, a spatial resolution of below 2 nm has been reported^[70].

For the dictated binding of nanomaterials to origami pegboards, the conjugation of sticky ends, molecular recognition elements or reacting groups to the staple units introduces functional anchor points to the DNA. The units act as capturing strands for the secondary precise chemical binding of components to the origami structures^[71]. A variety of chemical functional groups such as amino, sulfhydryl, azide or biotin can be introduced during solid phase DNA synthesis, which nowadays relies on phosphoramidite chemistry^[72-74], or as a postsynthetic modification on the solid support outside the synthesiser^[75]. In both cases, the DNA is fixed on the solid support and features hydrophobic protecting groups. Thus, the procedure can also be useful for attaching hydrophobic components such as synthetic polymers to hydrophilic DNA^[13,14].

However, attaching nanoscale objects to DNA origami utilises mostly sticky ends^[76]. The single strand protruding from the origami surface will be referred to as handle in this thesis, while the single strand attached to the objects will be denoted as oligodeoxynucleotide (ODN). The DNA double strand that results from the hybridisation of handle and ODN, and that eventually connects the object to the DNA origami will be named link (Figure 1.2 a).

Most studies utilise handles and ODNs made of one either nucleotide, often poly(T) or poly(A). Sequences, in which a subsequence is repeated several times, will be referred to as sliding sequences in the following^[77]. In contrast, sequences with all four nucleotides added in a non-repeating order will be called specific sequences. Using sliding sequences can be advantageous for the binding yield, because it does not matter which of its complementary bases a base binds as long as enough base pairs are formed to yield a double strand with a melting temperature above the surrounding temperature. Thus, sliding sequences tolerate errors in the DNA synthesis better. Furthermore, the single strands can slide along each other until the maximum number of base pairs is formed, without detaching in the process (Figure 1.2). In addition, they provide more possibilities for an initial attachment, which can translate into a higher attachment probability. Specific sequences, however, allow for the highest spatial binding resolution due to their uniqueness.

Apart from the sequence, the length of the link influences the binding yield, as it determines the melting temperature, too. To promote object binding, the cooperative effect of multiple links that bind one object can be used, which has been the case in many studies with metallic nanoparticles^[78-80].

²Other computational tools include Seeman's JUNKART^[63], the programs for sequence symmetry minimisation of oligonucleotides in DNA complexes SEQUIN^[64] and UNIQUIMER^[65] and the programs for the design, visualisation and analysis of DNA motifs and structures GIDEON^[66], TIAMAT^[67] and UNIQUIMER 3D^[68].

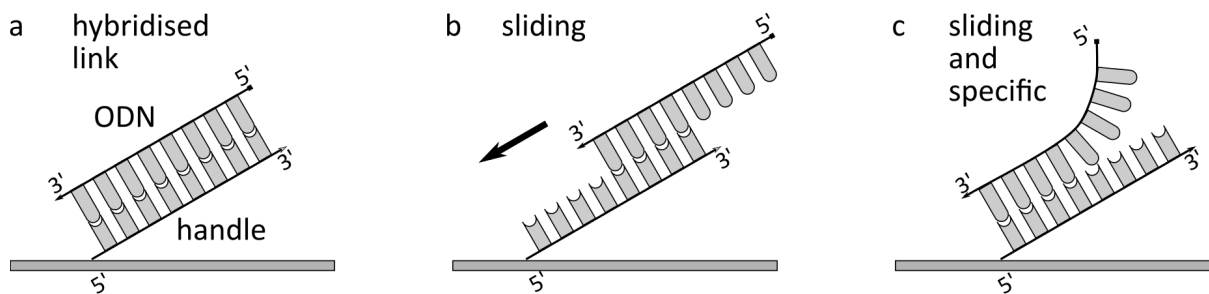


Figure 1.2: Forming a double-stranded DNA link with specific and sliding sequences. a) Double-stranded link with the handle fixed to a DNA origami at the 5' end, and the ODN hybridising from solution. b) Initial attachment possible with the sliding sequence: any base of the ODN can bind any base of the handle, and “slide” into the energetically most favourable position (direction indicated by black arrow), which yields the maximum number of base pairs without detachment in the process. c) Every base binds its complementary in the first place. For specific sequences, it is the only scenario that guarantees a full hybridisation without detachment in the process. Sliding sequences can behave like this as well.

Sequence engineering. It can be negative for the attachment yield if handles or ODNs can form secondary structures such as hairpins, if they fold back onto themselves (self-complementarity) or if they are so similar to a sequence in the DNA origami that they might rather bind there than at their designated place. Sequence engineering considers intrastrand and interstrand interactions during the sequence design to avoid the aforementioned complications. Computational sequence engineering tools are, for example, SEQUIN, UNIQUIMER or EGNAS (Exhaustive Generation of Nucleic Acid Sequences)^[77]. EGNAS was used to generate specific sequences for labelling of tPad, which will be discussed in Section 3.2.1.

Surface and cavities in 2D origami structures: pegboards, masks and frames

2D origami pegboards can have either continuous surfaces or feature cavities (Figure 1.3). 2D DNA origami with continuous surfaces allow for the full pegboard addressability, resolution and stability. Especially rectangular shapes such as the initial long rectangle^[45], also known as Rothemund rectangular origami (RRO), have become a standard structure for the assembly of various nanomaterials (see Section 1.2.2). The sides of the initial triangle have been used for the same purpose^[78,81]. For the co-assembly of proteins, a facial structure has been reported as well^[82].

2D origami with cavities can serve different purposes. Firstly, not filling a shape steadily saves material. As the scaffold length limits the DNA origami size, this is a mean to create bigger structures, which can also serve as frames for the incorporation of filling material like DNA tiles^[83]. Furthermore, complex, hollow shapes can serve as lithography templates^[3-5,84-86]. This can offer surface structuring as fine as with electron beam lithography, but at lower cost and in a highly parallel manner. A third aspect is arranging objects in the cavity. In some cases, such as constructing plasmonic devices^[87] or for fluorescence studies, it can be desirable to minimize an object’s interaction with DNA to reduce its effect on the device functionality. Several studies have used the cavity as stabilising moulds for nanoscale object deposition^[87-91], or as a framework structure for single-molecule studies, which was reviewed by Endo and Sugiyama^[92]. A fourth aspect is that objects in a cavity can directly interact with the substrate.

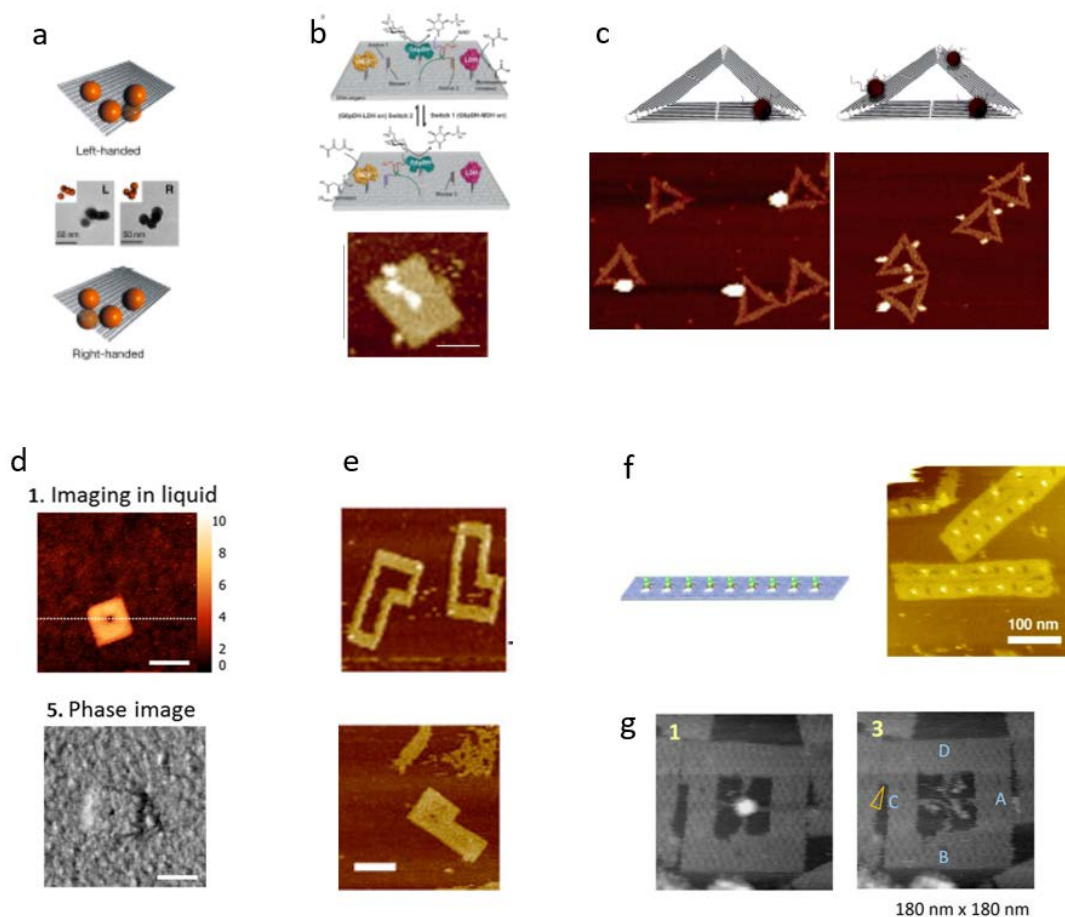


Figure 1.3: 2D origami with continuous surfaces and cavities for various applications. Continuous surfaces serve, e. g., as pegboards for a) gold nanoparticles, b) enzymes or c) quantum dots (assembled on a side of a triangular origami). Origami with surface cavities can be useful as d) lithography templates, e) as a frame for larger 2D origami, f) for the confined placement of proteins or g) as a frame for single-molecule studies. Images reprinted with permission from: a)^[93]. Copyright 2013 American Chemical Society, b)^[94]. Copyright 2016 WILEY-VCH Verlag GmbH & Co. KGaA, Weinheim, c)^[95]. 2014 Royal Society of Chemistry, d)^[5]. Copyright 2016 American Chemical Society, e)^[83]. Copyright 2014 American Chemical Society, f)^[89]. Copyright 2009 WILEY-VCH Verlag GmbH & Co. KGaA, Weinheim, g)^[92]. Copyright 2014 American Chemical Society.

1.2.2 Current fields of research

DNA origami application

As stated before, exploring applications plays a major role in current DNA nanotechnology research. DNA origami can be used without functionalisation, e. g., as a lithography mask (Figure 1.3 d), but most applications rely on hybrids of DNA origami and other nanomaterials. The key feature in many cases is the origami's templating ability in 2D and 3D, and especially assembling complex geometries in three dimensions is more feasible than with conventional lithographic approaches. For several applications excellent reviews are available, which include biosensing, drug delivery, protein functionalisation, scaffolding and enzyme cascades, DNA nanostructures for the structural elucidation of macromolecules, structural biophysics, and molecular scaffolding^[58].

The fields relevant to this thesis are nanoelectronics, nanophotonics and plasmonics, and DNA origami in fluorescence techniques. While they have been reviewed thoroughly as well^[96–99], brief introductions to the fields will be provided here to set the frame for this work. The topic of DNA origami in fluorescence techniques will be discussed in Section 1.3.

Nanoelectronics and nanophotonics. For electrical circuitry, DNA itself could serve as a nanowire given its size and shape. However, it is not conductive^[100]. Metallizing DNA strands, e. g., through seeded growth^[101], can create conductive paths. A first approach does this with small molecules that attach to the DNA, a second approach deposits nanoparticles. Using both, but focussing on the nanoparticle deposition, DNA origami metallisation was thoroughly studied as well^[102–105]. However, few reports mention electrical measurements^[103,104], which indicates that further research is needed.

Organising metal nanoparticles (NP) such as gold nanoparticles (AuNP) and silver nanoparticles, other semiconductor nanoparticles (NPs), or CNTs^[106] on DNA nanostructures is also the basis for plasmonic applications. As DNA can be attached to a gold surface easily using thiol-functionalised strands and the strong gold-thiol bond, and since AuNP show a surface plasmon resonance in the visible range, AuNP are the most frequently utilised among the attached nanoparticles. Researchers have created an abundance of plasmonic 2D and 3D structures, which include tile-based lattices as well as DNA origami. 2D origami structures include, for example, AuNP placed on origami nanoflowers^[107] or a line of AuNP placed size-selectively on a triangle^[78]. 2D origami sheets with a linear chain of AuNP have also been rolled up into DNA tubes to create chiral gold nanohelices^[108]. Another approach towards such helices used DNA origami tubes^[79]. For chiral gold tetramers, AuNP have been assembled on a 2D origami rectangle^[93]. Other 3D assemblies of AuNP rely on DNA polyhedral frames^[109]. Furthermore, gold nanorods (AuNR) have shown strong chiroptical activities as part of an assembly on 2D origami^[110]. They have been used in anisotropic dimer structures^[111] or AuNR helices with 2D origami as the connecting layer between them^[112]. Furthermore, AuNR have been used as part of dynamic plasmonic systems such a reconfigurable cross of two 14-helix bundles^[113] or a DNA-functionalised nanorod plasmonic walker on a DNA origami platform^[114]. With AuNP, SERS (surface-enhanced Raman scattering)-active structures^[87,115–118], nanolenses^[119] or polarisers^[79] have also been created.

Formation of DNA origami structures

As evidenced by the recent additions to the assembly strategies' toolbox^[53,54], structure formation continues to be a vibrant field of research as well. The following paragraph introduces some of the current topics under research, as they are relevant for this work, without aiming at a full overview.

Size increase, including the use of stacking interactions. Amongst others, research in DNA origami structure formation is concerned with making DNA origami suitable for large-scale applications, which involves, e. g., cost reduction or creating larger structures. Unlike in tile-based assemblies, the length of the scaffold limits the DNA origami size. To create larger structures, longer scaffolds^[120–122],

jigsaw approaches^[123,124], filling origami frames with tiles^[83], creating origami with smaller origami as building blocks^[125,126] or stacking approaches including shape complementarity^[127] have been discussed. So far, using origami as building blocks for larger origami has provided the most promising yields^[125,126]. Some of the upscaling efforts involve the base-stacking interactions introduced in Section 1.2.1. In both 2D and 3D origami with blunt ends on their edges, the base-stacking interactions of the terminal base pairs lead to aggregation, an effect that will be referred to as stacking in the following. For rectangles^[45] and for cubes^[128], chain formation has been reported where stacking has played a role. Besides occurring in chains, stacking has been used in the jigsaw approach^[123,124] towards larger origami.

While stacking can be useful on the one hand, it can lead to unwanted aggregation of origami on the other hand. The simplest approach to avoiding it is to replace blunt ends on the origami edges with single-stranded parts. Woo *et al.*^[129] have conducted an AFM-based study on how to control stacking of rectangular origami through the design of the origami edges. It investigated the ratio of single-stranded helix ends vs. blunt ends necessary to avoid stacking. Furthermore, it showed how different levels of confinement of the blunt ends influence the stacking behaviour of the origami.

Structural resilience. Several studies have investigated the structural and functional resilience of origami structures in respect of various chemical and physical parameters such as cation concentration, temperature, mechanical stress, or under conditions relevant for nanomedical applications. Hahn *et al.*^[130] have reported on the enzymatic digestions as well as the design- and time-dependent decay of origami structures upon cation depletion in cell culture medium. Jiang *et al.*^[131] have studied the degradation of a DNA origami box in serum, a nuclease degradation agent, in order to evaluate the *in vivo* stability of DNA origami. Wang *et al.*^[132] have screened compatible buffer conditions for both a tubular DNA origami and protein crystallisation. Ramakrishnan *et al.*^[133] have studied origami at varying temperatures in the presence of chaotropic agents that are used in the investigation of conformational changes in protein molecules. Kim *et al.*^[134] have focused on the structural preservation of 2D origami triangles bound to the surface of a silicon wafer upon thermal annealing, washing with organic or aqueous solvents and UV/O₂ treatment.

Melting in solution and folding. The thermal stability is crucial for the usefulness of origami templates. DNA origami can encounter elevated temperatures during annealing steps for the attachment of nanosized material, the formation of larger origami^[123,126,135], or *in vivo* when aiming for the use in nanomedicine^[136,137]. Several studies have investigated the melting behaviour with different methods. These studies are often part of folding studies. Two of the AFM-based studies in this regard were presented by Song *et al.*^[138] (melting and reassembly) and Lee Tin Wah *et al.*^[139] (folding and melting).

Folding. Understanding the folding pathways of origami structures is considered a great help to develop models^[140–142] that will aid in the designing of complex structures and improve the yield. Folding and melting are interconnected. Among the parameters to consider in the folding and melting are design choices such as origami bending and template permutation^[143], staple-strand routing and length^[141,143–145] or the staple excess^[139,146–148]. Furthermore, cooperativity in staple binding plays a big role^[139,143,144,149]. Different methods have been employed to monitor folding^[150], such as UV/VIS absorption spectroscopy^[151], real-time fluorometric monitoring of a folding reaction combined with cryogenic quenching for native gel electrophoresis and TEM studies of the folding intermediates^[143], or Förster resonance energy transfer (FRET)^[49,147,152] and single-molecule FRET^[47].

AFM has also been employed, and it has allowed for studies on the single-molecule level. The invention of the well-controlled hot stage AFM added a valuable tool and has been employed in studies by Song *et al.*^[138,146], Lee Tin Wah *et al.*^[139] and Majikes *et al.*^[148]. In these studies, the partly folded structures at different temperatures were imaged with AFM, and ideas about the folding pathway could be derived after image analysis. In the work of Lee Tin Wah *et al.*^[139], a semi-automatic image analysis routine based on ImageJ 2.0 has been employed.

1.3 Overview over the current techniques for the structural characterisation of DNA origami

Currently, origami templates and origami-based nanostructures can be characterised by a variety of methods. Only recently, Mathur *et al.*^[2] have provided an excellent overview of the state of the art of analytical methods in DNA origami. The summary table of their findings is reproduced here as Table 1.1.

Table 1.1: Overview of representative characterisation techniques for DNA origami. Adapted with permission from^[2]. Copyright 2017 American Chemical Society. The original references were included into this work’s references.

Name	Type of structure	Information provided	Drawbacks	Ref.
Electrophoresis	2D, 3D DNA structures; NP/ligand modified structures	Assembly yield; crude estimate of NP incorporation	Lacks single oligo resolution; cannot tell if all oligos are correctly incorporated	[42,60] [153,154]
AFM	2D DNA structures; NP/protein modified structures	Overall dimensional analysis; visualize structural reconstruction by counting structures	Invasive in nature and can disrupt structural integrity; cannot provide structural info on bp level	[45,153,155] [144,156]
TEM	2D, 3D DNA structures; NP-labelled structures	Overall dimensional analysis; visualize structural reconstruction by counting structures	Invasive in nature and can disrupt structural integrity; cannot provide structural info on bp level	[60,157] [52,158]
UV-absorbance	2D, 3D DNA structures; NP/dye-labelled structures	Whether NP/ligand incorporation was successful or not, quantification	Cannot distinguish between fully and partially labelled structures	[159,160]
Confocal microscopy	2D, 3D DNA structures labelled with dyes	Visual information on co-localisation of structures inside cell	Lacks resolution to provide info on spatial arrangement of dyes on DNA structures	[161–163]
Fluorescence spectroscopy	2D, 3D DNA structures labelled with dyes	Spatiotemporal dynamics of DNA structures; estimated incorporation of dyes and NP	Requires high concentration and large volume of sample; cannot distinguish fully vs. partially labelled structures	[49,143] [164,165]
DLS	DNA structures 5-10 nm per side or larger	Estimate dimensions	Requires high concentration and large volume of sample; lacks contrast to analyse NP-labelled DNA structures	[166–168]
Small-angle X-ray scattering	2D, 3D DNA reconstructible structures	Estimate dimensions	Invasive in nature, may be destructive, fine structure details not available	[49,169]

The most common methods are AFM, TEM (including cryo-EM), agarose and polyacrylamide gel electrophoresis, fluorescence microscopy and fluorescence spectroscopy techniques. The latter allows single-molecule or bulk measurements, exploiting, for example, FRET or fluorescence of deposited objects on a surface. The use of small-angle X-ray scattering (SAXS) and dynamic light scattering (DLS) has also been reported. The following subsection focuses on gel electrophoresis, AFM and fluorescence techniques including super-resolution microscopy, which are most relevant in this thesis. For these methods, the subsection describes their modes of operation, their application in DNA origami, and compares their advantages and shortcomings.

1.3.1 Gel electrophoresis

Gel electrophoresis is a common analysis method for macromolecules like DNA, RNA, proteins and fragments thereof that separates a bulk sample by molecule size and/or charge in an electric field. It can also be applied for nanoparticles^[170]. A porous agarose or polyacrylamide matrix is prepared by frame-casting molten agarose or a mixture of acrylamide and *N,N'*-methylene bisacrylamide monomers, the free radical stabiliser *N,N,N',N'*-tetramethylethane-1,2-diamine (TEMED) and the source of free radicals, ammonium persulfate (APS) that initiates the reaction. DNA and RNA appear negatively charged in aqueous solutions. Upon applying the electric field, the charged molecules will move towards the positive pole through the porous agarose or polyacrylamide matrix. Travelling through the matrix sieves the molecules, i. e. sorts them by length, because smaller molecules pass through more easily. The matrix preserves the separation and commonly, the gels are stained to visualise it after the preparation. Gel electrophoresis can be applied for analytical or preparative purposes^[171,172].

In DNA nanotechnology, gel electrophoresis was among the first tools ever used^[26]. It can provide structural information about the size of a DNA nanoobject as well as its structural integrity and stability. Fluorescent and radioactive labelling has been used in this technique as well^[173]. While gel electrophoresis allows for bulk characterisation of DNA origami structures in solution, it cannot provide information about single origami structures or surface-deposited origami.

1.3.2 Atomic force microscopy

Atomic force microscopy^[174] (AFM) is a type of scanning probe microscopy with resolution in the range of fractions of a nanometre for inorganic samples. The typical setup of an AFM is shown in Figure 1.4 a. The flat-spring-like component (a) is called cantilever. It is typically made of silicon or silicon nitride. It is fixed onto a substrate (b), which can be handled by the operator to transfer the cantilever into the microscope. On the free end of the cantilever is a tip (or probe) (c) with a radius of curvature in the order of nanometres. For imaging, the cantilever is raster-scanned over the sample (d), which is mounted to a sample stage (e). Depending on the instrument, scanning is done either by moving the sample stage or the cantilever (or both) in the *xy*-plane. The tip is placed at a height that permits its interaction with the sample on the atomic scale. Depending on the scanning mode, these interactions can be attractive or repulsive (Figure 1.4 b) and involve different forces such as mechanical contact forces, van der Waals forces, capillary forces, chemical bonding, electrostatic forces or magnetic forces. The interactions change with tip-sample distance according to the sample topography, causing a change in the cantilever motion. On the back of the tip, a laser beam is focused, which is reflected into a four-quadrant photodiode (Figure 1.4 f). It detects the deviation of the cantilever position from an expected value and converts it into an electric signal that is proportional to the cantilever's displacement.

There is a number of operational modes for the AFM suited for different applications. For imaging, the modes can be roughly divided into static and dynamic modes. Nowadays, a feedback loop is commonly used in either imaging mode. The static mode is also called contact mode, as the tip is in firm contact with the sample (and thus, also in the repulsive regime). The changes in the sample topography change the deflection of the cantilever directly, which is then used to generate the image (constant height mode). Alternatively, the feedback loop regulates the cantilever position to keep the tip force on the sample at a set value (constant force mode). In contact mode, the tips can wear off quickly and soft samples such as DNA can be damaged.

The dynamic modes can be divided into the non-contact mode and the tapping or intermitted contact mode. In non-contact mode, the tip is positioned above the surface and oscillated at either its resonance frequency or just above that to generate an amplitude in the range of a few nanometres (< 10 nm) down

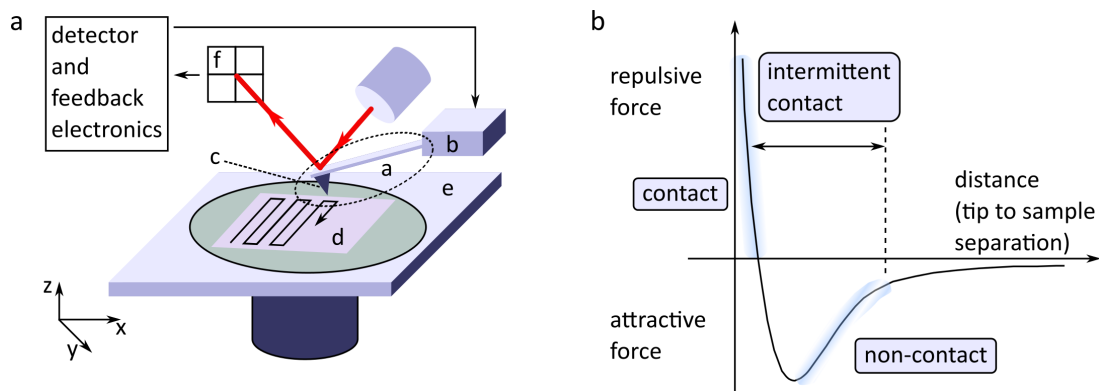


Figure 1.4: Atomic force microscopy (AFM). a) Schematic setup of an atomic force microscope. b) Changes in the force between tip and sample depending on the tip-sample distance.

to a few picometres. The interactions of the tip with the surface decrease the resonance frequency of the cantilever, and consequently, its current amplitude. The feedback loop will correct the tip-sample distance to keep either the frequency or the amplitude constant. The tip-sample distance is used to generate the topographic image. A major concern in non-contact AFM is the liquid meniscus that typically forms on a sample surface at ambient conditions. It can be included in the image, or the tip can be stuck during scanning, which both leads to image artefacts. Tapping mode circumvents this issue, and is the mode most frequently used under ambient conditions to date. Again, the cantilever is oscillated near its resonance frequency, but at an amplitude of several nanometres up to 200 nm, so the tip is pulled out of the liquid layers in each oscillation. Furthermore, the tip contacts the sample surface at the lowest point of the oscillation. The peak force the tip applies to the sample at the minimum point of the oscillation can be higher than the average force applied in contact mode. However, as the impact is short and retracting the tip prevents significant lateral forces, the sample damage tends to be less than in contact mode. As in contact mode, lowering the tip-sample distance changes the tip's resonance frequency and its amplitude. The feedback loop counteracts the amplitude decrease by lifting the tip until a previously determined set point amplitude is reached. Again, these corrections are used for image generation. In addition to topographic images, phase images can be acquired in tapping mode. They map the shift in the phase between the cantilever's oscillation and that of the driving signal. This phase shift provides information about the energy dissipation of the cantilever in each oscillation cycle. That is, regions of varying stiffness or adhesion properties can provide a contrast not visible in the topographic image. In addition to the topography, other sample properties can be mapped with similarly high resolutions. These can be mechanical properties like stiffness (Young's modulus) or adhesion strength, and electrical properties such as conductivity or surface potential. Furthermore, force spectroscopy can be performed as point measurement in either the static or the dynamic modes.

Atomic force microscopy is one of the preferred methods to characterise DNA nanostructures^[97] and was the first technique to visualise the structure and correct folding of DNA origami^[45]. It has been a versatile tool to characterise DNA in general because it allows direct imaging. Furthermore, AFM can be performed in air and in liquid, that is, in the aqueous natural environment of DNA, and in tapping mode it inflicts only moderate force on the scanned sample^[175]. Furthermore, sample preparation is straightforward and fast.

To avoid image artefacts and achieve nanometre resolution with AFM, the substrates must be atomically flat. The most common substrate used with DNA origami is mica, followed by silica. The use of highly oriented pyrolytic graphite (HOPG)^[176] and molybdenum disulphide (MoS_2)^[177] have also been reported. Both mica and DNA are negatively charged in aqueous media. The most popular strategy to adsorb DNA onto mica nevertheless is adding divalent cations to the DNA solution^[178,179] or (additionally) pre-incubating mica with a divalent cation solution, which render mica positively charged by replacing

the K^+ ions in the binding sites. Among the divalent cations appropriate for DNA binding are Ni^{2+} , Co^{2+} and Zn^{2+} , while for DNA origami, Ni^{2+} and Mg^{2+} are used most frequently. While transition metal cations such as Ni^{2+} form irreversible directional bonds to the mica and kinetically trap DNA, Mg^{2+} is constantly exchanged with residual K^+ and H^+ on the mica surface and provides only a relatively weak diffusion adhesion of the DNA. Lee *et al.*^[180] have utilised this to tune the translational freedom, which adsorbed the DNA strongly enough for high-speed scanning, but allowed enough mobility for DNA-protein-interaction to take place. Another adsorption strategy for DNA onto mica involves the peptide poly-L-ornithine^[172] instead of divalent cations.

As it probes a surface, AFM is particularly suitable for topographical imaging of 2D origami. High-resolution AFM images³ depict the weave formed by the parallel DNA double helices, which zigzag along their axis due to the periodically placed interconnects^[45].

AFM is also well suited to study a variety of characteristics. As mentioned in Section 1.2.2, Song *et al.*^[138] have studied the melting and reassembly of rectangular DNA origami bound on mica using thermally controlled AFM. Lee Tin Wah *et al.*^[139] have studied the folding and melting pathways of a rectangular origami in solution by quenching and imaging at different stages of the processes.

Various studies use AFM and DNA origami as the aiding structure for single-molecule studies^[181]. Voigt *et al.*^[182] have monitored single-molecule chemical reactions, that is, the site- and chemoselective cleavage of disulphide bonds and 1,2-bis(alkylthio)ethene moieties, as well as Huisgen-Sharpless-Meldal copper(I)-catalysed click reactions and amide bond formations between primary amines and *N*-hydroxysuccinimide ester moieties.

Fast scanning applications (high-speed AFM or HS-AFM^[183]) allow monitoring dynamic processes^[184]. Endo and Sugiyama^[92] have summarised the use of a DNA origami frame as a scaffold to directly observe single enzyme molecules such as DNA-methyltransferase, DNA base-excision repair enzymes (such as 8-oxoguanine glycosylase and T4 pyrimidine dimer glycosylase) and DNA recombinase. Furthermore, they describe the direct imaging of structural changes in DNA origami (such as G-quadruplex formation and disruption), of the hybridisation and dissociation of photoresponsive oligonucleotides and of the B-Z-transition of DNA in the equilibrium state, or the single-molecule observation of RNA-RNA kissing interactions^[185]. Furthermore, they have directly observed a mobile DNA nanomachine moving along a track on a DNA origami surface^[186].

Although AFM has been a versatile characterisation tool for DNA origami, the method has its shortcomings. Despite using the tapping mode, the AFM tip, surface deposition or the drying for AFM in air can damage the sample^[184,187]. Furthermore, surface deposition can alter the natural behaviour of DNA^[92,139,180]. Unless HS-AFM is used, AFM is slow and hence limited in sample throughput. As mentioned above, the choice of substrate is limited. Furthermore, AFM struggles with three-dimensional imaging and certain material contrasts, which, for example, hampers depicting the size of AuNPs correctly. Thus, for 3D origami and origami functionalised with, e.g., AuNPs or quantum dots (QDs), TEM provides the better image quality.

1.3.3 Fluorescence techniques

While gel electrophoresis, TEM and AFM cover the field of structural evaluation, fluorescence-based techniques have been the methods of choice for *in-situ* studies, and for monitoring dynamics processes involving DNA origami, such as the assembly and melting of 2D and 3D origami^[147], or for studies with origami as the substrate, e.g., for DNA walkers^[186,188], or multi-enzyme complexes^[189]⁴.

In fluorescence measurements, the object under study is illuminated with light of a wavelength that will be absorbed by the attached fluorophores such as organic dye molecules, quantum dots, metallic

³such as Figure 3.3

⁴Recently, HS-AFM has been employed for such studies as well.

nanoparticles or polymer molecules. This induces light emission from the fluorophores at wavelengths higher than that of the absorbed light. The emitted or fluorescent light is detected separately from the absorbed light using spectral emission filters. The fluorescent light yields qualitative and quantitative information, and is used for image generation in fluorescence microscopy. Figure 1.5 a shows the schematic setup of a fluorescence microscope⁵.

Fluorescence measurements on DNA origami can be performed on the surface or in solution, being less or non-invasive, respectively. First, fluorescence studies have been performed in bulk^[49,186,188]. However, this averages a sample and conceals the contributions of minor populations (such as malfunctioning devices, side products). Single-molecule fluorescence techniques can provide this information, and have become a staple in DNA nanotechnology. They will be discussed separately in the following.

One tool used frequently in both bulk and single-molecule studies^[70,190] is Förster resonance energy transfer^[191]. FRET is a mechanism of nonradiative energy transfer between a donor chromophore in its excited electronic state to an acceptor chromophore through dipole-dipole coupling. Structural parameters of DNA origami in a broader sense, such as origami dimerisation^[192,193] or the opening and closing of a DNA origami box with a lid^[49] have been studied using fluorescence quenching, single-molecule FRET and alternating laser excitation techniques (smFRET/ALEX), or FRET in bulk, respectively. The energy transfer is inversely proportional to the sixth power of the distance. Therefore, FRET is very sensitive to small changes in the chromophore distance, but functional at distances below 8-10 nm only. All of the studies mentioned before use organic dye molecules as fluorescent labels. For labelling, and more often as object under study, quantum dots are used as well^[81,95].

1.3.4 Super-resolution microscopy

Super-resolution fluorescence microscopy, or just super-resolution microscopy (SRM), includes a number of fluorescence microscopy techniques that overcome the diffraction limit in resolving details of an imaged specimen. The diffraction limit describes the fact that due to the diffraction of light on the lenses or mirrors of optical systems, even an infinitely small point source of light (also referred to as emitter or fluorophore here) appears as a finite volume spot. This spot is known as point spread function (PSF), and it is specific of every microscope.

If two point sources on a specimen are located so close that their PSFs overlap in the detected image, they cannot be resolved (Figure 1.5 b I). Frequently, the diffraction-limited resolution in the focal plane is quantified as approximately $0.5 \lambda / \text{NA}$, with λ being the wavelength of light and NA the numerical aperture of the microscope lens. This approximation is based on the works by Abbe^[194] and Rayleigh^[195]. Fluorescence microscopy uses UV or visible light in the range of approximately 400 - 700 nm. Using optical components with the highest NA, the resolution limit lies at around 200 nm in this case. However, if a single point source is isolated from any other sources in its vicinity, and given that sufficient photons occur in the spot, the centre of the PSF, which is equal to the centre of the emitting point source, can be located with arbitrary precision^[196]. For that purpose, the PSFs are approximated with fit functions as shown exemplarily in Figure 1.5 c with a 2D Gaussian fit to a resolution-limited raw data image.

Popular SRM techniques are stimulated emission depletion (STED) microscopy^[197], structured illumination microscopy (SIM)^[198], and single-molecule localisation microscopy (SMLM) techniques such as photoactivated localisation microscopy (PALM)^[199], fluorescent PALM (FPALM)^[200] or stochastic optical reconstruction microscopy (STORM)^[201] and direct STORM (dSTORM)^[202]. In the first SRM study on DNA origami, dSTORM and Blink Microscopy^[203] were applied to resolve a distance of about 89 nm between two dye molecules on an origami rectangle^[204].

To date, STED microscopy^[205] and STORM^[206] have been applied with DNA origami. These techniques

⁵Here, a particular setup for total internal reflection fluorescence (TIRF) microscopy is shown.

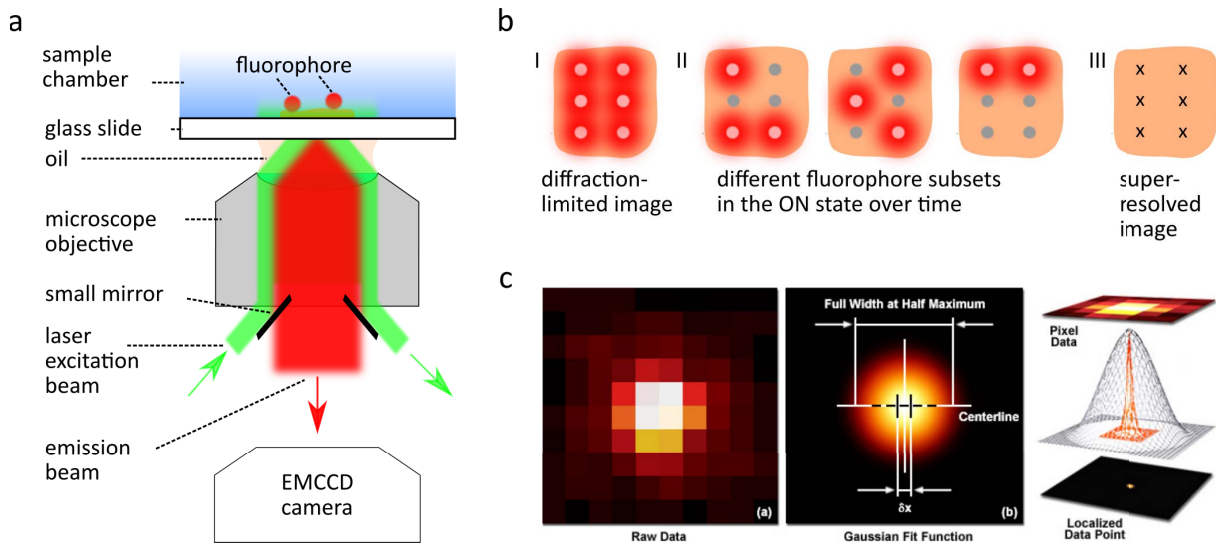


Figure 1.5: Super-resolution microscopy principles. a) Scheme of fluorescent imaging with total internal reflection (TIRF) excitation. b) Principle of overcoming the diffraction limit by isolating and stochastic switching of the emitters on a structure of interest. c) Determining the centre of a diffraction-limited spot with a Gaussian fit function. Reprinted with permission from Carl Zeiss GmbH.

use different principles to isolate emitters and generate the super-resolved images of the emitter positions. In STED microscopy, single or few point sources in a focal spot will emit photons at their usual fluorescence wavelength, while in their vicinity, stimulated emission causes a red shift of the wavelength of the emitted photon, allowing for ignoring them in the detection process. STED microscopy allows taking images at subdiffraction resolution, while STORM, and in general the SMLM techniques, use mathematical models to generate those images from many sets of diffraction-limited images. In each diffraction-limited image, a random but sparse subset of the multiple emitters on a specimen is put into the ON state. That is, this subset is emitting photons, which results in spatially separated PSFs. Both STORM and PALM use stochastic switching, but execute it differently. For both, the imaging procedure starts in the OFF state. PALM and FPALM use proteins that occur in the OFF state natively, and start emitting when excited. In STORM, illumination with light of the suitable wavelength and intensity sets emitters into the OFF state. When stochastically switching the emitters between ON and OFF state, the subset of active emitters changes randomly throughout the set of diffraction-limited images (Figure 1.5 b). Mathematically fitting the centres of the PSFs with sub-nanometre precision and trueness (Figure 1.5 c) in each image and combining all images of a set afterwards yields the super-resolution image.

SRM techniques have introduced a new quality to fluorescence microscopy studies of DNA origami in terms of single-structure evaluation. The techniques provide spatial resolution in the range of 5-10 nm in the xy -plane^[207] and 20 nm along the z -axis^[208], which is in the range of TEM and AFM. They are suitable for 2D and 3D origami and operate in buffer. Furthermore, they are fast and more flexible in scanned sample area and substrate material compared to TEM and AFM. Due to the comparably large fields of view in the range of above 50 μm , SRM potentially outperforms AFM and TEM in terms of sample throughput. As fluorophore signals yield highly contrasted images, software tools for image and data analysis can be implied straightforwardly, which is not the case for AFM or TEM. This opens up potential for automation.

A group of studies focuses on DNA origami as a tool in super-resolution microscopy. It was used, e. g., as a nanoruler both in 2D^[204,209] and 3D^[206] and for fluorescence intensity standard calibration^[210], method development^[211,212] or barcoding^[213]. For DNA nanorulers, protocols from production to data analysis have been carefully established^[214], which led to nanorulers becoming the first commercial product using DNA nanotechnology^[209]. Jungmann *et al.*^[215] used DNA origami as material under study to develop and demonstrate the DNA PAINT technique, which is a DNA-based derivative of the point accumulation for

imaging in nanoscale topography (PAINT) technique^[216]. As in other SMLM techniques, DNA PAINT utilises the successive localisation of single molecules, but provides the necessary switching of ON and OFF state through transient hybridisation. For that purpose, the object under study is equipped with DNA handles. When complementary, fluorophore-labelled, short ODNs (6-11 nucleotides^[209]) hybridise with the handles, it leads to a burst in fluorescence. As the formed double strand is thermally unstable, the ODN will detach after a period of time depending on the length of the double strand, and revert the handle position to the dark state. This setting considerably increases the site-specificity of the labelling in PAINT, as it uses the unique recognition properties of DNA. Besides DNA nanorulers and DNA PAINT, studies in DNA origami focus on biomolecular processes at the single-molecule level on the origami, i. e. hybridisation kinetics^[217], and, as mentioned before, on smFRET^[70,190].

Although it is not among the popular SRM applications described above, super-resolution microscopy can be used as well to evaluate the DNA origami itself. Possible properties of interest accessible with SRM are the presence of DNA origami objects at designated positions on a surface, their orientation on the surface, their deposition side and, given the sub-nm resolution of the methods, the structural integrity of the DNA origami objects. The term deposition side will be used here for the origami surface that faces the substrate⁶. However, few studies have focused on these possibilities so far^[2].

Regarding the presence of origami on a surface position, Pibiri *et al.*^[163] used single-molecule fluorescence microscopy to evaluate the placement of surface-bound origami labelled with one type of fluorophores within patterned surface cavities. For the structural characterisation of DNA origami, Iinuma *et al.*^[120], for example, have investigated structural properties of 3D origami polyhedra. Regarding the deposition side or orientation, no super-resolution technique has been used to determine that yet.

Most of the SRM studies in the evaluation of DNA origami use one type of fluorophore. However, this limits the possibilities of such investigations. It is not necessarily due to resolution, as distinguishing two fluorophores of the same colour at 6 nm distance on origami has already been demonstrated^[218]. However, evaluating the deposition site and orientation of the DNA origami on the surface, for example, is hampered, as it is difficult to create a pattern whose orientation can be assigned unambiguously to a certain case. Furthermore, achieving a high resolution with one type of fluorophores is time-consuming, because a large number of images with isolated emitters has to be obtained.

A multicolour approach abolishes some of these limitations. Multicolour SMLM uses the frequency space to isolate emitters in an image^[219,220] instead of the stochastic ON/OFF state switching, as in STORM and PALM. That is, different features of the structure under test are labelled with fluorophores with different excitation and emission wavelengths. Furthermore, they are imaged using different optical pathways in the imaging apparatus. In cell biology, this concept has been applied successfully for decades^[221].

For evaluating the structural integrity of surface-bound DNA origami, a set of target distances and angles between different fluorophores could be used. Such a target value approach has been demonstrated as well with one type of fluorophore in the aforementioned study on DNA origami polyhedra by Iinuma *et al.*^[120]. That work used 3D DNA PAINT to localise the vertices, which carry 18 docking strands each to ensure its imaging. Iinuma *et al.* have obtained a resolution of about 13 nm in x and y , and about 24 nm in z , with a localisation accuracy of the single DNA PAINT binding events of 5.4 nm in x and y , and 9.8 nm in z .

Using multiple fluorophore types and one permanently attached molecule per binding site can potentially improve these values. Furthermore, it is straightforward to generate chiral labelling patterns with more than one colour, which give unambiguous information about the origami placement, orientation and deposition side.

The multicolour approach in this work uses the principles of single-molecule high-resolution co-localisation

⁶Determining the deposition side can be of interest, e. g., for placing origami on a chip as part of electrical circuitry.

(SHREC)^[219]. This SMLM technique focuses on determining the distances between two single fluorescent molecules that emit at different wavelengths^[219,220,222,223]. The distances lie in the size range of 10-200 nm^[219], that is, between that of FRET and diffraction-limited microscopy. The SHREC approach also allows monitoring dynamic processes such as the walking mechanism of a myosin V molecular motor^[219], or, when the rotation of the emitter pair is blocked, studying the emitters' relative orientations^[220]. In the original work on SHREC^[219], the static distance of a Cy3 and a Cy5 molecule on a 30 bp DNA duplex with the length of 10.2 nm was determined as 10 ± 1 nm⁷. For Cy3/Alexa 647 pairs on DNA duplexes at distances from 105 bp to 145 bp, Pertsinidis *et al.*^[224] have reported an absolute distance accuracy of 0.77 nm⁸, with a statistical uncertainty in the localisation of a single fluorophore molecule of 0.3 nm.

In this work a SHREC approach with three different fluorophores will be applied, which are attached to the DNA origami prior to deposition.

1.4 Precision and trueness in SRM and multicolour co-localisation approaches

As SMLM techniques apply mathematical models and statistical techniques to determine super-resolved fluorophore positions, precision and trueness must always be discussed together with the absolute data. Instead of the term “trueness”, accuracy has been used frequently to name the same parameter. In this work trueness is used to follow the suggestions of ISO 5725-1:1994(en)^[225].

In this work fluorophore (emitter) positions are localised in the xy -plane, i. e. in 2D. If one determines the true position of the emitter coordinates $(x_t; y_t)$ as the average from the position in n images, the localisation precision describes the spread of the n single position measurements $(x_i; y_i)$ around their mean values $(\bar{x}; \bar{y})$. The trueness describes the deviation of the mean values $(\bar{x}; \bar{y})$ from the true position coordinates $(x_t; y_t)$. The mean position $(\bar{x}; \bar{y})$ is the fluorophore position in the super-resolution image. In the simplest case, these coordinates are calculated as arithmetic means as given in (1.1):

$$\bar{c} = \frac{\sum_{i=1}^n c_i}{n} \quad c = \{x; y\}. \quad (1.1)$$

Localisation precision and trueness for single fluorophores. In Chapter 5 the position of the same point source in n images $(x_i; y_i)$ is averaged to generate the super-resolution image with the super-resolved emitter position $(\bar{x}; \bar{y})$, and precision and trueness are discussed in that regard. The following part focuses on the precision and trueness of the point source position in a single one of these images based on the detected positions of the photons emitted by the point source.

The position of the emitter's centre in a single image, i. e. the centre of the PSF, is the location of maximum photon count. To approximate the PSF's centre from the position-depending photon count, mathematical models are computed. In this work a 2D Gaussian approximation of the PSF will be used. As they can be computed fast, these approximations are frequently used^[226] for emitters that are, as the ones described here, isotropic and in or close to the focal plane^[227]. That the emitters used in this work are isotropic can be assumed because the fluorophores are attached to flexible DNA linkers that allow a rapid thermal motion^[220].

For the localisation precision, the key factor is the number of photons detected from one emitter^[222].

⁷482 molecules, 95 % confidence interval from 1000 bootstrap distributions

⁸1 σ confidence interval

It can be limited because of the photostability of a fluorescent dye. That is, due to damage by the excitation light, the fluorophore will possibly stop emitting at some point in the experiment, which is referred to as (photo)bleaching. Furthermore, fluorescence intermittency, also called blinking, can play a role. Blinking is the random and not reproducible switching between the ON and OFF state under continuous emitter excitation, which is connected to the competition of radiative and non-radiative relaxation pathways^[228,229].

Several factors influence the distribution of the detected photons. There are static factors such as the emission profile of the emitter, the PSF of the microscope that can be distorted by spherical aberration, coma and astigmatism^[222], or the pixelation of the detector. Furthermore, there are two important categories of noise, i. e. stochastic factors. The first is shot noise. It results from a temporary distribution of the photons in a spot, which do not arrive steadily in a certain time interval, but follow a Poisson distribution. The shot noise is defined as the standard deviation of the Poisson distribution. The second noise category is background noise. It can occur due to out-of-focus fluorescence (extraneous fluorescence in the microscope, e. g., due to dust, cellular autofluorescence), readout noise, dark current, and other factors.

The best localisation precision theoretically possible is given by the square root of the Cramer-Rao lower bound (CRLB)^[230]. For modelling the emitter image in 2D, the limit of the localisation precision can be expressed through more simple analytical equations instead. For the localisation in two dimensions, Thompson *et al.*^[231] have derived equation (1.2) for a Gaussian approximation of the PSF, with u_c being the uncertainty in each dimension:

$$u_c = \sqrt{\langle(\Delta c)^2\rangle} = \sqrt{\frac{s^2 + a^2/12}{N} + \frac{8\pi s^4 b^2}{a^2 N^2}} \quad c = \{x; y\}. \quad (1.2)$$

This equation accounts for both shot noise and background noise, and it considers the role of pixelation noise in both of these. Here, N is the number of the photons collected, s is the standard deviation of the point spread function (here Gaussian), a is the size of a pixel, and b is the background noise.

Equations for calculating the localisation uncertainties are often directly implemented in image analysis routines for position tracking, for example, ThunderSTORM^[232], and provide u_c together with the position coordinates of a fluorophore in a single image. A way to limit background noise through out-of-focus fluorescence is using total internal reflection fluorescence (TIRF) microscopy^[233,234], which is schematically depicted in Figure 1.5 a. This technique uses an evanescent field to illuminate fluorophores. As the field decays exponentially, it only excites fluorophores in a restricted layer of approximately 100-200 nm above the glass-water surface, and omits fluorescent signals from deeper layers of the sample.

Systematic effects such as drift and vibration of the measurement setup, imperfections in the optics and detector or an asymmetric emission profile of the fluorophores influence the localisation trueness. Drift is a relative movement of the sample and the optical instrument during the imaging process due to temperature changes or mechanical relaxation effects. While SRM experiments can take up to hours, drift can be in the range of several hundred nanometres over the course of several minutes^[235], hence, it must always be corrected. In order to correct the drift, several approaches can be used. One of them is tracking fiduciary markers. Fiduciary markers are fluorescent objects that are introduced additionally to a sample, and that do not bleach significantly over time. Commonly used markers are, for example, gold nanoparticles, quantum dots or fluorescent beads.

The marker trajectories provide a reliable base to correct the drift. However, this requires the right marker concentration to avoid overpowering the structure of interest while providing enough signal for the correction, and adjusting the imaging parameters and the instrument for proper marker recording. This includes, for example, imaging the marker in exactly the same plane as the sample^[222]. An alternative approach to drift correction, which is applied in this work, uses the structure of interest itself instead of fiduciary markers^[236,237]. As the shape of the structure stays the same, cross-correlation techniques can

be applied to determine spatial shifts of the structure between subsequent images. Mlodzianoski *et al.*^[235] have demonstrated that cross-correlation can also be applied in SRM experiments, where different subsets of molecules emit over different points of the recording.

Co-localisation in multicolour SRM. Multicolour imaging makes a precise and accurate localisation of fluorophores inherently more complex than with one type of fluorophore. Firstly, the localisation errors $SE_{x,y}$ of the fluorophore coordinates can vary between different colour channels due to different emitter properties, variations in the different optical pathways, and varying noise and drift behaviour. Secondly, a multicolour approach has to ensure the correct co-localisation of the different fluorophores in the super-resolution image.

In multicolour imaging, different fluorophores can be imaged either sequentially, simultaneously or using different viewpoints^[222,238]. In this work the sequential approach is used. Here the fluorophore types are excited and captured one after the other on the full size of the camera’s CCD chip. While it is slower than the other approaches, it makes use of a larger field of view, reduces loss of light due to fewer components in the emission pathway, decreases optical aberrations, and introduces minimal crosstalk between the different colour channels^[222].

A key step in the multicolour method is image registration. That is combining images of the same field of view of different colour channels into one image that contains all fluorophore positions. However, switching between the different imaging pathways slightly shifts the field of view, and hence, the relative positions of the different fluorophores of one spot are error-prone. The position shift will be referred to as colour offset in the following. In this work it lies in the range of 50-100 nm in the x - and y -direction, which is already in the size range of the target distances. Therefore, instead of overlaying the images of the different colour channels, geometric transformations must be established between the datasets of fluorophore coordinates in order to view them correctly in the same coordinate system^[238].

Transferring the coordinates of one channel to a second channel is called mapping between channels^[219,220,222,223]. If more than two different fluorophores are used, one channel is chosen as the basis the other channels are mapped onto. To generate a set of coordinates to infer the mapping from, feature-based registration with fiduciary markers as in drift correction is common practice. For that purpose, fluorescent beads that emit in all the imaged colour channels are frequently used^[238]. Calibrating the mapping is inferring a function for the coordinate transfer. The simplest function would be a vector that is constant at any position in the field of view. However, there is a slow variation in the colour offset throughout the field of view due to chromatic aberrations of the optics^[223]. This could be modelled with an appropriate mathematical function, which would result in one global mapping function for the whole image. However, there are additional, short-range variations, for which different sources are suggested⁹. To account for the short range variations, several studies^[219,223,224] use local-weighted mean mapping. For that purpose, Goshtasby *et al.* propose a weighted sum of second-order polynomials that is determined locally around marker points visible in both colour channels^[239]. In this work the MATLAB function “fitgeotrans” of the Image Processing Toolbox, which replaces the “cp2tform” function used by Churchman *et al.*^[240], executes the mapping for all markers in a field of view. Applying a perfect mapping function should result in mapping the position of a marker in one channel onto its actual image in the other channel. However, instead of perfect mapping, random registration errors remain^[219,224], which determine the trueness of a fluorophore distance measurement. In this work (Chapter 5) this uncertainty due to the colour offset will be denoted as r .

⁹While some studies name small imperfections in the optics, especially the microscopes objective^[222] or the “mathematical shapes of lens designs and the actual physical shapes of lenses” in general^[223], Pertsinidis *et al.*^[224] propose the position-dependent response on the CCD camera, which they refer to as interpixel photoresponse non-uniformity (PRNU). Pertsinidis *et al.* state that “the mapping could be improved significantly if [...] all centroids [were imaged] on the same detector pixel”.

1.5 Towards the assembly of CP molecules with DNA origami and possible applications

As discussed in Section 1.2.2, nanoelectronics and nanophotonics are major fields of research for the application of DNA-based nanostructures, with most studies focussing on AuNP-DNA hybrids. Only recently, another type of nanomaterial with potential as electrical nanowire and photonic component has been introduced to DNA origami, which is conjugated polymers (CPs).

Unlike inorganic components, conjugated polymers combine semiconducting or conducting behaviour with properties of synthetic polymers such as mechanical flexibility or tuneable and low-cost synthesis that yield custom material characteristics. As also discussed in Section 1.2.2, arranging CPs with DNA origami is attractive for both augmenting DNA-based electronic and photonic structures, and as a new approach to placing CP molecules with nanometre precision for research purposes.

This work focuses on the AFM-based structural characterisation of a CP-DNA origami hybrid. However, choosing a polythiophene derivate as the CP, and building the hybrid the way it will be shown¹⁰ had in mind to enable the use of the hybrid for the aforementioned purposes in future research. In order to provide an understanding for the choices that were made consequently in the hybrid design, the following section introduces basic information on the structure of conjugated polymers and the structure-property relationships that need to be considered to yield functional material. Furthermore, the section gives an overview over approaches to arranging single or few CP molecules at the nanoscale using top-down and DNA-based bottom up techniques to shed light on possible applications of the novel hybrid.

1.5.1 Conjugated polymers

Since the discovery of CPs in the 1970's by A. J. Heeger, A. MacDiarmid and H. Shirakawa^[241–244], research efforts have resulted in a gamut of CP varieties and synthesis strategies. A comprehensive introduction to the field is beyond the scope of this thesis, and can be found in many reviews and books.

In order to introduce representative CPs and syntheses, Appendix Figure A.1 presents an overview according to Morin *et al.*^[8], who group CPs into three generations according to the progress in material properties and synthesis. According to the authors, the driving forces for proceeding from the first to the second CP generation was preparing solution-processable instead of infusible, insoluble rigid-rod conjugated polymers. Solubilising the polymers, which will play a role in this work as well, introduced peripheral flexible side chains to the polymer backbone^[245], which increased the structural complexity.

Charge carrier generation and transport

In contrast to the majority of polymers, conjugated polymers possess a system of conjugated double bonds along the polymer backbone. Thus, CPs display the electronic and optoelectronic properties of semiconductors or, if in a doped state, of metallic conductors.

If just two monomers hybridised, their p_z -orbitals would form a π - and a π^* -orbital as shown in Figure 1.6 aI. In a polymer chain, the hybridisation of all p_z -orbitals of a chain would increase the energy level density until a continuous, half-filled energy band would form. The π -electrons would be delocalised over the entire polymer chain, giving it the properties of a metallic conductor. However, instead of a completely delocalised system, the single and double bonds are localised due to the Peierls distortion^[246]. Therefore, a fully occupied π -band and an unoccupied π^* -band form (Figure 1.6 aII).

¹⁰that is, by attaching diblock copolymers to the origami through a single link each

The π -band is referred to as the valence band or highest occupied molecular orbital (HOMO), and the π^* -band as conduction band or lowest unoccupied molecular orbital (LUMO)¹¹. The energy gap between the HOMO and LUMO is called band gap, which has the band gap energy E_g . The band gap energies for conjugated polymers typically lie between 0.9 eV and 3 eV, which is in the range of a semiconductor (0.1 - 4 eV)^[247]. This energy range corresponds to radiation in the near ultraviolet, visible and near infrared regime (400 - 1400 nm). Absorption of the suitable energy promotes electrons from the valence band to the conduction band, leaving a positively charged hole in the valence band. On the one hand, these electron-hole pairs (excitons) can be separated by an electric field and become free electric charge carriers¹². This principle is used in organic field effect transistors (OFETs)^[11], for example. On the other hand, the electron can relax back into the valence band under photon emission. This photoluminescence provides the basis for optical applications of CPs such as organic light emitting diodes (OLEDs).

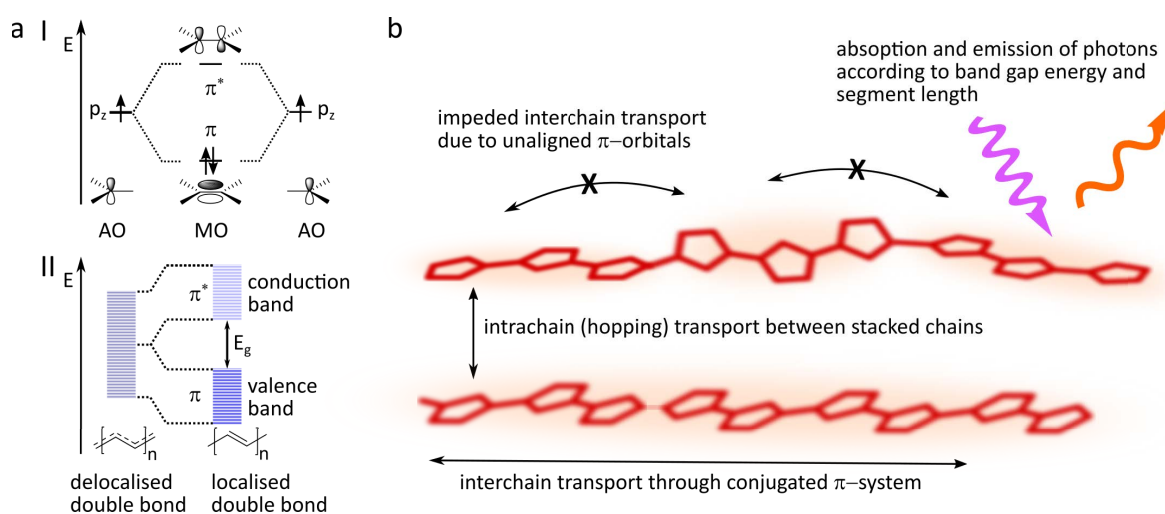


Figure 1.6: Conductance in conjugated polymers. a) Formation of π - (HOMO) and π^* - (LUMO) orbitals for polyacetylene as an example CP. (I) Two hybridised monomers. AO: atomic orbital; MO: molecular orbital. (II) Acetylene polymer chain: due to the Peierls distortion^[246], the double bonds are localised instead of delocalised, which leads to a separated conduction and valence bands. Adapted from^[11]. b) Excitons in a polymer chain. The intrachain mobility of excitons, which can be generated by photon absorption, is limited to segments of a polymer chain (red-shaped areas) if the alignment of the π -orbitals is disturbed. In addition to intrachain transport, interchain hopping transfer of excitons through space can occur towards lower energy segments, as well as photon emission from relaxing trapped excitons, which is specific for the conjugation length of a segment.

Intrachain transport is the charge carrier movement within one polymer chain (Figure 1.6 b). It is determined by the number of monomers in one plane, which is the conjugation length. Because the polymer chain conformation can be free to change through rotation and bending, the effective conjugation length is mostly not equal to the chain length. The effective conjugation length strongly affects the absorption spectrum of a polymer, which has been exploited, for example, for sensor applications^[248-251].

Interchain transport is the charge carrier transport along multiple chains (Figure 1.6 b), which involves transitioning of charge carriers between the chains (hopping). It largely affects the performance of organic semiconductor films^[10] as their microstructure displays a significantly higher structural and energetic disorder than present in inorganic solids. This includes localised states, chain ends and grain boundaries.

¹¹Recent publications on conjugated polymers use mostly the terms HOMO and LUMO only.

¹²The excitons are Frenkel excitons that are mainly located at one molecule by high bonding energies, and diffuse as uncharged electron-hole pair for few nanometres only. That is due to the weak intermolecular interactions in CPs compared to inorganic semiconductors, which limit the extension of the electronic wave function.

Structure-property relationships in charge carrier transport and synthesis strategies

For improving material and device performance, understanding the structure-property relationship regarding the CP and its charge carrier characteristics is key^[252]. In order to optimise intrachain and interchain transport, structural order must be maintained at multiple levels of CP-including devices.

To facilitate the hopping transport of charge carriers, close short-range π - π -stacking is beneficial, and more vital than a highly ordered crystalline structure^[253]. For short-range π - π -stacking, amongst others, the molecular structure of the single polymer molecule plays a key role. Already after the first syntheses of processable poly(3-alkylthiophene)s, for example, it became evident that a high degree of regioregularity was favourable for device performance^[254]. To achieve a high effective conjugation length for intrachain transport, reducing the conformational disorder is vital, which can be done, e.g., through coplanar repeating units and through minimizing torsion opportunities in the chain. Other influential properties are, for example, the molecular weight^[255–258], the dispersity^[259,260] and end-groups^[261–263].

Tuning the aforementioned and other structural properties on the molecular level requires highly controlled synthesis strategies. Here, transition metal-catalysed cross-coupling reactions such as Kumada, Suzuki-Miyaura, Heck, Stille, Negishi, Hiyama, and Sonogashira play a key role^[264–266]. Many of these cross-coupling reactions, such as the Stille and Suzuki coupling^[267,268] follow a step-growth polycondensation mechanism.

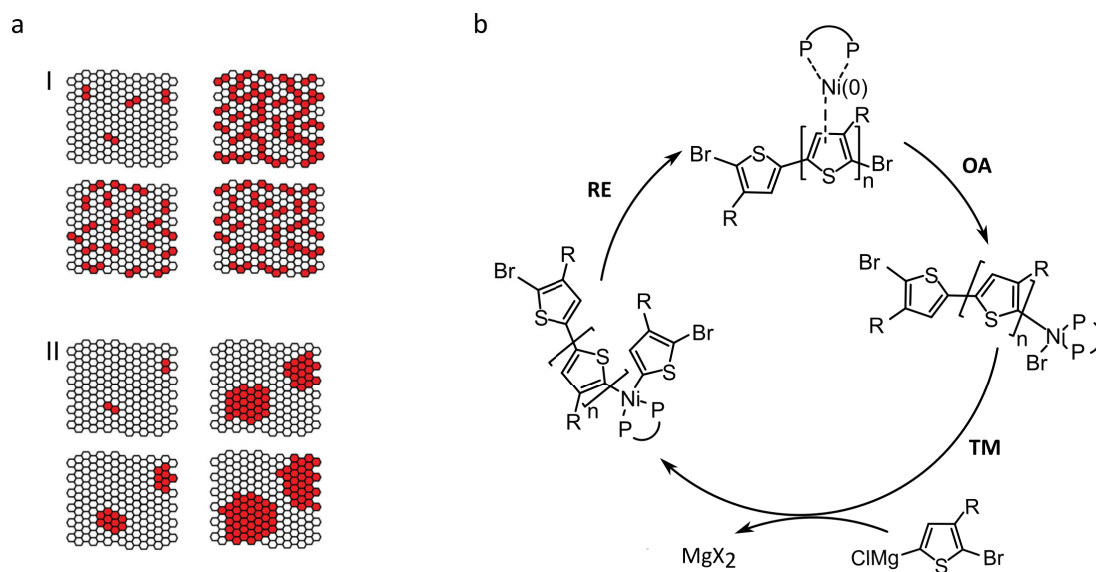


Figure 1.7: Mechanisms of metal-catalysed polymerisations. a) I: Step growth: increase of the molecular weight through reactions between monomers, oligomers and polymers. II: Chain growth: nucleation and repeated additions of monomers to a growing polymer chain. Reproduced with permission from^[269]. Copyright 2016 Royal Society of Chemistry. b) Catalytic cycle of the chain-growth Kumada catalyst-transfer polycondensation for poly(3-hexylthiophene). OA: oxidative addition; RE: reductive elimination; TM: transmetalation. The half circle connecting the two phosphorous atoms indicates a bidendate ligand. Adapted with permission from^[270]. Copyright 2011 John Wiley and Sons.

Step-growth polycondensations (Figure 1.7aI) proceed with little control over molecular weight, dispersity and end-groups. On the contrary, living chain growth polymerisations (Figure 1.7aII) provide this control, and numerous of these techniques have been established^[271]. The main approach to developing those is converting an uncontrolled polymerisation into a catalyst-transfer polymerisation (CTP)^[271]. CTPs utilise a system-specific affinity of catalyst and monomer that circumvents catalyst detachment from the growing chain during the reaction. As an example, the Kumada catalyst-transfer polycondensation (KCTP) for the synthesis of poly(3-hexylthiophene) is given in Figure 1.7b.

1.5.2 Polythiophene and water-soluble, regioregular, end-functionalised derivatives via state-of-the-art synthesis

In this thesis, a block copolymer (BCP) of DNA and the regioregular head-to-tail polythiophene poly(3-tri(ethylene glycol)thiophene)¹³ (P3(EO)₃T) is used for site-specific positioning on DNA origami templates.

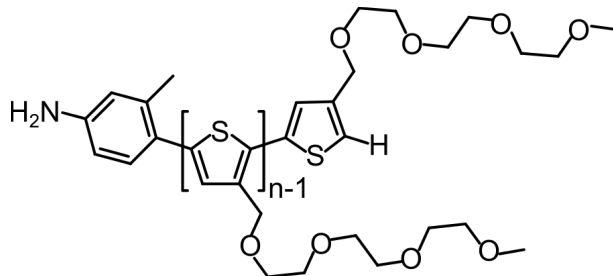


Figure 1.8: Regioregular, water-soluble poly(3-tri(ethylene glycol)thiophene) (P3(EO)₃T) with amine starting groups via *ex situ* initiated KCTP used in this work for the deposition on DNA origami^[172]. Adapted with permission from^[172]. Copyright 2017 American Chemical Society.

Polythiophenes are a group of conjugated polymers with backbones made from five-membered aromatic rings containing a sulphur atom. Unsubstituted polythiophene (PT) molecules are semiflexible in solution and tend to aggregate. Thus, PT is poorly soluble, which has spurred the research into PT derivatives. Both PT and its derivatives are amongst the most investigated conjugated polymers due to their excellent optoelectronic properties (such as a tuneable fluorescence, FRET, tuneable electrical conductivity)^[272–274], low-cost synthesis, excellent environmental and thermal stability, mechanical strength and magnetic properties^[275–279]. For several polythiophene derivatives, a large hole mobility, a narrow band gap (E_g about 1.9 eV) and a good solubility have been reported. The materials can potentially be used in sensors^[280–282], organic photovoltaics^[283–285], organic field-effect transistors^[286–288], organic light emitting diodes^[289–291], and for biomedical applications^[292–294].

The P3(EO)₃T used in this work proved to be a performant material. Its potential as a p-type semiconductor in organic field-effect transistors was reported by Shao *et al.*^[286].

Common strategies to obtain soluble PT derivatives are side chain functionalisation^[295–297], in most cases at the β -carbon atoms, the synthesis of copolymers of PT with processable polymers^[298–300], or a combination of both strategies^[301–303]. Introducing the side chains to the five-membered core allows fine-tuning the solubility and the optoelectronic properties as well^[304]. The P3(EO)₃T used in this work has triethylene glycol side chains to make it water-soluble¹⁴ in order to facilitate its use in the aqueous environment of DNA origami.

For PT derivatives with sidechains, a key factor for proper backbone alignment is the regiochemistry. Increasing the proportion of the head-to-tail (HT) monomer orientation in poly(3-alkylthiophene) chains, for example, has been identified as a significant performance enhancer soon after the first studies on the material^[254]. PT and its derivatives have been synthesised via electrochemical polymerisation^[306–308] and chemical oxidation polymerisation^[309–311].

The first syntheses yielded a HT proportion of 50–60 %^[312]. By introducing metal-catalysed polymerisation methods for poly(3-alkylthiophene)s McCullough^[252] and Rieke^[312] were able to increase the HT proportion to 91 % and 98.5 % \pm 1.5 %, respectively.

¹³an alternative name is poly(3-2,5,8,11-tetraoxadodecane thiophene)

¹⁴Water-soluble polymers have become a research focus in high sensitivity chemo- and biosensor applications. That is because processing in water or alcohol is usually less hazardous to the environment than in organic solvents, the devices are less susceptible to degradation under moist or atmospheric conditions, and the polymers are readily soluble in biological systems^[249,305].

However, these syntheses suffered from a high dispersity in and a low control over the resulting molecular weight. Because of these findings, step-growth mechanisms were presumed^[313].

As already shown in Figure 1.7 b, chain-growth polymerisations such as the Kumada catalyst-transfer polycondensation could be established for PTs instead^[270]. The “quasi-living” KCTP was also used here to synthesise a regioregular P3(EO)₃T with a defined molecular weight (MW). Furthermore, the KCTP allowed for introducing defined end-groups to the polymer chains, which were necessary for the coupling to DNA^[172].

1.5.3 Nanopatterning of conjugated polymers for single-molecule studies

An exemplary result of the past insights into the structure-property relationship and an essential factor for the success of CPs is the six orders of magnitude improvement in charge carrier mobility for organic semiconductors over the past 30 years^[314]. For OFETs, for example, the field-effect mobility (μ) has increased from values below $10^{-3} \text{ cm}^2\text{V}^{-1}\text{s}^{-1}$ 25 years ago to values above $1 - 10 \text{ cm}^2\text{V}^{-1}\text{s}^{-1}$, which are exceeding those of benchmark thin-film amorphous silicon devices ($0.5 - 1 \text{ cm}^2\text{V}^{-1}\text{s}^{-1}$)^[7,315-318].

As another result, models for charge transport such as band transport, hopping or multiple trapping and release could be developed^[253]. However, various sources^[44,253,319-321] agree, that neither the charge transport in CPs nor the details of the relationship of microstructure and electrical properties in CP devices are close to being fully understood, let alone incorporated in device fabrication.

For investigating the structure-property relationships in charge transport, single-molecule studies of CPs have provided significant insight into the physical properties of conjugated polymers^[44]. Furthermore, CP molecules are regarded as promising components for molecular electronics^[321,322], a field which aims at using single-molecules and assemblies to serve as electronic functional component such as a wires, switches or rectifiers^[321,322]. In fact, single chain polythiophene was used in the assembly of the first single-molecule light-emitting diode^[323].

However, research into CPs and CP applications has almost entirely focused on bulk studies. Also in molecular electronics, few studies have assembled molecular junctions with CPs as a component. That is because a highly controlled molecule alignment in junctions or well-organised monolayers on electrode surfaces, and single-molecule manipulation are still extremely difficult due to the long structures and the complex, strong interchain interactions in CPs^[321]. In order to perform molecular electronics studies, single molecules or monolayered molecules need to be incorporated between electrodes to form metal/molecule/metal junctions. Assembling such junctions relies heavily on top-down techniques such as lithography, single-molecule techniques such as STM or the break junction technique^[44,321].

Construction methods include the bridging of single CP chains between nanogap electrodes (Figure 1.9 a), pulling single CP chains with an STM tip (Figure 1.9 b) and assembling CPs into monolayers with top contact, where CPs are either erected on the bottom substrate in so-called “vertical” junctions or lie flat in “planar” junctions (Figure 1.9 c and d). Figure 1.9 displays schematics of the different junction types, and gives examples for each. In a first attempt of fabricating a nanogap junction, for example, He *et al.*^[324] have connected gold electrodes by *in-situ* polymerisation of aniline or pyrrole through potential cycling. Monitoring the current between the electrodes allowed for terminating the reaction after few or even a single polymer molecule bridged the gap. The first experiment to pick up a single CP molecule with an STM tip was performed by Lafferentz *et al.*^[325], who manipulated polyfluorene molecules (typically 20 nm long) that lay on an Au (111) surface. As the tip-molecule interaction is stronger than the molecule-substrate interaction, the molecule was gradually released from the surface and its conductivity was studied as a function of its length. While the nanogap and STM approach ideally allow studying single molecules, their construction is demanding and the junctions are poorly

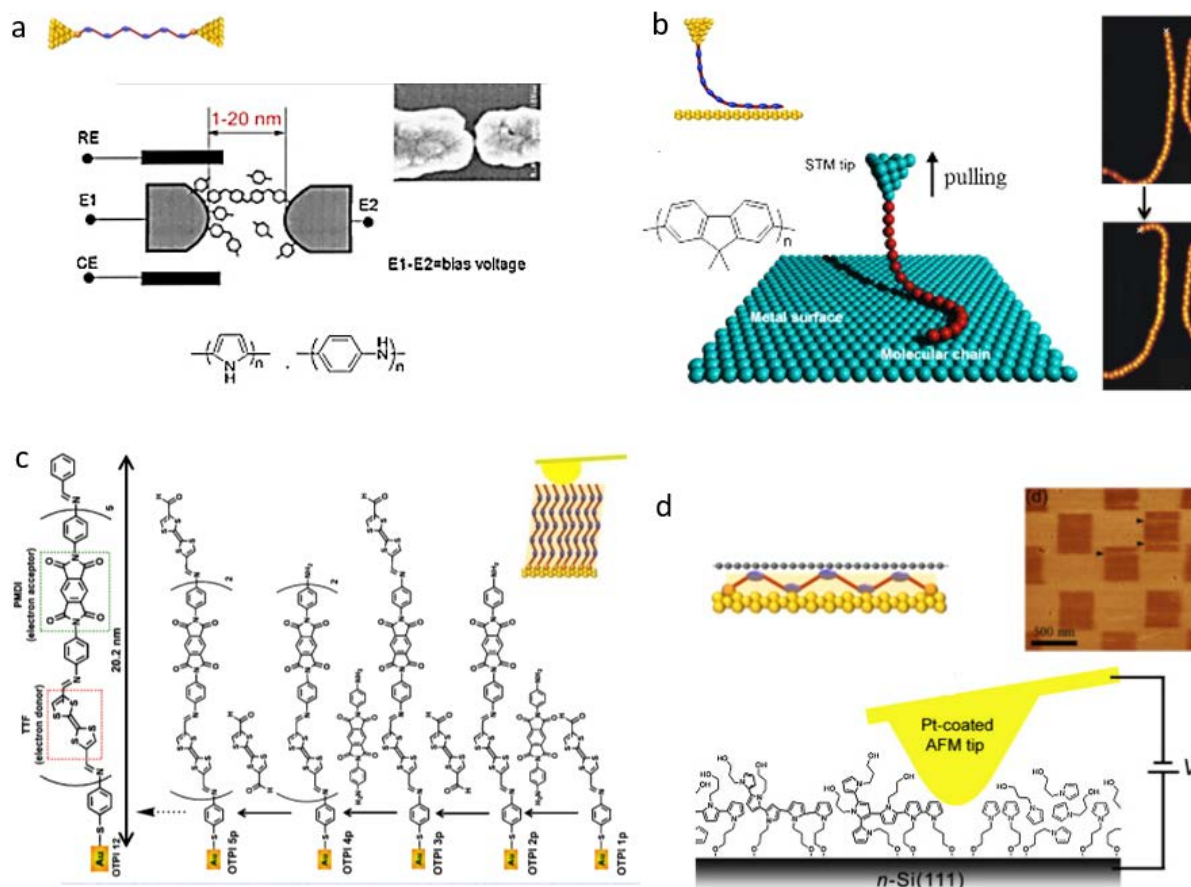


Figure 1.9: Representative metal/molecule/metal junctions for molecular electronics investigations. a) Nanogap electrodes with bridging CP molecule(s) as applied with the *in-situ* growth of polyaniline and polypyrrole. Reproduced with permission from^[324]. Copyright 2003 American Physical Society. b) STM tip pulling a single CP molecule on metal surface; schematic and STM images for polyfluorene. The STM images show conformation change and displacement after tip manipulation. Reproduced with permission from^[325]. Copyright 2009 AAAS. c) Monolayer junctions in vertical direction. Repetitive imine addition to yield a copolymer-based SAM that was topped by a CAFM tip. Reproduced with permission from^[326]. Copyright 2010 American Chemical Society. d) Monolayer junction in horizontal, i.e. planar direction. Localised electropolymerisation of pyrrole with a scanning CAFM tip and formed pattern of the polypyrrole monolayer. Reproduced with permission from^[327]. Copyright 2012 American Chemical Society.

reproducible. Monolayered CP junctions are a more robust approach. Due to their length, polymers do not intrinsically form self-assembled monolayers (SAMs) in which the single molecule protrude vertically from the surfaces. In order to construct such “vertical” junctions, stepwise growth methods have been employed. A repetitive imine addition was used by Choi and Frisbie to prepare CP-SAMs with lengths up to 20 nm on gold surfaces. The metal/SAM/metal junction was then completed by bringing an Au-coated AFM tip in contact with the SAM. Such a junction incorporated typically about 100 CP molecules in parallel and probably featured the longest CP wire-forming junction investigated with conductive AFM^[326]. Flat CP monolayers as they are required in planar junction have been prepared *in-situ* by electrooxidation of SAMs of electropolymerisable monomers such as thiophene, pyrrole and aniline. In the example shown in Figure 1.9c, Lee *et al.* have induced the surface polymerisation of pyrrole with a scanning CAFM tip^[327].

Despite the few successful studies, approaches that are more feasible are necessary for nanopatterning of CPs at the level of single or few molecules while accounting for proper interchain transport to conduct repeatable experiments in order to broaden the application of CPs in nanoelectronics and nanooptics, and to understand charge transport. In addition, applications such as biochips for cell-growth control, micro- and nanofluidic systems or photonic crystal materials would benefit from a feasible approach to nanopatterning of densely grafted polymers^[328]. For all these applications, DNA-based bottom-up approaches hold great potential.

1.5.4 Nanopatterning of conjugated polymers with DNA

In several attempts to nanopattern CPs, the self-assembly properties of DNA have been utilised.

Some attempts rely on non-covalent interaction of CP molecules and DNA. In their review about the use of conjugated polymers in DNA sensing, for example, Peng *et al.*^[329] have reported on the electrochemical entrapment of DNA into the sensing CP layer. Several studies have reported on templating nanowires through non-covalent interaction with DNA duplexes, e. g., for polyaniline^[330–332], polypyrrole^[333,334] and other types of polymers^[335–337]. In contrast to metals templated on DNA, the polymer nanowires appear regular and smooth over micrometre lengths^[338,339], and in addition, conductive^[333,336].

Other DNA-based nanopatterning approaches of CPs use covalent interactions. Lo and Sleiman^[340] have attached monomer units to nucleobases and have used DNA directly as a template for a conjugated daughter polymer. Further approaches use block copolymers, in which one or a few DNA strands (considered as biopolymers) are covalently bound to a CP molecule. Kamps *et al.*^[341], for example, have synthesised DNA-b-PTOTT, which includes the hydrophobic poly[3-(2,5,8,11-tetraoxatridecanyl)thiophene] (PTOTT) as polymer block, to study the amphiphilic self-assembly of this block copolymer into vesicles with controllable sizes, and into nanoribbons together with PEG-b-PTOTT. In general, block copolymers with DNA blocks have been synthesised with various types of polymers (e. g., DNA-b-PS^[342], DNA-b-PPO^[343]) and block copolymer architectures such as linear block copolymers, biological macromolecules grafted onto a synthetic polymer backbone and synthetic polymer side chains on a biomolecule backbone^[344].

In this work a linear diblock copolymer of P3(EO)₃T and an ODN will be synthesised. Such a structure provides only one DNA anchor to attach just one end of the polymer chain, which is probably beneficial for the electric and optical properties. Fixating the polymer block in multiple spots, for example, on both ends, could lead to torsional forces on the polymer backbone that lead to a misalignment of the π -orbitals, and hence impede charge carrier transport. Furthermore, adjacently bound molecules would experience fewer degrees of freedom to interact and self-assemble.

The synthesis of polymer-DNA block copolymers, i. e. the coupling reaction, can take place in solution

or as solid phase synthesis, or if it involves a hydrophobic polymer in an aqueous solution, a shuttle-approach^[75] can be employed. Solid phase synthesis usually involves amide couplings during an automated synthesis between immobilised DNA and, typically, hydroxylated polymers functionalised as phosphoamidites^[341,342,345].

Probably the more popular approach is coupling free-floating DNA strands and polymer molecules in solution. Among the coupling reactions typically used are the amide coupling between amines and carboxylic acids^[346,347], the disulphide formation between DNA and polymer that are both thiol-modified^[348], the Michael addition of thiols to maleimides^[349], or copper-catalysed azide-alkyne Huisgen cyclisation reactions (CuAAC)^[350]. Solution-based coupling can be advantageous, as a homogeneous reaction usually allows higher coupling yields, and it avoids the harsh chemical conditions applied in cleaving the DNA from the substrate or removing protective groups^[75]. To benefit from these advantages, solution-based block copolymer formation with copper-free, strain-promoted azide-alkyne cycloaddition (SPAAC)^[351] will be used in this work as the coupling reaction (Figure 1.10). As the P3(EO)₃T is water-soluble, the coupling can take place in aqueous solution, and the BCP is readily available for purification and coupling to DNA origami.

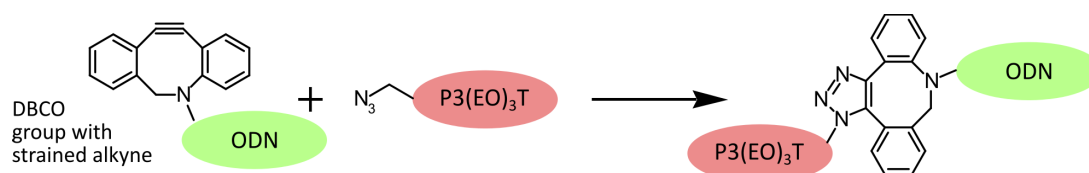


Figure 1.10: Strain-promoted azide-alkyne cycloaddition (SPAAC)^[351]. This Huisgen-type click reaction proceeds copper-free due to the strained triple bond.

1.5.5 State-of-the-art polymer-DNA origami hybrids

As mentioned in Section 1.2.1, hybrids of conjugated polymers and DNA origami are promising building blocks for nanoelectronic and nanophotonic circuit formation. However, up to and during the course of this work, only the two approaches presented by Wang *et al.*^[12] and Knudsen *et al.*^[13,14] have been reported.

Both have their strengths and weaknesses. The method of Wang *et al.*^[12] involves a polymerisation of aniline into polyaniline (PANI) catalysed by hydrogen peroxide that is produced by enzymes pre-positioned in desired locations on the DNA origami. Although PANI is an excellent conductor, its use as an active material in semiconducting devices is problematic because of its spontaneous oxidation into a permanently conductive state. In addition, the method of Wang *et al.*^[12] is restricted to polymers obtainable by oxidative polymerisation. Tokura *et al.*^[328] have demonstrated the site-specific growth of the biocompatible, but not conjugated polymer poly(ethylene glycol) methyl ether methacrylate (PEGMEMA) on DNA origami using solution-based atom-transfer radical polymerisation (ATRP). However, most of the high-performance semiconducting polymers are only accessible by metal-catalysed cross-coupling polycondensations. The work of Knudsen *et al.*^[13] reported the synthesis of a “bottle-brush type” polyparaphenylene vinylene-*graft*-DNA (PPV-*graft*-DNA) having ODN side chains. With this method, long PPV wires can be positioned on DNA origami templates. The monomer preparation procedure involves a solid-state DNA synthesis, which can be considered as a drawback that limits the scalability of the method. Furthermore, although PPV was the very first benchmark polymer for photovoltaic devices^[353–355], its suitability in electronic devices such as transistors was not demonstrated. The same approach of preparing a polymer with DNA side chains was also applied by Madsen *et al.*^[14] to prepare a polyfluorene-*graft*-DNA in addition to the (PPV-*graft*-DNA). Both polymers were assembled on

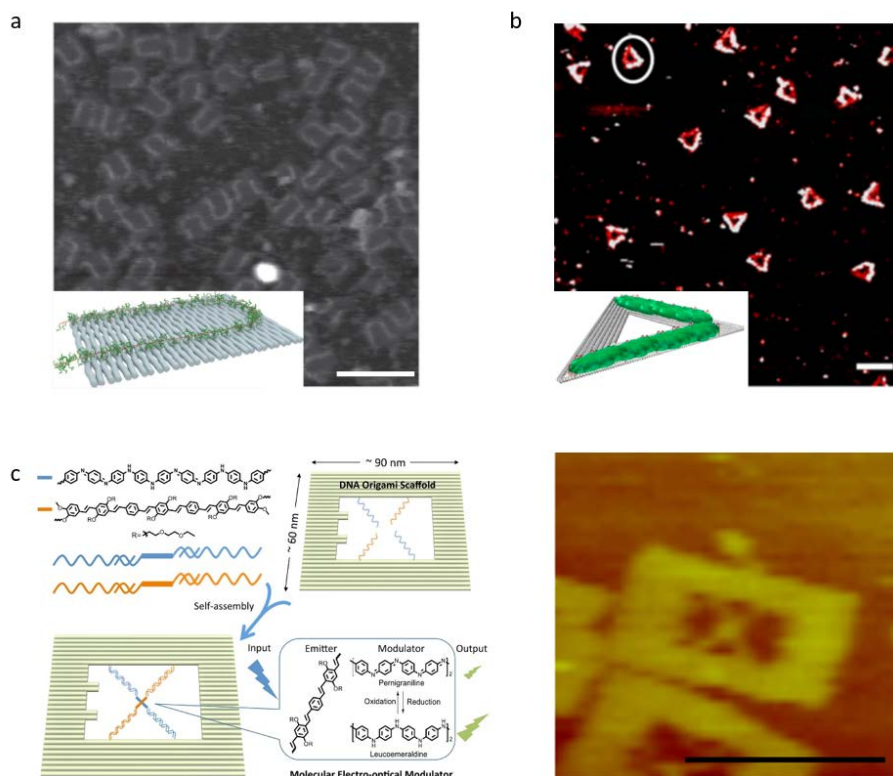


Figure 1.11: Hybrid formation from DNA origami and organic semiconductors. a) DNAzyme-directed synthesis of polyaniline (PANI) on a triangular DNA origami with H_2O_2 . Reprinted with permission from^[12]. Copyright 2014 American Chemical Society. b) Routing of a polyparaphenylene vinylene-b-DNA bottle-brush type block copolymer on a rectangular DNA origami. Reprinted with permission from^[13] Copyright 2015 Macmillan Publishers Limited. c) Prototype DNA based molecular electro-optical modulator with site-specifically placed poly(phenylenevinylene) heptamer (orange) and aniline octamer (blue). Scale bar in AFM image: 100 nm. Reprinted with permission from^[352]. Copyright 2018 American Chemical Society.

the same DNA origami structure in order to investigate inter-polymer energy transfer. The latter was not observed on DNA origami, but when directly coupling the two polymer types through direct hybridisation. Both of the discussed literature approaches to DNA-CP hybrids use step-growth polymerisations for the preparation of CPs, which suffer from a poor control over the molecular structure of the resulting polymers.^[328] After the results of this work had been published^[172], Wang *et al.*^[352] have reported on constructing a prototype of a DNA-based molecular electro-optical modulator (Figure 1.11 c) constructed from two different kinds of conjugated oligomers. A poly(phenylenevinylene) heptamer (HPV) acted as a fluorescent emitter. An aniline octamer (OANI) was able to absorb the emitted light when in the oxidised state but not in the reduced state. Each oligomer was coupled to two same ODNs via CuAAC on a solid-state support. Wang *et al.* have used a similar octanilin-DNA block copolymer for the successful incorporation into 3D DNA crystals that were constructed via tile-based assembly, and could already demonstrate the switching of the OANI's redox states^[39]. To couple OANI-DNA and HPV-DNA to DNA origami, a DNA frame was used which is similar to the tPad used in this work. Overall, Wang *et al.* have demonstrated one of the first functional hybrids of DNA origami and organic semiconductors. For that purpose, they relied on well-defined block copolymers with defined nanooptical properties, which are attached to the DNA origami template with high site-specificity and resolution. While executed differently, the work shown in this thesis embraces these successful principles as well.

For the structural characterisation of any DNA-origami based hybrids, AFM was employed. In all works, the structure formation was assessed qualitatively. Additionally, Wang *et al.* have estimated an overall yield of the hybrid formation of 40 % from the decrease in fluorescence intensity, but they have not studied the topic in details.

Chapter 2

Materials and Methods

After listing the materials used, the first part of the chapter describes the syntheses of the DNA origami, the P3(EO)₃T and the P3(EO)₃T-b-ODN block copolymers. Characterisation methods specific to one of these syntheses will be included right there. The second part focuses on experimental details of the two main methods of this thesis, atomic force microscopy and super-resolution fluorescence microscopy. Furthermore, it lists the protocols for UV/VIS spectroscopy, gel electrophoresis and benchtop centrifugal filtration, which were used on different occasions.

2.1 Chemicals

Unless stated otherwise, chemicals were purchased from Sigma Aldrich or Fisher. All chemicals were used without further purification.

M13mp18 single-stranded DNA was purchased from Tebu-bio. The unfunctionalised origami staples strands were purchased from Eurofins Genomics GmbH dissolved to a concentration of 100 μ M in water on 96-well-plates. The dibenzocyclooctyne (DBCO)-functionalised oligodeoxynucleotides were ordered from Biomers or IBA GmbH. Unfunctionalised body staples and ODNs with sliding handles were purchased HPSF-purified. ODNs with specific handles and ODNs with fluorophores were purchased HPLC-purified. All DNA samples were used as received without further purification. Agarose was purchased from Biozym, acrylamide/bis-acrylamide (40%) and TEMED were purchased from Serva. Deionised water was produced with a Thermo Scientific Barnstead Genpure Pro UV/UF system, and will also be referred to as MilliQ water in the following.

2.2 DNA origami synthesis

All origami was assembled using either a peqSTAR 2X (peqlab, VWR) or a MJ Research PTC-200 Thermal Cycler (Marshall Scientific) and Eppendorf PCR tubes. The origami was stored in either those tubes, Eppendorf Safe Lock tubes or Eppendorf DNA LoBind tubes.

Pad synthesis

A buffer stock solution of 10x TE (400 mM Trizma base, 20 mM EDTA acid) with 125 mM MgCl₂ was prepared with the pH adjusted to 8.0-8.3 using HCl. This kind of TE buffer will be referred to as *pad buffer*. All staples and the M13mp18 template were mixed in a 5:1 ratio. The template target concentration, which is supposed to be equal to the origami target concentration, was 30 nM. Buffer

Table 2.1: Constant-rate synthesis for pad origami (≈ 5 h).

heating	T = const. for 10 min	cooling at 0.1 K/30 s
0 °C to 85 °C	T = 85 °C	85 °C to 24 °C

stock solution and deionised water were added to a final concentration of 1x TE and 12.5 mM MgCl₂. The sample was divided into aliquots of 50 μ L which were then transferred into a thermocycler and cooled from 85 °C to room temperature in a 5 h assembly protocol given in Table 2.1.

Synthesis of the tPad

A stock solution of 10x TAE buffer with 125 mM magnesium acetate (Mg(OAc)₂) was used. The TAE buffer was prepared using 400 mM Trizma base, 200 mM acetic acid and 20 mM Na₂EDTA, and the pH was adjusted to 8.0-8.3 using HCl. This kind of TAE buffer with Mg(OAc)₂ will be referred to as *tPad buffer*. In a synthesis solution with a final concentration of 1x TAE with 12.5 mM Mg(OAc)₂, the about 220 tPad staples¹ and the M13mp18 template were mixed in a 5:1 ratio. The template concentration was varied between 3 and 50 nM. Smaller concentrations were used to save material in experiments without consecutive steps after the synthesis. According to the experiment, different synthesis protocols were used as well. Tables 2.2, 2.3 and 2.4 list the assembly conditions for the tPads according to the experiments.

Table 2.2: Constant-rate synthesis (≈ 11 h).

heating	cooling at 0.1 K/min
0 °C to 90 °C	90 °C to 24 °C

Table 2.3: Constant-temperature synthesis to determine the assembly temperature T_A (≈ 1.5 h).

	stage 1	stage 2	stage 3
heating	cooling at 18 K/min	T = const. for 1 h	cooling at 18 K/min
0 °C to 90 °C	90 °C to T _A (Test)	T = T _A (Test)	T _A (Test) to 24 °C

Table 2.4: Two-rate synthesis for the fluorophore-bearing tPads (≈ 7 h).

	stage 1	stage 2
heating	cooling at 1.0 K/min	cooling at 0.067 K/min
0 °C to 90 °C	90 °C to 60 °C	60 °C to 24 °C

2.3 AuNP and AuNR attachment to the pads and tPads

The AuNP and AuNR were prepared and attached to the origami by Dr. M. Lakatos. Spherical gold nanoparticles with 2-3 nm and 20 nm in diameter were prepared according to the method of De Mey^[356]. The 40 nm gold nanorods, were prepared via a previously reported seed-mediated method for AuNR with different aspect ratios^[357,358].

To functionalise the AuNP and AuNR with ODNs, different protocols were used. For spherical gold nanoparticles 20N' and ATT₅ ODNs were attached to the 2-3 nm and 20 nm AuNP, respectively, as described in Henning-Knechtel *et al.*^[359]. 18T ODNs were used for the functionalisation of the AuNR according to a method by Pal *et al.*^[360].

¹the number of staples varies with design choices such as single-stranded edges etc.

DNA-functionalised AuNPs were added to the pad or tPad origami solution at a 5-fold excess per attachment site, and left for attachment at room temperature overnight. DNA-functionalised AuNR were added to the pads at a twofold excess per attachment site and attached using a cycling temperature interval program with 60 cycles. One cycle comprises of keeping the sample at 40 °C for 5 min, and then at 25 °C for 15 min.

2.4 Formation of P3(EO)₃T-b-ODN BCPs and hybrids of BCPs and origami pads

Block copolymer synthesis

Based on the work of Senkovskyy *et al.*^[361] and Adachi *et al.*^[362], Johanna Zessin has developed and executed the synthesis of the azide-functionalised poly(3-tri(ethylene glycol)thiophene)² (P3(EO)₃T), and characterised the resulting polymers. Synthesis and polymer characterisation are described in detail in Zessin *et al.*^[172]. To provide an overview in this work, Appendix Figure A.4 was reproduced with permission from the aforementioned publication.

To couple the azide-functionalised P3(EO)₃T to DBCO-functionalised ODNs via strain-promoted azide alkyne cycloaddition, 5 mg (0.001 mmol) of the polymer were dissolved in 1.1 mL of cold water (890 µM) and filtrated with a syringe filter (0.22 µm). The P3(EO)₃T solution was then mixed with the ODN solution (100 µM) in a molar ratio of at least 10:1. The mixture was kept on an Eppendorf ThermoMixer C at 15 °C for 24 h.

Block copolymer purification

The block copolymers were purified with reversed-phase HPLC using a Dionex ICS 5000⁺ HPIC System (Thermo Fisher) with an Acclaim 120 C18 column (diameter 4.6 mm, length 150 mm, Thermo Fisher) and a SecurityGuard Analytical Guard Cartridge System (Phenomenex). The temperature was kept at 25 °C and the solvent flow at 1 ml/min. As solvents, 20 mM triethylammonium acetate buffer (TEAA; AppliChem PanReac) at pH 7 and acetonitrile (ACN; HPLC grade, VWR Chemicals) were used employing the gradient listed in Table 2.5.

Table 2.5: Solvent gradient for block copolymer purification with RP-HPLC. TEAA: 20 mM triethylammonium acetate buffer (pH 7), ACN: acetonitrile.

time [min]	20 mM TEAA [%]	ACN [%]
0	95	5
1	95	5
13	50	50
15	0	100
18	0	100
21	95	5

The eluent was collected in 96-well-plates. The wells of one fraction were combined in 50 mL glass vials. The vials were sealed, the seal was pinched with cannulas, and the vials were left in the oven at 40 °C under vacuum over night to evaporate 80 - 90 % of the solvent. The solution was transferred into a smaller glass vial and kept in the freezer for up to 3 months. The BCP concentration was determined via UV/VIS spectroscopy (see below).

²an alternative name is poly(3-2,5,8,11-tetraoxadodecane thiophene)

Hybrid formation

For hybrid formation, purified P3(EO)₃T-b-ODN and filtered pad origami were combined at a ratio of BCP:handle $\approx 20:1$. As the BCP is in aqueous solution, 10x TE-buffer was added to yield a final concentration of 1x TE with 12.5 mM MgCl₂ and 300 mM NaCl. The NaCl concentration was varied in the range of 0 - 3000 mM during a set of experiments discussed in Section 4.1. The solution was held on an Eppendorf ThermoMixer C at 15 °C and 350 rpm for 24 h, and then filtrated as described in Section 2.5.

2.5 Methods used on multiple occasions

Benchtop filtration

Origami and P3(EO)₃T-pad hybrids were purified from excess staples or excess block copolymer using centrifugal filter units with MWCO = 100 kDa by Amicon or Pall, and an Eppendorf Centrifuge 54300.

For the tPad, the excess of staple strands was removed by filtration with Amicon 100 kDa filters. 400 μ L tPad-containing solution were centrifuged at 4000 rcf for 5 min. For that purpose, 400 μ L of 1x tPad buffer were added and the centrifugation was repeated. This washing step was performed three times in total. Then, the filter was placed upside down in a clean filter tube and spun for 1 min at 1000 rcf to release the filtered origami.

For the pad and the hybrid, 400 μ L of solution were placed in a 100 kDa Pall filter and centrifuged at 10000 rcf for 5 min. Three washing steps followed that include adding 400 μ L of 1x pad buffer (containing 300 mM NaCl when filtrating hybrids), and centrifugation at 10000 rcf for 5 min, before the supernatant containing the purified origami was pipetted into a clean Eppendorf tube.

UV/VIS spectroscopy

UV/VIS spectroscopy measurements were acquired using an Analytic Jena SPECORD®PLUS for the determination of the P3(EO)₃T-b-ODN concentration, or a Nanophotometer P360 for testing the concentration of staples and DNA origami. Measurements rely on the Lambert-Beer law (2.7.2):

$$E_\lambda = \log_{10} \left(\frac{I_0}{I} \right) = \epsilon_\lambda \cdot c \cdot d \quad (2.1)$$

Here, E_λ is the wavelength-specific extinction, I_0 and I are the intensities of the light beam before and after passing through the sample, ϵ_λ is the extinction coefficient at a given wavelength, c is the sample concentration and d is the cuvette thickness. The BCP concentration was determined after HPLC purification using the absorption peak of the polymer at 409 nm. If the concentration was too high to yield absorption in the linear range of the Lambert-Beer-Law, the solution was diluted with MilliQ water. The typical concentration were in the range of 2 - 20 μ M.

To determine staple or origami concentration with the Nanophotometer P360, 1 - 2 μ L of the DNA solution were applied and covered with the lid No. 10. The DNA concentration was calculated using the DNA absorption at 260 nm. For staples, the extinction coefficients given by the manufacturer were used. For origami, an average ϵ_{260} was calculated from the approximate number of base pairs per origami 7248 determined by the M13mp18 scaffold length, and the average molecular weight of a base pair of 660 g/mol:

$$\epsilon(\text{origami}) = 7248 \cdot 660 \frac{\text{g}}{\text{mol}} = 4783680 \frac{\text{g}}{\text{mol}}. \quad (2.2)$$

Gel electrophoresis

The gel documentation was performed using a GE Healthcare Typhoon FLA 7000. An excitation laser with a wavelength of 473 nm and a low bandpass (LB) filter at 580 nm were used to image stained origami and unstained DNA labelled with Alexa Fluor 488 or Atto 488. A 532 nm laser and a LB 575 nm emission filter were used to image Rhodamine Red and Atto 550 on unstained origami and staples. For Alexa Fluor 660, Atto 647 N and unstained polyacrylamide (PA) gels with P3(EO)₃T-b-ODN block copolymer, a 635 nm laser and a LB 665 nm emission filter were used.

Agarose gel electrophoresis

In a 200 mL Erlenmeyer flask the required amount of agarose was weighted out, was dissolved in a microwave in 100 ml of 1x of the pad or tPad buffer depending on the investigated origami. The hot solution was allowed to cool for 5 min before casting in a kuroGEL Midi 13 horizontal electrophoresis chamber (VWR). After solidifying for at least 30 min, the origami was applied. Prior to that, Gel Loading Dye, Blue (6X) (New England BioLabs) was applied to the origami solution to yield a final concentration of 1X. In one or two lanes of the gel, a 2-log DNA ladder (New England BioLabs) was applied for relative size comparison. 15 μ L sample were applied per pocket. The gels were run at $U = 90$ V for 60 - 120 min. Afterwards, the gel was either imaged directly to visualise fluorophore labels. Alternatively, it was stained by applying 6 μ L of Sybr Gold Nucleic Acid Gel Stain (Thermo Fisher) to 200 mL of running buffer and rocking the gel in it for 20 min, and imaged afterwards.

Polyacrylamide gel electrophoresis (PAGE)

For quality control for the HPLC-purified block copolymer and for testing the hybridisation of the fluorophore-bearing ODNs to their complementary handles in the tPad, 12 % PA gels were used. All components listed in Table 2.6 were combined in that order and quickly cast into a vertical electrophoresis chamber (VWR), and left to polymerise for at least 30 min before adding 0.5x TBE buffer as a running buffer. 10 μ L of sample were prepared for each pocket, including the appropriate amount of Gel Loading Dye, Blue (6X).

For checking the quality of the HPLC purification of the block copolymer, the gel was loaded and run at 120 mV for 2 h. Prior to staining the DNA with Sybr Gold, the gel was imaged using the 635 nm laser and the LB 665 nm emission filter, while the 532 nm laser and the LB 575 nm emission filter were used after staining.

For the fluorophore-bearing ODNs, the gel was run at 100 mV for 2 h. The gel was imaged before staining with Sybr Gold using the fluorophore-specific lasers and filters as described above. After staining the DNA for 20 min, the gel was imaged using the 532 nm laser and the LB 575 nm emission filter. The 5x TBE buffer was prepared with 445 mM Trizma base, 445 mM boric acid and 10 mM Na₂EDTA. Gels were cooled during the run and kept from daylight by placing the electrophoresis chamber in the fridge.

Table 2.6: Preparation of 12 % polyacrylamide gels. The components are given in the order of mixing. Acrylamide/ Bis 40 %: solution of acrylamide and *N,N'*-methylene bis-acrylamide (Bis) in deionised water, 40 wt%. TEMED: *N,N,N',N'*-tetramethylethane-1,2-diamine. APS: ammonium persulfate.

component	V [mL]
MilliQ water	5.9
5x TBE buffer	2.4
Acrylamide/ Bis 40 %	3.7
TEMED	0.02
APS	0.2

2.6 Atomic force microscopy

2.6.1 Sample preparation for scanning in air and high-resolution scanning in liquid

AFM imaging of bare origami and P3(EO)₃T-pad hybrid structures was performed using an Asylum Cypher ESTM Environmental AFM. If necessary, origami or hybrids were diluted to 2-3 nM in 1x origami buffer prior to the sample preparation to avoid overcrowded images.

For tapping mode in air, TESPW silicon tips (Bruker) were used. The upper layer of a mica slide affixed on stainless steel AFM sample plates (Tedpella) was exfoliated with general purpose sticky tape. 10 μ L of the origami sample were applied and after 2 min, excess solution was wicked away with a tissue. Following this, the sample was washed three times with 100 μ L MilliQ water.

For tapping mode in liquid, BL-AC40TS-C2 cantilevers (Olympus) were used. On a freshly cleaved mica substrate, 15 μ L of a 0.1 mg/ml poly-L-ornithine solution were incubated for 45 s, rinsed off and air-dried. 2-10 μ L of the origami solution was dropped onto the functionalised surface and incubated for 5-10 min. For scanning, 100 μ L of 1x TE buffer with 12.5 mM MgCl₂ was added on top of the origami solution.

2.6.2 Melting studies

In-situ thermal test

For the *in-situ* thermal test of the tPad, the sample was prepared like a standard sample for tapping mode in liquid. During the experiment, 80 μ L of buffer had to be added to replace evaporated liquid. Despite the distortion, the weave was resolvable throughout the experiment.

Melting in solution

50 μ L of a sample of folded and filtrated tPads were put into an 200 μ L Eppendorf tube and heated in a thermocycler to 50 °C, 55 °C or 60 °C, respectively, within few seconds. After 10 min, 20 min, 30 min, 60 min and 110 min, 1 μ L samples were quickly pipetted from the samples and immersed into origami buffer cooled to 4 °C to quench the origami melting. Each sample was briefly mixed on a Vortex shaker, then 5 μ L of it were applied onto a freshly cleaved mica piece, left to sit there for 3 min, rinsed with three times with 100 μ L of deionised water, and then dried in blowing air.

2.6.3 Locating of the BCP in hybrids in high-resolution liquid AFM images using the FindFoci algorithm

FindFoci allows to identify “peak intensity regions in 2D and 3D”^[6] 16 bit greyscale images. The localisation algorithm works as shown in the schematic in Figure 2.1. First, a threshold is assigned to separate the background from the foreground. Second, the local maxima, that is, the potential peaks, are determined above this threshold. Third, the maxima are expanded into peaks. This takes place by progressively assigning points of lower intensity to the peak area above it. As a result, all points above the background initially belong to a peak. In an optional fourth and final step, insignificant peaks are merged with their neighbouring peaks or dismissed from the result list. A peak can be identified as insignificant through either a height or an area threshold set by the user.

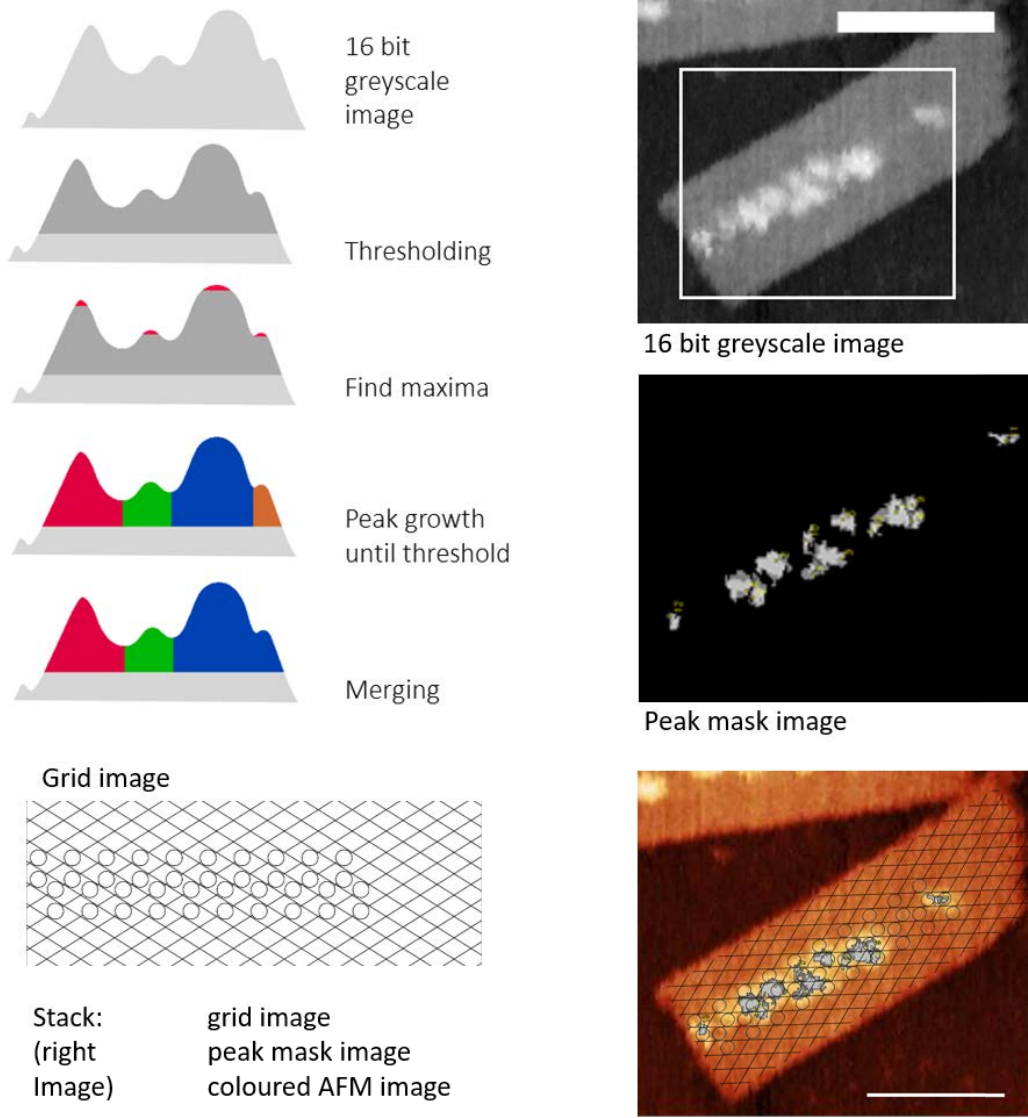


Figure 2.1: Schematic of FindFoci peak assessment algorithm (adapted from^[363]), example 16 bit greyscale input image and peak mask output image. As an example, the grid image of the type III pads is displayed as well as a stack image of AFM, peak mask and grid image. All scale bars: 50 nm.

FindFoci yields a peak (mask) image (Figure 2.1) with the object positions determined through the peak outlines and peak maxima. It further yields a peak table, which lists, amongst others, the grey value of each peaks' maximum and each peaks' area in the image plane in pixels. Pixel size and grey value correspond to the x -, y - and z -values in nm from the AFM image and can hence be used to determine an object's height and basal area on the pad.

To generate the 16 bit greyscale images from the .ibw AFM image the program Gwyddion^[364] is used. Image processing with Gwyddion includes correcting artefacts, mainly a tilted background and scars (faulty lines), which would interfere with the FindFoci algorithm. Gwyddion assigns the white value 65535 of the grey scale to the height maximum in the image and black to zero. The scale is linear.

For locating an object, not only the object position (determined with FindFoci) has to be known but also the position of the handle origins on a pad. In order to mark them, an auxiliary grid image was drawn using Inkscape. Figure 2.1 shows the grid for type III pads as an example. The grid has the size of a pad, displays the origami weave with rhomboids and the handle positions as circles. The corners of the rhomboids mark the positions of the staple crossovers, the lengths of their edges account for the size parameters of B-DNA and the crossover distance of 1.5 helical turns. The radius of the circle was defined as 2.28 nm (including the contour thickness). Although the handles with the different sequences are of different length, the same radius ought to be chosen for all pad types to use the same settings for all hybrids. In theory, the radius could have been defined as 2 nm. This is 1/3 of the average distance of next-neighbour handles, and would have assigned equal parts of the distance to each handle position and the position between the handles. It is probable though, that this would have biased the results towards the position between the handles. That is because the handle lengths, which vary from $8A = 2.72$ nm to $20N' = 6.8$ nm, allow placing the BCP centre away from the actual handle origin, while the BCP is still attached to said handle only. Estimating the smallest distance of next-neighbour handles with 6 nm, using $r = 2.28$ nm assigns $\approx 75\%$ of the distance between two handles to the two positions **a** on a handle, and $\approx 25\%$ to the positions between the handles (either **b** or **c**). This was considered a valid estimate. Next, the grid image, the peak (mask) image and the greyscale image (or the same, coloured AFM image of the origami) are merged into a stack (Figure 2.1). The origami weave, which is visible in high-resolution AFM images, and the pad size are used to position the grid correctly on the pad. In the stack, the object positions can then be located on the grid. In general, an object can sit either directly on a handle position or in between handles. Depending on the grid type different positions are possible in the latter case, which will be discussed in Section 4.2.2.

Object positioning on a lane in type III pads. Taking the notation of the possible object positions **a** to **d** as given in Figure 4.3, the number of objects per lane L1-L4 on type III pads are calculated as follows. The indices 1-4 correspond to the respective lanes. Position **c** is always located between two lanes and therefore, it is characterised by two indices. Position **b** is always located between L2 or L3, the index is omitted for simplicity.

$$N(L1) = a_1 + d_1 + 0.5c_{1\ 2} \quad (2.3)$$

$$N(L2) = a_2 + 0.5b + 0.5c_{1\ 2} \quad (2.4)$$

$$N(L3) = a_3 + 0.5b + 0.5c_{3\ 4} \quad (2.5)$$

$$N(L4) = a_4 + d_4 + 0.5c_{3\ 4} \quad (2.6)$$

2.7 Super-resolution fluorescence microscopy

2.7.1 Protocols

TPads. Both design I and design II tPads were synthesised as described with scaffold loops at the vertical edges, and with the fluorophore staples present in a 10-fold excess instead of a 5-fold. For the standard origami sample, the tPads were filtered and their concentration was determined with UV/VIS spectroscopy as described above. AFM images in liquid or air were taken prior to fluorescent imaging to determine the yield. For the standard sample, the concentration of the origami stock solution was 3,5 nM, which was diluted 1 : 100 for imaging. For the unfiltered, noisy sample, scaffold concentration in the assembly solution of 15 nM was considered as origami concentration. The solution was diluted 1 : 100 for imaging.

Fluorescent beads. For the mapping calibration between the two channels, Tetraspeck fluorescent beads with a diameter of 200 nm (Invitrogen, T7280) were used. These are polystyrene spheres stained throughout with four different dyes to yield separable excitation/emission peaks at 365/430 nm (blue), 505/515 nm (green), 560/580 nm (orange), and 660/680 nm (dark red), respectively. The stock solution with a bead density of $\approx 2.3 \cdot 10^{10}$ particles/mL was diluted by 1 : 500 in filtered PBS buffer to use in the flow cell. Here, the green, orange and dark red dyes were imaged. Diffraction-limited spots of the beads were imaged using the same routine as for the tPad samples. It was assumed that all dyes were distributed similarly within a bead.

Buffers. The buffers used in the course of the experiment were prepared with machine-filtered ultrapure water (MilliQ, Millipore Cooperation). The first buffer is phosphate-buffered saline (PBS) prepared from NaCl, KCl, Na_2HPO_4 and KH_2PO_4 by Corina Bräuer in the Diez Lab at the B CUBE Dresden.

From PBS filtered through a 0.2 μm Nylon syringe filter, antibody buffer and blocking buffer were prepared as given in Tables 2.7 and 2.8.

Table 2.7: Antibody buffer (100 μL).

V [μL]	reagent	stock	final
95	PBS buffer	1x	ca. 1x
5	Anti-biotin antibody	1 mg/mL	0.05 mg/mL

Table 2.8: Blocking buffer (5 mL). ^a if not prepared: 50 mg in 500 μL MilliQ.

V [μL]	reagent	stock	final
4500	PBS buffer	1x	ca. 1x
500	10 wt% F127 ^a	10 wt%	1 wt%

Furthermore, a flushing buffer was prepared on the basis of a 10x tPad synthesis buffer (10x TAE with 125 mM $\text{Mg}(\text{OAc})_2$) as given in Table 2.9. It was filtered through the 0.2 μm Nylon syringe filter.

For imaging the dyes with enhanced photostability and brightness, an anti-fade imaging buffer was also prepared from the TAE buffer as given in Table 2.10. The anti-fade buffer with the oxygen scavenger system glucose oxidase and catalase was prepared just before use to avoid acidification of the buffer solution.

Dichloro-dimethyl silane (DDS)-coated coverslips. DDS-coated coverslips were prepared by Corina Bräuer in the Diez Lab at B CUBE, Dresden. For cleaning, glass coverslips (Menzel # 1, 18 x 18 mm² and 22 x 22 mm²) placed in a Teflon holder were kept in acetone at room temperature for 30 min and

Table 2.9: Flushing buffer (15 mL: sufficient for more than one experiment).

V [mL]	reagent	stock	final
13.35	MilliQ	-	-
1.5	10x TAE 125 mM Mg(OAc) ₂	10x	1x
0.15	Tween 20	10 wt% ^a	0.1 wt%

Table 2.10: Anti-fade buffer (400 μ L, 1 : 200).

V [mL]	reagent	stock	final
396	FB	1x	ca. 1x
1	glucose oxidase	19.5 mg/mL	0.049 mg/mL
1	catalase	2 mg/mL	0.005 mg/mL
2	glucose	2 M	0.005 M

then sonicated for 20 min in the same solvent. Next they were rinsed under a continuing stream of deionised water and afterwards soaked in piranha solution (100 ml H₂O₂ and 200 ml of H₂SO₄) at 60 °C for 30-40 min. Then the Teflon holder was removed from the piranha solution, immersed in ultrapure water and subsequently rinsed with ultrapure water for another minute. The Teflon holder was subsequently soaked in a 0.1 M KOH solution for 15 min, followed by an immersion and rinsing with ultrapure water as in the previous step. Afterwards, the coverslips were blow-dried with filtered nitrogen. For silanisation, the Teflon holder with the cleaned coverslips was immersed in a solution of 125 μ L of dichloro-dimethyl silane in 250 ml of trichloroethylene for 60 min. To clean the coated coverslips afterwards, they were first sonicated in methanol for 5 min, then the methanol was changed and sonication continued for 15 min before they were finally dipped in ultrapure water. Residual water was blown off with nitrogen again and the coverslips were stored in airtight containers at room temperature.

Flow cell preparation. Schemes of a flow cell typically used in these experiments are shown in Figure 2.2. The flow cell's bottom surface was functionalised with anti-biotin antibody to bind the biotin protruding from the tPad, and blocked with F127. This is to ensure that, in principle, only the tPads will stick to the surface, while leftover staples are removed in the flushing of the channel.

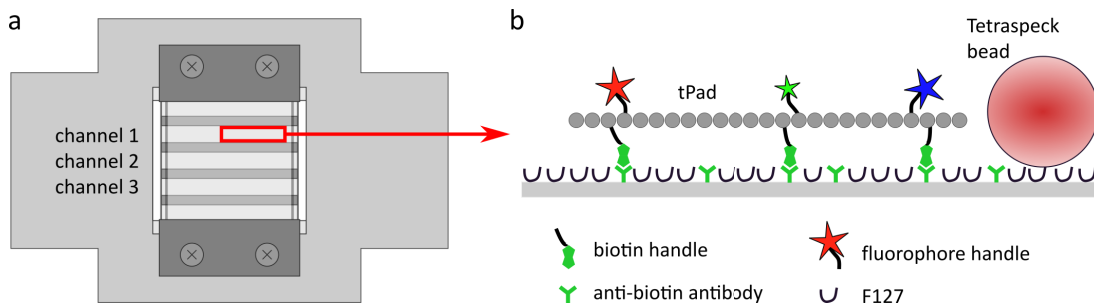


Figure 2.2: Schemes of a flow cell with three channels prepared as described. a) Top view of flow cell in holder. b) Zoomed-in side view on one tPad anchored to the glass surface via biotin-anti-biotin linkages. Between the anti-biotin antibodies, the glass surface is blocked with F127.

Flow cells were assembled from coverslips functionalised with DDS as follows. On a 22 x 22 mm² coverslip, three channels were formed with four parallel strips of parafilm (Bemis) and topped with a 18 x 18 mm² DDS coverslip. The two coverslips were briefly pressed together and placed on a heat plate set to 60-80 °C for about 1 min. After removing from the heat, the top coverslip was gently pressed onto the parafilm with tweezers to seal the channels. Optionally, silicone grease or two-component dentist glue was applied to enhance the separation of the channels. The sealed flow cell was firmly mounted on a metal sample holder. Then 20 μ L antibody buffer were quickly flushed into each channel and incubated for 3 min. To overcome the repulsion of the hydrophobic DDS layer and to ensure a fast flushing, a pipette tip-capped

Table 2.11: Filter cubes for imaging the blue (488 nm), green (561 nm) and red (647 nm) channel.

	488 nm imaging filter	λ [nm]	561 nm imaging filter	λ [nm]	647 nm imaging filter	λ [nm]
laser bandpass	F37-473	457 - 493	F49-555	542 - 568	F39-628	608 - 648
dichroic longpass	F48-486	502	F48-558	565	F48-643	657
emission bandpass	F37-521	502.5 - 547.5	F37-609	582 - 636	F47-700	662.5 - 737.5

hose connected to a benchtop vacuum pump was used to lower the pressure at one end of the channel while the buffer was pipetted into the other end. After the incubation, 100 μ L of blocking buffer was flushed into the channel and kept for 2 h to block the remaining surface. To prevent drying, a drop of blocking buffer was kept on both ends of the channel and the sample holders were kept in a petri dish wrapped in parafilm.

After blocking, each flow cell channel was flushed with 100 μ L of flushing buffer by pipetting drops onto one end of the channel and drawing the liquid with a piece of filter paper from the other side of the channel (note that the flushing direction was the same as in the previous flushing steps). The so-prepared flow cells in the sample holders were mounted onto the sample stage in the microscope before flushing in the origami solution and the Tetraspeck beads. To ensure a precise fluorophore localisation, the Tetraspeck beads and the tPads were deposited sufficiently sparsely. In the standard experiment, the filtered, 3.5 nM tPad solution (design I) was diluted by 1:100. In the experiment with strong background noise, the unfiltered, 15 nM tPads (design II) were diluted 1:100. Tetraspeck beads as bought were diluted by 1:500. On all three occasions, flushing buffer was used for dilution. A volume of 20 μ L of any sample was flushed into its designated channel and incubated for 5 min. Then excess sample was removed by flushing with 100 μ L of imaging buffer using a filter paper as described before. In experiments with tPads, the Tetraspeck beads were added to a second, origami-free flow cell channel and imaged after the tPads were imaged.

The flow cell remained unsealed. The background was found to be homogeneous.

Microscope setup. The experiment was conducted on a commercially available N-STORM microscope, whose main component is an inverted TIRF fluorescence microscope Nikon Eclipse Ti-E. An oil immersion TIRF objective lens (Nikon, CFI TIRF Apochromat 100x, NA 1.49, WD = 0.12 mm) was used. The microscope offers 1.5x tube liners to increase the magnification by 50%, which were, however, not used in these experiments.

The focal plane was manually adjusted to the diffraction-limited spots from the Tetraspeck beads or single molecules. The sample holder with the flow cell was firmly mounted onto the Nikon motorized x-y-stage with 0.1 μ m step size and 0.5 μ m resolution; the movement in z was conducted through a Nano-Z100 piezo (Mad City Labs; 100 μ m range, 0.2 nm resolution). Once the focus was set, the stage was moved in the xy-plane to change the field of view. The microscope system was situated in an Okolab incubator to keep temperature changes, mechanical disturbances and the influence of external light to a minimum. After switching on, the system was given at least 2 h to equilibrate prior to imaging. As excitation system, a monolithic laser combiner (MLC) 400 by Keysight was used, that combines four diode lasers into one fibre. At the fibre tip, the intensities of the four lasers (denoted by their wavelengths) are 20 mW for 405 nm, 80 mW for 488 nm, 80 mW for 561 nm and 125 mW for 647 nm. The fluorescent dyes in the presented experiments were excited either by the 488 nm (“blue channel”), the 561 nm (“green channel”) or the 647 nm (“red channel”) laser. Of the available filter cubes, the ones listed in Table 2.11 were used. A filter cube consists of an excitation and emission filter as well as a dichroic mirror.

The light of all colour channels was directed onto the same area on the Andor iXon Ultra 897 EMCCD camera (56 fps at 512 x 512 px, pixel size: 16 μ m) for detection.

For operating the microscope, the NIS Elements microscope imaging software was used. In the software, an imaging routine was programmed to execute the loop-repeat routine (see Figure 5.3)

semi-automatically. The fields of view were chosen by manually translating the sample in the xy -plane. The experiments were conducted as summarized in Figure 5.3 steps 1 - 8. In case origami was flushed into two channels, these were imaged before imaging the Tetraspeck beads in channel 3. The imaging time was adjusted to yield sufficient photon count for precise localisation, but avoid unnecessary bleaching. The focal plane was maintained throughout the imaging to ensure that the Tetraspeck beads can be used for the mapping calibration of the sample^[221].

Image processing. A Matlab routine splits the stack of $n \cdot k$ images of a field of view into the n stacks of k images of the same colour. In each stack of 100 binary images the fluorophore positions are tracked and drift-corrected. Both steps were executed consecutively using the ThunderSTORM^[232] plugin of the Fiji^[365] image analysis software.

In order to calculate the uncertainty of a single incident's coordinates as well, the number of photons in an image must be known. For that purpose, ThunderSTORM requires the calibration data for the EMCCD camera. For the standard sample, the pixel size was set to 104 μm , the count of photoelectrons per A/D was set to 15.5, the basis A/D count level was set to 1, and the EM gain was set to 100. For the sample with strong background noise the pixel size was set to 106 μm , the count of photoelectrons per A/D was set to 15.5, the basis A/D count level was set to 100, and the EM gain was set to 300. For both origami and the Tetraspeck beads, weighted least-squares fitting and Integrated Gaussian functions as model PSFs were used. This kind of PSF allows for slight variations in the focal plane, because the centre of this symmetrical PSF stays the same for different focal planes. For the drift correction the fiducial markers option is used.

Mapping calibration. As the Tetraspeck beads were separated well enough, finding the corresponding centre in another channel's image was straightforward. A given point in the FOV was mapped between channels, by linear least-squares-fitting two second-degree polynomials in both coordinates (Matlab: `fitgeotrans`). Although a mapping should ideally result in perfect coordinate transformation, the map determined by two such fitted polynomials does not perfectly map the fiducial beads onto their actual images. The vector difference between a bead's mapped coordinates and actual coordinates show no spatial correlations; these errors are essentially random.

For distance measurements, the weighted average lengths of the vectors between two fluorophore positions are calculated. As weights, the inverses of the uncertainty of the fluorophore positions are used, which were determined by ThunderSTORM.

2.7.2 Error propagation

Assuming that there is no correlation between variables, the following propagation-of-error formula^[366] is used for any function depending on multiple variables:

$$s_f = \sqrt{\left(\frac{\partial f}{\partial x}\right)^2 \cdot s_x^2 + \left(\frac{\partial f}{\partial y}\right)^2 \cdot s_y^2 + \left(\frac{\partial f}{\partial z}\right)^2 \cdot s_z^2 + \dots} \quad (2.7)$$

It was applied with (5.3) to yield an expression for the overall uncertainty of a fluorophore distance measurement s_d with contributions for the statistical localisation uncertainty of a fluorophore position ∂l and the colour-offset residue r as well as the broadness of the colour-offset residue distribution in one image ∂r . Here, l denotes the fluorophore distance and α is the angle between the actual distance vector \mathbf{l} and the colour-offset residue vector \mathbf{r} as will be shown in Figure 5.5.

For l , the fluorophore distances according to design will be chosen, while the values for r , ∂r and ∂l will be determined experimentally.

$$d = \sqrt{l^2 + r^2 - 2lr \cos \alpha} \quad (2.8)$$

$$d = \sqrt{m} \quad (2.9)$$

$$m = l^2 + r^2 - 2lr \cos \alpha \quad (2.10)$$

$$n = l^2 \quad (2.11)$$

$$p = r^2 \quad (2.12)$$

$$o = -2lr \cos \alpha \quad (2.13)$$

$$\partial n = 2l \partial l \quad (2.14)$$

$$\partial p = 2r \partial r \quad (2.15)$$

$$\partial o = \sqrt{(2r \cos \alpha \cdot \partial l)^2 + (2l \cos \alpha \cdot \partial r)^2 + (2lr \cdot \partial(\cos \alpha))^2} \quad (2.16)$$

$$s_d = \partial d = \frac{1}{2} \cdot \frac{\partial m}{\sqrt{m}} \quad (2.17)$$

$$\partial d = \frac{2}{2} \cdot \sqrt{\frac{(\partial l)^2 \cdot (l^2 + r^2 \cos^2 \alpha) + (\partial r)^2 \cdot (r^2 + l^2 \cos^2 \alpha) + l^2 r^2 \cdot (\partial \cos \alpha)^2}{l^2 + r^2 - 2lr \cos \alpha}} \quad (2.18)$$

The angle α can assume any values in the interval $[0; 2\pi]$. A dataset of evenly distributed values for alpha in that interval yields the mean value $\overline{\cos \alpha}$ and the uncertainty $\sigma_{\cos \alpha}$ as given below:

$$\cos \alpha = \overline{\cos \alpha} \approx 0.637 \quad (2.19)$$

$$\partial \cos \alpha = \sigma_{\cos \alpha} \approx 0.709 \quad (2.20)$$

$$(2.21)$$

Chapter 3

Construction and characterisation of two 2D DNA origami structures with emphasis on AFM-based investigations

In this thesis, two kinds of 2D DNA origami serve as objects under study. These are a rectangular structure that is referred to as pad in the following and a frame with a square shape named tPad. The pad's surface is continuously filled, while the tPad has a rectangular cavity in its centre.

The first section is about constructing the pad and the tPad. The generic principles of 2D DNA origami designing and synthesis are explained for the pad and applied for the tPad. Then the origami syntheses and the structural stability are discussed.

Both types of origami can serve different purposes, but for any kind of application, structural resilience is key. Compared to a continuous 2D object, a cavity-bearing structure will presumably differ in its thermal and mechanical properties. While these properties are well studied for rectangular origami, there is less data on cavity-bearing structures. The tPad structure is studied here with the objective to investigate the behaviour of a frame-like origami, which includes also the stacking behaviour.

The second section discusses the rational design of sticky ends. Furthermore, the pegboard qualities of tPads and pads are evaluated taking nanosized gold objects as example.

3.1 Design, synthesis and characterisation of pad and tPad

3.1.1 Design and synthesis

The layouts of the 2D origami pad and tPad are shown in Figure 3.1 and 3.2. The pad and the tPad were designed using previously described principles^[45] and the computer program CaDNAo^[59]. The scaffold strand is circular single-stranded M13mp18 virus DNA (7249 b) in both origami, which runs in loops to form the desired shape. For each origami, a set of about 200 custom-designed single-stranded DNA staples cross-links the loops. The staples hybridise with adjoining scaffold parts so that cross-linked parallel DNA double helices form. The crosslinks between the helices occur at every 1.5 helical turn, i.e. every 16 bp. Most origami body staples (black in Figure 3.1 and 3.2) are 32 b long¹. In both origami, most body staples are routed in a z-like curve as can be seen in Figure 3.2 bI.

¹To account for an origami's shape specificities, some staples are shorter or longer.

The staple end locations are points of interest, because here the single-stranded handles for binding nanoscale objects can protrude from the origami surface at the most favourable angle, which is around 90° with respect to the origami plane. The staple ends point to either the top or the bottom of the origami plane, so they intrinsically form a hexagonal lattice of addressable pixels on both origami surfaces. Due to the hexagonal lattice of possible handle sites, each handle can have up to six next neighbours, which occur at a distance of approximately 6 nm.

In the following, the design specificities for pad and tPad origami are given.

The pad

The basic layout of the pad was designed by Dr. Andreas Heerwig.

The double-stranded body of the pad (Figure 3.1) was designed to be $a = 45.5$ nm wide and $b = 146.5$ nm long. For this theoretical width, the interhelix gap is approximated with the minimal value given by Rothmund^[45], which is 0.9 nm. The pad's approximately 210 staples² route the scaffold into 16 parallel 431 bp double helices. The bottom eight helices are shorter. That is, two adjacent helices are of the same length, respectively and each pair is one helical turn short relative to the former pair. This bevels the lower right vertex as a chirality marker for AFM imaging. In total, the pad has three chirality markers. The second is a 232 b scaffold overhang protruding from its top right vertex. The third are the single-stranded DNA handles for binding nanoscale objects. They are supposed to protrude from one side only. For the block copolymer binding described in Chapter 4, pads with different handle pattern will serve as template, which will be discussed in detail in Section 4.2.

The pad must not form chains due to stacking. To prevent it, blunt ends are avoided: the left vertical edge (a in Figure 3.1) of the pad features 7 b single-stranded scaffold loops, the right vertical edge (c in Figure 3.1) features staples with 5'-TACACT-3' overhangs.

The pad is twist-corrected as described by Woo *et al.*^[129] to achieve a helical twist of 10.4 bp/turn. This involves leaving one base of the scaffold unpaired every 21 bases. This prevents a global twist in the origami, which is disadvantageous for its templating properties and surface deposition.

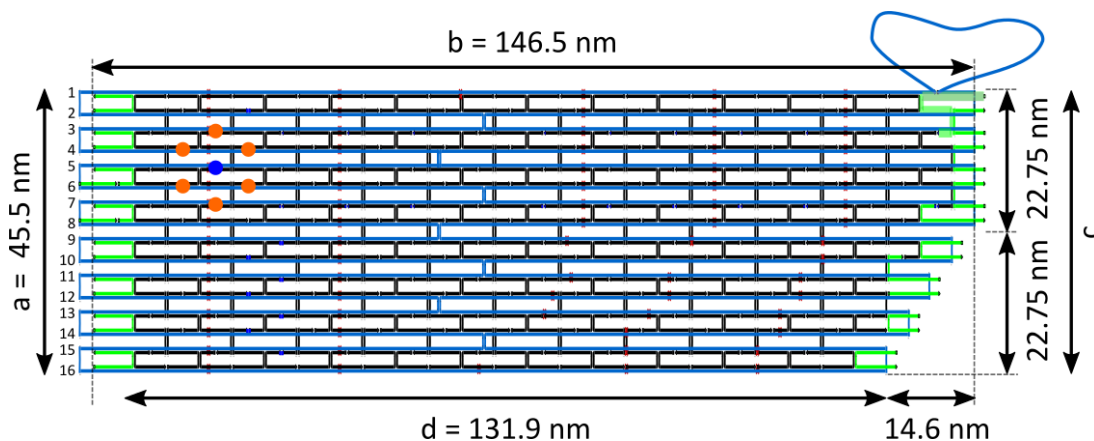


Figure 3.1: CaDNAno-based design scheme of the pad origami with theoretical edge lengths of the double-stranded body based on the size characteristics of B-DNA and a gap of 0.9 nm between the helices. The numbers of the 16 helices are denoted at the left vertical edge a . The M13mp18 scaffold, which goes into a 232 b loop on the top right of the pad, is depicted in blue. The 32 b body staples are shown in black. The green staples at the left vertical edge a leave 7 b of scaffold unpaired. The staples on the right vertical edge c feature 5'-TACACT-3' overhangs. Blue and orange circles mark seven example positions of staple ends, which can be prolonged into handles protruding to the top surface of the pad. The hexagonally arranged orange circles mark next-neighbour positions to the blue circle at a distance of about 6 nm.

²the actual number depends on design choices

The tPad

Figure 3.2 displays a tPad scheme including the lengths of all edges. To form this approximately square frame, staples fold the M13mp18 scaffold into 34 parallel helices. Only the helices 1 to 7 and helix 26 below the cavity span the full 288 bp width ($b = 97.9$ nm). The helices 8 to 25 consist of two 80 bp segments that flank the 128 bp cavity. The helices 27 to 34 are shortened to create the bevelled vertex as chirality marker as it was done for the pad. Additional markers are three scaffold loops that point into the cavity from the helices 7, 16 and 17. The loops can anchor objects in the frame's cavity as well. As described previously by the author^[367], the scaffold loops can be used to anchor a three-armed DNA strut. The struts' arms were made of either one or two DNA double helices. The struts can be used to enhance the visibility of the scaffold loop markers, or to immobilize nanosized objects at designated points in the cavity. Due to this noticeable feature that resembles a vertically flipped letter T, this origami was named 'tPad'.

Three types of vertical edges a and c were used, which resulted in stacking and non-stacking tPads. Non-stacking tPads feature 64 b scaffold loops at the helix ends (32 b per helix, Figure 3.2 b I). This type of tPad is used in the synthesis optimisation (Section 3.1.3), the testing of the thermal and mechanical stability (Section 3.1.4) and the super-resolution microscopy (Chapter 5). For stacking tPads, two types of end staples were investigated, because the staple design influences how adjacent structures are oriented in a chain of stacking origami (Section 3.1.5). The first end staple type is shaped like the letter z (Figure 3.2 b II), which is the routing of most body staples as well. The second end staple type looks like the letter u turned by 90° (Figure 3.2 b III). In the following, they are referred to as z- or u-staples, respectively. Both staple types are of the same length, but the z-staples crosslink three helices, the u-staples just two. At any type of edge, there are scaffold crossovers from one helix to an adjacent one. The z-staples introduce additional staple crossovers, which the u-staples do not. Consequently, on edges with z-staples all helices are fixed to the adjacent ones, and the terminal base pairs display a strained configuration with an almost 180° angle between them (Figure 3.2 b II).

The tPad is not twist-corrected. This design choice is based on the design of a frame-like DNA chip used by Sugiyama and co-workers^[368,369]. They found a non-twist-corrected frame to be assembling well enough to serve as pegboard for single-molecule studies^[92], and resilient enough for HS-AFM^[184].

Origami synthesis

According to previous work, DNA origami synthesis usually takes place in buffer with pH 8.0-8.3, 10-20 mM Mg^{2+} and an excess of staples to scaffold in the range of 5x to 10x^[45,51,368]. Here, the 2D origami were assembled with 20-30 nM template DNA and a 5x staple excess. Pads were assembled in 1x TE buffer and $MgCl_2$, tPads in 1x TAE buffer and $Mg(OAc)_2$.

3.1.2 Structure evaluation

Synthesis, yield, thermal and mechanical stability as well as stacking are evaluated based on the structural integrity of the surface-deposited origami. In this work, an origami structure is considered well-formed if its shape matches the design and if it does not display a shape-damaging lack of staples. In order to assess the origami with AFM, topographical imaging with tapping mode AFM has been used in liquid and air. AFM in air on dried samples is a quick, but yet sufficiently resolving way to assess whether the outer shape has formed according to design. Liquid AFM is more suitable to evaluate the size of the origami in solution, as shrinking caused by drying is avoided. Furthermore, liquid AFM is one of the few techniques that resolves the origami weave and allows characterising origami with single staple resolution. Amongst others, it was used here for tracking protruding handles or gaps of missing staples. Resolving the origami

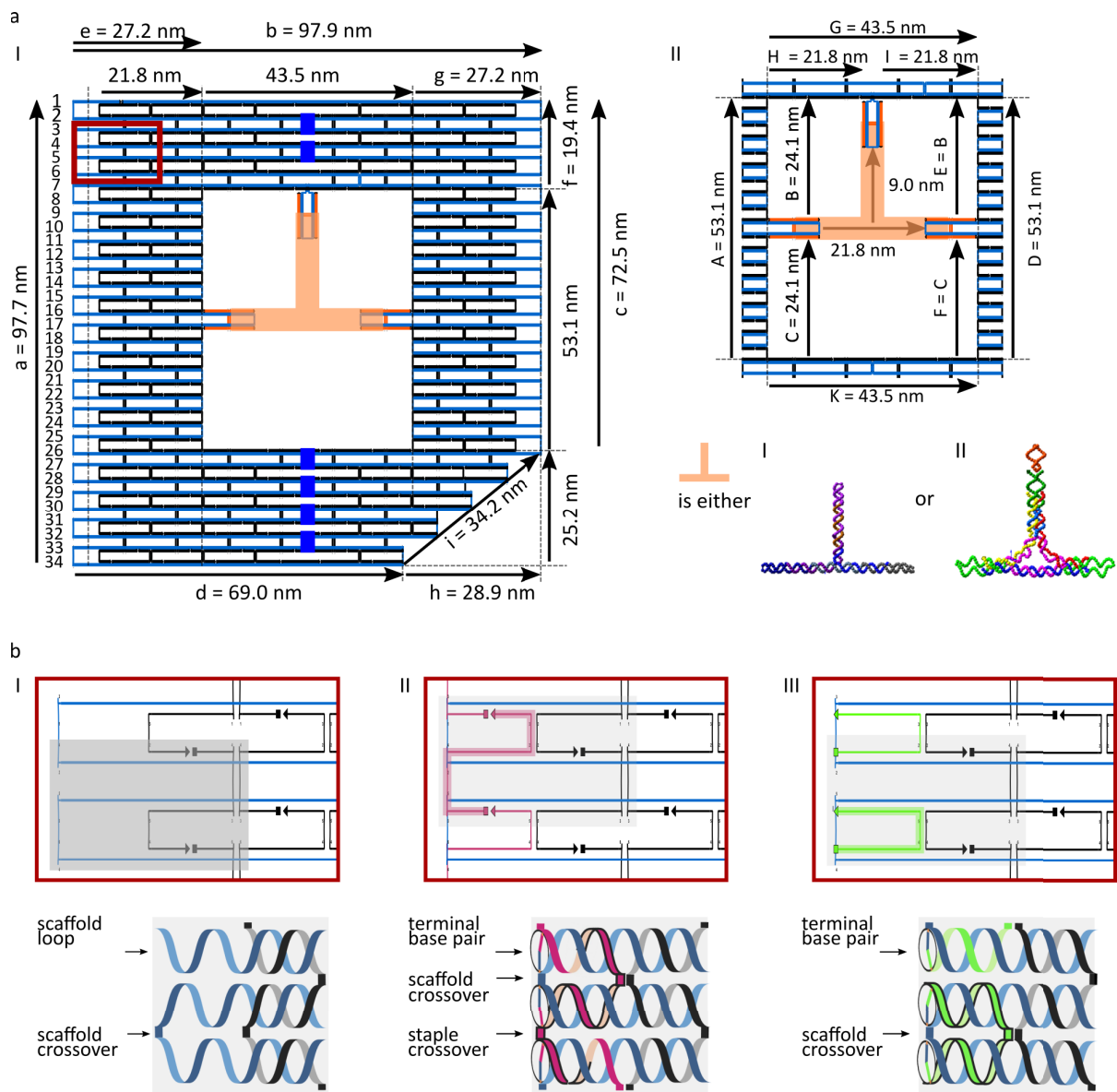


Figure 3.2: CaDNA-based design schemes of the tPad origami. a) I) Body of a non-stacking tPad made of 34 parallel double helices with theoretical edge lengths based on the size characteristics of B-DNA and a gap of 0.9 nm between the helices. The mostly 32 b body staples are shown in black. The M13mp18 scaffold is depicted in blue and runs in 64 b scaffold loops at the vertical edges (32 b per helix). Blue rectangles mark the tPad's central scaffold crossovers. An orange, vertically flipped T marks the position of an optional strut connecting the three anchor points in the tPad's cavity. The red rectangle marks the zoom-in area of b). II) Cavity of the tPad with characteristic dimensions. Below this, an one-helix and a two-helix strut are displayed that were incorporated into the tPad body during or after synthesis in a study by Fischer *et al.*^[367]. b) Different edge designs for non-stacking tPads with 64 b scaffold loops (I) and two types of stacking tPads with z-staples (magenta, II) and u-staples (green, III). In the bottom, the schematics with grey background display the course of the double helices in the area highlighted in grey in the red-framed schematics above. In the bottom schematic of (II) and (III), one z- and u-staple is highlighted, respectively, and the scaffold- and staples crossovers and terminal base pairs are displayed. For z-staples, the base angle is almost 180° due to the scaffold and staple crossovers at the edge. U-staples omit the staple crossovers and place less strain on the terminal base pair, which results in a base angle closer to that of typical of B-DNA.

weave was achieved in several liquid scans for the tPad and in $> 90\%$ of the liquid scans with the pad. Sometimes staples were removed by the tip during the scan, or the object was moved, but usually, the presented liquid AFM protocol (Section 2.6) allowed scanning at this resolution for several hours³.

In the following, the origami dimensions will be discussed using the dimension labels introduced in the Figures 3.1 and 3.2. Figure 3.3 a shows an example of a correctly assembled pad. The missing staples do not impair the structural integrity. 80-90 % of the pads of any handle pattern were found to be correctly formed. The pads occur as single objects as it was intended by placing single-stranded DNA pieces at their vertical edges (see Section 3.1.1). The dimensions of the pads were determined from images in liquid. On average, a pad is $b \approx 148.0 \text{ nm} \pm 4.6 \text{ nm}$ long and $a \approx 48.5 \text{ nm} \pm 2.6 \text{ nm}$ high⁴. That matches the calculated values given in Figure 3.1 well. Small errors are due to the overestimation of lengths in the xy -plane due to the tip radius, which makes an AFM image a convolution of the geometries of the sample and the tip^[370]. From the experimental value, an interhelix gap of 1.1 nm can be calculated. The chirality markers, that is, mainly the bevelled vertex and the scaffold overhang, allow determining the deposition side of a pad.

When imaging pads with single-stranded handles arranged at any of the patterns investigated⁵, for approximately half of them (55%) the handles face the tip (face-up), while for the other half (45%) the handles face the substrate (face-down).

High-resolution liquid AFM was used to control the presence of the 8 b, 15 b or 20 b handles of the pads for the block copolymer attachment. The different handle patterns are discussed further in Section 4.2, in the context of attaching P3(EO)₃T-b-ODN block copolymers.

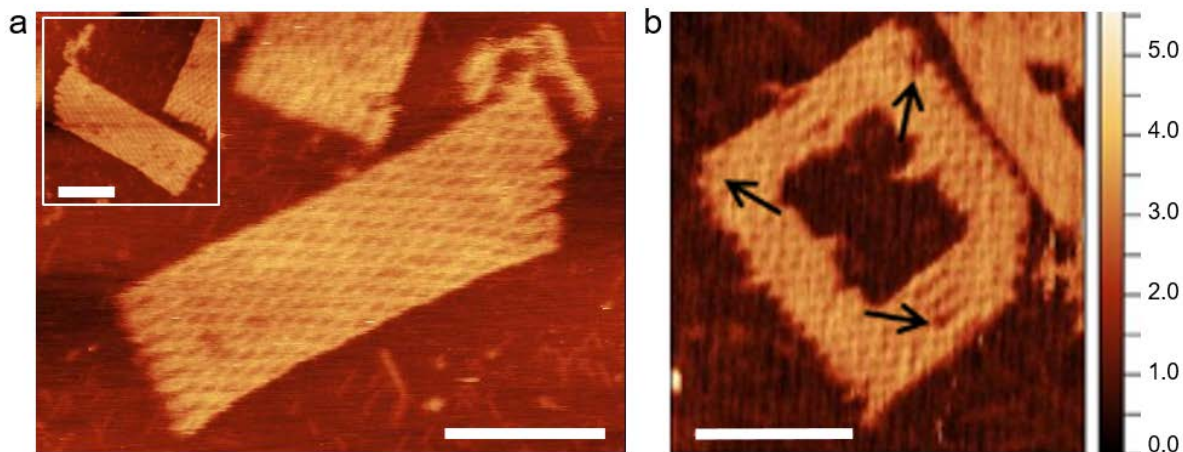


Figure 3.3: Structure evaluation with high-resolution liquid AFM. The origami weave is resolved and missing staples can be detected (black arrows). a) Pad with 40 handles (design as shown in Figure 4.3 c). In the large image, the handles (not visible) face up as they do for 55 % of the pads. The inserted figure shows a pad where the handles face down to the substrate, as it is the case for the remaining 45 %. b) tPad with three marked gaps (black arrows) that were produced deliberately by leaving out the staples. These mark the fluorophore positions in the tPads used in Chapter 5. Scale bars: 50 nm. Height scale in nm accounts for all images.

Figure 3.3 b shows a tPad that is considered well-formed. For this origami type, several structural details were measured in addition to the height a and width b . The average value for 20 characteristic dimensions of 31 non-stacking tPads scanned in liquid and 16 non-stacking tPads scanned in air are given in Table 3.1 I) that lists ten dimensions of the outer frame and Table 3.1 II) with ten dimensions of the cavity. Both AFM experiments yielded dimension values in the range of the theoretically expected values, and similar standard deviations of the measurements with $s_{liquid} = 3.6 \text{ nm}$ and $s_{air} = 4.2 \text{ nm}$.

³All images in Figure 3.7 b, for example, were acquired during one scan that lasted 5 h.

⁴means \pm sample standard deviations for $N = 25$ pads

⁵see Section 4.2

Scanning in liquid yielded closer matching values than the scanning in air, which is due to drying effects. Compared to the outer tPad dimensions in liquid, the tPads scanned in air display shorter vertical edges a and c , and slightly longer top and bottom edges b and d . Apparently, drying reduces the interhelix gaps, probably because the Holliday junctions close. The interhelix gap lies around 1.0 nm for tPads in liquid, but around 0.8 nm after drying. Simultaneously, the DNA helices seem to elongate slightly. This is not only indicated by the larger top and bottom edge, but also by the slightly wider left and right part e and g , and the slightly decreasing width of the inner cavity G and K . Two other effects contribute to this finding. The image resolution achievable with the air-scanning tips was lower than for the liquid mode tips. Thus, the scaffold loops at the outer vertical edges have probably been counted as part of double-stranded tPad body. The second effect is the aforementioned feature broadening due to the width of the AFM tip.

Table 3.1: Dimensions of the tPad scanned with AFM in air ($N = 16$) and liquid ($N = 31$). The theoretical values are given in the row “design”. The average standard deviations for all dimension values are: $s_{liquid} = 3.6$ nm and $s_{air} = 4.2$ nm. Dimension labels correspond to Figure 3.2 a I) for the outer frame and II) for the inner cavity.

I) Outer frame	a [nm]	b [nm]	α [°]	c [nm]	d [nm]	e [nm]	f [nm]	g [nm]	h [nm]	i [nm]
design	97.7	97.9	90.0	72.5	69.0	27.2	19.4	27.2	28.9	34.2
air	89.7	90.0	91.2	65.7	65.8	25.6	20.9	24.9	24.8	35.6
s_{air}	5.8	5.8	3.1	5.5	4.8	2.7	2.8	3.7	3.2	4.9
liquid	98.7	88.2	90.6	76.6	63.5	24.5	20.9	24.2	26.7	35.0
s_{liquid}	4.6	6.5	6.6	3.8	4.2	2.5	1.7	2.8	2.3	3.1

II) Cavity	A [nm]	B [nm]	C [nm]	D [nm]	E [nm]	F [nm]	G [nm]	H [nm]	I [nm]	K [nm]
design	53.1	24.1	24.1	53.1	24.1	24.1	43.5	21.8	21.8	43.5
air	48.5	16.0	20.6	45.7	18.6	18.8	40.4	14.4	15.3	37.7
s_{air}	2.7	3.0	3.8	8.1	3.7	8.4	3.5	2.8	2.9	3.6
liquid	51.4	21.9	22.2	51.7	22.4	21.8	41.0	17.6	15.6	40.7
s_{liquid}	3.4	3.1	3.6	4.1	3.4	3.7	3.3	2.5	3.1	3.3

In Figure 3.3 b black arrows indicate that three tPads staples are missing. In this tPad batch, they were left out deliberately during the synthesis. These staples carry the handles for the fluorophore attachment in the super-resolution microscopy-based structure evaluation discussed in Chapter 5. Leaving these staples out creates a marker of the fluorophore positions in AFM images to evaluate the handle position, which could be recognized more easily than one protruding handle. By measuring the distances of the gaps left by the missing staples, the fluorophore distances could be determined from AFM images and provided a value for comparison with the super-resolution microscopy. The results will be discussed in Section 5.1.2.

3.1.3 Yield determination and synthesis variations to improve the yield

Agarose gel electrophoresis and AFM were used to evaluate the synthesis results. While gel electrophoresis reveals qualitative aspects, yield determinations were based on counting intact origami structures in AFM images. Mica samples of intact and ill-shaped pads and tPads have always appeared similarly covered, suggesting a similar deposition behaviour. Thus, it was assumed that the proportion of correctly folded origami in the AFM images represents that in solution. In order to evaluate the influence of the AFM protocol on the count of intact structures, the yields of the origami syntheses were assessed for scanning in air and in liquid for both the pad and the tPad. Variations in the count of intact structures were found to be within the statistical variations as they occur amongst samples. Thus, the yields of scanning in air and liquid will be directly compared in the following.

For the pad, a 5 h synthesis protocol was used (see Section 2.2). This protocol is based on a constant

cooling from 85 °C to 24 °C in 0.1 K steps, where each step lasts 30 s. The 85 °C are first held for 10 min. Figure 3.4 a gives an impression of a typical pad sample. For pads with any kind of handle pattern the yield was found to be above 90%. This lines out with published data for the RRO^[45] and reflects a robust design and suitable protocol. For the pad, shorter syntheses routes were established too, but not used in the present work.

The tPads assembled poorly with the pad protocol. A first successful protocol comprised of cooling from 90 °C to 24 °C in 1 K steps, where each temperature was kept constant for 10 min. This protocol lasts 11 h. The yield was found to be in the range of 45-70%. For the latter, Figure 3.4 b shows a typical field of view. In any case, the tPad yield was below the yield of the pads, and it varied strongly between samples. In order to improve this, several parameters can be adjusted. This includes the staple : scaffold ratio, the type of the assembly buffer including the salt concentration, design changes, or the optimisation of the synthesis protocol. Amongst these, this work focuses on adjusting the synthesis protocol, which will be discussed in the following.

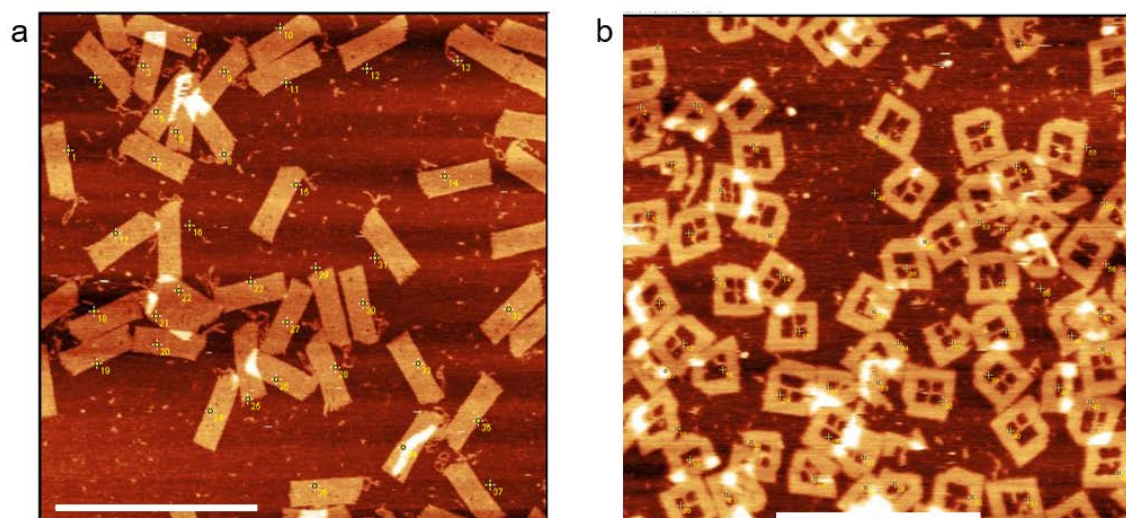


Figure 3.4: Overview AFM images of correctly synthesised pads (a) and tPads (b) obtained in liquid. Scale bars: 500 nm. Yellow dots and numbers were set during yield determination. Structures at the edge and in undefined multilayers were not counted.

For a planar, rectangular structure Sobczak *et al.*^[143] have reported how a customisation of the synthesis protocol has led to a sevenfold yield increase. For that purpose, they have exchanged the constant-rate-synthesis by a constant-temperature-synthesis at a previously determined, origami-specific annealing temperature.

In order to improve the tPad yield by synthesis adjustment, the annealing temperature (T_A) range was probed with a three-stage protocol that resembled the one of Sobczak *et al.*^[143]. According to the latter and Song *et al.*^[146], there is an interplay between the temperature, the folding time and the staple excess used in such isothermal syntheses. Here, a rapid cooling from 90 °C to $T_A(\text{Test})$ (stage 1), keeping $T_A(\text{Test})$ for 1 h (stage 2), and then rapidly cooling to room temperature (stage 3) at a staple : scaffold ratio of 5 : 1 was chosen. In total, that protocol takes 1.5 h. $T_A(\text{Test})$ was chosen to account for the fact that a melted DNA double strand reassembles correctly with the highest probability when it is kept in a temperature range of 25 K below its T_M ^[17]. As the histogram in Figure 3.5 shows, the melting temperatures of most tPad staples lie in the range of 76-78 °C.

Therefore, $T_A(\text{Test}) = 52.0$ °C was chosen as the first temperature under test. Then, $T_A(\text{Test})$ was varied in a stepwise manner to identify the lowest and highest temperatures that yielded correctly formed tPads. This resulted in a test range of 58.0 °C to 28.0 °C. For six $T_A(\text{Test})$, the yield was determined by counting intact structures in AFM images, of which zoomed parts are shown in Figure 3.6 a. Figure 3.6 b summarizes the yields of intact tPads at every $T_A(\text{Test})$. Figure 3.6 c displays single, partly assembled

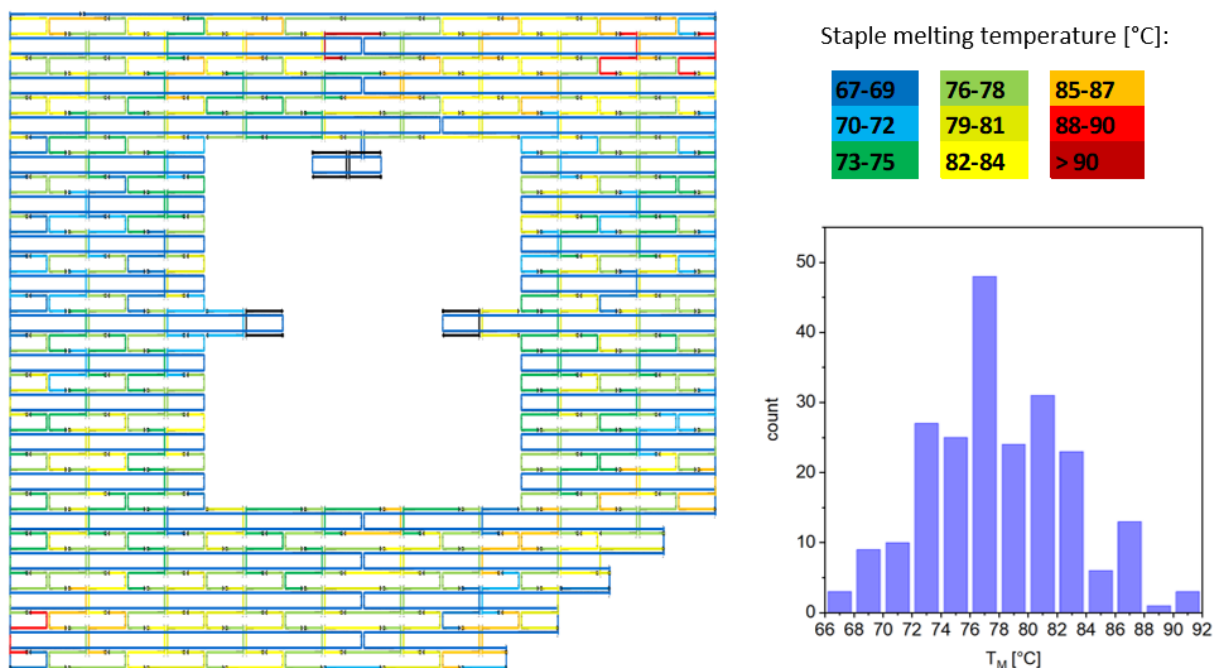


Figure 3.5: tPad heatmap and distribution of the staple melting temperature for the 223 tPad body staples for z-staple tPads. All staples are coloured according to their melting temperature except for the four staples covering the anchor sites in the cavity, which are marked in black.

tPads at $T_A = 58.0^\circ\text{C}$ and schematics of the segments already formed. Furthermore, Figure 3.6 d displays agarose gels loaded with tPads synthesised at all $T_A(\text{Test})$ used in this work.

In the agarose gels, bands that lie above the bare M13mp18 band are found for all temperatures, indicating that folding takes place at any of the investigated $T_A(\text{Test})$. The most intensive band in all lanes is at approximately the same height, which is similar to the height of tPads obtained from the 11 h protocol (“long” in Figure 3.6 d). This indicates correctly folded structures in all cases. However, the AFM images of the 58.0°C and the 28.0°C samples contradict this finding. Overall, the yield increases in a range from 58.0 - 47.0°C before it decreases again. A yield of at least 45% of fully formed tPads can only be found in the range from 52.0 - 38.0°C (Figure 3.6 b). Apparently, tPads that are not fully formed have almost the same gel mobility as correctly formed ones. This suggests that a gel can only provide limited information on the structure formation. Another observation to consider is the appearance of further, higher bands. There are up to three additional bands in a lane. In every lane, one clearly visible band occurs above the main band. It could be due to a secondary structure or due to clusters. Upon extraction from this band, only single, correctly folded tPad structures were observed, which points in the direction of a temporary aggregation. The band occurs with greater intensity in the lanes of the constant-temperature folding than in the lane with the constant-ramp-folding, i. e. the 11 h-protocol. In contrast to the findings of Sobczak *et al.*^[143], secondary structure formation did not decline with synthesis protocol adaption. In the lanes for 58.0°C and 47.3°C and 45.8 - 35.0°C , a third band is clearly visible. In the range of 40.0 - 35.0°C another, fourth band is visible that becomes the more intense the lower the temperature gets. The third and fourth bands are faint or not visible in the temperature range that yields predominantly well-formed tPads, therefore they most probably contain ill-formed structures. Apparently, these structures differ towards the higher and lower edges of the temperature range, as the fourth band only occurs in the lower range.

In Figure 3.6 a it can be seen for 58.0°C and 28.0°C that characteristic, partly folded structures form at given temperatures. This lines out with the distribution of the staple melting temperatures. For 58.0°C , the top and bottom rectangular segments of the tPad are already well-formed, while the left and right sides lack staples (Figure 3.6 c). As shown in Figure 3.5, the proportion of staples with a $T_M > 78^\circ\text{C}$ is

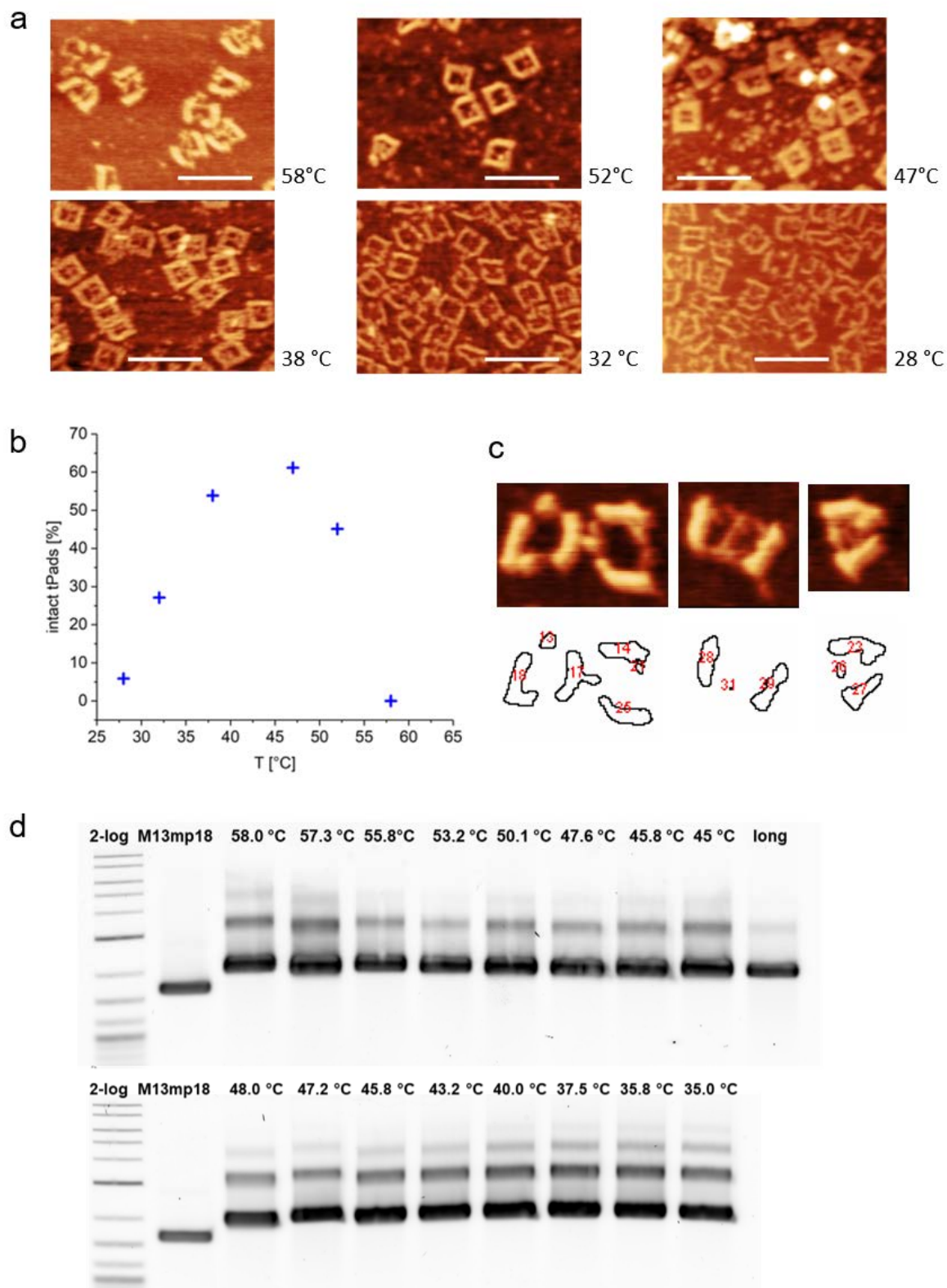


Figure 3.6: Annealing temperature screening for the tPad. a) AFM images taken in air for six $T_A(\text{Test})$. Scale bars: 100 nm. b) Yield of correctly formed tPads at the six $T_A(\text{Test})$ imaged in a). c) Single, partly folded tPads at $T_A(\text{Test}) = 58.0^\circ\text{C}$ and the outline of the top and bottom horizontal rectangular segments that form typically. d) 1% agarose gel of 16 $T_A(\text{Test})$. A 2-log ladder, the M13mp18 scaffold and tPads assembled with the 11 h protocol were applied for comparison. Despite different folding states, the resulting tPads show a very similar mobility in agarose gel electrophoresis. Gel running artefacts such as the slight, concave arch between 47.2°C and 35.0°C probably play a larger role regarding the variations of the origami band position than differences in the origami structure formation.

significantly higher in the upper and lower rectangle than in the sides. Apparently, the folding proceeds hierarchical, starting with these staples with a large T_M . For 28.0 °C, all tPad parts seem to form, but the structures appear frayed. This is probably because most of the staples did not anneal correctly.

Overall, the maximum yield of correctly folded tPads did not increase in this short protocol compared to the long protocol. Yet, the shorter protocol saves time and supposedly reduces the thermal stress imposed on the DNA^[143], although that was not investigated directly here. For investigating the aggregation behaviour (see Section 3.1.5), tPads were assembled using $T_A = 49$ °C, and directly compared to the 11 h protocol. There was no apparent trade-off in structure stability or a change in aggregation behaviour. For the fluorescence microscopy, a 7 h protocol was employed. It consisted of heating to 90 °C followed by cooling at a fast rate of 1 K/min to 60 °C (stage 1) and at a slow rate of 1 K/15 min to 24 °C (stage 2). The tPad yield was found to be between 50 % to 70 %, which is in the same range as for the 11 h protocol. The 7 h protocol is shorter than the initial 11 h protocol, but it allows more time for each staple to incorporate than the three-stage-protocol. As a fluorophore will be anchored to one handle only, a longer protocol was thought to create the best premises for a successful labelling. This follows the findings of Sobczak *et al.*^[143], who reported that folding was not at equilibrium after 2 h at a constant temperature, but rather after 2 d.

In conclusion, both structures assemble as designed. The twist-corrected pads displayed synthesis yields above 90 %. For the tPad, the yield was below that of the pad and could not be increased by refining the synthesis protocol. Apparently, the synthesis is not the main reason for the yield decrease. Two factors could have played a role here and might be investigated further. Firstly, the staple : scaffold ratio could be increased. Several studies have investigated the influence of the this ratio on the assembly temperature T_A ^[139,146–148] and found that the yield has benefitted from a higher staple excess. The second factor is that the tPad is not twist-corrected. It was assumed, that the cavity would relax the structure sufficiently. However, that is not the case as CanDo^[60,61] model calculations show, which were generated after the synthesis tests (resulting simulation images: Appendix Figure A.3). The twist could have introduced an energy penalty in the DNA hybridisation, which prevents higher yields.

3.1.4 Thermal and mechanical stability

As discussed in the introduction, several studies have investigated the temperature resilience of continuous rectangular origami^[138,139,143,147], which resembles the pad. As there are fewer studies on a cavity-bearing structure, only the tPad will be discussed in the following.

The tests will be conducted for tPads in solution and bound to mica, because both processes can be relevant when using DNA origami as a pegboard. It is assumed that the melting will start at higher temperatures for the surface-bound origami than for the origami in solution. That is because in surface-bound origami, not just the intermolecular interaction within a DNA double helix stabilise the structure, but also attractive interactions between the substrate and each DNA strand. Furthermore, the surface-bound DNA has fewer degrees of freedom to untwist, and the staples can only depart from the structure into half the directions available for origami in solution. Both limitations kinetically impede the dehybridisation process. Song *et al.*^[138] proposed such a stabilising effect for 2D rectangular origami bound to mica. They found that the melting started at 55 °C. This is similar to the value found for a 3D object in solution^[60], which should melt at a higher temperature because melting can only take place at the surface. The enhanced resilience of the surface-bound origami supports the assumption of a stabilising surface effect.

The experiments presented in this work focus on whether the outer tPad frame loses its integrity in a 22-65 °C temperature range. Determining the synthesis protocol has shown that this includes the most relevant range for origami folding, and hence, for sticky end-based nanoobject attachment.

Melting in solution

For the melting experiment in solution, tPads were filtered to remove excess staples. Then they were heated to the temperature under test within few seconds, and kept for the targeted time. Next, an aliquot was withdrawn with a pipette and quenched in buffer cooled to 4 °C. Directly afterwards the sample for AFM in air was prepared⁶.

The protocol was set up following three objectives. First, origami that had not suffered from thermal stress before (for example, through a long, gradual heating process^[139]) was exposed to a discrete temperature under test. Second, the effect of the length of keeping the discrete temperature was considered. Overall, this resembles an annealing procedure, which can be a step, e.g., in labelling reactions or nanoobject binding. Third, the rapid preparation of dry samples for AFM in air accounts for freezing the state of the origami without allowing time for staples to detach further⁷, or for healing. An unwanted healing can take place by reassembling of detached staples from solution or re-hybridisation of partially attached staples. To eliminate reassembling as much as possible, filtered samples were used. Furthermore, the quenching step involved a 20x dilution in buffer, which dilutes the concentration of detached staples enough to make a reassembly unlikely. Using cold buffer and preparing the AFM samples quickly after quenching was thought to impede the re-hybridisation of partially attached staples. To test whether healing occurs in sample solutions treated like this, a second set of AFM samples were prepared from quenched solutions after keeping them at 4 °C for one day. Changes in the structures' appearance that indicate a significant reincorporation of detached staples were not visible in the AFM images.

Example images of the samples at 50 °C, 55 °C and 60 °C are shown in Figure 3.7a I-III, while Figure 3.7a IV displays the sample after filtration prior to the thermal stresses for comparison. The yield of intact tPads in that sample was 17 % (N = 496 tPads), while it was 59 % before filtering. The damage due to cleaning will be discussed later in this section.

It was found that tPads heated in solution keep their shape until 50 °C. Also after 110 min at 50 °C the yield of intact tPads was 21 % (N = 33 tPads), which agrees with the yield after filtering within statistical variations. However, heating to 55 °C for 10 min has already decreased the yield of intact tPads to zero, leaving partly folded structures behind. At 60 °C, only entangled coils were visible. Apparently, the melting is at its thermal equilibrium quickly, which lines out with the findings of Sobczak *et al.*^[143].

Taking a closer look at the shape of the partly folded origami at 55 °C (Figure 3.7a II) reveals that the upper and lower rectangular segments are more persistent than the left and right side. This is a hint that the melting proceeds as the reverse of the folding. Folding intermediates with the same segments have occurred in the synthesis test with 58 °C as the annealing temperature (Figure 3.6c), while at $T_A = 55$ °C, most tPads displayed a well-formed short vertical side additionally. Apparently, the melting proceeded at a lower temperature than the folding. Studies of the Rothmund rectangular origami have found an opposite hysteresis^[139,143]. Looking at just the structure itself, this is plausible due to a cooperative effect. In the beginning of the melting, only the staple is free to diffuse away, while the scaffold is held in place by other staples. This increases the local concentration of the DNA sequence complementary to the staple, which shifts the reaction equilibrium towards the hybridised state. In contrast to the studies mentioned above, the tPad melting was studied in a filtrated sample. That is, a staple is more likely to diffuse away from the origami and a void is less likely to be filled due to the low surrounding DNA concentration.

⁶For details of the protocol see Section 2.6

⁷Non-heat related damage could result from decay over time. Furthermore, it can be caused by mechanical stress during pipetting and by rinsing with deionised water, as Lee Tin Wah *et al.* have found for the RRO^[139]. The pad and tPads, however, were found unchanged by pipetting and rinsing on other occasions. Furthermore, the scan quality for water-rinsed mica samples was much better than for unrinsed samples. Consequently, pipetting and rinsing were kept in the protocol.

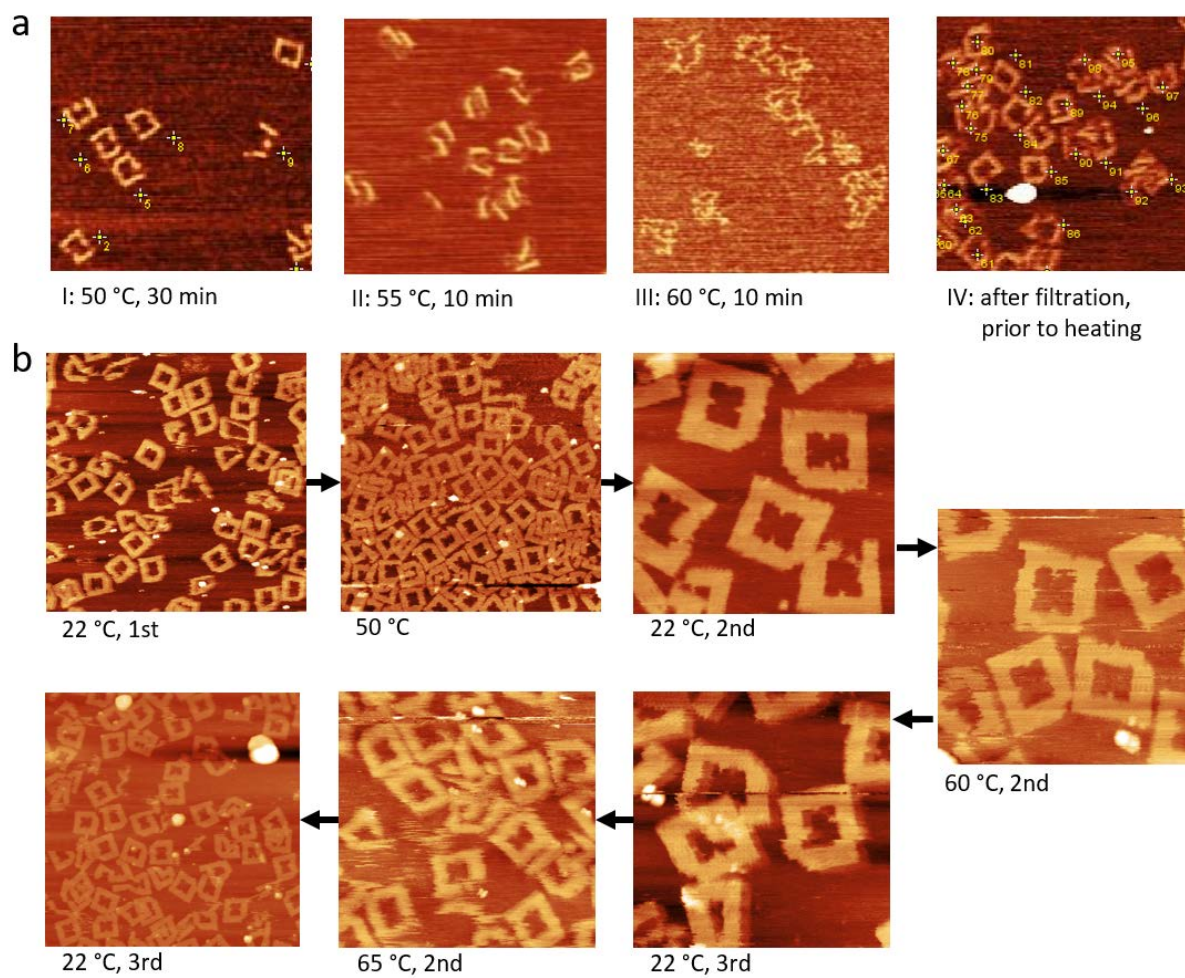


Figure 3.7: Thermal stability of tPads (a) heated in solution prior to immobilisation (temperatures and times given in the images) and (b) deposited on a mica surface prior to heating. Yellow crosses and numbers indicate the use of these images for yield determination. The image series in b) was acquired from one samples that was heated and cooled as given.

The thermal stability of surface-bound tPads

That origami is significantly more stable to elevated temperatures when deposited on a surface was, e. g., described by Song *et al.*^[138].

Figure 3.7 b displays AFM images of tPads under an oscillating heating ramp. The ramp started at 22 °C followed by heating to a temperature under test and keeping that temperature for 30 min before cooling to 22 °C again and heating to the next temperature under test. The protocol is given in detail in Section 2.6. As temperatures under test, 50 °C, 60 °C and 65 °C were chosen. Each temperature was kept for 30 min to ensure reaching the temperature under test, and to allow the system to equilibrate. Between the first and last image taken, the sample was scanned for five hours. During the heating, the tip lost contact with the sample because of heat-induced movements of sample and scanning buffer. In order to avoid an experiment termination due to unnecessary wearing of the tip, the tPads occurring at the tip position after re-engagement were scanned instead of searching for the former field of view.

As can be seen, damage or a considerable removal of staples that would result in disassembly of the tPads did not occur, even though the same area was scanned repeatedly and over at least half an hour at each temperature under test. Damaged tPads have already occurred at the first 22 °C stage, which most likely stem from filtering the tPads. Over the course of the experiment, the number of image artefacts such as scan lines and blurry tPads edges has increased. In the 65 °C image the scanning resolution was worst, and some tPads seemed to disengage from the surface. These findings are most likely related to thermally induced movements in the sample and some unavoidable wearing of the tip over the long scan time, and not due to damage of the origami. That is because at the final 22 °C stage, the tPads seem in a similar state as in the first stage. During this *in-situ* thermal test of the tPad, buffer had to be added due to evaporation upon heating, nevertheless, the weave was resolvable throughout the experiment and the tPads were not damaged. The poly-L-ornithine, which is used as a deposition-aiding agent here, plays a key role for these findings. Apparently, it ensures a strong adhesion of the origami to the mica, which aids in keeping it assembled.

Overall, the temperature at which basically all tPads in solution display a disintegrated outer shape was determined in the range of 50 °C to 55 °C⁸, which agreed with the temperature at which fully folded structures occurred first in the folding process. On the contrary, tPads deposited on mica with poly-L-ornithine as a positively charged deposition agent did not even suffer the loss of staples until the highest temperature under study of 65 °C. This lines out with the expected stabilising effect of depositing origami on a surface.

This qualitative study of the thermal stability of the tPads was useful to determine the experimentally relevant breaking temperature of the tPads in solution, and to establish a protocol for hot stage AFM with the tPads. First hints towards a hierarchical folding and melting are given by the occurrence of characteristic rectangular folding intermediates at the tPad top and bottom at distinct temperatures in both the folding and melting process. The presented hot stage AFM protocol provides the basis for further work on a qualitative folding and melting study as executed for rectangular origami by Lee Tin Wah *et al.*^[139]. Such a study will reveal further folding intermediates and clarify the hysteresis behaviour of the folding and melting.

Mechanical stability

A common mechanically demanding situation for pads and tPads is purification by centrifugal filtration. Detailed protocols are given in Section 2.5. When used as a pegboard, tPads usually undergo three buffer washes and centrifugation in a benchtop centrifuge at a rotational speed of 4000 rcf in filters (Amicon) with a molecular weight cut-off (MWCO) of 100 kDa to remove the excess staples. Pads are filtered using the same filters, or filters with the same MWCO produced by Pall, and centrifugation at 10000 rcf. The

⁸Note again, that the temperature decreases during assembly, while melting studies start at lower and proceed to higher temperatures.

yield of intact pads after filtration lies in the range of 85-90% of the initial synthesis yield, and decreases slightly with increasing rotational speed. For tPads, the filtration usually decreases the proportion of intact tPads to 30-50%, in rare occasions even to 10%. Figure 3.8 shows the intact proportions of filtered pads (grey markers) and tPads (blue and orange markers) relative to the initial yield that were obtained in a test with two filter brands and different rotational speeds. In the Amicon filters, two membranes are on opposite sides of the tube, while one membrane is at the bottom of the Pall filters.

During the filtration, the centrifugal force presses origami and staples against the membranes. While the staples pass the membrane, the origami has to withstand this mechanical stress. With Amicon filters, the last step is a filtration at 1000rcf with the filter placed upside down in a fresh tube to detach the origami from the membranes. For the Pall filters, origami is recovered through pipetting. Both processes impose additional mechanical stress.

The proportion of intact origami was determined with AFM. As expected, the pad quality decreases slightly with increasing mechanical stress at higher rotational speeds. However, the yield of intact structures remains well above 80%, in contrast to the tPad yield. Interestingly, the proportion of intact tPads increased in two of the occasions presented here. Probably, destroyed structures had formed aggregates that remained in the filter. However, it was found that such occasions cannot be reproduced deliberately.

Overall, the mechanical stress of filtration affected the tPads in a primarily detrimental way, while the pads were indifferent to it. The same behaviour was found for the other purification techniques freeze'n'squeeze and electro elution⁹. Probably, the twist of the tPad and its cavity play a role regarding its mechanical stability.

For the hybrid formation, pads were filter-purified, as it is faster than gel-based techniques, but yet sufficient. For the fluorescence microscopy, filtered and gel-purified tPads were used and quality control with AFM after filtration was always performed.

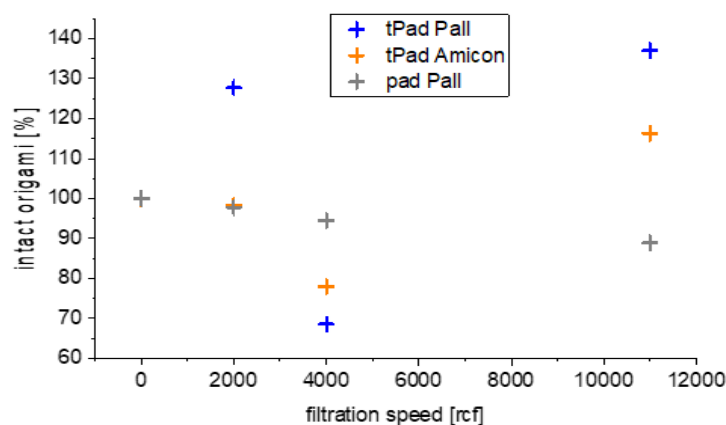


Figure 3.8: Intact origami after filtration in benchtop centrifuges at different rotational speeds with centrifugal filters of the companies Amicon and Pall with a molecular weight cut-off of 100 kDa. While the proportion of intact pads barely changes, tPads are significantly disturbed. An increase of the intact tPad proportion can be due to the removal of misfolded structures that have aggregated upon centrifugation.

⁹For both techniques origami is purified in an agarose gel first. In freeze'n'squeeze the origami band is cut out then and the origami-containing liquid is strained from it in a filtration step. In electro elution, the origami band is cut out and placed in a sealed membrane container. The container is then placed in the electrophoresis chamber, and the origami is moved from the band by an electric field. Electro-elution thus involves only minimal mechanical stress occurring during the movement of the origami through the agarose electrophoresis gel.

3.1.5 Stacking

As discussed in the context of the design of the pad and tPad (Section 3.1.1), the aggregation of DNA origami structures due to stacking can be controlled through the design of the helices ends. In that way, larger structures can be built up deliberately, or the interaction can be avoided. For the pad, the aim was to have single origami structures, so scaffold loops and staple overhangs at the helix edges were used to prevent stacking. For tPads, the chain formation due to stacking was investigated^[367] in the course of this work, as this behaviour had not been described in detail for a cavity-bearing structure before.

While virtually 100% of the tPads without end staples occur as single objects, tPads with blunt ends were always found in the form of aggregates. Long chains as well as shorter aggregates of two to five tPads or chain clusters such as shown in Figure 3.9a were found for both z- and u-staple featuring tPads.

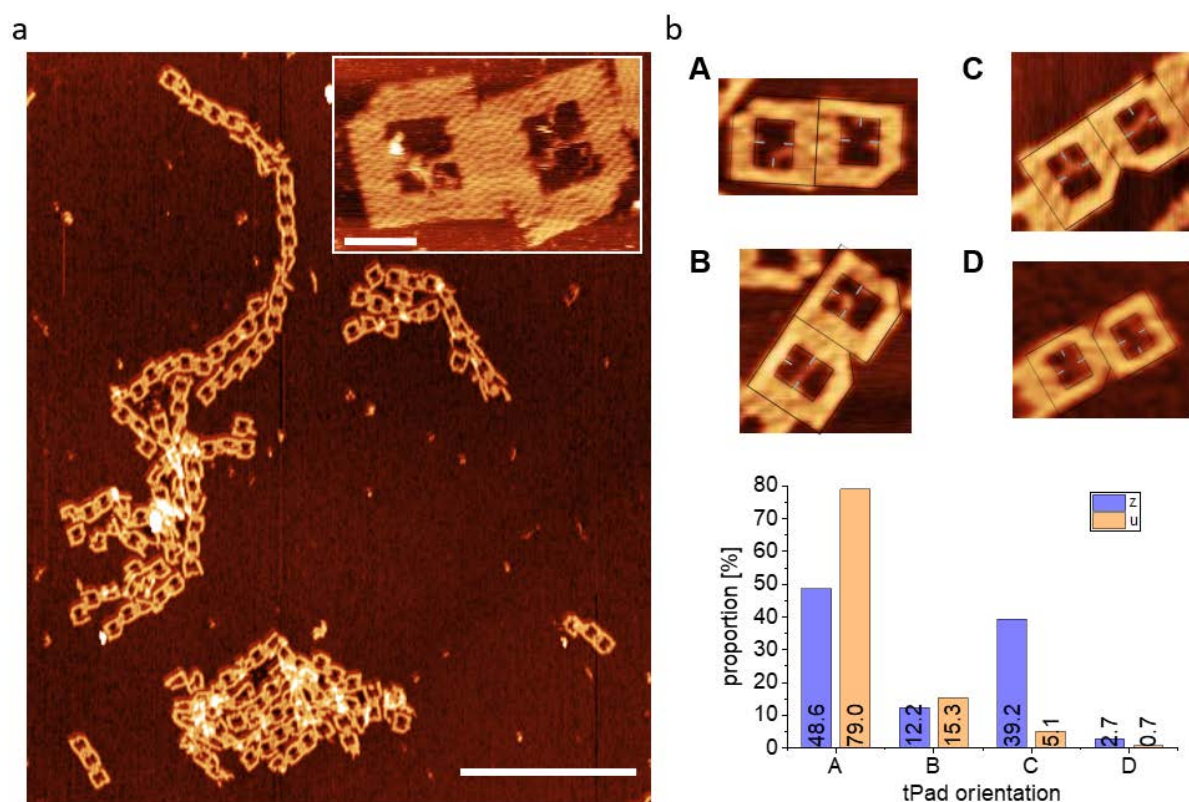


Figure 3.9: Aggregate formation of tPads due to base stacking. a) AFM image of a typical field of view for z-staple tPads with chain aggregates of different lengths. Similar aggregates form with u-staple tPads. Scale bar: 1 μm . The inset AFM image shows a high-resolution image of two stacking tPads where the interacting DNA helices with blunt ends are resolved. Scale bar: 50 nm. b) AFM images (including schematic outlines) of pairs of stacking tPads with different relative tPad orientations: rotated (A), head-to-tail (B), horizontally flipped (C) and vertically flipped (D). The histogram displays the relative occurrence of the orientations for tPads with z- or u-staples.

A typical field of view with z-staple tPads is shown in Figure 3.9a. Dilution in 1x TAE with 5 mM $\text{Mg}(\text{OAc})_2$, did not dissolve the aggregates significantly.

In general, z-staple and u-staple tPads showed a similar stacking behaviour. However, there were differences in the relative orientations of two adjacent tPads in a chain. In total, two tPads in a chain can assume four possible orientations, which are shown in Figure 3.9: rotated (A), head-to-tail (B), horizontally flipped (C) and vertically flipped (D). All orientations were found using z-staples (see Figure 3.2 bII), while for u-staple-featuring tPads, almost exclusively the head-to-tail and the rotated orientations were resolved. A similar specificity of the aggregation has been previously described for stacking origami rectangles^[129], which are similar to the pad. In their report, Woo *et al.*^[129] have attributed this behaviour to orientation-dependent differences in the strength of the stacking bonds

between the terminal base pairs of two origami. Using terminal G-C pairs only, Woo *et al.* assumed that the different crossover distributions at the edges for the z- and u-staple origami have caused the different bond strengths. As Woo *et al.* have discussed in detail, sufficiently strong stacking bonds for u-staple origami can only occur in the head-to-tail and the rotated orientation. As shown in Figure 3.2 b III, the terminal base pairs display an almost natural base angle, so the interacting area is not at its maximum for the flipped orientations. For DNA origami structures with z-staples, the stacking bond strength does not significantly differ between the orientations, because the combined scaffold and staple crossovers at the z-staple edges stretch the base angle to almost 180°. Consequently, z-staple DNA origami structures can be arranged in all orientations while the flipped orientations should be intentionally avoidable in u-staple origami chains.

While Woo *et al.* could show that origami rectangles show exactly this behaviour, the aggregation specificity of the tPads was not as dependable. As can be seen in the Figure 3.9 b, the flipped orientations occasionally occurred in u-staple tPads as well. Presumably, this is because other parameters than the end staple design alone influence the stacking. Buffer and ionic strength conditions are approximately the same in the investigations presented here as in the study by Woo *et al.* Therefore, they are not the reason for the differences described herein. Probably, the cavity in the tPads enhances the structure’s flexibility and allows the stacking base pairs to assume energetically favourable orientations in the flipped orientations as well.

3.2 Towards decorating DNA origami

As the last part of constructing 2D origami pegboards, this section introduces the sticky end sequences used for the block copolymer (Chapter 4) and the fluorophore attachment (Chapter 5). Sliding and specific sequences are discussed. Choosing different sequences on one template allows for the parallel assembly of different nanoscale objects. As a proof-of-principle study, the parallel assembly of different gold nanoobjects on the pad is presented. The EGNAS software^[77] is used to optimise the binding abilities of the specific sequences.

3.2.1 Design of the link sequences

As discussed in the Section 1.2.1, the link consisting of the origami-bound handle and the object-bound ODN (see Figure 1.2) plays a crucial role for the yield of nanoobject binding to DNA origami via sticky ends. Table 3.2 lists the sequences used for the pad and the tPad. Both sliding and specific sequences were employed to study the influence of the sequence on the attachment yield of the block copolymer binding to the pad. Specific sequences were employed to attach different fluorophores to the same tPad.

Table 3.2: Sequences of the handles and oligodeoxynucleotides (ODNs) used as links for nanoobject attachment to the pad and the tPad, respectively. The first three rows list sliding sequences, the remaining rows specific sequences. All specific sequences were engineered with the EGNAS software^[77].

	handle name	handle sequence (5' - 3')	ODN name	ODN sequence (5' - 3')
pad	15A	AAAAAAAAAAAAAAAA	18T	TTTTTTTTTTTTTTTT
	8A	AAAAAAAA	10T	TTTTTTTTTT
	AAT ₅	AATAATAATAATAAT	ATT ₅	ATTATTATTATTATT
	20N'	GACAAAGCCGACCACAAAG	20N	CTTTGGTGGTCGGCTTTGTC
tPad	blue handle	GACTGCTGGATGACTACTGG	blue ODN	CCAGTAGTCATCCAGCAGTC
	green handle	CGCACACTCTCCACAACACTAC	green ODN	GTAGTTGTGGAGAGTGTGCG
	red handle	GTGTAGTCCGTGTGTGTTGC	red ODN	GCAACACACACGGACTACAC

Both the binding of BCPs to the pads and the fluorophores to the tPads rely on one link to bind one nanoobject. This strategy refrains from using the cooperative effect of multiple links per nanoobject in order to attach the objects with a high site-specificity. To achieve a high binding yield nevertheless, this places demands on the handle regarding the availability, the ease of initial ODN binding, and the stability of the formed double strand. Choosing appropriate handle lengths usually guarantees the latter. As discussed in Section 1.2.1, sliding sequences allow more initial binding events than specific sequences of the same length, making an initial binding less likely for the latter. In order to optimise the initial binding chances for specific sequences, sequence engineering can be used to ensure the availability of the handle on the origami pegboard. The availability could be reduced by competing binding events due to secondary structure formation or binding of the handle to the scaffold.

For the sliding sequences used on the pad, the competing binding events were not assessed, as they were considered a minor problem in the proof of principle experiments discussed here. The 20N' specific sequence used in the pad handles was supposed to be part of different handle patterns on the pegboard, changing the possibilities for competitive binding each time. As adapting the link each time would have resulted in incomparable systems, sequence engineering was only applied for the specific links on the tPads that are involved in the fluorophore attachment. Initially, another specific sequence was generated for the attachment of block copolymers to the tPads. However, as the tPad is not well suited to serve as a pegboard (see Section 3.2.3), it was not used there. Since this engineered sequence does not form hairpins, it was used for block copolymer attachment to the pads in the 20N'/20N link. All engineered sequences were generated with the EGNAS software^[77] using the selection options and criteria of the algorithm given in Appendix B.

3.2.2 Testing the binding capabilities of the links

In order to proof that the sticky ends listed in Table 3.2 readily bind their complementary sequences, two sets of experiments were performed.

For the specific 20N'/20N link that was used in the block copolymer attachment (Chapter 4), J. Zessin has investigated the hybridisation with surface plasmon resonance spectroscopy (SPR)^[172]. In this study, thiol-modified handles with the 20N' sequence were immobilised on a gold surface of an SPR chip using a microfluidic system. The ODNs were dissolved in the mobile phase overflowing the handles. Hybridisation was monitored as a shift of the SPR minimum.

With the complementary ODNs 20N in the mobile phase, a shift in the SPR minimum occurred, which was not the case when using the 20N' handle sequence itself in the mobile phase instead. This proved that the binding takes place, and proceeds specifically. Furthermore, the block copolymers P3(EO)₃T-b-20N and P3(EO)₃T-b-18T were tested in the same setup. For the latter, thiol-modified 18A handles were immobilised on the SPR chip. It could be shown that also the bulkier block copolymers bind specifically to their complementary sequences.

For the specific sequences used for the fluorophore attachment to the tPad, a qualitative PAGE was performed. The gels are displayed in Appendix Figure A.2. It was found, that each handle selectively binds its complementary ODN also when the other two ODNs are present.

3.2.3 Testing the pegboard qualities of tPads and pads by arranging nanoscale gold

The next experiments aimed at probing whether the respective origami is capable of providing available handles for nanoobject attachment. The tests serve as a general proof of principle, thus, the binding will not be discussed quantitatively in the following. Gold nanoparticles (AuNP) and nanorods (AuNR) were chosen as objects to be templated, because they are easily detectable in AFM and TEM images. For the pad, the two sliding sequences 15A/18T and (AAT)₅/(ATT)₅ were used in the links, while the specific 20N'/20N sequence of the block copolymer attachment was used on the tPads.

Dr. Mathias Lakatos has synthesised the gold nanoobjects and has performed all steps of attaching them to the origami templates. Furthermore, he obtained the TEM images shown in Figure 3.10 b. The author has designed and synthesised the DNA origami (Figure 3.10 a) and performed the AFM imaging (Figure 3.10 c).

Figure 3.10 a displays the handle patterns on the tPad and the pad, respectively. On the tPad there are a horizontal and a vertical line of handles. In the vertical line the handle distance is approximately 6 nm, while it is about 11 nm in the horizontal line. On the pad, 15A and (AAT)₅ handles were arranged in a dense pattern that resembles the pad type III used for block copolymer attachment¹⁰. The pattern was modified compared to the type III pad to create more distinctive sites for the two sequences that are tested simultaneously.

To the tPads, 2-3 nm AuNP coated with the 20N ODNs were attached. These small AuNP were chosen to attempt binding one AuNP to each handle. For that purpose, the AuNP had to be small enough to not imply steric hindrance that would prevent binding to the handles next to their binding site. Furthermore, the AuNP should be functionalised with one ODN ideally, to avoid binding to multiple handles. This is more likely for a small AuNP surface area. For the dense handle pattern on the pads, attaching AuNP at every handle positions was unlikely, so bigger objects were chosen that attach to multiple handles. AuNR with a length of 40 nm coated with 18T ODNs were supposed to attach to the 15A handles, while AuNP with a 20 nm diameter coated with thiolated (ATT)₅ were supposed to attach to the (AAT)₅ handles¹¹.

For the pad, the binding proceeded with 100% site selectivity, and in good yields (Figure 3.10 b). As ten out of 15 bases are complementary for the handle/ODN-pairs 15A/ATT₅ and AAT₅/18T as well, a cross-binding between the 15A/18T link and the AAT₅/ATT₅ link could take place. Yet, it did not seem to be favourable for this system.

For the tPads, the binding yield was moderate to low (Figure 3.10 c). While every pad in Figure 3.10 b I has all AuNR and AuNP attached to it as designed, the ratio is lower for the tPads (Figure 3.10 c I). Furthermore, three AuNP were found on a tPad at most instead of one AuNP per each of the 17 handles (Figure 3.10 c II). Evaluating different tPads showed that AuNPs preferred the same handles. Probably, those were more available in the binding process than the unoccupied ones. Some tPads seem to convulse around the AuNP (e. g., tPad 2 in Figure 3.10 c II). Apparently, more than one handle had bound to the AuNP in this case, which kinks the origami.

Using a specific sequence could have contributed to the low binding yield due to a reluctant initial binding as discussed in Section 1.2.1. Furthermore, functionalising the small AuNP was probably not as successful as for the larger AuNP and AuNR with a higher surface area. However, choosing an appropriate AuNP excess accounted for that. Overall, the low binding yield has resulted most likely from steric hindrance and using only one handle per attachment. The latter is uncommon in gold nanoobject binding, apparently because the binding yields are not satisfying. Nevertheless, binding events were found. This proofed qualitatively that the specific sequence can be used to bind bulky nanoobjects, and that the tPad can serve as a pegboard. However, handling the tPads in the attachment process appeared more difficult

¹⁰see Figure 4.3 c

¹¹For the attachment protocol see Section 2.3.

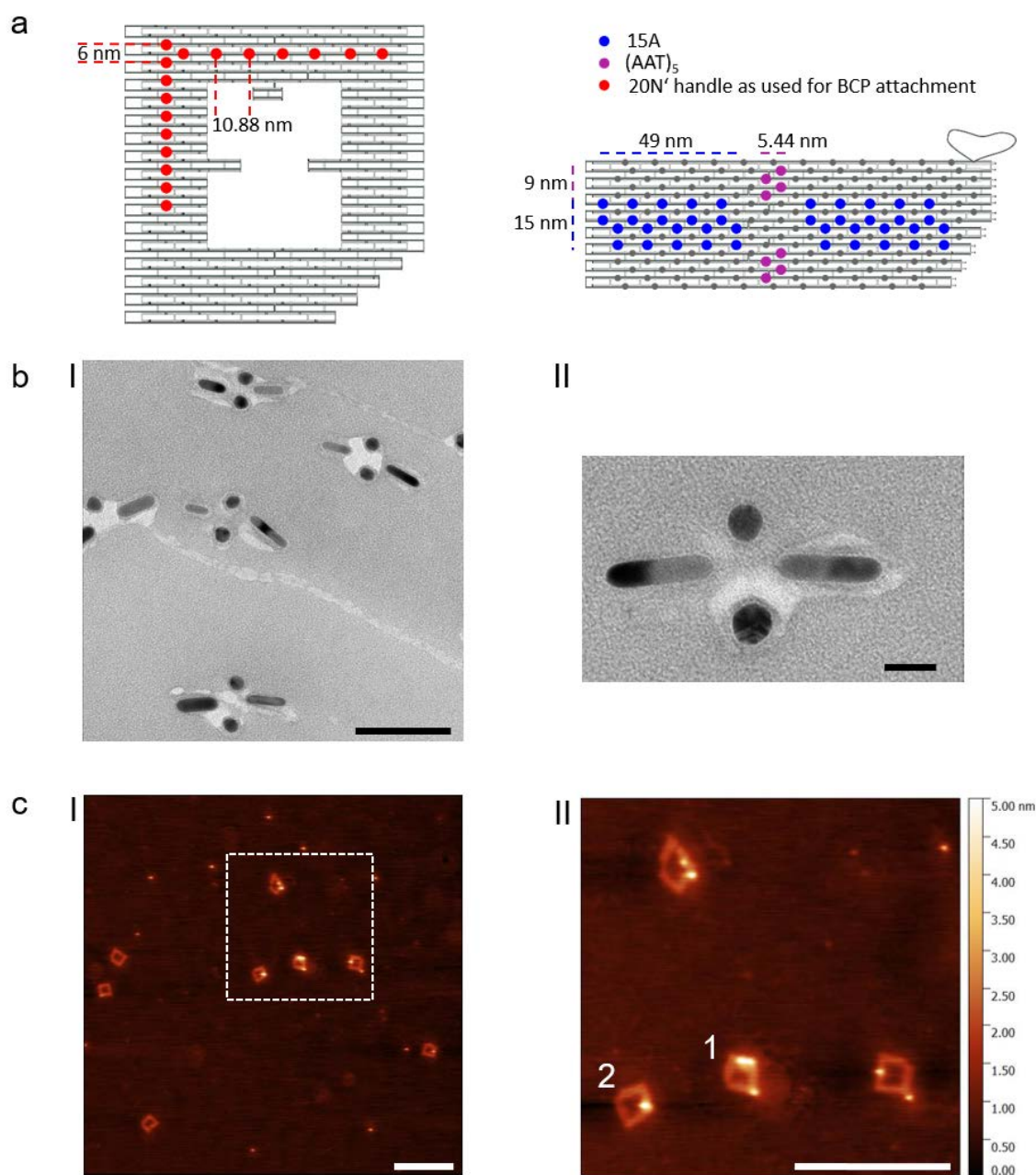


Figure 3.10: Arranging different gold nanoobjects on the pad and tPad to test the origamis' pegboard qualities. a) Design scheme of the tPad (left) and the pad (right) for the gold nanoobject attachment. Blue dots symbolise 15A handles, violet dots (AAT)₅, and red dots the specific 20N' sequence used for block copolymer attachment in Chapter 4. b) TEM images of pads with 40 nm AuNR and 20 nm AuNP attached site-specifically and in high yields as can be seen in (I). Cross-hybridisation has not been observed. Scale bar (I): 100 nm, (II): 20 nm. c) AFM images of the tPads after adding 2-3 nm AuNP. The labelling yield is low to moderate (I). Image (II) shows a zoom into the marked area of image (I) with four tPads with AuNP attached. The maximum number of AuNP per tPad was three (tPad 1). Some tPads seemed kinked due to multiple handles binding the same AuNP (tPad 2). Scale bars in (I) and (II): 400 nm.

than with the pad due to the fragility of the tPads. The mechanical and thermal stress of the process decreased the final concentration of intact tPads considerably.

Overall, the availability of the handles for nanoobject binding to the origamis could be shown. For both origami, the binding proceeded site-selectively.

3.3 Summary

Overall, for both 2D origami, design and assembled origami have matched. The pads have presented themselves as resilient origami template. Compared to them, the more complex and delicate tPads have displayed both a lower synthesis yield and a lower mechanical stability.

As there were less studies of synthesis, folding, thermal stability and stacking behaviour of cavity-bearing structures than of continuously filled origami such as the pad, such studies were presented for the tPads here. Refining the synthesis procedure for the tPads did not increase the yield. However, an assembly temperature range of $45\text{ }^{\circ}\text{C} \pm 7\text{ }^{\circ}\text{C}$ could be determined in which a yield above 45 % was achieved. Furthermore, the studies resulted in a timesaving synthesis protocol. In melting studies in solution, tPads have kept their shape until $50\text{ }^{\circ}\text{C}$. When they were bound to a mica surface via electrostatic interactions, they have remained intact up to the highest temperature under test, which was $65\text{ }^{\circ}\text{C}$. This has lined out with found trends^[138]. The studies on the thermal behaviour of the tPad suggested that the folding proceeds via intermediate folding states, and that the hierarchical folding and melting behaviours include similar intermediates. The protocols used here could be extended in future work to yield more detailed and quantitative results for these behaviour studies. Furthermore, the tPad stacking behaviour was steered through the design of the origami edges, which lined out with rectangular origami^[129] in broader terms. However, the target stacking structures did not form as exclusively as for the rectangular origami. This was a hint that design components can alter the stacking behaviour, which needs to be investigated further.

Furthermore, a proof-of principle experiment has shown that both templates can serve as pegboards for gold nanoparticles and nanorods. The pads have successfully templated AuNP and AuNR site-specifically with two different sliding sequences, achieving high yields as well. Templating of AuNP with a specific link on tPads proceeded site-selectively as well. However, the chosen handle pattern and most probably the lacking resilience of the origami prevented a higher binding yield.

Summing up all characterisation experiments, the pads have appeared as suitable origami for large-scale fabrication or for templating bulky nanoobjects. The more fragile tPads appeared to be less suitable for the latter. However, their structural features could be useful in single-molecule studies^[92,184,368,369] that do not require a quantitative origami yield, and as a structure under test to evaluate delicate DNA origami. Therefore, the pads were chosen as the template in the hybrid formation discussed in Chapter 4. The tPads are used in Chapter 5.

AFM was found to be the versatile method of choice to investigate the 2D origami pad and tPad. In bulk studies, AFM was superior to gel electrophoresis for the structural characterisation of the tPads, where ill-shaped structures could not be sufficiently distinguished from correctly formed structures. Basic tapping AFM was useful in characterising the structure, the synthesis and the mechanical stability of the two 2D origami structures. Tapping AFM at ambient temperature in air and in liquid provided similar structural measurements.

Hot stage tapping AFM in liquid, a relatively new tool for investigating the folding and melting behaviour of DNA origami, could be implied with the same protocol as liquid AFM and was found to retain the high resolution up to $65\text{ }^{\circ}\text{C}$. This work has stopped at qualitative folding and melting studies, while the hot stage tool can easily provide more detailed and quantitative data on, e. g., folding intermediates in further experiments.

AFM can provide bulk data, but without fast scanning, often at the cost of long measurement times. Quantitative data, such as origami sizes and formation details were obtained here through manual analysis. In the chosen imaging mode, image analysis had to rely on height contrast. As the height contrast was small here, computational analysis routines could not be implied. Analysis routines based on other signals would be worth developing.

The usefulness of AFM is limited when it comes to 3D origami and material interacting strongly with the tip, such as gold nanoparticles. The latter problem was encountered here as well. However, as correct sizing of the AuNP was not the aim of this investigation, it did not affect the results. However, for soft or organic material that provides little contrast in other techniques such as DNA, proteins or synthetic polymers, AFM is a suitable technique. Therefore, it will be used for characterising the hybrids from pads and polythiophene-DNA-block copolymers in the following Chapter 4. To concentrate the discussion in one point, Section 4.3 will cover the limitations of AFM investigations with respect to both the hybrids structures and DNA origami templates in general.

Chapter 4

Qualitative and quantitative characterisation of polymer-DNA origami hybrids with AFM

This chapter discusses the binding of diblock copolymers (BCPs) consisting of an ODN block and a poly(3-tri(ethylene glycol)thiophene (P3(EO)₃T) block to the DNA origami pads with different handles and handle patterns. For the first time, such a binding approach utilises a polythiophene derivative and a 1:1 BCP that can be attached to the DNA origami in a highly site-specific manner.

The first section presents the three-step process of the hybrid formation. The first step is the synthesis of the water-soluble polythiophene derivate P3(EO)₃T with functional starting groups. This step is briefly introduced with focus on the resulting polymer. The second step is the formation of the 1:1 block copolymers of a P3(EO)₃T molecule and ODNs with different sequences. In the third step the resulting P3(EO)₃T-b-ODN BCP molecules were placed on the pads site-specifically through sticky end ligation. The second section of the chapter describes the qualitative and quantitative analysis of high-resolution liquid AFM images of the hybrids with a semiautomated particle finding routine based on ImageJ^[15] with the FindFoci^[6] plugin. The attachment of BCPs with three kinds of ODNs to three types of pads will be discussed that differ in terms of handle sequences, handle length and handle patterns.

4.1 Three step hybrid fabrication

Polythiophene synthesis and block copolymer formation

The semiconducting polymer of choice in this work is the regioregular head-to-tail polythiophene poly(3-tri(ethylene glycol)thiophene¹ P3(EO)₃T. As discussed in Section 1.5.2, these P3RT-types of polythiophene derivatives are water-soluble, biocompatible, well-known for their excellent optoelectronic properties, and the potential of P3(EO)₃T as p-type semiconductor in organic field-effect transistors has already been reported^[286]. To a large extent, the favourable properties originate in the structural regularity of the P3(EO)₃T, the controlled molecular weight and a perfectly controllable end-group composition, which result from the chain-growth character of the “quasi-living” Kumada catalyst-transfer

¹an alternative name is poly(3-2,5,8,11-tetraoxadodecane thiophene)

polycondensation (KCTP) used as the synthesis method².

As stated in Section 2.4, the optimisation of the polymer synthesis and the polymer characterisation are beyond the topic of this thesis. Information of that kind will just be given as far as it is useful to discuss the hybrid formation. Detailed information was published by Zessin *et al.*^[172].

For the P3(EO)₃T batch used in this work, a molecular weight of about $M_n = 4922$ g/mol ($M_w = 5698$ g/mol)³, a dispersity of 1.16 and a degree of polymerisation of 19 were determined. The degree of amine functionalisation was 38%. NMR proved that the resulting P3(EO)₃T exclusively showed a head-to-tail arrangement of the monomers in the chains. Dynamic light scattering (DLS) measurements revealed a hydrodynamic diameter of the polymers of 3-6 nm in 50 mM Tris · HCl buffer. The maximum of absorption and emission spectra in solution were found at 409 nm and 596 nm, respectively^[172]. The polymer's optical properties were used to determine the block copolymer concentration and to identify the polymer-containing fractions in the HPLC-based purification visually.

For attaching P3(EO)₃T to an ODN, strain-promoted azide-alkyne cycloaddition (SPAAC) is used (Figure 4.1). For that purpose, the amine starting groups of the polymer chains were converted into azide groups first using a bifunctional crosslinking reagent. ODNs with a dibenzocyclooctyne group (DBCO-group) were purchased. The P3(EO)₃T was added to the ODN in excess of at least 10:1 in order to functionalise all present ODNs in water.

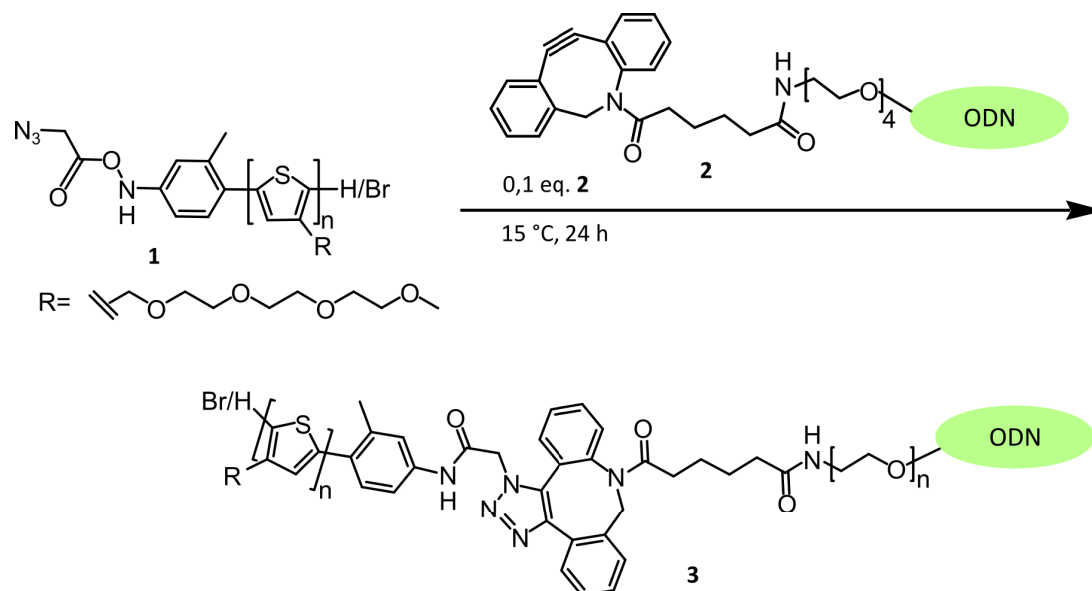


Figure 4.1: Block copolymer synthesis. The polymer block is an azide-functionalised poly(3-tri(ethylene glycol)thiophene) (1)^[172]. Attaching a commercially available dibenzocyclooctyne-functionalised ODN (2) via strain-promoted azide-alkyne cycloaddition yields the block copolymer P3(EO)₃T-b-ODN (3).

Block copolymer formation kinetic

Reversed-phase high pressure liquid chromatography (RP-HPLC) was used to monitor the click reaction over a time period of 48 h (Figure 4.2 a). For that purpose, P3(EO)₃T and ODN were mixed in at least a 10:1 ratio. About 2 min after the reaction had started, the first measurement (“2 min” in Figure 4.2 a) was started, and finished about 25 min after the reaction. For comparison, the chromatogram of pure P3(EO)₃T is displayed as well. P3(EO)₃T yields a series of equidistant peaks between 17.2 min and 20.8 min. Those stem from polymer chains of different lengths. Their equal distances indicated that they differ by the same number of monomers, most probably a single one. There was a baseline rise during the elution of P3(EO)₃T. That was due to the accumulation of P3(EO)₃T on the column, which is caused

²A schematic of the catalytic cycle of the KCTP is given in Figure 1.7. Note that here, an *ex-situ*-initiated KCTP was applied^[172].

³GPC against polystyrene standard

by attractive interactions between the hydrophobic C18 column material and the hydrophobic polymer backbone. In order to prevent a further baseline rise throughout the monitoring of the click reaction, the column was washed with intermediate blank runs.

In the “2 min” run, only the ODN (peak at elution time of ≈ 10 min) and P3(EO)₃T were present. As can be seen, the ODN peak decreased over time, while a new series of peaks appeared between 16.0 min and 17.2 min and increased throughout the monitoring (see zoom-in in Figure 4.2 a). These peaks eluting before P3(EO)₃T corresponded to the BCP, which is more hydrophilic than P3(EO)₃T due to its ODN block. The peak series reflected that in the BCP the well-defined molecular structure of the P3(EO)₃T was maintained. That the monomer peak almost completely vanished over time indicated that the reactions proceeded with a high yield.

Plotting the peak areas over time (Figure 4.2 b) revealed that the decrease of the ODN concentration proceeded as a first order reaction, while the BCP concentration increased in a zero order reaction. As the click reaction is bimolecular, the zero order is a pseudo-order. Apparently, the presence of the two educts was not the rate-determining factor. Another hint was that it took 48 h until the ODN peak stayed constant (indicating no further reaction), while the click reaction should proceed immediately. As the reactions were not catalysed, the pseudo-order might have occurred due to the limited presence of a reactive intermediate. Probably the coiling of both types of educt molecules played a role here, as it shielded the reactive groups from each other. The reaction rate constants are $k_{ODN} = -0.0578$ and $k_{BCP} = 0.252$ a.u./h. Note that the rate constants cannot be compared directly, as they originated from reactions with different orders.

Block copolymer purification

In order to separate unreacted educts from the BCP after the click reaction, RP-HPLC can be performed. As shown in Figure 4.2 a, HPLC can resolve the different BCP fractions that emerge as different peaks in the BCP region. In this approach, these fractions were combined to yield more block copolymer.

PA gels were used in this work for evaluating the HPLC purification. A typical PA gel is shown in Figure 4.2 c both prior to and after staining. The lane labelled “ODN” contained the pure DBCO-functionalised ODN, while the lane “BCP cr” contained the crude reaction mixture. The first and second fraction after HPLC purification were run on the lanes “F1” and “F2:BCP”.

As can be seen in the stained gel (right image), the unreacted ODN yielded two bands, which suggests that ODNs of different lengths, and probably functionalised as well as without the DBCO end-group were present. In the crude reaction mixture, P3(EO)₃T appeared as a smear near the gel pocket. It could be identified without staining though its orange-red colour (black in left greyscale gel image). The smear reflected the molecular weight distribution of the polymer. That it stayed near the pocket was because the rather hydrophobic and uncharged material displayed a limited mobility in the gel. In the stained gel, the crude reaction mixture displayed a band at the height of unreacted ODNs as well as a new smear signal between that and the P3(EO)₃T smear. This new signal, which was also visible in the unstained gel, was caused by the newly formed BCP. It combined properties of both blocks. While it displayed the colour and smear of the polymer fraction, it was more mobile in the gel due to the negatively charged DNA block. Note that the presence of the DNA in the BCP could not be verified unambiguously by staining, as the staining dye’s fluorescence could not be separated from the polymer fluorescence. In the lane “F2:BCP”, the BCP smear was visible, while no bands occurred in the regions where P3(EO)₃T or the pure ODNs have appeared. Apparently, HPLC purification had separated the BCP clearly from its educts. In lane “F1”, an unknown band appeared that was also present in the lane “F2:BCP”. Apparently, a hydrophilic compound remained in the BCP fraction. As it did not prevent the hybrid formation from BCPs and pads, it was tolerated. In order to reduce the contamination at least, only fraction F2 was used for the hybrid formation.

The concentration of the BCP after purification was determined with UV/VIS at the 409 nm absorption maximum of the polymer.

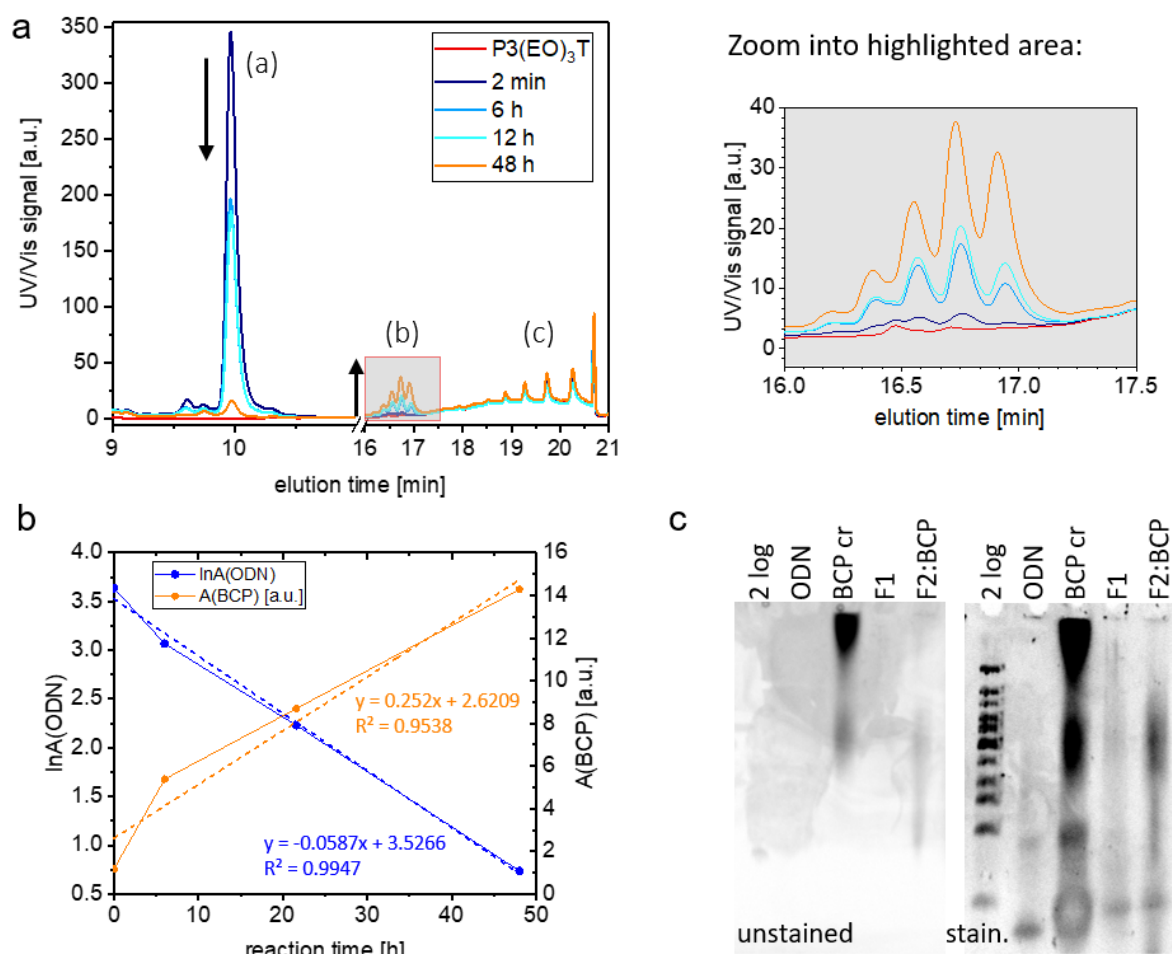


Figure 4.2: HPLC and PAGE of the block copolymer formation via SPAAC click reaction. a) HPLC chromatograms of a BCP formation at different reactions times over 48 h and of pure P3(EO)₃T for comparison: (a) ODN peak; (b) BCP peak series (also in zoom-in); (c) unreacted P3(EO)₃T peak series. b) Determination of reaction kinetics from fitting linear expressions of the rate laws to the values of the peak areas of the ODN peak and the BCP peak series plotted over time. The ODN consumption (blue) proceeds as a first order reaction, the BCP formation (orange) as zero order reaction. c) Unstained (left) and stained (right) polyacrylamide gel of the crude reaction mixture (BCP cr), fractions of the HPLC-purification (F1, F2:BCP) and the bare ODN for comparison. A 2-log-DNA ladder is given for size comparison.

Hybrid formation

Pad origami templates

In order to investigate the binding with different sequences and handle patterns, pads with three types of handle patterns were designed, which will be referred to as type I, II and III. In Figure 4.3 the design sketches as well as AFM images of the bare pad templates are shown. In the sketches, **a** denotes the handle position, while **b** is the position between next-neighbour handles⁴ on adjacent helices, and **c** is the position between next-neighbour handles that are situated one above the other on next but one helices. Both lengths **b** and **c** are about 6 nm. In the following, the term next-neighbour handle will always be

⁴For the hexagonal positioning of the six possible next-neighbour handles around a handle on the surface of the pad see Figure 3.1.

used to refer to a handle at approximately 6 nm distance from a given handle. The theoretical distance of neighbouring handles on the same helix is 10.88 nm, and the space between these handles will be referred to as position **d**. The same position labels will be used in all pad types if applicable. The black rectangles in the pad sketches mark the unit cell of a handle pattern, i. e. the origami part that must be repeated to create the handle pattern.

As will be discussed for each pad type in the following, the ability of the handles to hybridise with their complementary ODNs on the pad was tested. The resulting structures were imaged with AFM in order to resolve each handle. The images are given in Appendix A.

With the first hybrid, the attachment with the specific sequence is discussed. The hybrid will be referred to as type I (Figure 4.3 a). The handles on type I are arranged in three lines running in parallel to the short edges of the pad⁵. The distance between the lines is about 50 nm. The two outer lines, further referred to as line I1 and line I3, are made of four handles each that sit one below the other on every third helix. The central line between I1 and I3, line I2, is a double line of 2 x 7 handles that sit on every other helix. Thus, all handles have either two or three next-neighbour handles. The double line was chosen in this first try of the hybrid formation to provide an ample amount of handles, and because it was assumed, it would produce a significant feature in AFM imaging. The handles in the lines I2 and I3 have the 20N' sequence. The handles in line I1 are 15A and serve as a control for the binding specificity. Based on the area of the unit cell, the handle density in I1 and I3 is 0.0077 handles/nm², while it is 0.0204 handles/nm² for I2.

In AFM images of the bare pads, the single handles of the central double line were resolved in most images. This was not the case for the four 20N' handles or the four 15A handles in the lines I1 and I3. However, as there were no gaps in the place of the handle-bearing staples, the handles were considered present. AFM images of type I pads after adding 20N ODNs have shown pronounced structures in the area of I2 and I3, indicating that the ODNs have bound specifically (Appendix Figure A.5). As the AFM tip has easily manipulated the structures, the binding could not be quantified for each handle. Adding 8T ODNs did not result in visible structures in I1, probably because of the low melting temperature of the resulting dsDNA strand.

That P3(EO)₃T-b-20N BCP is able to hybridise with a staple containing the 20N' complementary sequence in bulk was proven by SPR^[172].

In order to investigate the attachment behaviour with a sliding sequence (Section 3.2.1) the pad type II with 15A handles was designed (Figure 4.3 b). It was assumed that the sliding sequence would result in a higher binding yield than the specific sequence of pad type I, as it provides more opportunities for an initial BCP attachment. Like type I, type II possesses three lines running in parallel to the short pad edges. The distance between neighbouring lines is 50 nm. However, each line II1 to II3 is a single line of seven handles placed one below the other on every other helix. In contrast to line I2 of type I, most handles in II1 to II3 have two next-neighbour handles instead of three, which are situated below and above them. This pattern was designed to relieve the steric hindrance in comparison to a double line while providing more handles than the lines I1 and I3 to aim for a continuous path of attached objects. As for the pad type I, the templates with single-stranded handles were investigated with AFM prior to the attachment. The 15A handles were not always visible but the handle-bearing staples were all present. Adding a complementary 8T strand did not result in a visible binding under the experimental conditions used, but 18T or 23T strands resulted in visible structures (Appendix Figure A.6). Dot-like protrusions have been distributed statistically along the lines. Apparently, the handles were able to hybridise, and the random distribution of the dsDNA structures indicated that all handles were present. In addition to small dots that could have represented binding to a single handle, larger dots were found. These seemed to involve two handles at the same time, which was possible given the length of the 23T ODN of 7.8 nm length. The handle density in the unit cell highlighted in Figure 4.3 b is 0.0153 handles/nm².

⁵ a, c in Figure 3.1

Object positions on a pad:

a = position on handle

b, c, d: position between handles:

b \approx 6.2 nm

c \approx 6 nm

d \approx 10.9 nm



unit cell

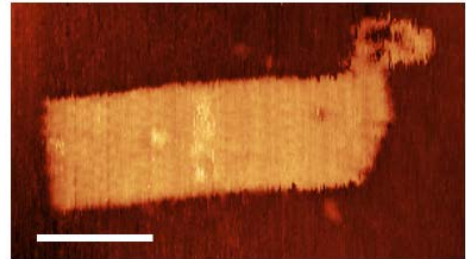
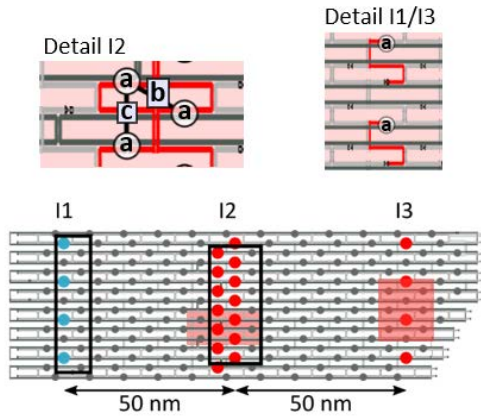
• staple ends (potential handle positions)

• handle with 20N' sequence

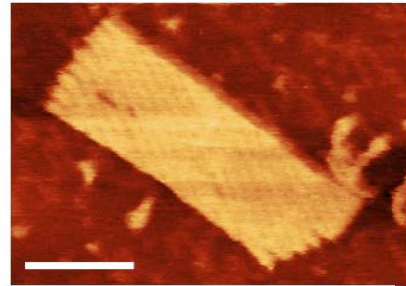
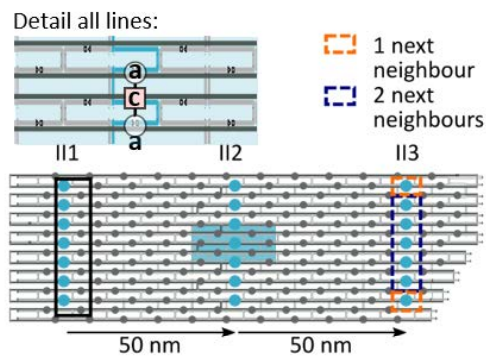
• handle with 15A sequence

• handle with 8A sequence

a



b



c

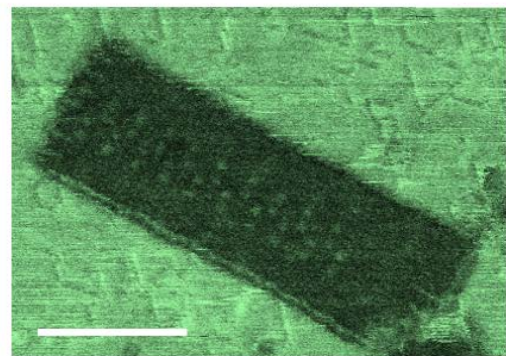
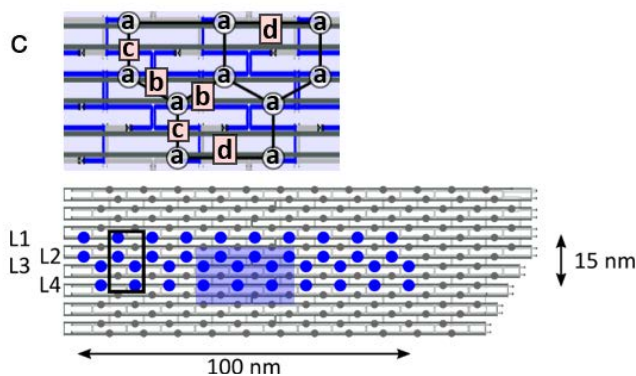


Figure 4.3: Design sketches of the three pad types. Coloured dots mark the handle positions, and black frames the unit cells of the handle patterns. For each pattern, a zoomed-in scheme shows the potential object positions **a**, **b**, **c** and **d** in detail. On the pad sketches, the areas of the zoomed-in detail are coloured in red for the 20N' handles, light blue for the 15A and dark blue for the 8A handles. AFM images show the assembled templates with single-stranded handles. All scale bars: 50 nm. a) Pad type I with a central double line I2 with 2x7 handles and two vertical lines I1 and I3 with four handles. b) Pad type II with the three vertical lines II1, II2 and II3 of seven handles. c) Pad type III with 40 handles arranged in four lanes L1 to L4 of ten handles each. The length and width of the handle pattern is given, too.

In order to investigate a pattern for creating a larger, dense array of attached BCPs, the type III pad was designed (Figure 4.3 c). It consists of four lines running parallel to the longitudinal pad axis. These horizontal lines will be referred to as lanes L1 - L4. Each lane is made of 10 handles. Lane L1 is situated on the 6th helix (counted from top), and the lanes L2 - L4 on the 8th, 9th and 11th helix, respectively. As stated above, the space between two handles on a lane, position **d**, is 10.88 nm in theory. Most handles in L1 and L4 have two neighbouring handles at this distance, and one next-neighbour handle situated right above or below them with position **c** in between. In L2 and L3, most handles have three next-neighbour handles that surround them with a threefold rotational symmetry. As for the type II pad, the BCPs are attached with ODNs that allow sliding, because this is supposed to provide higher binding yields. However, instead of the 15A handles 8A were used, which shortens the handle length from 6.15 nm to 2.72 nm. Thus, two 8A handles, even if fully stretched, or double-stranded and tilted, and with their 5' ends pointing towards each other, do not touch, so less steric hindrance should be inflicted by this link. AFM investigation of the type III pads with single-stranded handles has resolved the 8A handles in the phase image and has proven that all of them were present. Appendix Figure A.7 a and b show the pads after adding 23T ODNs. The pads display distinct, dot-like protrusions along the handle positions, indicating that the handles are available for hybridisation. As for pad type II, a dot did not necessarily correspond to a single handle, because the 23T ODN was long enough to bind more than one ODN. Furthermore, the largest numbers of dots was found on face-down pads, where the pad shields the bound objects from the AFM tip. Due to the length of the 23T ODN and scanning artefacts, the images are not fit for a quantitative evaluation of the binding to a handle, as it was the case for the other pad types. Appendix Figure A.7 c shows a pad after adding 8T ODNs. This has resulted in protruding structures according to the handle pattern. However, they were prone to manipulation with the AFM tip and thus, not ideal for a quantitative evaluation either.

For the different pad types, Table 4.1 summarises the characteristics of the handle patterns (handle distances, handle densities, number of next-neighbour handles) and the sequences of handles and the complementary ODNs used is the BCPs.

Protocol. For the hybrid formation, the P3(EO)₃T-b-ODNs and pads with complementary handles were mixed with a 20-fold BCP excess per handle in 1x TE-buffer with 12.5 mM MgCl₂ and 300 mM NaCl, and held on a thermomixer at 15 °C for 24 h. This protocol has emerged as a standard protocol from testing different hybrid formation times, temperatures, BCP : pad - ratios and buffer environments. The BCP binding yield was determined coarsely as how many pads were occupied, and in more detail as the number and position of objects attached (see Section 4.2).

For all three pad types, hybrid formation has already considerably progressed after 2 h. In order to let the hybrid formation come closer to its equilibrium, hybridisation times of one day have been used in all experiments.

The temperature of 15 °C was chosen as a compromise that allows sufficient Brownian motion of all components while preserving the pad origami. For all pad types, hybridisation tests at room temperature did not result in increased binding yields, but the resulting hybrids appeared to be less tolerant to the mechanical stress of filtration. Furthermore, it was expected that for hybridisation at a lower temperature the interaction between the polymer parts of the BCPs would increase, which would result in a higher hybridisation yield. Therefore, the hybridisation to the pad type III was tested for both P3(EO)₃T-b-10T and P3(EO)₃T-b-18T at 5 °C. However, no significant difference was found for the yields or object distributions. As it did not seem effective, lower temperatures were not tested.

As the concentration of the BCP could not be determined without error, the excess ratio of BCP : handle = 20 : 1 was an approximation. However, the excess was sufficient, as for all pad types, higher BCP excess did not result in a higher binding yield (data not shown).

For P3(EO)₃T-b-18T on the type III pad, the attachment was attempted at different NaCl concentrations as well (Figure 4.4). This was done having a possible attachment of nanoparticles as a second component

on the pad in mind, which might demand adjustment of the NaCl concentration. It was found that between zero and 3 M NaCl, the binding happens with approximately the same yield, leaving a broad range of experimental conditions to choose. In the standard protocol 300 mM NaCl was chosen by default.

Overall, the standard protocol was found to be the best compromise between sufficient BCP attachment, using an origami concentration that still avoids clustering, and providing a BCP concentration that can be removed in one filtration step, which minimises the mechanical stress on the origami.

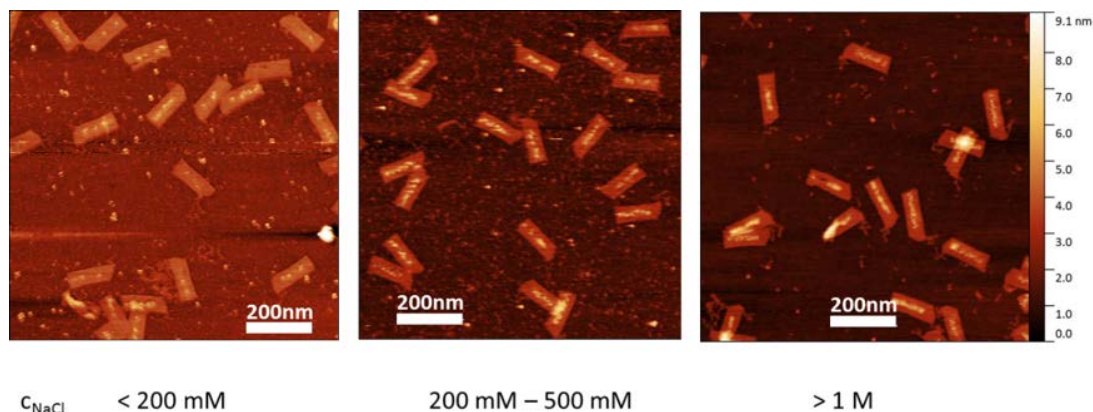


Figure 4.4: Hybrid formation with 0-3 M NaCl in the assembly buffer. The attachment yield stayed approximately the same over the concentration range tested.

The successful hybrid formation can be proofed with AFM. Figure 4.5 shows hybrids with the different pad types, i. e. link sequences and handle patterns. Globular objects appear sites-specifically along the handle line patterns of the imaged pads. Figure 4.5d shows type III pads where just the P3(EO)₃T polymer instead of the BCP was added. There was no attachment, indicating that unspecific interactions of single-stranded DNA and the polymer did not occur, and that the hybrid formation must be due to DNA-mediated binding. The type III pads were chosen for this test, because they provided the highest number of handles. For the three pattern-sequence combinations with the pad types I to III that will be discussed quantitatively in the following section, the standard protocol yielded more than 90% of the pad templates with at least one object attached.

4.2 Results of the quantitative analysis of high-resolution AFM images of polyhiophene-DNA origami hybrids

High-resolution AFM imaging does not just allow assessing whether BCPs have attached to a pad, but it allows for a quantitative estimation of how many BCP attach per hybrid, and how their locations correspond to the handle pattern. In order to count, locate and evaluate the size of BCPs on a hybrid, high-resolution AFM images were analysed with the FindFoci^[6] routine of ImageJ^[15]. The application of the routine is described in Section 2.6.3.

One step of the BCP identification required setting a binary threshold. Here, the handle's contribution to the height of attached objects is accounted for. As shown in Appendix Figure A.8, the areas with handles on a bare pad display a height increase of about 1 nm compared to the pad height of about 2.5 nm in AFM images. Thus, the binary threshold was set at 140% of the value of the average pad height. Choosing this relative threshold over adding an absolute value to the pad height was done to account for variations in the tip pressure that are applied in different images and that introduce variations in the pad height. In an image where, for example, the pad height is comparably high due to low tip pressure, the contribution of the handle to the attached objects height will be high as well. A relative correction accounts better for this than adding a fixed value.

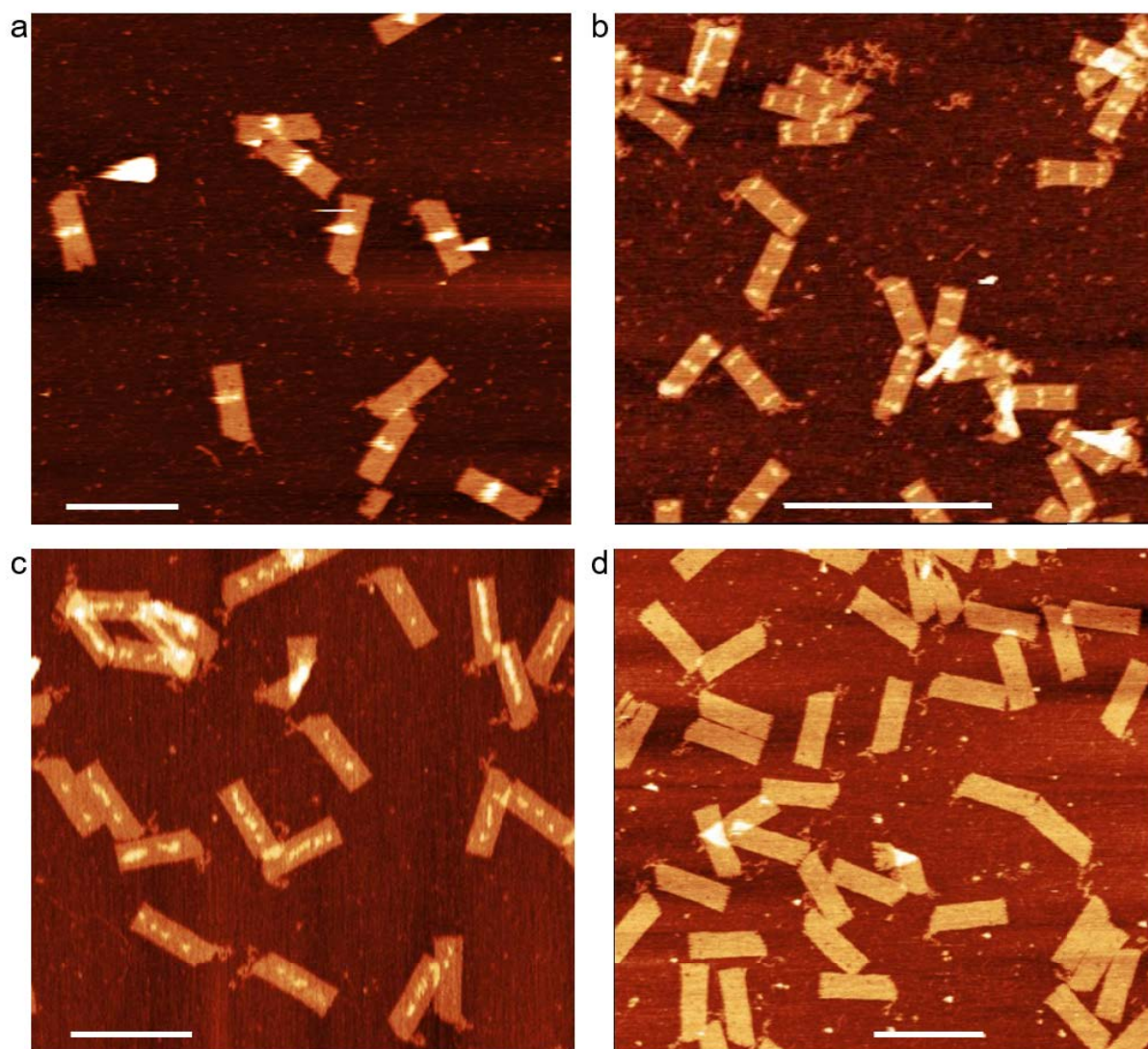


Figure 4.5: Hybrid formation. For any type of hybrid investigated, more than 90% of the pads displayed attached BCPs. a) P3(EO)₃T-b-20N on pad type I. Scale bar: 500 nm. b) P3(EO)₃T-b-18T on pad type II. Scale bar: 200 nm. c) P3(EO)₃T-b-18T on pad type III. Scale bar: 200 nm. d) Adding P3(EO)₃T to type III pads does not result in any attachment. Scale bar: 200 nm.

Note that the binding yield will be discussed in a conservative approach. For that purpose, the term “object” will be used in the following instead of BCP. An object is one attached item identified by FindFoci. In contrast to a BCP, an object is not necessarily a single molecule. On the one hand, this is due to the routine itself. The resolution of the AFM images was probably insufficient on occasion. A second point is that the FindFoci localisation routine can resolve touching items on pads in general, but this might not always be successful. On the other hand, it is just an assumption that an item causing a peak is a single BCP. The size distributions of the polymer determined with DLS and asymmetric flow field-flow fractionation^[172] do not exclude that small oligomers (dimers, trimers) are present in solution, and if they are, they might not necessarily break up during the BCP formation. Overall, discussing object attachment will rather underestimate yields than euphemising them, and thus, provide a realistic picture of the hybrid formation.

The following sections will discuss the object size, the object count per handle and the object positions. As will be discussed, design parameters such as the BCP and link lengths, the link sequences or the number of next-neighbour handles in a pattern influence the binding yield. To clarify correlations of design and experimental results, Table 4.1 summarises key design parameters, and already lists the binding yields and object sizes for the different hybrids studied.

Table 4.1: Summary of pattern features and experimental results for hybrids from the pad types I-III. Design parameters of a handle pattern: dist_{min} , dist_{max} : minimum and maximum distance of neighbouring handles; $n(\text{n.n.})$: possible number of next-neighbour handles; $\bar{n}(\text{n.h.})$: number of neighbouring handles averaged for all handles; y: yes; n: no; * no next neighbour handle in 6 nm distance; ** neighbouring handle on same helix. Experimental results: \bar{h} : average object height; $s_{\bar{h}}$ standard deviation of the heights; $n(\text{objects})$; number of investigated objects.

		type I		type II	type III		
		I2	I3; I1	II1, II2, II3	all		
design parameters	dist_{min} [nm]	6.00	12.00*	6.00	6.00		
	dist_{max} [nm]	6.15	12.00*	6.00	10.88**		
	$n(\text{n.n.})$	1	n	*	y	y	
	occurring in	2	y	n	y	y	
	pattern	3	y	n	n	y	
		4	y	n	n	n	
	$\bar{n}(\text{n.h.})$	3.57	1.00*	1.71	0.95		
	handle density [handle/nm ²]	0.0204	0.0077	0.0153	0.0204		
handles	sequence	20N'	20N'; 15A	15A	8A		
	dsDNA length [nm]	6.80	6.80; 5.10	5.10	2.72		
ODN	sequence	20N	20N	18T	18T	10T	
	BCP length [nm]	12.80	12.80	12.10	12.10	9.40	
experimental	yield [object/handle]	0.26	≈ 0	0.33	0.25	0.27	
	\bar{h} [nm]	4.88		5.10	5.23	5.27	
	$s_{\bar{h}}$ [nm]	0.77		0.92	0.66	0.85	
	$n(\text{objects})$	44		133	183	97	

As the pad is a chiral structure, its deposition side can be determined. While bare pads display a 55 : 45 ratio of pads with handles facing the AFM tip (face-up) and handles facing the mica (face-down) (see Figure 3.3) this ratio shifted to 70 : 30 for the hybrids. Interestingly, this ratio is about the same for all pad types studied here. Most probably, two factors cause this behaviour. First, the BCP is bulkier than the handle, and hydrophobic. Thus, face-down pads might not interact as strongly with the mica surface as face-up pads, so more of them are removed in the sample preparation process. Second, the more hydrophobic BCPs might be repelled from the surface, so that fewer hybrids reach the surface oriented face-down in the first place.

4.2.1 Object size

The size parameter of an object discussed here quantitatively is the object height. As the peak height, it is part of the FindFoci output. Figure 4.6 shows the object heights h found on the pad types I to III. The x -axis is scaled to reflect the theoretical BCP lengths. To calculate these lengths, it was assumed that the P3(EO)₃T block would be coiled due to the hydrophobic polymer backbone, and that the ODN would be stretched out as if hybridised to its complementary sequence. Assuming a length of 6 nm for the coiled P3(EO)₃T block as determined by DLS^[172], the theoretical BCP lengths are 12.8 nm for P3(EO)₃T-b-20N, 12.1 nm for P3(EO)₃T-b-18T, and 9.4 nm for P3(EO)₃T-b-10T. Compared to this, the height distributions are narrow, with 95% of all heights occurring in a 2 nm span. The mean heights and the corresponding standard deviations for a given number of objects on pads are summarised in Table 4.1. Another size parameter delivered by FindFoci is the basal area of a peak, which corresponds to the space occupied by the object in the xy -plane. Usually, the basal area appears roughly circular, so an equivalent diameter is calculated from it. That is the diameter of a circle with the same area as the basal area. The basal area includes errors from the exaggeration of lateral sizes in AFM imaging and a subjective component through setting the binary threshold in FindFoci. These errors propagate into the equivalent diameter. As it is the only measure of the objects in the xy -plane in this analysis, values are given in Appendix A to provide an idea of the objects' 3D shape. Taking into account the variation introduced by the scanning process and the tip pressure, height and diameter can be considered equal, i.e. the objects appear globular-shaped. Given the persistence lengths of the link and the P3(EO)₃T block, and the possibility of interaction with next-neighbour objects, a rod-like shape would have been plausible as well. The globular shape can occur due to the coiling of the polymer block in the hydrophilic aqueous environment. Furthermore, the shape probably reflects a resolution limit in the measurement. Instead of tracking the structure, the attractive interactions between the AFM tip and the polymer as well as the movement of the objects in the aqueous scanning environment lead to a levelling down of structural details.

The height values match with average diameter values determined for P3(EO)₃T in aqueous solution^[172], so apparently, the dsDNA link did not significantly contribute to the height. One reason can be the threshold setting discussed before. However, given the persistence length of dsDNA of 50 nm^[371] and their lengths in the range of 2.72-6.80 nm, the links are probably not cut by the threshold completely. That their influence is not detectable is probably because the polymer block of the BCP incorporates the DNA in its coil. Furthermore, the AFM tip compresses the BCP during measurement, while P3(EO)₃T does not experience such strong forces during the DLS.

Applying the Shapiro-Wilk test to the object heights from different pad types reveals that the objects of type II and type III can be considered as being of the same size, while the objects on the type I pad are smaller. This indicates again that the dsDNA links did not contribute significantly to the object height, because type I actually features the longest link. As the size difference is not high, this probably reflects measurement conditions only. It can also indicate that there small oligomers amongst the attached objects on the type I pad, at least more than on the type II and type III pads. Contradicting this assumption, all of the height distributions appear unimodal and indicate that one BCP species attaches to all pads, and that one object could indeed be a single molecule. It is possible though that the resolution of the AFM is not high enough and blurs the size differences of the attached objects. To clarify the kind of attached object form the height, measurements with higher-resolving tips could be performed.

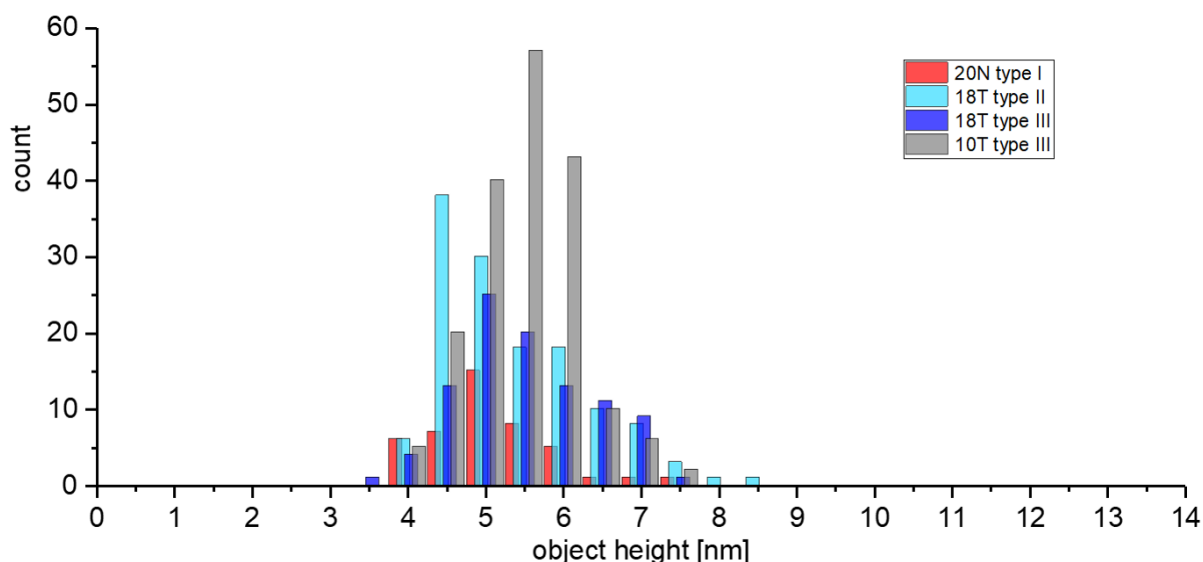


Figure 4.6: Object heights for 456 objects on 47 pads of all types (sorted by ODN block and pad type: 20N type I: 44 objects on 12 pads; 18T type II: 133 objects on 19 pads, 18T type III: 183 objects on 17 pads, 10T type III: 97 objects on nine pads). The x -axis was scaled to reflect the theoretical BCP lengths in the range of 9.4-12.8 nm.

4.2.2 Number of objects and object positions on the different pad types

The binding yield and the position of the objects attached appeared to depend on the sequence as well as on the handle pattern.

Specific sequence and type I pads

To the pads of type I, P3(EO)₃T-b-20N was added to attach to the 20N' handles in the lines I2 and I3. As can be seen in the images in Figure 4.5 a, virtually all hybrids displayed an attached object. For most hybrids, the bare eye identifies one or two high structures. They sat almost exclusively in the central double line I2 (see also Figure 4.7), and barely on the four-handle line I3. An attachment to the 15A control line I1 was not observed.

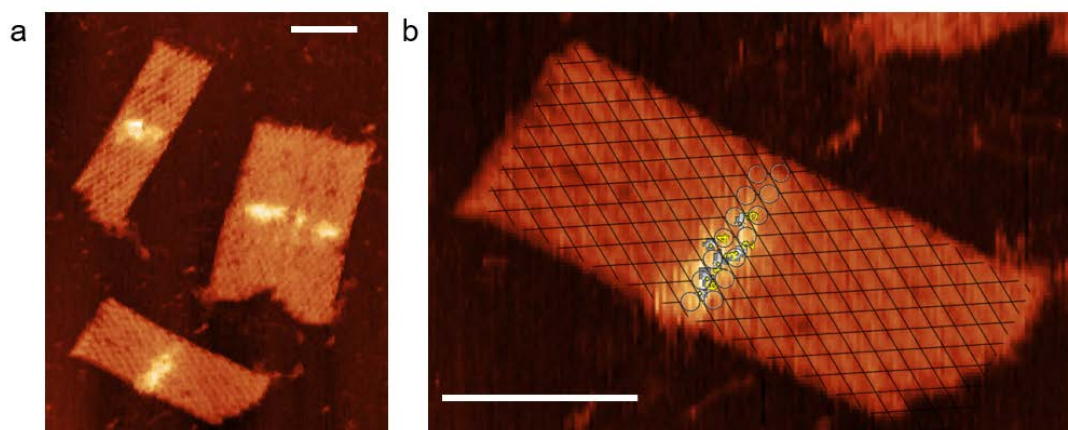


Figure 4.7: High-resolution AFM images of hybrids of the pad type I and P3(EO)₃T-b-20N. a) Four hybrids with BCPs attached to the central double line of handles, I2. b) Stacked image of a hybrid, the Find Foci mask image with the localised objects (grey spots) and the grid structure that marks the handle positions of the central double line. The BCPs occur along the handle line, but due to imaging artefacts, single BCPs cannot be correlated to a handle position. Scale bars: 50 nm.

Many of the high structures seemed to consist of several objects, but resolving them with AFM appeared difficult. That is that, regardless of the amount of tip pressure applied, the bound objects were prone to manipulation by the tip. Consequently, scarred scan lines appeared in the images that impeded the image analysis with FindFoci (Figure 4.7 b). Therefore, only the object number and heights will be discussed without considering the object location. Furthermore, none of the twelve pads chosen for image analysis displayed attached objects on line I3. As the attachment has taken place in the central line I2, the different handle patterns in I2 and I3 have most likely played a role. In order to account for that, binding to I2 and I3 will be discussed separately.

In the high structures on line I2, between one and six single objects could be identified. On average, 3.7 objects are found on I2, which corresponds to a binding yield of 0.26 objects per handle. This is considered the binding yield with the specific sequence in general, as, given that objects were attached to virtually every pad in I2, the handle pattern did not seem to impede the binding here.

Still, it was a moderate yield, which may have had several reasons. On the one hand, steric hindrance could have occurred due to the handle pattern of I2. That is that an attached object blocks the attachment to adjacent handles. The 20 bp link is 6.8 nm, and the whole BCP, if stretched out, is approximately 12 nm, while in I2 the distance between adjacent handles is about 6.2 nm at maximum. Thus, an attached BCP could have reached adjacent handles easily. Another reason could have been the aperiodicity of the specific sequence. To satisfy the dictate of the Watson-Crick base pairing during hybridisation, the sticky ends for attachment should be flawless. However, the error rate in commercial oligodeoxynucleotide synthesis after purification is estimated at one in 200 nt^[372], and the likelihood of introducing an error increases with increasing oligodeoxynucleotide length. The 20N' handles are the 3' end of an origami staple strand made of > 35 b, a size for which commercial DNA providers recommend additional purification such as reversed-phase cartridge, RP-HPLC or PAGE. However, standard RP-HPLC as applied for the 20N'-bearing staples still comes with a guaranteed purity of > 85 % only^[373]. Therefore, even though AFM imaging has proven the presence of the handles, not all of them might have been able to bind a BCP.

Faulty DNA single strands probably contributed to the rare attachment to I3, which consisted of four handles only. However, given the binding yield in I2, at least one handle should have been occupied on average. Thus, as mentioned above, the handle pattern seems to play a role. In I2, objects frequently have occurred so close to each other as if bound to adjacent handles. This does not contradict the assumption of steric hindrance, but additionally, the attachment could have been induced as follows. Given that the BCP can form small oligomers in solution, binding one BCP of such a dimer or trimer increases the chance that the other BCPs hybridise with an adjacent handle due to an increase in the local concentration. Whether a small oligomer has attached or whether two BCPs have started to interact after attachment cannot be judged from this experiment. Attaching a small oligomer from solution could be more likely than the attachment of a single BCP. That is because small oligomers provide more than one ODN, which multiplies the chance of an initial attachment. This increase in likelihood could have been significant here as it balances that a specific sequence does not provide as many stable initial hybrids as a sliding sequence (which will be discussed in the following paragraph). The sparse binding in line I3 supports this assumption. The handles are placed approximately 12 nm apart, which lowers the handle density by a factor of 2.7 compared to I2, and induced binding can most likely not occur.

Overall, the BCPs attached site-specifically to DNA origami with specific sequence links. The binding yield per handle was moderate. Possible reasons could be production mistakes in the DNA sequences or steric hindrances in the handle pattern on the DNA origami pad. Eliminating the steric hindrance at the cost of reducing the handle density has resulted in less binding in this pattern. Probably, the attachment of small BCP oligomers present in solution played a role. It could be more likely than the attachment of a single BCP as they provide more than one ODN, which increases the chance of an initial binding and the attachment stability.

Sliding sequences and type II pads

After attaching P3(EO)₃T-b-18T BCPs to the pads of type II, high structures occurred on virtually all lines on all pads. These hybrids appeared more robust to scanning than the hybrids with the specific sequence, which allowed locating the objects (i. e. comparing their positions to the handle positions as described in Section 2.6.3) in addition to counting and height determination. In a high structure, the FindFoci algorithm located one maximum, i. e. one object, in most cases. Occasionally, two objects were identified; the maximum found was three objects.

The average number of objects per line was three for II1 and four for II2 and II3, which is an insignificant difference. The yield for the handle lines located near the edge of the origami (II1, II3) was similar to the middle line (II2). That is, the hybrid formation did not include the behaviour reported by Rinker *et al.*^[374], where handles located in the origami centre were found to be less occupied. In total, the binding yield for the whole type II pad is 0.33 objects per handle.

Upon locating 133 objects, a majority of 60 % could be assigned to a handle position **a**, however, 40 % were found between two neighbouring handles. Almost all objects stayed on a fictional line that would directly connect the neighbouring handles, i. e. in position **c** (Figure 4.3 b). Only for five of 133, the mass centres were significantly tilted away from this position. The distribution of the objects on the lines was random; i. e. all handles seemed to be able to bind a BCP. However, the five handles that had two next neighbours (marked in II3 in Figure 4.3 b) were occupied 2.5 times as often as the two handles with one next neighbour (Figure 4.8 b). As can be seen in Figure 4.8 a, differently sized gaps occurred in every line. Figure 4.8 c displays a histogram of the distribution of the distances between the centres of two neighbouring objects. They were found to be in the range of 4-28 nm, while a full line length is 36 nm. Maxima have occurred around 6 nm and 16 nm.

Compared to the type I pad, the binding yield for the type II pad has slightly increased from 0.26 objects per handle to 0.33. This increase was expected. It probably reflects both the benefit of the sliding sequence and a favourable handle density and pattern.

The handle density per nm² for the lines II1 to II3 lies between that of the lines I2 and I1/I3 in type I (Table 4.1). Regarding the handle pattern, increasing the proportion of handles with two next-neighbour handles⁶ seemed to benefit the binding yield. This lines out with the finding that I1 and I3 are barely occupied, while I2 was occupied for more than 90 % of the pads. In fact, if only the two-neighbour handles are considered, the binding yield on the type II pads was 0.40 objects per handle. This is a more significant increase compared to the type I yield than the average type II yield.

Probably, the increase in local handle density for two-neighbour handles compared to one-neighbour handles provided more opportunities for initial object binding, and it could have been favourable for keeping the BCP attached. A hybridisation process with a sliding sequence presumably involves binding, (partial) dissociation and rebinding until the energetically most favourable state forms. Having another handle close increases the number of binding states in that process. Furthermore, a higher handle density in a line results in a higher chance for the attachment of small oligomers, which was discussed as induced binding with the type I pads. Another yield-enhancing feature of the type II handle pattern could have been that just single lines instead of double lines were present. Steric hindrance could occur from two sides only, which kept the handles more accessible for BCPs in solution than, for example, the handles with four neighbours in line I2 on pad type I.

It is noticeable that two fifth of the objects were not found on the handle positions **a** (scenario 1, Figure 4.8 d), but between them, and that virtually all objects off **a** are located on the distance **c** between neighbouring handles. While the induced binding is a scenario that has probably contributed to the occupation of **c**, three more possible scenarios are given in Figure 4.8 d: tilting (2), π - π -stacking (3), and bridge binding (4).

⁶that is, neighbouring handles with a distance of approximately 6 nm between them

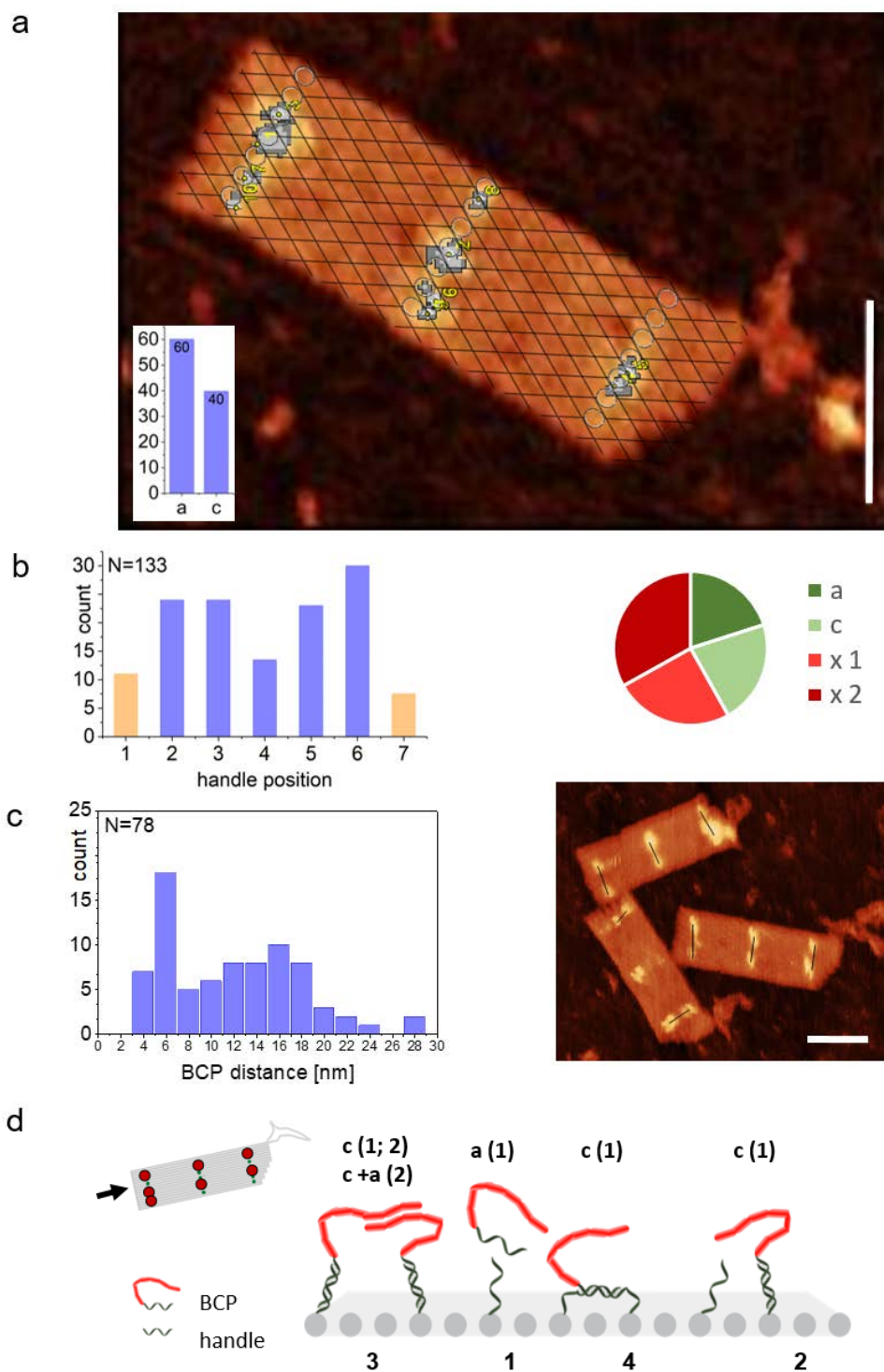


Figure 4.8: Hybrid formation from pad type II and P3(EO)₃T-b-18T. a) Stack image of hybrid, FindFoci mask image with the localised objects (grey) and grid structure with handle positions. Inset: distribution of the attached BCPs on the possible binding positions **a** or **c**. Scale bar: 50 nm. b) Occupation of the handle positions along the lines from top (1) to bottom (7) considering all three lines of 19 pads. Orange bars: one-neighbour-handles (handle 1; 7); blue bars: two-neighbour-handles (handles 2-6). Pie chart: occupation state of the handles. They are either involved in binding an object in position **a** or **c**, or they are unoccupied while having (x1) or lacking (x2) a fully occupied neighbour. c) Distances between neighbouring objects measured as shown in the AFM image with maxima at 6 nm and 16 nm. Bars appear above class means. Scale bar AFM image: 50 nm. d) Possible binding and interaction scenarios of objects on a line. The scheme depicts a side view onto the vertical edge of a hybrid as indicated by the black arrow. Ideally, one BCP binds one handle (1). Already bound objects can wield steric hindrance by tilting (2). The polymer blocks of two adjacent objects can engage in π - π -stacking (3). An object can bridge-bind to two handles (4). The letters a and c denote the positions the scenarios result in, the numbers in brackets count possibly bound objects.

The tilting scenario describes that the 5.1 nm dsDNA link with a persistence length of 50 nm^[371] allows the objects to gyrate freely around the handle origin and tilt in the direction of a next-neighbour handle. That is, the position would be occupied by chance. The π - π -stacking scenario involves two objects bound to next-neighbour handles that interact. As there is no random interaction of P3(EO)₃T with ssDNA (Figure 4.5 d), the interaction must be due to the polymer backbone. Most probably the BCP interaction is based on π - π -stacking of the P3(EO)₃T blocks, or to be precise, the hydrophobic conjugated backbones of the polymer chains. Note that induced binding results in the same object configuration and cannot be distinguished from a π - π -stacking that started after the attachment. In the bridge-binding scenario, the ODN of one BCP binds to two handles.

The occupation of **c** is interesting with regard to the formation of continuous polymer paths on origami. On the one hand, it indicates that an interaction of adjacent polymer molecules, which probably involves π - π -stacking, can take place. Adjacent objects sharing a border have often occurred. This is reflected in the mode in the distance distribution at 6 nm (Figure 4.8 c). On the other hand, the occupation of **c** can be perceived as yield-lowering. Bridge binding and, to some extent, tilting include one BCP on two handles (Figure 4.8 d). The π - π -stacking scenario might involve two objects but neither have they been detected as such, nor could they be identified through being larger than objects on **a**, which is likely due to the resolution limit of AFM. However, the tilting scenarios must not always be yield-lowering. In fact, the proportion of handles blocked due to the occupation of **c** is small. A binding yield of 0.33 objects per handle means that⁷ 67% of the handles are unoccupied. However, the pie chart in Figure 4.8 b revealed that 58% of the handles (sum of the partitions x1 and x2) were not involved in any occupation of a position **a** or **c**. Thus, only 9% of the handles could possibly be unoccupied because a position **c** is occupied.

Despite the improvement of the binding yield, its absolute number is still moderate. The distance distribution in Figure 4.8 c displays a second maximum at around 16 nm, which corresponds to the distance of handle 1 and 4 in a line. The corresponding peak is broad, which can be attributed to the 5.1 nm contour length of the link. This preference of skipping handles suggests that already attached objects yield steric hindrance to their neighbouring handles on a line. In fact, the unoccupied 58% of the handles include 25% that have a fully occupied neighbour⁸ (x1 in pie chart in Figure 4.8 c). However, the other 33% are not adjacent to a fully occupied handle (x2 in pie chart in Figure 4.8 c). As these numbers are similar, they do not exclude an influence of the already attached objects, but they also suggest other influence. The hybridisation ability of the BCP-handle-system should not have lowered the yield significantly. As mentioned in Section 3.2.2, the bulk ability of the P3(EO)₃T-b-18T BCP to hybridise with an 18Å counterpart was already proven by SPR^[172]. The BCP was used in excess, and it was given ample time for hybridisation, so the providing and binding ability of the BCP should not have been the reason. Furthermore, the BCPs did not repel each other. Probably, the low binding yield originated in the attachment kinetics to a free-floating pad. Its thermally induced bending could have made an initial attachment less likely. Objects already attached could have enhanced this effect, which could account for the peak at 16 nm in the object distance distribution. The combined effect could have lowered the chances for an initial attachment in a way that fully occupied lines did not occur.

However, in order to form a continuous polymer path along a line, every handle must be occupied. As stated above, the hydrodynamic diameter of the P3(EO)₃T is 3-6 nm^[172]. It was assumed that P3(EO)₃T is coiled due to its hydrophobic backbone, and that it can potentially stretch out when interacting with a neighbour, so it would bridge the 6.15 nm gap between the handles easily. Using a larger polymer block would possibly compensate a missing BCP in the line, but it might attach with a lower yield as the larger P3(EO)₃T shield the ODN block more. Overall, it is conceivable that this handle pattern might not allow for depositing enough polymer material to form a continuous path.

⁷if all objects on position **c** are single objects, that is, yield-lowering bridge binding or tilting has occurred in all cases

⁸A fully occupied neighbour is involved in binding an object in position **a**, or lies between two objects in position **c**.

Overall, analysing the object positions on type II pads with FindFoci has suggested three parameters of the pad design that influence the yield. The first is the link, and in particular its sequence. Compared to the specific sequence, the binding yield with the sliding sequence has increased slightly. The second parameter is, as also suggested by the observations of pad type I, the handle pattern. The binding yield increased with increasing the number of two-neighbour handles. The third parameter is the possibly impeding role of already attached objects in the handle pattern. Taken all observations into account, a full occupation of a line of handles III1 to III3 in this pattern does not seem to be the preferred packing. Possibly, a handle pattern that enhances the probability for initial binding by offering more handles per area can further improve the yield, and allows creating a continuous polymer path. However, the yield improvement would be achieved at the cost of localisation precision and resolution.

Testing the sequence specificity. In order to study the specificity of the binding, an experiment with two different sequences on the type II pad was conducted.

For that purpose the 15A sequence in the first line is replaced by (AAT)₅. That is, the same two sliding sequences were used as in the gold nanoobject attachment to the pad (see Section 3.2.3). The gold nanoobject attachment proceeded site-specifically. However, the size and multiple binding per gold nanoobject might have prevented a mismatch while binding the BCP with one handle and one ODN might tolerate it. In AFM images of bare pads with two handle types, all handles were visible.

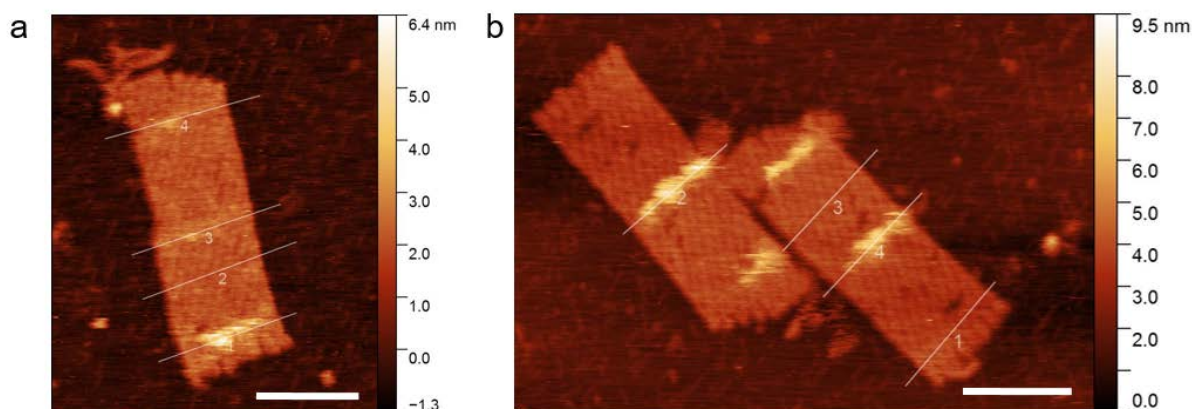


Figure 4.9: Sequence-guided attachment to a modified pad type II. The pads possess (AAT)₅ handles in III1 and 15A handles in II2 and II3. Addition of either a) P3(EO)₃T-b-(ATT)₅ or b) P3(EO)₃T-b-18T results in exclusive binding to the complementary handles. Scale bars: 50 nm.

The pads were mixed either with the P3(EO)₃T-b-18T BCP or the P3(EO)₃T-b-(ATT)₅ BCP (Figure 4.9). On average, two objects occurred on the (ATT)₅ line and two to three on the 15A line. This yield agrees well with the one found for the attachment on the type II pad with 15A handles only. In any case, the BCPs just attached to the line with their respective complementary handle, so a 100% specificity was found. This is in line with the gold nanorod attachment discussed in Section 3.2.3.

A sliding sequence and type III pads

Taken the observations for type I and type II pads into account, the type III pattern contains the same number of one-neighbour handles and handles with more than one neighbour to directly investigate the influence of the handle pattern. The handle density in the unit cell of the pad type III pattern is the same as in pad type I (0.0204 handles/nm²), however, most handles have one or three direct neighbours. The latter are arranged with a 120° spacing around the central handle. Furthermore, the shorter 8A handles are used to lower the influence of steric hindrance.

The type III pads were used with P3(EO)₃T-b-18T BCPs because these was used with type II as well. In addition, the type III pdas were used with P3(EO)₃T-b-10T BCPs to investigate a system with minimum steric hindrance and without bridge binding.

After adding P3(EO)₃T-b-18T BCPs to type III pads, ten objects were found per pad on average, so the total yield for a whole pad was 0.25 objects per handle. Instead of a continuous polymer path, five high structures are scattered over the pad on average. 27% of the high structures were single objects, while the other 73% contained at least two objects that share a border in the FindFoci peak mask. The structures contain 2.7 objects on average and involve 4.1 handles, which corresponds to an object density of 0.66 per handle (see Table 4.2).

As for the type II pad, objects occur on the handle positions **a** as well as between them on position **c**. As additional positions between handles, the positions **b** and **d** can be occupied.

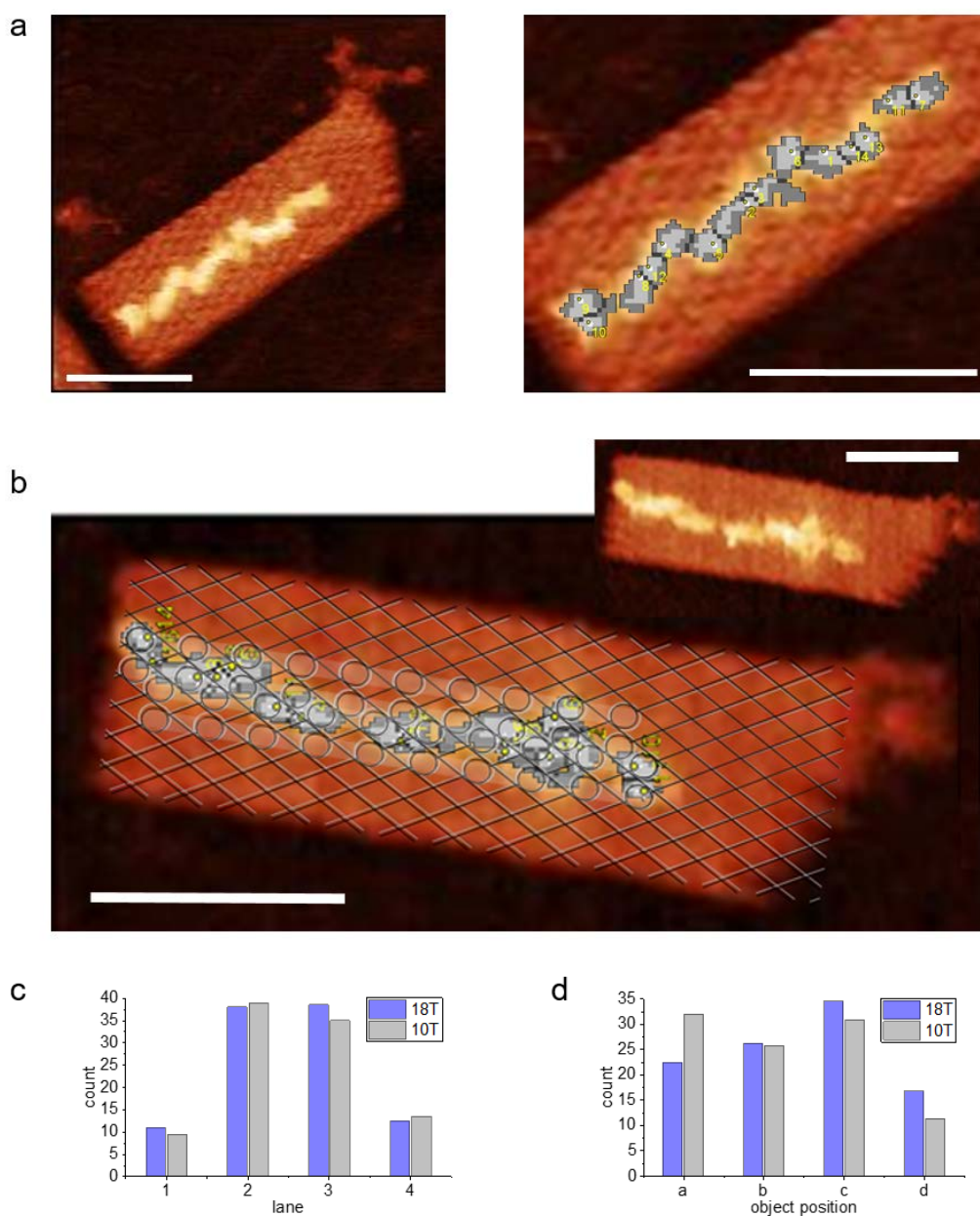


Figure 4.10: Hybrid formation from the type III pad and a) P3(EO)₃T-b-10T and b) P3(EO)₃T-b-18T. Image a) displays a hybrid and the same hybrid with the FindFoci mask image with localised objects (grey), while image b) displays a stack image of hybrid, FindFoci mask image and grid structure with handle positions. These examples show almost continuous lines with touching objects and patches. Relative occupation of c) the lanes L1 - L4 and d) the positions **a** - **d** marked in Figure 4.3 c for attaching P3(EO)₃T-b-18T and P3(EO)₃T-b-10T. All scale bars: 50 nm.

Table 4.2: Occupation of the hybrids of type III pads and P3(EO)₃T-b-18T as well as P3(EO)₃T-b-10T. Object distribution amongst single objects and patches; objects per patch; handles per patch, attachment yield within a patch and the total structure; handles occupied with objects in the position **a** or **b, c, d**; handles unoccupied but participating in a binding in position **b, c, d** and handles unoccupied and not participating in binding an object.

	object distr. [%]		objects/ patch	handles/ patch	yield [%] patches	total	handles occupied [%]		handles unocc. [%]	
	single	patches					a	b,c,d	b,c,d	not binding
18T	27	73	2.7	4.1	66	25	6	18	13	63
10T	46	54	2.5	3.9	64	27	8	19	14	59

Note that locating the position of an object provides a statistical overview of on which lane the objects occur (Figure 4.10 c) and whether they sit on a handle position or between handles. The positions **a**, **b** and **c** occurred in roughly the same frequency, while the position **d** was barely occupied (Figure 4.10 d). However, as will be discussed in Section 4.3, due to the resolution limit of the AFM image and due to the abundance of positions in this handle pattern, the precision regarding a single object's position is limited. One example is the position **d**. In theory, it marks the distance of adjacent handles in every lane, but in the lanes L2 and L3, positions **b** and **c** involving adjacent lanes are available so close to **d**, that many objects might be assigned to multiple positions. Position **d** is the least likely in any of these cases, because it involves an object interaction over ≈ 11 nm, while **b** and **c** are about 6 nm⁹. Therefore, all objects in the lanes L2 and L3 were assigned to the positions **a**, **b** or **c** only. As **d** can be determined unambiguously for the lanes L1 and L4, the number of **d** in Figure 4.10 d includes the lanes L1 and L4 only. As the lanes L1 and L4 have one-neighbour handles only, they are sparsely populated, which contributes to the fact that **d** barely occurred.

The number of objects located on or off a handle position (i.e. on position **a**, or on one of the positions **b**, **c** and **d**); Figure 4.10 d) and the object count on a lane (Figure 4.10 c) were found to be robust against single positioning errors. Thus, they will be discussed in the following as the representative characteristics for the object distribution on the type III handle pattern. Regarding the object count of a lane, objects on **a** can be assigned straightforwardly, while the objects positioned on **b**, **c** and **d** are included as given in the equations 2.3-2.6 (Section 2.6.3). It was found that three times the number of particles bound to the inner two lanes (L2+L3) compared to the outer two (L1+L4). Figure 4.10 c displays the object distributions on the lanes L1 to L4 for both BCP types. Table 4.2 compares the binding yields and patch characteristics for P3(EO)₃T-b-18T to those of P3(EO)₃T-b-10T on the pads.

It is remarkable that all of the parameters given in Table 4.2, that is, the binding yield and the distribution of the objects over the handle pattern, were in principle the same for P3(EO)₃T-b-18T and P3(EO)₃T-b-10T. For P3(EO)₃T-b-18T the resulting steric hindrance on a neighbouring handle, for example, could be expected to be bigger than for P3(EO)₃T-b-10T because of the 10T domain left single-stranded in P3(EO)₃T-b-18T after it hybridises to the 8A handle. For the contour length of single-stranded DNA, various sources report values between 0.64 nm^[375] and 1.6 nm^[376], so the domain is most probably coiled, but it adds to the object size and it can be stretched out. A slight shift in the occupancy from position **c** to **a** with P3(EO)₃T-b-10T could reflect the stronger confinement of the system, but the variations might as well lie in the range of statistic deviations. In the AFM images, the objects appeared more globular for P3(EO)₃T-b-10T, however, this observation is just qualitative.

Although type III offers more handles and the sliding sequence, the binding yield over the whole handle pattern was below the yield for pad types I and II. On the one hand, the shorter link could be a reason as it has a lower melting temperature and hence provides a less stable binding. On the other hand, the handle pattern includes more one-neighbour handles. Lining out with the former findings, the proportion of

⁹The 8A handle is 2.72 nm, and the stretched-out P3(EO)₃T-b-18T and P3(EO)₃T-b-10T BCPs are 12.1 nm and 9.4 nm long, respectively.

unoccupied handles is about three times higher amongst those handles that have just one next neighbour at the 6 nm distance. This is expressed as a significant preference of the objects for the inner lanes L2 and L3, where the two- and three-neighbour handles are located (Figure 4.10 c). Taking just the handles in these lanes, the binding yields are 0.36 and 0.41 objects per handle for P3(EO)₃T-b-18T and P3(EO)₃T-b-10T, respectively. This in turn is in the range of the yield for the two-neighbour handles on pad type II.

As Table 4.2 sums up, two to three times the number of objects is located between handles (**b**, **c**, **d**) compared to being located on the handle position **a**. The proportion of objects between handles increased compared to the pad type II because more positions between handles are available on the pad type III. As for the pad type II, occupying these positions indicates object interaction, which is favourable, but can be yield-lowering as well.

The objects seemed to favour the positions where they could interact, as it presumably increases the binding stability. That is because the interaction could act as second attachment in addition to the DNA link involving the short 8A handle. In this way, the objects differ from metallic nanoparticles, which tend to repel each other. On some pads, the attached objects seemed to form an almost continuous line (e.g., Figure 4.10 a and b).

The binding scenarios discussed for pad type II (induced binding of small oligomers, tilting, π - π -stacking and bridge binding) can occur with different handles and positions on the pad type III as well, even though the non-touching 8A handles are about half as long as the handles on the pad type II. For the pad type III, the binding of small oligomers could be promoted because of the handle density and the fact that the attachment to multiple 8A handles counteracts the yield-lowering effect of the smaller melting temperature. In the long 18T ODN, the unbound 10T domain can facilitate the π - π -stacking, because it can act as a flexible spring in the object positioning. For the 18T ODN, bridging can occur as well. It is less likely than on pad type II, as it requires a complex positioning of two handles and the BCP. In addition, the double-stranded parts per 8A handle are shorter than per 15a handle, which results in smaller melting temperatures. For the 10T ODN, bridge binding is impossible. However, this did not influence the object distribution on the handle pattern notably. On the one hand, this reflects the minor influence of the bridge binding scenario on the binding yield. On the other hand, it is a strong indicator that π - π -stacking¹⁰ plays a major role in the BCP interaction, because it is the only interaction left to account for the frequent occurrence of touching objects.

Already attached objects are likely to play a role in the moderate binding yield, but as discussed for the pad type II, they are most probably not the only reason. While 13 % and 14 % of the handles are involved in **b**, **c** and **d** and unoccupied, about four to five times that number of handles is unoccupied but not involved in any binding (see Table 4.2). Furthermore, the majority of these unoccupied handles do not have a fully occupied neighbour that could wield steric hindrance. A key contributor to the moderate yield are probably the one-neighbour handles, as discussed before.

Within the multi-object structures, binding yields of 66 % for P3(EO)₃T-b-18T and 64 % for P3(EO)₃T-b-10T are higher than anything found before on other pads. This proves that the objects can be packed closely. However, pads with 100 % occupation of all handles did not occur. The gaps in the patches did also not close using the shorter P3(EO)₃T-b-10T BCP. Probably the steric effect did not ease off sufficiently, but links shorter than 8A could not be chosen because of the melting temperature.

To sum up, attaching the BCP in a 2D pattern instead of a line, and using a shorter link with the sliding sequence has resulted in a slight decrease in the binding yield. Most probably, a decrease in binding stability due to the shorter link played a role. That it is favourable to introduce more than one next-neighbour handle can be seen in the attachment ratio of one-neighbour handles in the lanes L1 and L4 vs. two- and three-neighbour handles in the lanes L2 and L3.

¹⁰either occurring on the pad after two single objects attached, or already occurring in solution and form small oligomers

Furthermore, there were patches of multiple touching objects on every pad. As for the other pad types, the touching of the objects leaves room for the assumption that the polymer blocks interact, which would, for example, be favourable for charge carrier transport along the polymer backbone. An argument in favour of the occurrence of π - π -stacking is the object distribution with P3(EO)₃T-b-10T block copolymers, whose ODNs are too short to contribute to any kind of interaction.

Even with that smaller BCP, a binding yield above 67 % in the object patches on the pad has not occurred, indicating that the attached objects can wield steric hindrance on neighbouring handles, as it was also assumed with the pad type II.

Some hybrids displayed almost continuous lines along the pattern that involved mainly the lanes L2 and L3. This suggests that the pattern there is suitable to deposit enough material to form continuous structures. Probably, a longer P3(EO)₃T block is favourable for that.

4.3 Influence of the scanning on the samples and limitations of AFM

As discussed in the Sections 3.1.2 and 3.1.3, AFM on mica-deposited origami was used to evaluate the structure of the origami under varying conditions, and to determine the synthesis yield based on the ratio of faulty to intact origami. As in every analytical approach, the random and systematic errors of the method contribute to the experimental results. Random errors of the AFM-based origami evaluation include, for example, damaging the structures during the deposition onto the mica substrate, distorting the origami with the tip or removing staples during scanning. As imaging without noticeable tip influence cannot be guaranteed, a reference yield cannot be determined, and the tip-induced damage cannot be quantified. In order to account for local quality variations due to the preparation, the images of a sample were obtained from different spots on the mica. It is assumed here that the sample preparation protocol provides samples of comparable quality, so for the yield determination, at least two images were taken from one sample each time. In order to quantify the random error of the sample preparation, preparing and scanning of several samples from the same origami solution is recommendable in further work.

With regard to the systematic errors, Section 3.1.3 mentions two aspects, for which assumptions were made. First, the yields determined from scanning in liquid were directly compared to the yields for scanning in air. The assumption is valid because the yields of samples from scanning in air and in liquid have differed only within statistical deviations that would occur from sample to sample as well. The second assumption is that the state of the origami on the surface was assumed representative for its state in solution. This assumption relies on the qualitative observation that the mica surfaces were equally covered whether intact or ill-shaped origami (with the same DNA concentration) were deposited. In principle, this finding justifies the assumption sufficiently for the purpose of this work, but further experiments could aim at determining a quantitative value here. For that purpose, the yield of a sample could be determined from AFM images and TEM images likewise, and from a quantitative evaluation of the band intensities for faulty and intact origami in gel electrophoresis. For each method, the random errors and the sample preparation errors must be quantified through repeat experiments. If comparable yields are determined with these methods, it will not just prove that the presented AFM method provides accurate results, but that TEM and gel electrophoresis do as well. When one compares, for example, experimentally determined tPad dimensions and the values expected from design (see Table 3.1), the errors caused by AFM are not significant, and AFM accurately evaluates the origami.

For the accuracy and trueness of the localisation of the BCP on origami as presented in Section 4.2.2, one has to keep the siting inaccuracies in mind. These occur through movement of the objects with the tip during imaging. This becomes evident when an object is scanned multiple times and/or under different

angles and/or with different tip pressures. In addition to the scanning-induced variations, mistakes are introduced by the image processing in Gwyddion (mainly through the line correction tool) and by the subjectivity of the criteria selection in the FindFoci plugin.

To assess the impact of the scanning, one pad was scanned two times under different scan angles (Figure 4.11). To assess the influence of the Gwyddion processing, one raw image was processed twice. To assess the FindFoci routine's reliability, the same image was subjected to it twice (with choosing the criteria each time freshly). It was found that all of the sources of error have a similar impact. On average, each causes one to two positions per pad to vary when they should be the same. As all of the errors are random, they tend to compensate one another, leading to a sum error in the same range. That is, with an average occupation of ten objects per pad, 10-20% of the positions are error-prone, so the precision of the localisation is limited. As the errors are distributed statistically, and multiple pads have always been evaluated (see Table 4.1), the average percentages given for occupations of a position must be close to the true value.

Overall, the localising method is accurate in a way that it is true but not very precise, and always demands a statistically relevant number of samples to yield valid results.

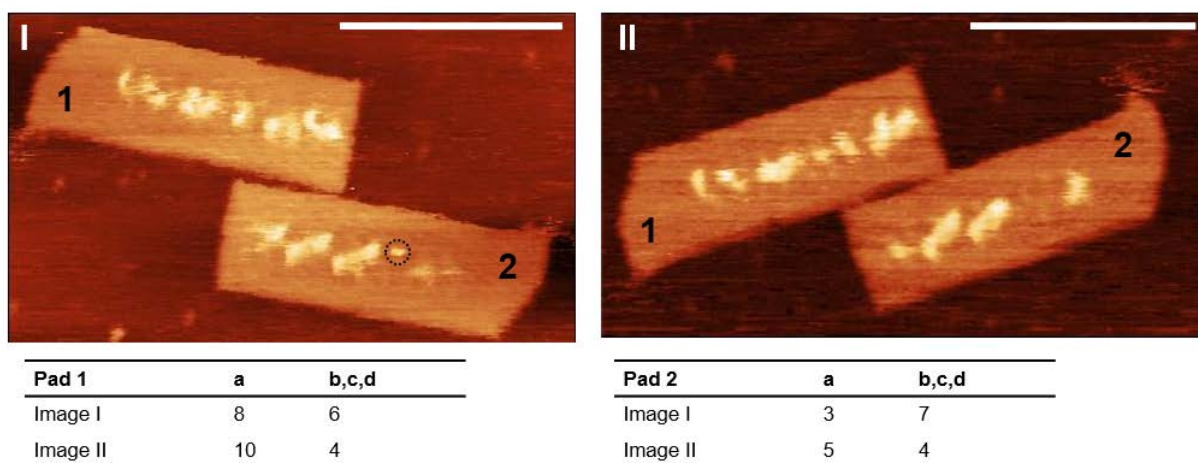


Figure 4.11: Limits of the BCP localisation accuracy. Image I and II show the same two pads scanned from different angles. For each pad, the tables list how often an object has appeared on a handle position (**a**) or between handles (**b, c, d**). On average, up to two objects appear in different locations. For pad 2, one object visible in image I does not appear in image II (black dotted circle). However, such object removal by the tip is exceptional. Scale bars: 100 nm.

4.4 Summary and outlook

Quantitative analysis of the hybrid structures. AFM was well-suited for evaluating the block copolymer (BCP) attachment to the DNA origami pads at the single object level, which lies in the sub-10 nm range. For the first time in AFM-based studies of synthetic polymers on DNA origami, the FindFoci^[6] plugin was used. It has provided a semi-automated routine that allowed analysing each image using well-defined parameters, which has always been beneficial to derive comparable results from different experiments. For the sufficiently resolved AFM images of the type II and type III hybrids, the routine provided precise data on the location of the origami-bound BCPs. This allowed comparing the BCP locations to the handle pattern of the pads. Furthermore, attachment yields per handle could be determined and parameters that influence the BCP attachment could be suggested. Another quantitative measure provided was the average object height.

A limiting factor for the precision of the method was the imaging resolution. Besides the tip radius, the tip pressure has played a crucial role. It has influenced the object height as well as the object position in a way that strong tip-sample interactions could lead to squeezing or position shifts of the bound BCPs. Thus, the analysis yielded a single block copolymer position with an uncertainty of 10-20%. However, this did not impede the trueness of the method, as long as a statistically relevant number of block copolymers per pad type (between 44 and 107 in this work) and robust properties were investigated. Depending on the handle pattern, those properties were either the positions of single objects on or between the handle positions (type II) or combinations of single types of positions into events such as occurrence “on a handle” vs. “between two handles” and along a lane of handles (type III).

Hybrid formation. A new method to assemble conjugated polymers onto DNA origami was established successfully. For that purpose, 1:1 diblock copolymers consisting of a conjugated polymer block and an oligodeoxynucleotide block were synthesised. As polymer block, a water-soluble, end-functionalised, regioregular head-to-tail P3(EO)₃T polythiophene derivate was synthesised via a customised *ex-situ*-initiated Kumada catalyst-transfer polycondensation^[172]. The ODN was joined to the P3(EO)₃T with copper-free strain-promoted azide-alkyne cycloaddition^[351].

HPLC was found to be suitable for the BCP purification. The HPLC-based kinetics study of the hybrid formation suggested a pseudo-zero-order kinetics and a near completion of the reaction after a 48 h. Both findings indicate that not the presence of the educts is rate determining, but probably the presence of a reactive intermediate.

The standard conditions to attach BCP to the DNA origami pads, which is a buffer environment of 1x TE with 12.5 mM MgCl₂, 15 °C and 300 mM NaCl, have resulted in 90% of the pads having at least one BCP attached. The hybrid formation was found to work with this yield in the temperature range from 5 °C to 15 °C and at concentrations of the monovalent salt NaCl in the range of 0-3 M. The attachment could be shown for sliding and specific sequences and origami pads with different handle patterns. Table 4.1 summarises important design parameters of the handle pattern as well as the attachment yields for the different pad types. The objects sizes of BCP with different DNA blocks were found to be similar.

With the FindFoci-based analysis of high-resolution AFM images, four factors were identified that play a role in the attachment. The first factor was the handle pattern, and here in particular the number of next-neighbour handles that have a 6 nm distance to the observed handle. Handles that have more than one next-neighbour handle were three to four times more likely to be occupied than handles with one next neighbour. Second, already attached objects seemed to play a role. In type II and type III hybrids, 25% of the handles were unoccupied and located next to an occupied handle, indicating that objects might have wielded steric hindrance. Third, the already attached objects were not the only reason for the moderate attachment yield, because about 33% of the handles were unoccupied and not next to a fully occupied handle. Fourth, attaching small oligomers from solution could play a role. That lined out

with the observation that handles with more than one next neighbour are occupied preferably, and the fact that attached objects have frequently shared borders.

In parts of a hybrid, the conductive polymer molecules have been attached to the DNA origami pegboard achieving the origami-typical site specificity and a spatial resolution down to 6 nm. However, given the yields observed, attaching a BCP to every available handle position on a pegboard surface appears to be challenging.

On all three pad types, objects have shown tendencies to interact. At least, they have tolerated each other in close vicinity, which metallic NP would probably not. Hints have appeared that π - π -stacking could have played a role in that. These kind of stacking interactions are most interesting for forming continuous paths of (semi-)conductive polymers that allow charge carrier movement.

Attaching one of the 1:1 BCPs to one handle on the DNA origami has provided more control over the attachment resolution than the methods introduced before^[12-14]. However, the high resolution comes at the cost of a moderate yield currently. Providing more handles per attachment site, as it is commonplace for metallic nanoparticles, or having more than one ODN attached to the polymer block in the BCP^[13,14] will probably increase the yield, but lower the resolution at the same time. Another way to increase the proportion of conjugated polymer on a hybrid is using polythiophene blocks with a larger molecular weight. This allows keeping the resolution. However, the larger polymer block could shield the ODN from binding to the handle.

Following this basic research, the P3(EO)₃T-b-DNA BCP could be used in nanoelectronic or nanophotonic elements. Research on nanophotonic hybrid structures is currently underway.

Furthermore, the BCP formation presented here can be used with any type of water-soluble, functionalised polymer. Placing the resulting BCP on DNA origami can introduce new functionalities. As proof of principle, Appendix Figure A.9 shows the attachment of commercially available PNIPAAm. This polymer is biocompatible and thermo-responsive with a lower critical solution temperature of 32 °C. Introducing such a temperature-sensitive switch could be useful for medical applications of DNA origami.

Chapter 5

Characterisation of surface-deposited 2D DNA origami with multicolour super-resolution microscopy

This chapter presents a method that uses super-resolution fluorescence microscopy (SRM) and the principles of single-molecule high-resolution co-localisation (SHREC)^[219] to evaluate surface-deposited DNA origami structures. For the first time, a fluorescence microscopy method aims at characterising the structural integrity, the placement, the orientation and the deposition side of surface-bound DNA origami structures within one experiment through multicolour labelling. The method allows evaluating both single molecules and the bulk and it has the potential to do it for wafer-scale scanning areas.

Section 1.4 has introduced the methodical challenges of multicolour super-resolution microscopy. In Section 5.1 the basic principles, the procedure and the structures under study of this work will be introduced. Section 5.2 presents the results of the mapping calibration based on 200 nm Tetraspeck beads as fiducial markers, and the proof-of-principle experiments with the tPads. This includes discussing the trueness, precision and lower resolution limit of the method with the microscope used here. Further discussions focus on the origami properties, in particular, on the structural integrity and the deposition behaviour. Section 5.3 summarises the findings.

The author has developed the method in close cooperation with Dr. Friedrich W. Schwarz and Dr. Philip A. Gröger (Diez Group, B CUBE Dresden). Dr. Schwarz has provided the idea and guidance through the fluorescence experiments. Dr. Gröger and Dr. Schwarz have developed the data analysis algorithm. The author has designed the DNA origami, and has executed the experimental work and the data analysis presented in this chapter.

5.1 Basic principles, origami under test and method procedure

This section introduces the basic setup including the sample labelling, the origami objects under test, and the stepwise procedure of the multicolour method, including the data acquisition and the data processing routine. The experimental settings for obtaining the results discussed in Section 5.2 are given in Section 2.7.1.

5.1.1 Basic principles and labelling

The structural characterisation of origami provided by this method is the evaluation of the shape of the origami, which is referred to as the structural integrity here. The measures of the structural integrity are defined by a marker pattern that comprises of a set of characteristic marker distances d and, in the case of three or more markers, of characteristic angles (see Figure 5.1). These distances and angles will be referred to as the target values in the following. An origami is considered structurally intact if the experimentally obtained target values match the theoretically expected values. In that way, single-staple resolution is only obtained for the marker-carrying staples. However, for most applications not every staple has to be provided but the overall origami shape, and probably selected staples that provide functionality. These are the features this method can obtain.

To set the target values, an m -dimensional object is labelled with $n = m+1$ fluorescent markers with distinguishable spectra. Primarily, that means that the light emitted by the markers must be of different wavelengths. The markers are distributed in a pattern that allows assessing the shape of the object. For the square tPad, for example, triangles are chosen (Figures 5.1 and 5.2). In addition to the structural evaluation, localising the marker pattern on a surface provides the object's position. Due to the different marker colours, it is easy to design chiral patterns, which allow determining the deposition side and the orientation of the object as well.

In order to allow for a high resolution and short imaging times in each channel, a marker set that defines a target value consists of all different markers, or ensures maximum distance between markers of the same kind. In order to guarantee well-resolved markers, the used dyes exhibit minimal crosstalk in not just for the emitted light, but also regarding the excitation.

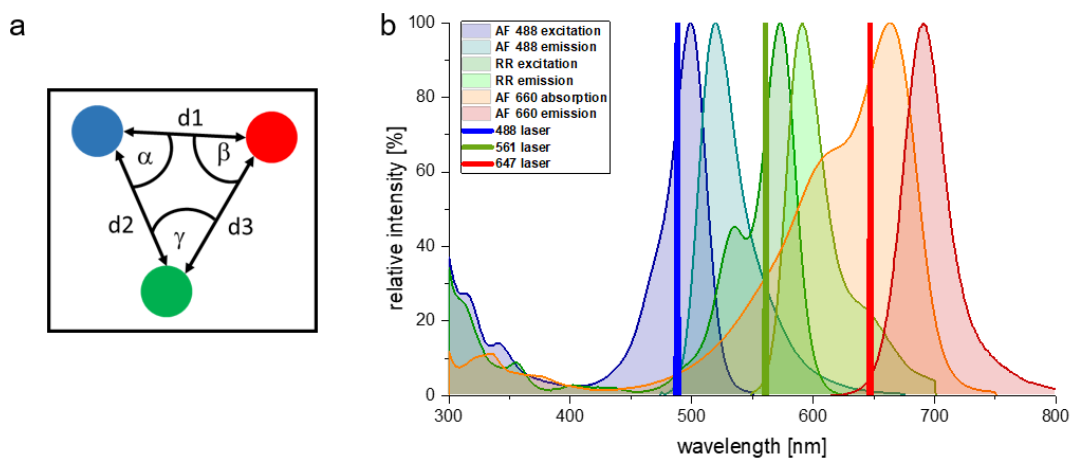


Figure 5.1: Labelling a 2D structure with spectrally distinguishable fluorophores for structural evaluation and position determination. a) Labelling of a 2D structure with three spectrally distinguishable fluorophores in a triangular pattern. The three fluorophores mark the corners, which creates six target values for structural evaluation: the target distances d_1 , d_2 and d_3 , and the target angles α , β and γ . b) Excitation and emission spectra for the three dyes Alexa Fluor 488 (blue), Rhodamine Red (green) and Alexa Fluor 660 (red). The three excitation spectra are overlapping to a small extend only, as are the emission spectra. This marker set is used in the tPad design I. The wavelengths of the lasers used for excitation are displayed as vertical lines as well.

5.1.2 The two tPad designs

Two designs of the tPads were studied, which will be referred to as design I and design II in the following (Figure 5.2).

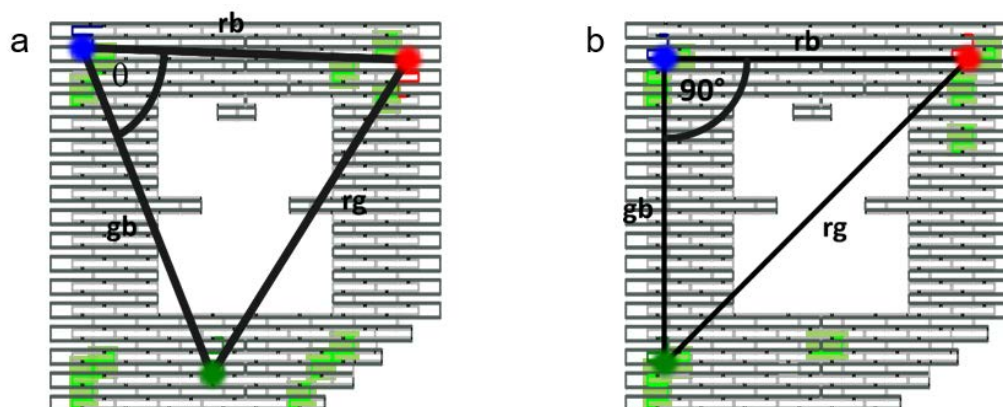


Figure 5.2: The two tPad designs with the fluorophores marked as spheres on the 3'-end of the staples that attach them. These staples are shown in the respective colour. Biotin staples are highlighted in light green in the four sites per tPad. a) Design I with the dyes Alexa Fluor 488 (blue), Rhodamine Red (green) and Alexa Fluor 660 (red) and eleven biotin staples. b) Design II with the dyes Atto 488 (blue), Atto 550 (green) and Atto 647 N (red) and with nine biotin staples.

In both designs, the tPads are labelled with three different, commercially available organic dyes. The dyes are arranged as a triangle that covers as much of the tPad surface as possible. Each of its corner positions features one unique handle or dye-labelled staple to attach each of the dyes site-specifically. Using one handle or staple and one fluorophore was chosen to yield maximum precision and trueness in the marker localisation. If not altered by threading^[377], all handles or labelled staples protrude to the same side of the tPad. To anchor the tPad to the flow cell surface, handles with biotin protrude to the opposite side in four sites per tPad.

In design I, eleven biotin handles are used, which are prolongations of tPad body staples. The fluorescently labelled ODNs carry one dye molecule each. Depending on the position they ought to sit, that is either one of the Alexa dyes Alex Fluor 488 and Alexa Fluor 660 or Rhodamine Red. The dyes form a triangle with arbitrary angles.

In design II, nine biotin handles as described above are used. For the fluorescent labelling, the design keeps the one-attachment-setup. In order to improve the labelling stability, the dye-carrying DNA strands are tPad body staples this time, with prolongations protruding to the top side of the origami that are labelled with the dye molecules. In order to increase the fluorescence signal intensity, the dye set of design I was replaced with the Atto dyes Atto 488, Atto 550 and Atto 647 N. Also for signal increase, each ODN features three of the same dye molecules¹. Despite their distances of about 1 nm on the staple, the three dyes are treated as one fluorophore because of the coiling of the staple, which will most probably minimize their distances. Thus, the principles of single-molecule co-localisation are applied to design II tPads as well. The marker pattern of design II is a triangle with a 90° angle. Two of its edges, i. e. two marker distances, run in parallel to the tPad edges. This was set up to provide a more straightforward measure for the tPad shape.

Both tPad designs are labelled prior to immobilisation to the flow cell surface. This makes the system susceptible to bleaching. To avoid irradiation-induced stress for the dyes prior to imaging, DNA PAINT could have been performed. However, using the one handle as the only anchor point, the binding statistics are most probably unfavourable. Furthermore, the setup in this work has aimed at avoiding long imaging times and laborious flushing steps in the experiment.

¹The option of self-quenching was discussed with the ODN producer. They claimed that it was not a matter of concern.

Section 5.2 will introduce two sets of experiments with the tPads. One is a standard experiment, i.e. how the method is supposed to be used with DNA origami. The other is an experiment with a strong background noise, which will discuss whether the method can extract origami signal in difficult circumstances. Both tPad designs could have been used for both sets of experiments without changing the conclusions. In order to present both designs without repetitions, the standard origami experiment focuses on design I and the origami experiment with strong noise on design II.

Design II was created mainly to improve the design I in terms of labelling. As will be discussed, the labelling of the origami with one fluorophore per colour results in few origami counts per field of view. Using tPad body staples to attach the dye and more than one dye molecule per staple was supposed to yield a larger number of labelled structures and a stronger fluorescent signal with design II tPads compared to design I tPads. Whether there was an improvement will be discussed in Section 5.2.2.

Investigation of the design I and II assembly with AFM

Table 5.1 provides a comparison of the theoretical fluorophore distances and the ones obtained from AFM images for each of the two designs. In order to determine a fluorophore position, the tPad body staple involved in its binding was left out and the distances of the gaps were measured. A gap can appear with a diameter of around 5 nm, which must be considered as an error that lowers the precision of this measurement. However, the site determination is still sufficiently true and precise to yield a value for comparison to the SRM results.

Table 5.1: Fluorophore distances red-blue (rb), red-green (rg) and green-blue (gb) according to design and mean distances \bar{d} measured in AFM images for a) ten design I tPads and b) 14 design II tPads. $SE_{\bar{d}}$ is the standard error of the mean distance.

a)	rb	rg	gb	b)	rb	rg	gb
design I	81.3	92.2	87.5	design II	76.5	110.3	79.5
\bar{d}	76.6	92.1	88.5	\bar{d}	80.4	107.0	72.9
$SE_{\bar{d}}$	0.8	1.3	1.9	$SE_{\bar{d}}$	1.4	2.3	1.2

For tPads stretched out on mica, all fluorophore distances for ten design I pads and 14 design II pads line out with the theoretically expected distances. The rb distance (top part) of design I is about 5 nm shorter than the theoretically expected value. This could have occurred due to variations in the outer shape occurring amongst samples. Lee Tin Wah *et al.*, for example, have observed a 10 % variation of the length of Rothemund Rectangular origami in the course of different measurement days^[139]. As stated in Section 3.1.3, AFM suggests a yield of correctly formed tPads in the range of 45-70 % after synthesis, which can decrease to 10-40 % due to cleaning.

5.1.3 Method procedure

In the following, the stepwise procedure of the method from experiment to data analysis and result generation is discussed. Figure 5.3 visualises the workflow of the method. For general explanations, the terms object or sample, fiducial (marker), and marker are used instead of tPads, Tetraspeck beads, and fluorescent dye, respectively.

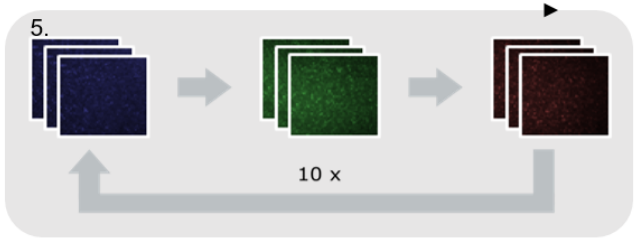
I Fluorescence measurement

Setup

1. Flow cell preparation (includes blocking)
2. Flow cell mounting + raw focus adjustment
3. DNA origami sample (flush-in – incubation – flush out)
4. Optics adjustment (focus, laser power, TIRF depth)

Imaging

sample



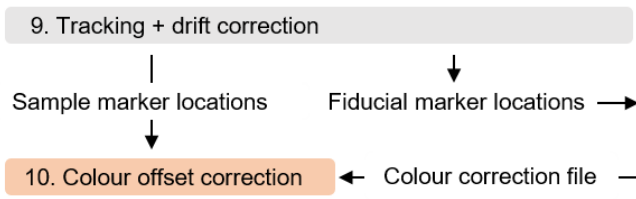
Tetraspeck bead

6. Tetraspeck bead flush-in
7. Optics re-adjustment
8. Tetraspeck bead imaging



II Image data processing

Raw data processing



Cluster identification

11. Colour data merging
12. Thresholding (cluster parameter I: incident threshold)
13. Binning (cluster parameter II: binning pixel size)
14. Dilation (cluster parameter III: structural element)
15. Filter I: colour threshold
16. a: Filter II: size
16. b: Filter III: shape
17. Filter IV: user

Data output

18. Calculate and output target values

Figure 5.3: Method procedure. The method consists of the experimental part named I) fluorescence measurement, and the computational part II) image data processing. Step 5 will be referred to as loop repeat in the following. Performing the procedure for the fiducial markers instead of an origami sample yields the colour correction file. In this case, step 10 is omitted. All steps in orange boxes are performed by Matlab routines.

I: Fluorescence measurement (step 1 - 8)

The first part of the procedure is a fluorescence imaging experiment (see Figure 5.3 steps 1-8). Objects labelled as described in Section 5.1.2 are investigated in a standard flow cell setup (see Section 2.7.1). In the following, a TIRF microscope will be used, but given sufficient signal strength, a standard fluorescence microscope can be used as well.

Several micrometre-sized fields of view are imaged. Obtaining super-resolved marker positions requires a number of images of the field of view k in each of the colour channels n . The number of images in one channel k depends on the signal intensity of a marker and its blinking behaviour. A larger k can compensate images where the marker signal is not present. For imaging, the multicolour method proposes a sequential loop-repeat routine (Figure 5.3 step 5). A loop includes sequential imaging in all n colour channels, but taking few images in each one. The loop is repeated to yield the desired k images per channel. For an origami labelled with three fluorophores, for example, ten images per colour might be taken per loop, which is 30 images in one repeat. The loop may be repeated ten times to yield 100 images per colour and $n \cdot k = 300$ images in total. With the loop-repeat routine, the markers of all colours are subjected to similar doses of laser radiation before they are imaged, not just concerning the respective excitation laser, but all lasers used. Considering the radiation-induced bleaching^[199], it seemed more reasonable to decrease the signal of each colour channel gradually instead of risking a significant signal loss in the channel imaged last. After imaging the sample, fiducial markers for the mapping calibration are imaged (Figure 5.3 step 6-8). Since they provide intense fluorescence signals, fewer images are needed to localise a fluorophore position precisely, and the loop-repeat is not necessary in step 8.

In the first and second experiment presented here, a field of view is typically $53.50 \mu\text{m}$, and $54.27 \mu\text{m}$ in the third experiment². Tetraspeck beads with a diameter of 200 nm serve as fiducial markers. They were flushed into an origami-free channel to avoid overpowering the origami signal. For imaging them (step 8), 20 images per colour were taken in a single loop. For tPad imaging (step 5), 100 images per field of view and colour were taken running ten loops of ten images per colour.

II: Image data processing (step 9 - 18)

The second part of the procedure covers the image data processing. It involves drift correction and marker localisation as well as calibrating the mapping functions for the colour-offset correction, which is summed up as raw data processing (steps 9 and 10). Furthermore, it includes cluster identification and filtering (steps 11 to 17) and the calculation of the target values (step 18). A Matlab routine performs the steps 10 to 18 (orange in Figure 5.3).

Raw data processing. As input data, the cluster identification (steps 11 to 17) requires the n matrices of the marker localisation data from the sample (one for each colour channel) that list the fluorophore positions of the k images of each channel, and such matrices from the fiducial markers. In order to obtain these localisation matrices, the respective image stacks (denoted as sample image stacks and fiducial image stacks in Figure 5.3) are submitted to a single particle detection and localisation algorithm in ThunderSTORM^[232], which is a plugin of the Fiji^[365] image analysis software. For this step 9, ThunderSTORM combines marker localisation (tracking) and lateral drift correction. For the latter a cross-correlation method was chosen that ThunderSTORM provides³.

For the tPads, the dyes are supposed to move around freely, and the Tetraspeck beads are supposed to emit evenly throughout the bead. Thus, in both cases the point spread functions are approximated with 2D Gaussians in ThunderSTORM in order to determine the centres of the PSFs, i.e. the marker localisations. The output files of these tracking and drift correction processes are the n sample marker locations matrices and the n fiducial marker locations matrices (Figure 5.3).

²For fields of view of that size, errors introduced through monochromatic aberrations are negligible^[222].

³This software can use fiducial markers or cross-correlation methods^[232,235].

Apart from the sample marker localisations, the cluster analysis requires the mapping functions for correcting the colour offset⁴. The mapping functions are calibrated for two channels at a time. The input data for that purpose is referred to as the colour correction file. It contains the fiducial marker positions in each colour channel without a colour correction. These positions are obtained from the n fiducial marker localisations matrices with a modified Matlab routine that contains the steps 11 - 18 only. In other words, after tracking and correcting the drift for the fiducial marker locations in step 9, they are submitted to a cluster identification that starts with step 11. The modified routine determines each fiducial's position in each colour channel as the cluster centre of the k positions a fiducial appears in in the k images per colour channel⁵.

Step 10 of the sample-processing procedure starts with loading the colour-offset file into the non-modified routine. As discussed in Section 1.4 the routine then calibrates the mapping functions using the local weighted mean transformations embedded in the “fitgeotrans” function of Matlab. It infers the translation, rotation and scaling necessary to superimpose the position data matrix of the fiducial markers of one colour channel onto the position data matrix of the fiducial markers of a reference channel with minimum residue. The function requires at least six beads evenly distributed in the respective field of view, while twelve is recommended^[378].

Cluster identification. Next, the possible origami objects are identified. For that purpose, the routine searches for locations in a field of view, where sufficiently dense clusters of marker signals occur in all channels and in close proximity. As a starting point, step 11 combines the sample marker locations of all colour channels in one image. In step 12 the user is asked to set values for four parameters that will be utilised in the following steps. These parameters are (CIP stands for clustering parameter, FP for filter parameter):

CIP 1 2D binning pixel size
 CIP 2 event threshold for the binary image
 CIP 3 size parameter of structural element
 FP 1 colour thresholds for each colour channel.

In step 13, a grid of square containers, i. e. binning pixels, is superimposed onto the merged image of step 11. The edge length of a square binning pixel is the 2D binning pixel size (step 12, CIP 1) in nm. The merged image is treated as a single channel binary, and all marker signals are binned into the square binning pixel containers. For binning pixels with signal counts equal to or above the event threshold for the binary image (step 12, CIP 2), an image dilation is performed in step 14. The image dilation here is performed with a yet another square as structural element, whose edge length is given in number of binning pixels sized as described above. The number of binning pixels is defined by setting the size parameter of the structural element (step 12, CIP 3). If CIP 3 is set to five and the 2D binning pixel size CIP 1 is set to 50 nm, for example, a dilated area will be 250 nm x 250 nm and in its centre the binning pixel that initially met the requirement of the event threshold for the binary image (CIP 2) will be situated.

Cluster filtering. The dilated areas contain the initial set of clusters. As the cluster identification parameters are generous, filtering needs to separate noise from origami objects in the following. In step 15, the first of four filters of the routine is applied, which is the colour threshold filter. For that purpose, the colour information of the signals is considered again. For each initial cluster, the number of signals from one colour channel is compared to the respective colour threshold, which was set in step 12 (FP 1). Only those initial clusters with signal counts above the thresholds in all colour channels pass on to step 16. Here, filter 2 and filter 3 are applied, which are a size filter and a shape filter. The values for FP 2 and FP 3 are hard-coded into the Matlab routine prior to running it. The shape filter

⁴As described in Section 5.2, the colour offset for the microscope used here, for example, lies in the range of 50 - 100 nm in the x - and y -direction, respectively. This is already in the size range of the target distances, and must be corrected.

⁵For imaging the multicolour origami barcodes, Lin *et al.*^[213] have used a similar principle.

dismisses single colour point clouds that diverge strongly from a circular shape, as the localisations are expected to display a Gaussian distribution around the point cloud centre. To apply the filter, the cluster centres are calculated first. Their xy -coordinates result from calculating the mean x - and y -values of all marker localisations of that colour in that cluster. The standard deviations s_x and s_y for the x - and y -coordinates are calculated next. The shape filter sets an upper and a lower threshold to the ratio $\frac{s_x}{s_y}$, which is referred to as eccentricity in the following. That is because the closer the setting is to $[1; 1]$, the more the cluster should resemble a circle.

The cluster centres will be referred to as marker positions in the following, and their Euclidean distances as marker distances. The size filter sets thresholds to the marker distances.

In step 17, all valid clusters are presented to the user as the fourth and final filter instance (FP 4). This serves the purpose of eliminating any clusters that have met the other filter criteria by chance. The user filter introduces a subjective element. Whether it biases the result or whether adjusting the other filter criteria can render it obsolete will be discussed in the Section 5.2.3.

In step 18, the target values are determined in the valid clusters. For that purpose, the weighted mean cluster centres are calculated. Here, each x and y element in the calculation of the mean is weighted with its uncertainty as given in (5.2).

The target value data for each field of view is combined in a summary file. A second Matlab routine sums up the target value data of all the fields of view of a sample, puts out value tables and histograms and calculates the deposition side automatically.

For the experiments with the Tetraspeck beads and the tPads presented here, the three clustering parameters CIP 1-3 and the three filter parameters FP 1-3 were set as given in Table 5.2.

Table 5.2: Settings for the clustering parameters CP and filter parameters FP for the experiments presented. FP 4, expelling faulty clusters by the user, was applied as well. For FP 2 and FP 3, the lower and upper boundaries are given. As shape filter, the eccentricity (ex) is used.

CP 1	CP 2	CP 3	FP 1	FP 2	FP 3
2D binning pixel size [nm]	event threshold for binary image	size parameter of structural element	colour thresholds for each colour channel	size filter [nm]	shape filter
50	6	5	20	0/500	ex: 0.28/3.5

In the origami experiment with considerable background noise (Section 5.2.3), the influence of the parameters settings on the results was discussed by changing one parameter at a time. These settings will be given in Table 5.12.

5.2 Results

In order to characterise the method’s capabilities and its performance with a model origami, three sets of experiments will be presented here. A representative experiment of each set will be discussed in detail. Section 5.2.1 presents the first experiment, which is evaluating the colour-offset correction that the local mapping functions inferred here can provide in the image registration. For that purpose, a flow cell with Tetraspeck beads only is used, so their image data provides the sample and reference dataset at the same time. The quality of their co-localisation after mapping is a measure for the lower distance resolution limit of the method. Section 5.2.2 presents the other two experiments that evaluate two designs of tPads as model origami. In Section 5.2.3, the influence of the colour threshold filter (FP 1), the shape filter (FP 3) and the user filter (FP 4) on the results will be discussed.

5.2.1 Colour offset after mapping

In order to determine the lower resolution limit, that is, the smallest fluorophore distance that can be determined reliably with the method, to evaluate the trueness and to contribute to the discussion of the precision of the method, the colour offset after mapping will be discussed with Tetraspeck beads as the sample. This allows evaluating whether the method is practically suitable to characterise origami.

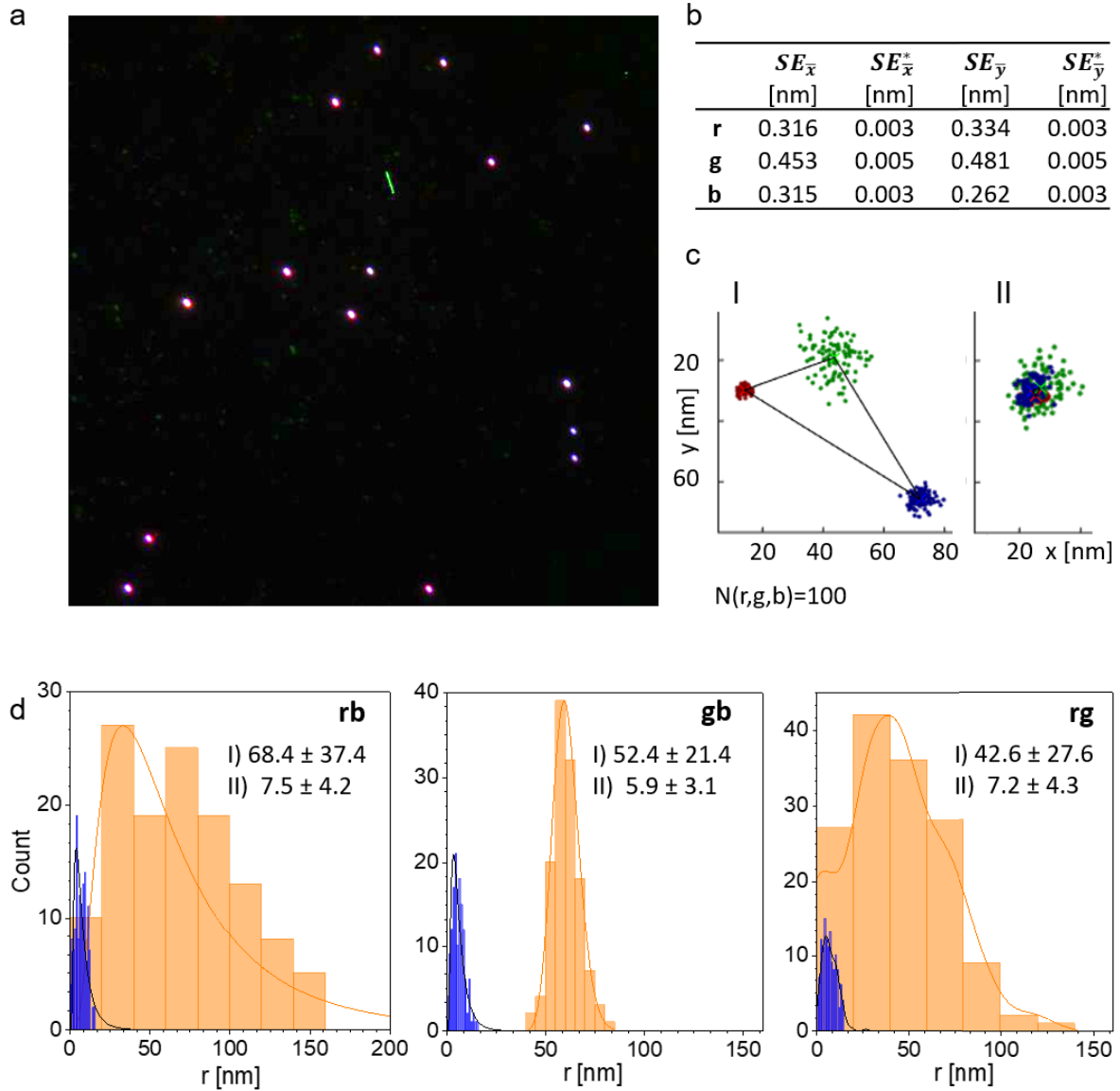


Figure 5.4: Mapping calibration and colour-offset residue with Tetraspeck beads as the sample. a) Field of view with 15 Tetraspeck beads scattered over the area, prior to tracking. This field of view provided the fiducial marker locations for the mapping in the standard origami sample (first mapping). b) Standard errors of the mean prior to ($SE_{\bar{x};\bar{y}}$) and after ($SE_{\bar{x};\bar{y}}^*$) weighting with the localisation uncertainties of the single incidents (for calculation see (5.2), p. 106). c) Registered image of the point clouds (100 single incidents per colour) of a single Tetraspeck bead prior to (I) and after (II) mapping. d) Fluorophore distance distribution for the second mapping for the distances red-blue (rb), green-blue (gb) and red-green (rg) before (orange) and after (blue) mapping. As fiducial marker dataset, the 137 Tetraspeck beads of the mapping in the noisy origami sample were chosen (second mapping). The insets state the means and standard deviations of the distributions before (I) and after (II) the mapping in nm.

Two local mapping calibrations based on Tetraspeck beads will be discussed. They will be referred to as first and second mapping, and they will be used in the standard experiment and the experiment with strong background, respectively (see Section 5.2.2).

The mapping function of the first mapping was derived from a field of view with 15 Tetraspeck beads, which is shown in Figure 5.4a prior to tracking. After tracking (Figure 5.3 step 9), the cluster identification steps 11-17 were used to remove beads that have moved during imaging. In step 18, the coordinates of the point cloud centres $(\bar{x}; \bar{y})^6$ were calculated as weighted means $(\bar{x}^*; \bar{y}^*)$ as given in (5.1). Equation (5.1) augments (1.1) by weighting each fluorophore position in a single image $(x_i; y_i)$ with the inverse of its localisation uncertainties $u_{c;i}$ with $c = \{x; y\}$ to achieve a more precise localisation. As discussed in Section 1.4, $u_{c;i}$ summarises the localisation uncertainties of a fluorophore position in a single image $(x_i; y_i)$ depending on the number of detected photons, shot noise, background noise and pixelation noise, and is calculated during the fluorophore tracking with ThunderSTORM according to (1.2).

$$\bar{c}^* = \frac{\sum_{i=1}^n u_{c;i}^{-1} \cdot c_i}{\sum_{i=1}^n u_{c;i}^{-1}} \quad c = \{x; y\} \quad (5.1)$$

As a result, the standard errors of the mean $SE_{\bar{x}; \bar{y}}^*$ calculated according to (5.2) are two orders of magnitude smaller than the unweighted $SE_{\bar{x}; \bar{y}}$.

$$SE_{\bar{c}}^* = \sqrt{\frac{\sum_{i=1}^n u_{c;i}^{-1} \cdot (c_i - \bar{c}^*)^2}{n(n-1) \cdot \sum_{i=1}^n u_{c;i}^{-1}}} \quad c = \{x; y\} \quad (5.2)$$

Figure 5.4 b lists both values as averages for the 137 point clouds per colour for the second mapping. The values are small, indicating that the localisation of the point cloud centre is precise.

Figure 5.4 c displays the point clouds of all three colour channels of one bead in a registered image before and after applying the derived mapping function. It can be seen that the mapping leads to a considerable decrease in the fluorophore distances.

However, a registration error remains. Figure 5.4 d illustrates this quantitatively. It displays the distributions of the distances of the red and sblue (rb), green and blue (gb) and red and green (rg)⁷ point cloud centres of the Tetraspeck bead before (orange) and after (blue) applying the mapping function. All histograms show unimodal distributions that were fitted with the Gaussian function displayed.

The first mapping calibration was derived from a field of view with 15 Tetraspeck beads. The resulting fluorophore distance distributions before and after the mapping are similar to those resulting from the second mapping calibration, and given in Appendix Figure A.13.

After an ideal mapping, the fluorophore distance distributions should display their global maxima around 0 nm, but that is not the case for any of the six distributions in Figure 5.4 b and Appendix Figure A.13 due to residual errors. Note that the fluorophore distance distributions display the absolute values of distance vectors. The fluorophore distance vectors of the Tetraspeck bead sample after mapping will be referred to as residue vectors \mathbf{r} in the following and their absolute values r will be denoted as residues. It was found that the absolute values and directions of the residue vectors depend on their position in the field of view, but that their variations do not follow global trends, which lines out with previous observations^[223,224]. The medians for all residue distributions lie in the range of 3-5 nm for the first mapping (given in Appendix Figure A.13) and 5-8 nm for the second mapping (see Figure 5.4 d). Including more beads in the mapping calibration, as it was done in the second mapping compared to the first, does not result in

⁶that is, the super-resolved positions of the fluorophores

⁷For better readability, the indices of rg, rb and gb will be mostly denoted in brackets after the symbol instead of in a subscript.

Table 5.3: Mean residues \bar{r} and sample standard deviations s for applying a colour-offset file to a field of view it was not derived from (test errors). The reference residues and standard deviations for the same field of view (training error) are given in the row “ref”. The test errors were derived from a different FOV of the same flow cell (FOV), a FOV on the same flow cell off focus (“focus”) and a FOV from another flow cell (“sample”). All values in nm.

	rb		gb		rg	
	\bar{r}	s	\bar{r}	s	\bar{r}	s
ref	7.5	4.2	5.9	3.1	7.2	4.3
FOV	12.6	6.7	10.8	5.7	12.3	6.3
focus	14.1	9.6	11.8	6.7	13.6	8.7
sample	14.7	6.7	12.8	5.7	13.9	6.3

smaller average residues or standard deviations. Probably, more beads contribute more local variations, which counteracts the decrease of statistical errors.

The mean of the residue distribution that results from the local mapping function was found to increase if the mapping was applied to a field of view it was not derived from. In machine learning, the error after applying a model to the dataset it was derived from is the training error, while applying the model to a new, independent dataset yields the test error. Here, different setups were tested for the second mapping. The test error is larger than the training error, which was expected. In order to evaluate different test setups, the colour correction file has been applied to a different field of view of the same flow cell (setup “FOV”), a field of view off focus from that flow cell (setup “focus”) and to a field of view from a different experiment (setup “sample”). For these setups, rows 2-4 in Table 5.3 list the means and standard deviations of the residue distributions.

For any of the setups the means and standard deviations have approximately doubled compared to applying the colour correction to the field of view it was derived from (setup “ref”, row 1). The setup similar to the experiments discussed in this work is the FOV setup. Its means lie well above 10 nm. The largest mean of ≈ 15 nm, which marks the least precise setup, occurred for the distribution of $r(\text{rg})$ for the setup sample.

The following discussion focusses on to what extent the findings influence how the method can structurally characterise DNA origami. Overall, for the trueness and the precision of the method, one must consider that any fluorophore distance measured on origami involves a residue from the colour offset, which can be up to 15 nm in the experiments discussed here.

Any fluorophore distance can be described as the absolute value d of a vector \mathbf{d} that is, the vector sum of the fluorophore distance vector of the origami according to the design layout, \mathbf{l} , and the residue vector \mathbf{r} of the position where the origami is located in the field of view (see Figure 5.5).

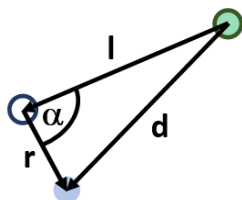


Figure 5.5: Scheme to describe the uncertainty in the fluorophore distance determination introduced by the colour-offset residue vector \mathbf{r} . The detected fluorophore distance d is the absolute value of a vector sum of the fluorophore distance vector on origami according to the design layout \mathbf{l} and the residue vector \mathbf{r} of the colour offset. Here this is shown for the distance of the green and the blue fluorophore. For the markers of the fluorophore positions, a coloured outer frame labels them as true fluorophore position, a coloured filling indicates experimentally determined positions. The green marker features both, as it is taken as a reference point. In theory, the distance l should be measured, but due to \mathbf{r} the experiment provides the distance d .

The angle between \mathbf{l} and \mathbf{r} will be referred to as α . It can assume any value in the interval $[0; 2\pi]$, because the origami is deposited randomly on the flow cell surface. As α is distributed uniformly, the direction of \mathbf{r} does not play a role for the precision or trueness, while the absolute value of \mathbf{r} does.

In the following, two numerical examples are presented of how the colour-offset residue influences the gb distance distribution. Each example considers one of the two mapping calibrations used in the experiments described later. Lining out with the scheme and notation in Figure 5.5, each distance in the distributions was calculated with equation (5.3).

$$d = \sqrt{l^2 + r^2 - 2lr \cos \alpha} \quad (5.3)$$

As stated above, the values for α are uniformly distributed in the interval $[0; 2\pi]$. The values for r are elements of the Tetraspeck beads' $d(\text{gb})$ distributions resulting from the first mapping (Appendix Figure A.13) or second mapping (Figure 5.4), respectively. These $d(\text{gb})$ distributions are depicted again in Figure 5.6 for comparison. Note that these distributions are training error distributions. That is, they will introduce the minimal influence of the colour correction on the trueness and precision that must be expected from the two mapping calibrations.

For the absolute value of \mathbf{l} , the gb distance of the design II tPads, $l(\text{gb}) = 79.5 \text{ nm}$, is taken. In order to get two comparable numerical examples, this $l(\text{gb})$ is used for both of them, although the first mapping is used with the design I tPads (with $l(\text{gb}) = 87.5 \text{ nm}$) in the actual experiments.

As the method is evaluated here, the numerical examples consider only the contribution of the registration error. That is, a constant distance $l(\text{gb})$ is taken here, although in an experiment, the locations of the fluorophores and hence the fluorophore distance l on origami displays a statistical distribution as well.

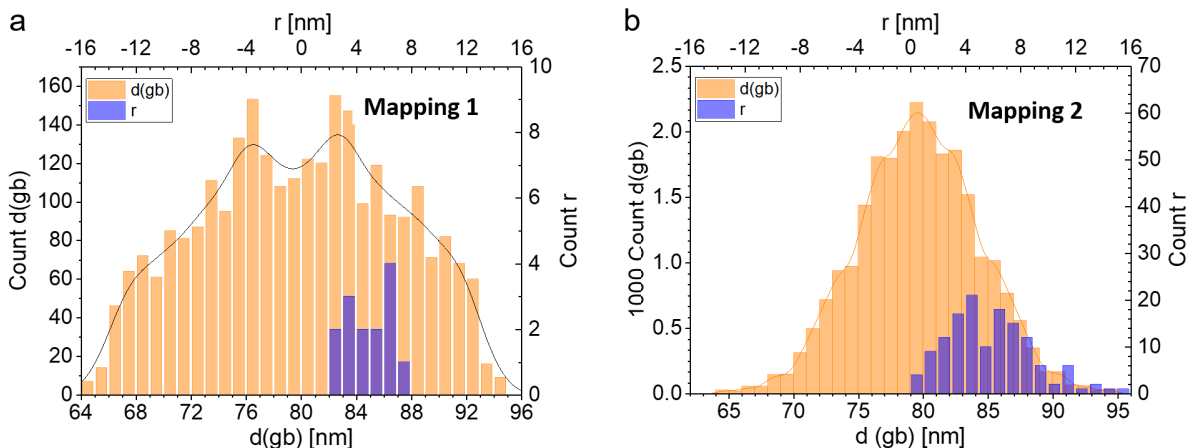


Figure 5.6: Numerical examples of two distance distributions for $d(\text{gb})$ to illustrate their broadening due to the colour offset (orange). Values for d were calculated using (5.3). The true value of $d(\text{gb})$ is $l(\text{gb}) = 79.5 \text{ nm}$. The distributions of the residues r after mapping are given in blue. a) Histogram derived from the first mapping calibration for $n(\text{gb}) = 2714$ based on $n_{\text{TSB}}(\text{gb}) = 15$. b) Histogram derived from the second mapping calibration for $n(\text{gb}) = 24660$ based on $n_{\text{TSB}}(\text{gb}) = 137$.

Figure 5.6 shows the example distributions of $d(\text{gb})$ for both the first (a) and the second mapping (b). Figure 5.6 a plots 2714 values based on 15 Tetraspeck beads, while Figure 5.6 b plots 24660 values based on 137 Tetraspeck beads. Mean, median and experimental standard deviations, as well as the experimental standard deviations of the mean and the 2.5th and 97.5th percentiles (as a robust measure for the width of the distribution instead of the interquartile range) are given in Table 5.4.

For both example distributions the sample size n is large enough to evaluate the trueness of the method by comparing the sample means to the theoretically expected fluorophore distance $d(\text{gb})$. For both distributions the sample means differ from $d(\text{gb}) = 79.5 \text{ nm}$ with an error of 0.14 nm at maximum. That

Table 5.4: Statistics of numerical example distributions of $d(\text{gb})$ derived with the first and second mapping: n = sample size, \bar{d} = mean $d(\text{gb})$, s_{gb} = standard deviation of the sample, $SE_{\bar{d}}$ = standard error of the mean, \tilde{d} = median, Q_1 ; Q_3 : lower and upper quartile, $P_{2.5}$; $P_{97.5}$: 2.5th and 97.5th percentile.

	n	\bar{d} [nm]	s_{gb} [nm]	$SE_{\bar{d}}$ [nm]	Q_1 [nm]	\tilde{d} [nm]	Q_3 [nm]	$P_{2.5}$ [nm]	$P_{97.5}$ [nm]
$d(\text{gb})$ with mapping 1	2714	79.60	3.53	0.07	76.93	79.64	82.34	73.24	85.81
$d(\text{gb})$ with mapping 2	24660	79.64	4.68	0.03	76.49	79.64	82.75	70.66	88.63

indicates a high trueness of the method despite the registration errors.

In order to evaluate whether the error of 0.14 nm stems from a bias, random errors, or both, the method's random errors must be quantified and compared. For that purpose the experimental standard errors of the mean $SE_{\bar{d}}$ for both distributions are calculated and given in Table 5.4. Both $SE_{\bar{d}}$ are in the range of 10^{-2} nm, which is narrow. From the experimental standard errors of the mean the confidence intervals at a confidence level of 99.7% can be calculated as $\bar{d} \pm 3 SE_{\bar{d}}$. For the two distributions, these confidence intervals are $79.64 \text{ nm} \pm 0.09 \text{ nm}$ and $79.60 \text{ nm} \pm 0.20 \text{ nm}$, respectively. For the second distribution, $d(\text{gb}) = 79.5 \text{ nm}$ lies within the confidence interval, while for the first distribution, it lies just outside the interval. This indicates that with a probability of 0.3% there is a systematic error component in the second mapping while this probability for the first mapping is slightly higher. For large sample sizes, this bias becomes more unlikely on the one hand. On the other hand, the error lies in the range of $< 0.1 \text{ nm}$, while lengths on origami here are in the range of 50 nm to 130 nm. Hence, it is negligible. Overall, the method provides negligible bias and a high trueness.

For both distributions of $d(\text{gb})$, the mean and the median coincide, which lines out with the assumption that the distributions are symmetric. The distribution in Figure 5.6 a is bimodal, while Figure 5.6 b displays a unimodal distribution. That is probably because $d(\text{gb})$ and $r(\text{gb})$ in Figure 5.6 b include more values than the distributions in Figure 5.6 a. Both distributions of $d(\text{gb})$ display local maxima that seem to correlate with the maxima in the respective residue distributions. Apparently, the positions of the local maxima exert a more considerable influence on the width of a $d(\text{gb})$ distribution than the largest value of the residue distribution. That is, a mapping function may include higher registration errors without being detrimental for the trueness and precision of the method as long as these values comprise a small share.

In order to discuss the influence of the mapping on the precision, i. e. on how much a single distance can vary from the mean, the widths of the gb distributions must be considered. The width is characterised, for example, by the standard deviation. As can be seen in Table 5.4, for both distributions the example standard deviations lie below 5 nm. In a normal distribution, there is a known relation between the standard deviation and the percentage of values lying in the range of $\pm s_{\text{gb}}$ around the mean. 95.45% of the sample values lie within 2x the standard deviation, for example, which gives a good measure of how much single values will vary. As the distributions here are not normal, an alternative measure is taken based on the 2.5th and the 97.5th percentile as robust estimators for the width. They are considered here to give the range where the central 95% of the data points are situated. That range lies at $79.6 \text{ nm} \pm 6.3 \text{ nm}$ for the first distribution and $79.6 \text{ nm} \pm 9.0 \text{ nm}$ for the second distribution. Apparently, the way the mapping is performed in this multicolour approach introduces a loss in precision, which increases with increasing mean residue values from the mapping. Considering the ranges given above, it can be approximated with 7-10 nm for the test error. This variation of a single measurement from the mean, however, is still considered small for a multicolour approach^[379].

The standard error of the mean is defined as $SE_{\bar{d}} = s/\sqrt{n}$. As evident from this definition and the fact that despite the high confidence level of 99.7% the confidence intervals $\bar{d} \pm 3 SE_{\bar{d}}$ of both distributions lie below $\pm 1 \text{ nm}$ around the mean, the sample size n plays a key role to achieve the high trueness, as it

counteracts the influence of the registration errors. The $SE_{\bar{d}}$ of both numerical examples lie in the same size range despite the fact that for the second distribution the sample size n is approximately ten times that of the first distribution. That is because the residue distribution of the first mapping is less broad and features a lower average residue than the residue distribution of the second mapping to begin with. The sample size n necessary to achieve a desired experimental standard error of the mean can be calculated from the defining equation of $SE_{\bar{d}}$ given above when the experimental standard deviation is given. As discussed above, the numerical examples were derived from residue distributions that introduce the minimal error the two mapping calibrations will cause (training errors). As the values in Table 5.3 suggest, the mappings will introduce larger uncertainties in an origami experiment. To avoid underestimating the resulting errors here, a value according to $\bar{r}(\text{gb})$ in Table 5.3 will be considered as the experimental standard deviation s instead of the s_{gb} of the numerical example for the second mapping. This is thus a conservative approach in determining the method's precision. Looking at the $\bar{r}(\text{gb})$ values in Table 5.3, a residue of 14 nm is taken as a worst case example. In order to achieve a standard error of the mean below 1 nm with $s = 14$ nm, about 196 data points have to be acquired⁸. This is well in the size range of a typical sample dataset, so there is no practical limitation to achieving the trueness theoretically possible for this method.

As discussed before, and as can be seen in Figure 5.6, the second mapping is based on more beads than the first mapping, but contradicting the expectation, it has resulted in a broader residue distribution. Naturally, this has propagated into a broader fluorophore distribution, while using more beads intended the opposite. Apparently, further tests are necessary to see what number of Tetraspeck beads and what distribution pattern in a field of view are favourable for narrow residue distributions.

Overall, the method has the potential to be true and precise. The numerical examples derived from the mappings that will be used in the experiments in the following suggest that with the chosen setup (microscope and local mapping), average fluorophore distances on the origami can be determined accurately. As suggested by the values in Table 5.3, the mapping residues contribute an uncertainty caused by the colour offset r in the range of 10-15 nm to a single distance measurement. Considering the target distances on the origami, this error lies in the range of 15-20%.

Note that the fact that the residue vectors do not lead to a considerable bias here is because the origami is placed randomly. If the origami was oriented, that is, (α) was fixed for each residue vector, a bias determined by the residue distribution will be introduced.

5.2.2 Characterising the structural integrity of origami samples

This subsection describes the application of the method to characterise samples of two different tPad designs. Since the surface of the flow cell for the sample deposition was not furnished with a regular pattern, the tPad evaluation focuses on the structural integrity and the deposition side ratio. The labelling of the two designs will be compared. The fluorophore distance distributions will be compared to the theoretical values. The results presented allow for discussing the method's capability to characterise DNA origami and for evaluating the structural integrity and deposition side ratio of the tPads.

Model of the fluorophore distance distribution

As discussed in Section 5.2.1, an experiment will yield a statistical distribution for each fluorophore distance. The numerical examples in Figure 5.6 have evaluated one factor that influences the broadness, which is the colour offset. In practice, the localisation uncertainties of the fluorophore positions play a role as well. For a single marker the localisation uncertainty stems from fitting the point spread

⁸This does not yet consider the influence of the origami on the distribution broadening.

functions of a fluorophore to the measured intensity distribution^[223]. Therefore, the single marker positions scatter statistically in the k images of a field of view. This could also be enhanced here because the dye molecule is located at the end of the 6 nm link and can move on the origami structure between imaging. In combination, both the colour offset and the localisation uncertainty are propagated into the uncertainty of a fluorophore distance. The following paragraph discusses a model to describe this uncertainty mathematically.

The fluorophore distance distribution can be described as distribution⁹ of the Euclidean distances between two random points in a 2D space (5.4).

$$L = \sqrt{(X_a - X_b)^2 + (Y_a - Y_b)^2} \quad (5.4)$$

In (5.4), L denotes the fluorophore distance, which lines out with the notation in (5.3) and Figure 5.5. The random points form the point clouds $A(X_a; Y_a)$ and $B(X_b; Y_b)$, which are illustrated as large red and green filled circles in Figure 5.7.

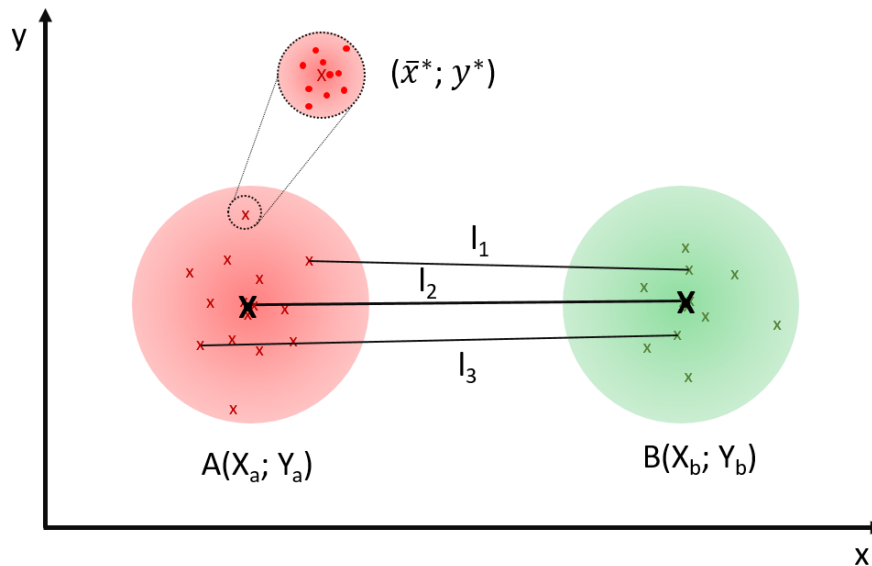


Figure 5.7: Model to derive the distribution of the fluorophore distances. The black Xs mark the true fluorophore positions on the origami. Each red or green x is a point cloud centre that belongs to an experimentally found cluster. For each $x(\bar{x}_a; \bar{y}_a)$ in the red point cloud, there is the corresponding $x(\bar{x}_b; \bar{y}_b)$ in the green point cloud that mark the end points of the fluorophore distance $l(ab)$. For the latter, three examples l_1 , l_2 and l_3 are shown. Above point cloud A, a smaller red point cloud of k red dots around a single red x is displayed. It illustrates that each x is the experimentally determined position $(\bar{x}^*; \bar{y}^*)$ of a fluorophore calculated according to (5.1) as weighted mean of the single fluorophore positions found in the k images of a field of view.

For the model, consider all origami of a sample stacked on top of each other, and aligned according to their theoretical fluorophore positions. Then the point clouds A and B are the hypothetical distributions of experimentally determined fluorophore positions around the true, i.e. theoretical positions of two fluorophores. Figure 5.7 illustrates this: the black cross in a point cloud centre marks the true fluorophore position. Each coloured cross is an experimentally determined fluorophore position of one of the aligned origami of the sample, and it has a corresponding marker in the other point cloud. Figure 5.7 shows three example distances l_1 to l_3 between such corresponding fluorophore positions. Now consider that each experimentally determined fluorophore position, i.e. each x, is a point cloud centre itself that was calculated from the positions of that fluorophore in the k images taken of field of view. In Figure 5.7 such a point cloud of k fluorophore positions around a point cloud centre x is shown as a zoom-in onto

⁹Upper case letters L , X and Y indicate random variables, while the respective lower case letters refer to their realisations.

one red x.

The coordinates of the point cloud centres of A and B , i. e. $X_a; X_b; Y_a; Y_b$ are independent random variables. As there is no restriction in the dye movement, it can be assumed that the point cloud centres are normally distributed around the true fluorophore position¹⁰ and that the standard deviations s_X and s_Y are equal for the same point cloud. Consider that the difference of two normally distributed random variables is a normally distributed random variable as well, therefore:

$$X = X_1 - X_2; \quad X \sim N(\mu_X; s_X^2) \quad (5.5) \quad Y = Y_1 - Y_2; \quad Y \sim N(\mu_Y; s_Y^2) \quad (5.7)$$

$$s_X^2 = s_{X1}^2 - s_{X2}^2 \quad (5.6) \quad s_Y^2 = s_{Y1}^2 - s_{Y2}^2 \quad (5.8)$$

and

$$L = \sqrt{X^2 + Y^2} \quad (5.9)$$

As $s_{X1} = s_{Y1}$ and $s_{X2} = s_{Y2}$, the standard deviations of both random variables are equal and will just be referred to as s .

Again, X and Y are independent. As X has the arbitrary mean μ_x and Y has the arbitrary mean μ_y , there exists a unique $\theta \in [0; 2\pi)$ and ν with

$$\nu = \sqrt{\mu_x^2 + \mu_y^2} \quad (5.10)$$

such that

$$\mu_x = \nu \cos(\theta) \quad (5.11) \quad \mu_y = \nu \sin(\theta). \quad (5.12)$$

Consequently, X and Y can be rewritten as circular normal random variables^[381]:

$$X \sim N(\nu \cos(\theta); s) \quad (5.13) \quad Y \sim N(\nu \sin(\theta); s). \quad (5.14)$$

Thus, L can be considered as a circular bivariate normal random variable with potentially non-zero mean. The probability distribution of the magnitudes of such a variable is a Rician distribution^[380] $R(\nu; s_t^2)$. The variance s_L^2 is

$$s_L^2 = s^2 + s^2 = 2s^2. \quad (5.15)$$

The fluorophore distributions obtained for origami should yield Rician distributions with ν equal to the fluorophore distances according to design. For the tPads $\nu \approx 80$ nm, and for large ν such as these, the Rician distribution can be approximated as a Gaussian distribution^[380].

Overall, the model suggests a Gaussian distribution, or in broader terms, a bell-shaped curve, for the fluorophore distance distributions. For the broadness, the localisation uncertainties and the colour offset play a role (see Section 5.2.1). It was demonstrated that the colour-offset residues broaden the fluorophore distance distributions symmetrically (see Figure 5.6). As a result, the distances are not necessarily normally distributed; however, a symmetric distribution is expected.

¹⁰Actually, Figure 5.7 depicts sample means, i. e. the point cloud centres, dispersed around the population mean, i. e. the true position of a fluorophore on a tPad. Thus, the point cloud centres are distributed normally around the true marker position, while in the point cloud of a single fluorophore, the emission incidents are not necessarily normally distributed. A distribution of sample means around the population mean is usually described by the Student's t -distribution. For large sizes n of the samples, typically for $n > 30$, the t -distribution can be approximated as a Gaussian distribution^[380]. As for this method, $n \geq 100$, this assumption is valid here.

A measure of the broadness will be the overall uncertainty of the fluorophore distance measurement s_d . To derive an expression for s_d , a propagation-of-error formula^[366] was derived from (5.3). The stepwise procedure is given in Section 2.7.2. Equation (5.16) states the resulting expression. As can be seen, the actual fluorophore distance l and the uncertainty introduced through the colour offset in the form of the residue r are relevant variables for calculating d . Furthermore, an uncertainty of the residue ∂r , and a localisation uncertainty ∂l are propagated into s_d .

$$s_d = \sqrt{\frac{(\partial l)^2 \cdot (l^2 + r^2 \cos^2 \alpha) + (\partial r)^2 \cdot (r^2 + l^2 \cos^2 \alpha) + l^2 r^2 \cdot (\partial \cos \alpha)^2}{l^2 + r^2 - 2lr \cos \alpha}} \quad (5.16)$$

In order to calculate numerical examples for s_d for the two experimental datasets presented here, Table 5.5 lists the components and the resulting s_d for $d(\text{gb})$ for the first mapping with design I and for the second mapping with design II. The localisation uncertainties ∂l in (5.16) are the average weighted localisation uncertainties s_l^* of all $d(\text{gb})$ measurements for the standard sample and the noisy sample, respectively. For l , the gb distances according to the designs are used. For r , the respective mean residues \bar{r} of the first or second mapping are taken. For ∂r , the standard deviations s_r of the respective mapping residue distributions are taken. Both \bar{r} and s_r are doubled compared to the values given in Figure 5.4 and Appendix Figure A.13 to account for the fact that in the experiments, the mapping calibration is derived from a field of view the samples distances are not derived from (see discussion in Section 5.2.1.).

Table 5.5: Total fluorophore distance uncertainties s_d for the distance $d(\text{gb})$ of the two experiments with tPads calculated according to (5.16). The experimentally determined values for \bar{r} , s_l^* and s_r were used. The value for \bar{r} and s_r are doubled compared to Figures 5.4 and A.13 to account for the fact that the sample will not be derived from the same field of view as the mapping calibration. The values for $\overline{\cos \alpha}$ and $s_{\cos \alpha}$ were calculated as given in Section 2.7.2.

	l	s_l^* [nm]	$2 \cdot \bar{r}$ [nm]	$2 \cdot s_r$ [nm]	$\overline{\cos \alpha}$	$s_{\cos \alpha}$	s_d [nm]	$3 \cdot s_d$ [nm]
design I	87.50	0.17	9.32	3.64	0.64	0.71	7.49	22.48
design II	79.50	0.12	11.73	6.19	0.64	0.71	10.13	30.38

It becomes evident, that the uncertainty introduced through the colour-offset residue r contributes most to the overall localisation uncertainty. The value $3 \cdot s_d$ given in Table 5.5 provides the confidence interval that holds at least 89% of the sample values around the mean (according to Chebyshev's inequality for non-normal distributions^[382]). Due to its smaller mean residue \bar{r} , the mapping in the design I experiment yields a narrower distribution. Yet the values underline that the mapping has to be improved to make the method applicable for single-molecule measurements.

Design I: experimental results

Figure 5.8 displays a zoom into a typical field of view with all colour channels stacked after the colour-offset correction. Clusters with single fluorophores as well as two or three fluorophores are visible. The clusters are separated well. It can be assumed that clusters with three fluorophores stem from an immobilised tPad¹¹. For a single fluorophore, most point clouds display a circular shape but, in contrast to the Tetraspeck beads, elongated shapes occur as well. In general, considerably less localisations form a cloud. As the flow cell surface is not structured, the orientation of the origami on the surface is random, and a preferred orientation introduced, e. g., during the sample preparation was also not detectable. As the point clouds are localised well, the anchoring of the origami on the surface has worked as expected. In the following, the labelling and the fluorophore distances in that sample will be discussed.

Fluorophore distances and deposition side. For 127 tPads in this sample that were found labelled with all three fluorophores, the target values will be discussed in the following. Note that fluorophore

¹¹The probability of random co-localisations will be discussed in Section 5.2.3.

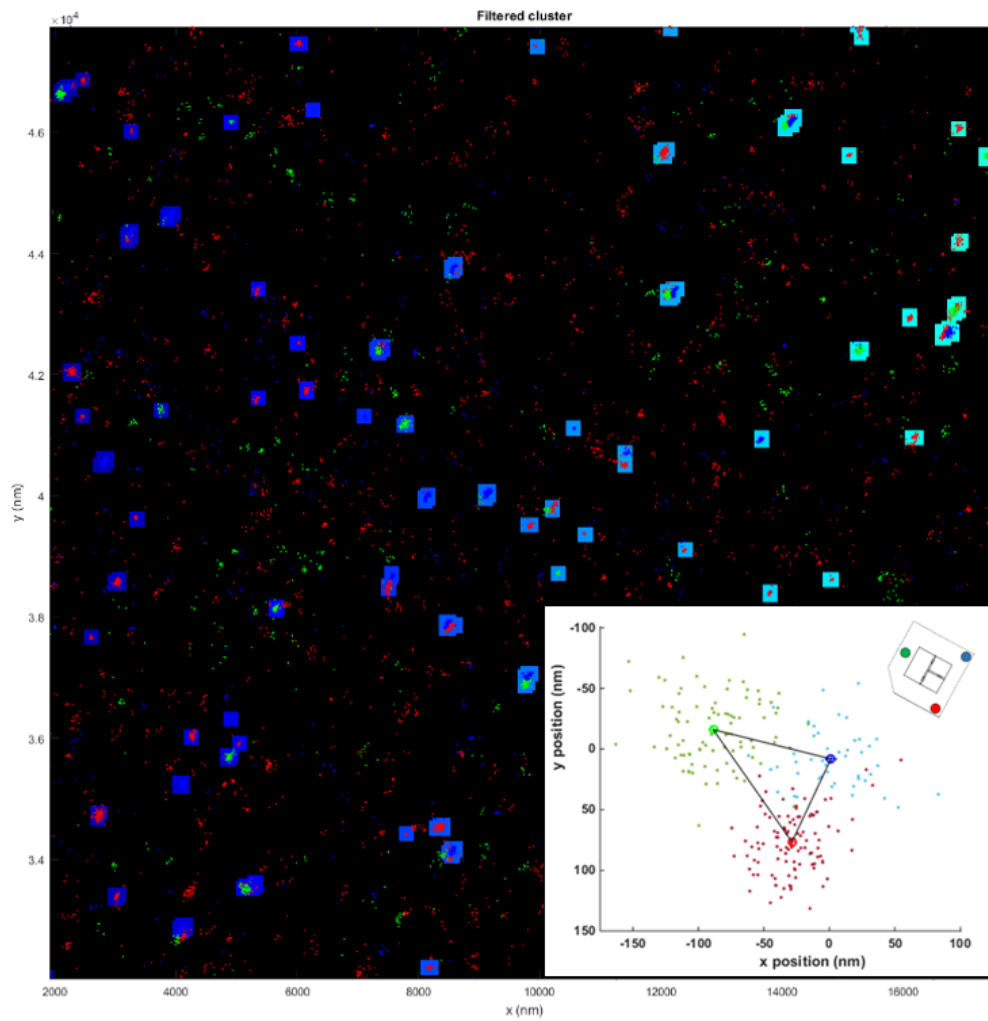


Figure 5.8: Zoom of a typical field of view. Pixel size: 10 nm. The inset shows typical point clouds in the three colour channels that mark a tPad.

distances from two-colour clusters are not part of this statistics. The reason will be discussed together with the random co-localisation (see Section 5.2.3).

Figure 5.9 displays the histograms of the fluorophore distances rg , rb and gb and of the angle θ . For comparison, the theoretically expected values are given as dashed black lines.

All fluorophore distances yield statistical distributions. For all of them, the mean and median, given as continuous and dashed blue lines in the histograms, lie below the theoretically expected distances. Furthermore, the distributions are broad, with minimum values < 10 nm and maximum values > 200 nm¹². All of them display a global maximum and a tailing to the right (positive skew).

By design, $\theta = 53.7^\circ$. Figure 5.9 d displays its distribution and denotes the mean and median. While the mean is close to the theoretically expected value, the median accounts for the tailing of the distribution and appears to be the more representative statistic. There are single values from 0° to almost 180° .

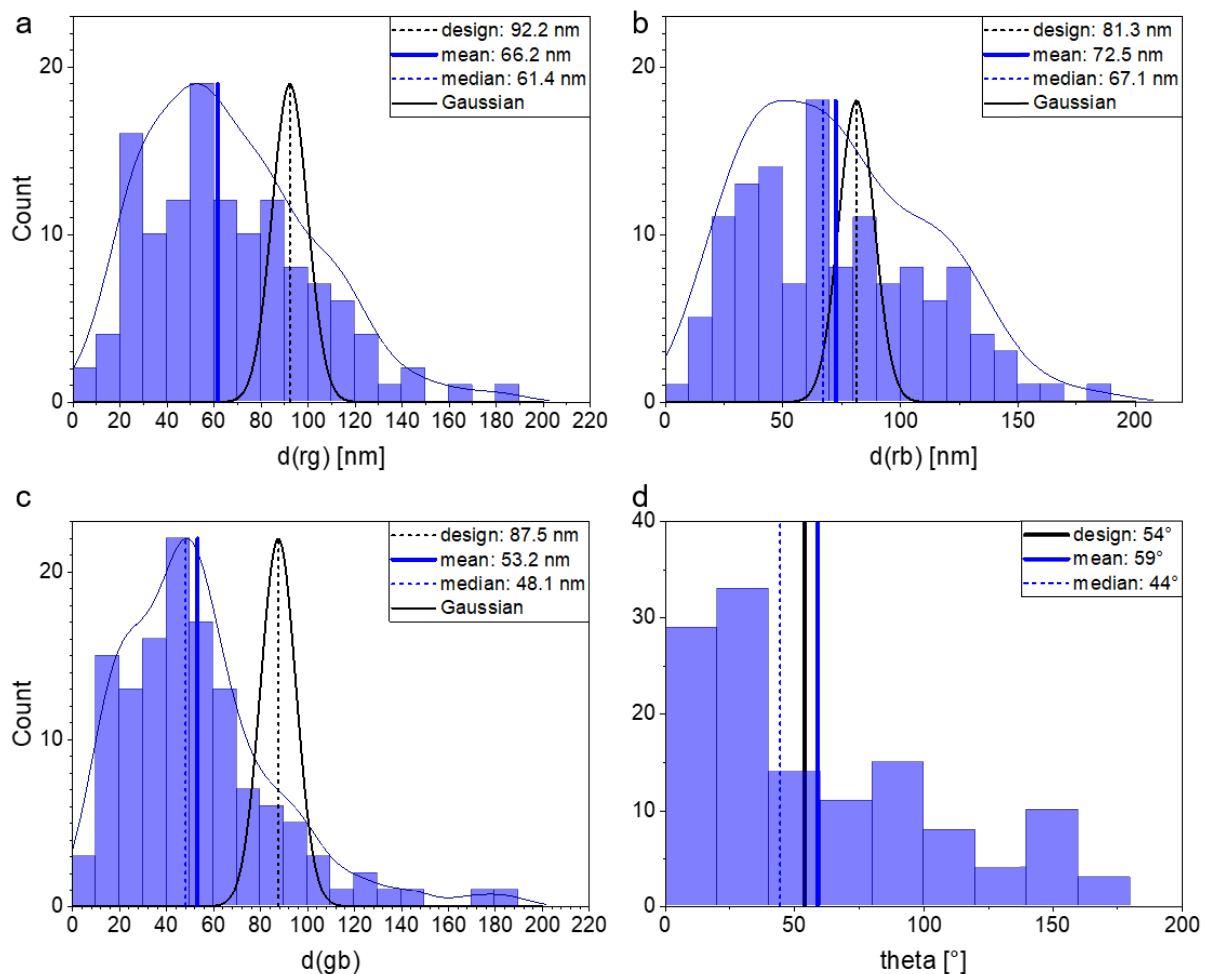


Figure 5.9: Distributions of the fluorophore distances a) red-green (rg), b) red-blue (rb) and c) green-blue (gb) as well as of d) the gbr angle θ for a standard, design I tPad sample. Black dashed lines mark the values according to design, continuous and dashed blue lines mark the experimental mean and median, respectively. Gaussian bell curves (black) illustrate the fluorophore distribution theoretically expected. They account for the mapping residue and statistical variations in the fluorophore positions. The experimental fluorophore distributions display kernel density fits (blue curves).

Comparison of distance model and experimental data. In the Figures 5.9 and 5.12, Gaussian bell curves with maxima at the design fluorophore distances and s_d as given in Table 5.5 are added to the experimental $d(gb)$ distributions (black curves). They illustrate the expected distributions that include a broadening according to the model. However, the distributions found experimentally are not Gaussian or at least symmetric.

¹²Note that in the cluster filtration the size filter was set to 500 nm. That is, the filter did not affect the maximum.

Table 5.6: Fluorophore distances in design I tPads labelled with all three fluorophores. a) Absolute number and proportion of tPads with 1, 2 and 3 fluorophore distances within $\pm 3 s_d \approx \pm 22$ nm of the designed distance. The total number of tPads is 127. b) Absolute number and proportion of measured distances rb, rg, and gb within ± 22 nm of the designed distance in the 127 tPads.

a)	3	2	1	b)	rb	rg	gb
n	2	32	43	$n(exp)$	47	41	25
n_{rel} [%]	1.6	25.2	33.9	$n_{rel}(exp)$ [%]	37.0	32.3	19.7

On the one hand, these findings can stem from methodical errors. The distributions could include too few values. Furthermore, errors in determining the Euclidean fluorophore distances can occur when the imaged dyes were not always in focus^[220].

On the other hand, the skewed distributions can display the actual state of the tPads. Probably, not just intact tPads contribute signals, but several ill-shaped tPad subsets are present with fluorophore distances that differ from the design value. A hint into that direction is given by the width of the distribution. If one compares the expected Gaussian distributions to the experimentally found distributions, the latter are significantly broader. Another strong argument in favour of this assumption is that the tPad disintegration due to issues with the structural integrity was already observed by AFM (see Section 3.1.3). Furthermore, assuming that ruptured tPads and tPad fragments are present lines out with the images displayed in the user filter step, and the cluster count.

The subset that is relevant for the three-colour cluster count and thus for the experimental distributions is ruptured tPads¹³. These tPads display a full cut through the origami frame, but contain all the material of a tPad, that is, also all three fluorophores. In ruptured tPads, the fluorophore positions are less correlated, as tPad parts can move relative to each other. As this results in a range of possible fluorophore distances instead of one expected value, the resulting distance distributions cannot line out with the expected Gaussian distributions.

However, if there is a subset of intact tPads, the expected Gaussian distribution will be present as well. Thus, the histograms can be the result of an overlap of the Gaussian distribution of the intact tPads with the non-Gaussian distribution of the ruptured tPads. It is challenging though to infer further information about the ruptured tPads from the experimental distributions. Ruptured tPads might cause a single non-Gaussian distribution, however, all experimental distributions here display local maxima or peak shoulders. This could indicate that there are several subsets of tPads, which probably occur due to several preferred rupture spots. It is likely that rupture in different spots leads to detectable subsets, as each ruptured tPad provides a different residual structural integrity, which imposes a specific correlation to the fluorophore positions. However, as only 127 values constitute each experimental distribution here, the local maxima probably just occur due to statistic variance and binning.

If the local maxima persisted with increasing tPad number, it would confirm the presence of several ruptured tPad subsets. In order to identify the distributions or clusters they cause, methods like a kernel density estimate or the Jenks natural breaks optimisation might be employed.

In order to provide a quantitative measure for the state of the tPads on the flow cell surface, Table 5.6 a summarises how many tPads (that are labelled with all three fluorophores) display one, two and three distances within ± 22 nm ($3 \cdot s_d$, see Table 5.5) around the theoretically expected values.

In total, about 61 % of the tPads display at least one expected distance, and 27 % display at least two expected distances. Only two in 127 tPads, that is 1.6 %, display all three distances as expected. In addition, Table 5.6 b summarises the proportions that meet the expected values for each of the three fluorophore distances. Apparently, the rb distribution contains the most expected values, while the gb

¹³In theory, the disintegration will result in two general tPad subsets, ruptured tPads and fragments. Fragments are parts of tPads, which can have biotin staples as well as one or two fluorophores attached to it. Thus, fragments can be part of the one- or two-colour cluster count. As random co-localisation (see Section 5.2.3) is unlikely to result in three-colour clusters, fragments do not contribute to the histogram.

distribution contains the least. This lines out with AFM images. In the folding and melting studies, for example, the top part of the tPad that bears the blue and red fluorophore proved to be resilient as well. Overall, all distance yields lie in the same size range. The broad histograms with maxima not coinciding with the expected fluorophore distances and the numbers in the Tables 5.6 a and 5.6 b suggest a poor state of the tPad on the flow cell bottom. Comparing the numbers mentioned above to the yields obtained by AFM (10-40% intact after filtering), the sample ranks among the lower values in the yield range.

Note, that the yield of tPads with all three fluorophores in the expected size range is not directly comparable to the AFM yield. Both yields are biased, that is, in both experiments only subsets of the tPads present in the images were considered. The subsets are similar, but not necessarily the same. For AFM, only freestanding tPads were evaluated. That is, in the aggregates that were also present in the images, tPads were not counted as they could not be distinguished from one another. In the fluorescence microscopy, labelling insufficiencies induce that the number of tPads with all three fluorophores in the expected size range includes neither the absolute number of intact tPads nor the total number of tPads on the flow cell surface. It is possible though that fluorescence microscopy might still include more broken structures from the total count than AFM. Another fact that adds to in the poorer yield compared to AFM is that intact tPads were determined manually for AFM, while in fluorescence microscopy, target values had to meet numeric values. This sets stricter quality requirements. Fragments were not considered in either method.

Although the yield determination routine partly accounts for the low yield, there might be mechanisms that lower the yield compared to AFM. There are three main factors. Firstly, in addition to sample filtration, which is the main cause of damage in AFM, flushing the sample into the flow cell could introduce mechanical stress and damage.

A second factor might be the flow cell surface. Neither the presence of anti-biotin antibodies nor F127 damages DNA origami in general. However, the anti-biotin antibodies are up to 5 nm high^[383]. Thus, the surface is more rough than, for example, the mica for AFM investigations. That prevents the tPads from stretching out. AFM involves depositing the origami on a mica surface, which means stretching it out, as the whole origami surface interacts with the mica surface. For the fluorescence microscopy, the interaction of origami and surface relies on a three-point fixation, i. e. on three spots with biotin-antibiotin links. Both the surface roughness and the three-point anchoring of the tPads can introduce a creasing to the origami, so a structurally intact origami would display unexpected fluorophore distances. As there is no comparable effect for the deposition on mica, this might contribute to the low yield. Note that the majority, i. e. 50-80% of the sample distances lie below the given range around the expected values. This supports the creasing assumption and indicates damaged, crumbled structures. Apparently, the range is the same for all structures, so no distance seems to suffer from particular damage. Furthermore, assuming that in the majority of cases, tPad parts are shifted against each other, lines out with the broad distribution of θ .

Thirdly, the deposition behaviour of the tPads might change on the flow cell surface compared to mica, which might shift the proportion of intact structures amongst the deposited origami. An argument in favour of this is that clusters of multiple fluorophores that suggest aggregates as found on AFM images do not occur. Apparently, such clusters are either flushed out or dissolved. Again, the anchoring to the anti-biotin antibodies is a key factor for the behaviour. Probably, fractured or ruptured tPads provide more flexibility in their parts, so they are more likely to attach to a stabilising number of anti-biotin antibodies.

In order to evaluate the influence of the surface more thoroughly, it is recommended to use a more resilient origami as structure under test.

The deposition side of a tPad on the surface can be determined from the direction of the gbr angle θ . This is referred to as circularity. As the origami-anchoring biotin staples are supposed to protrude to one

side, the tPads are supposed to stick to the surface with that side, making gbr clockwise. However, only half of the tPads (about 55 %) follow the expectation. That there is a deviation from 100 % can be due to incomplete binding, as a tPad might lack biotin staples due to filtration or other processing, or biotin staples might lack the biotin, e. g., as a results of a synthesis error. As a main contributor, for 2D DNA origami, the threading of staples^[377] has to be considered. That is that staples set by design to protrude to one side will slip through the origami weave to the other side, if they are long enough. The biotin staples feature a 20 b spacer to introduce more degrees of freedom to the binding and thus to avoid a bottleneck for surface deposition. However, at that spacer length, threading is likely.

Overall, the method indicates that there is more than one subset of tPads on the flow cell surface and that the majority of the tPads does not display the expected fluorophore distances. This lines out with the result from AFM images. In that way, the method proved to be useful to characterise origami in solution qualitatively and quantitatively.

Labelling. In order to evaluate the labelling setup of a tPad design, and to relate the fluorophore signals in a field of view to the structures they represent, the distribution of one- two- and three-colour clusters will be discussed. Figure 5.10 displays the labelling distribution for the 3105 structures found in this experiment. Note that in order to identify these clusters, only the colour threshold filter (FP 1) has been applied yet. To what extent that leads to including non-origami originated structures in the count will be discussed in the following. The background of the flow cell was routinely checked prior to flushing in origami and found to be clean. Columns 3 to 9 (“r” to “rgb”) in Table 5.7 give the cluster count sorted by colour. For the three-colour clusters, the numbers after the size (FP 2) and shape (FP 3) filter as well as after all four filters are given, too (columns 10 and 11). The latter value is the only one that plays a role in discussing the fluorophore distance distribution (see above).

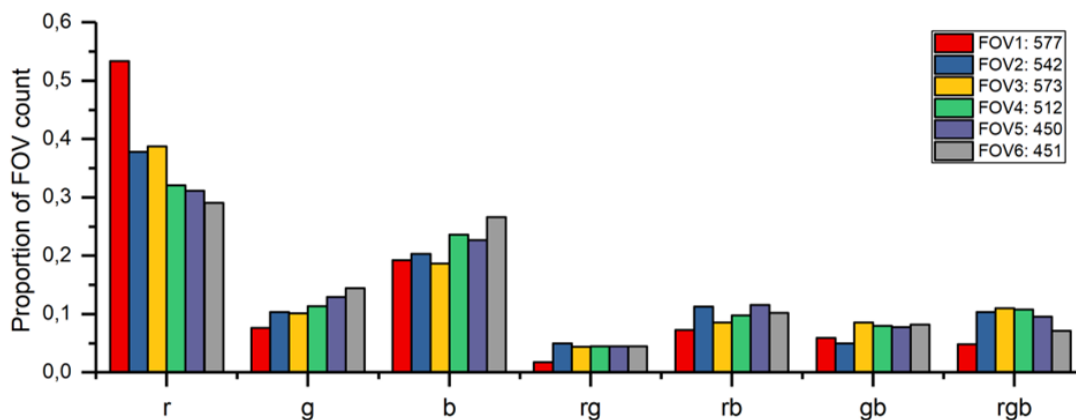


Figure 5.10: Labelling in the standard, design I tPad sample. Ratio of the clusters in six fields of view (FOV) labelled with one to three fluorophores found after applying the colour threshold (FP 1). The cluster type (r, g, b, ...) is given in the x -axis. The distributions of cluster types is similar throughout the sample. Comparing FOV 1 and 6, the Alexa Fluor 660 (red) bleaches the most over time.

Table 5.7: Cluster counts and proportions for the sum of all FOVs of Figure 5.10 after the colour threshold (FP 1), and for the rgb clusters after additional size and shape filters (FP 2+3), or all filters (FP2-4). Most clusters contain one fluorophore. The user had to remove about half the rgb clusters due to ill tracking of at least one fluorophore position.

cluster	after FP 1							rgb after		
	total	r	g	b	rg	rb	gb	rgb	FP 2+3	FP2-4
count	3105	1170	339	671	125	300	223	277	263	127
%		37.7	10.9	21.6	4.0	9.7	7.2	8.9	8.5	4.1

With around 70 %, clusters with one fluorophore represent the largest subset of the labelled structures. Around 21 % display two labels, only around 9 % of the clusters were initially identified as three-colour

clusters. The fact that less than a tenth of the structures are labelled as desired can be due to issues with the labelling, the structural integrity of the tPad (rupture and fragmentation) or with the surface blocking of the flow cell, which as a consequence could not hold off fluorophore ODNs. Table 5.8 summarizes how every type of cluster can occur due to multiple reasons.

If the surface blocking with F127 was insufficient, not just tPads but also fluorophore-carrying ODNs present in solution, for example, due to dehybridisation after filtration or insufficient filtration would sediment onto the flow cell surface. As the tPads are labelled with one fluorophore per colour, an ODN signal does not differ in intensity from a tPad signal, and primarily, the fluorophore ODNs would increase the count of one-colour clusters. In this experiment, however, even an insufficient blocking would not be harmful, because the concentration of fluorophore-carrying ODNs proved to be negligible. That is, the agarose gels of the filtered tPads showed no or faint bands of fluorophore ODNs (Appendix Figure A.14), and ODNs at a concentration close to the gel’s detection limit could most probably not have caused the large subset of one-colour clusters. Furthermore, even if a fluorophore ODN occurs on the surface, it probably sticks less tight than the ones on the biotin-anchored origami. Thus, ODNs might be removed during the flushing step, or their poorly located signal might not meet the colour or the shape filter.

Table 5.8: Overview over structure subsets that can contribute to the colour cluster types. “Intact origami” is well-formed tPads that can still be labelled incompletely. Ruptured origami has a fissure through its structure, while fragmented origami has broken into two pieces at least.

clusters:	1 colour	2 colour	3 colour
intact origami	yes	yes	yes
rupture	yes	yes	yes
fragmentation	yes	yes	unlikely
random co-localisation	impossible	yes	unlikely
fluorophore ODNs	yes	unlikely	unlikely

Two major contributors to the labelling distribution might be the structural integrity of the tPad, or to be precise, the tPad fragmentation discussed before, and the labelling setup for the tPads. Relying on one handle and one fluorophore ODN per colour for labelling requires well-connecting handle-ODN pairs and a high labelling quality of the fluorophore staples. Determining a yield of the pairing on the single-molecule level is challenging. The PA and agarose gels (Appendix Figures A.14 and A.2) proof only qualitatively that handle-ODN-pairs form from staples, and on tPads. Due to their design, neither handles nor ODNs form hairpins or other secondary structures. The melting temperatures of all pairs lie in the range of 59.3 °C to 61.1 °C, which is sufficiently above room temperature to prevent detachment. Thus, the handle-ODN-pairs seem functional. A major contributor to the labelling insufficiencies is the bleaching. For example, in PALM 30 % of the molecules are reported to bleach before they can be included into the analysis^[199].

Bleaching and labelling quality seem to differ amongst the fluorophores. Figure 5.10 shows the cluster count per fluorophore and per field of view (FOV), where FOV 1 was taken first, and FOV 6 last in the experiment. As can be seen, the red dye bleaches considerably during the experiment, while the number of green and blue localisations per field of view stay about the same. Probably, the quickly bleaching subsets of the green and blue dye molecules have already stopped emitting prior to imaging. Regardless of that, the red signals still outnumber the other fluorophores signals on average. The ratio r : g : b should be 1 : 1 : 1, but on average, it is approximately 2 : 1 : 1.5.

Another issue here would be an effect that will be referred to as random co-localisation. That is that randomly arranged excess staples, fragments or aggregates can form two- or three-colour clusters that meet the filter criteria. This effect will be discussed in greater detail in Section 5.2.3. In this sample and at this stage (without the filters 2 to 4), the number of random co-localisations amongst the two-colour clusters can be up to 25 %. Note that for rgb, this number is 1 % only. Thus, random co-localisation does not affect the fluorophore distance distributions.

The results of the labelling analysis can be summarised as follows: The method revealed the fragmentation and rupture of the tPads after filtration also in the distribution of the one-, two- and three-colour clusters. This finding lines out with the AFM images and the broad fluorophore distance histograms that the method as yielded as well. To the low yield of three-colour clusters, labelling insufficiencies most likely contribute as well.

Evaluating the fragment subsets quantitatively, or gathering the labelling yield for each colour from the ratio of the cluster counts would be interesting. However, as both the bleaching and structural issues of the tPads contribute at the same time in this experiment, it is not possible to distinguish the effects.

Design II: experimental results

Performance compared to design I. Design II was set up primarily to yield more three-colour clusters through a different labelling strategy. The result of multiple experiments was that this could not be achieved. The main reason is the fragility of the tPads. That is, the origami has always fragmented so much that, as for design I, the structural issues of the origami determined the ratio of the one-, two- and three-colour clusters instead of the labelling. The fragmentation also prevented further investigation of the right-angled triangular fluorophore pattern, which was newly introduced in design II to study, e. g., length changes depending on the salt concentration. However, the intensity count of the fluorophore signals roughly tripled, as expected from tripling the number of dye molecules per staple. For experiments with other structures, this aspect should be kept in mind.

Bearing all these facts in mind, an average sample of design II does not provide more findings than the sample of design I discussed before. Thus, an unfiltered sample will be presented in the following to discuss the influence of the cluster density and of method parameter settings on the fluorophore distributions. The parameter settings will be discussed in Section 5.2.3 and the six fields of view included in this sample will provide the dataset for it. First, the sample will be evaluated like the sample for design I.

AFM revealed that the yield of intact structures in the sample presented here was with 6% at the very low end, especially since it was not subjected to the mechanical stress of filtering. Figure 5.11 displays a field of view at the same stage of image processing as Figure 5.8. Comparing these images, the intended increase in cluster density, which is about 6.5 times higher in Figure 5.11, is obvious. Furthermore, the inset in Figure 5.11 gives an impression of the point clouds found. Many of them are more scattered and elongated. This could indicate the presence of fluorophore staples despite the surface blocking, as their abundance in the unfiltered sample makes a deposition more likely. It might also indicate that for this design, the ruptured and fragmented tPads are not fixed as tightly on the flow cell surface as for design I.

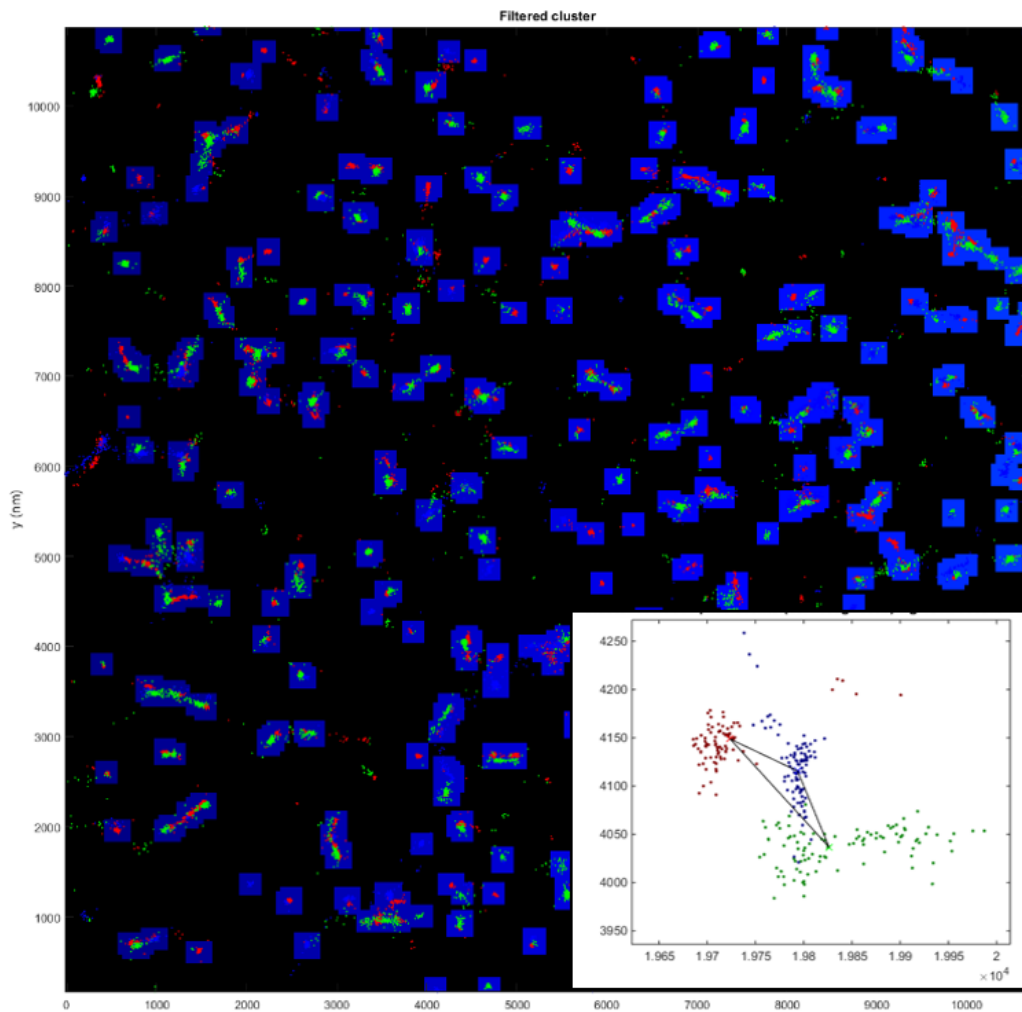


Figure 5.11: Zoom of a typical field of view of the noisy design II sample. The inset shows a three-colour cluster with the widespread point clouds typical of the sample. The green fluorophore is localised poorly.

Fluorophore distances and deposition side. In order to account for a higher cluster density compared to the sample for design I when obtaining the fluorophore distance distribution, the upper limit of the size filter FP 2 was lowered from 500 nm to 250 nm. The other parameter settings were kept as listed in Table 5.2 to not exclude origami in the first place. Figure 5.12 shows the resulting distributions of the fluorophore distances and θ .

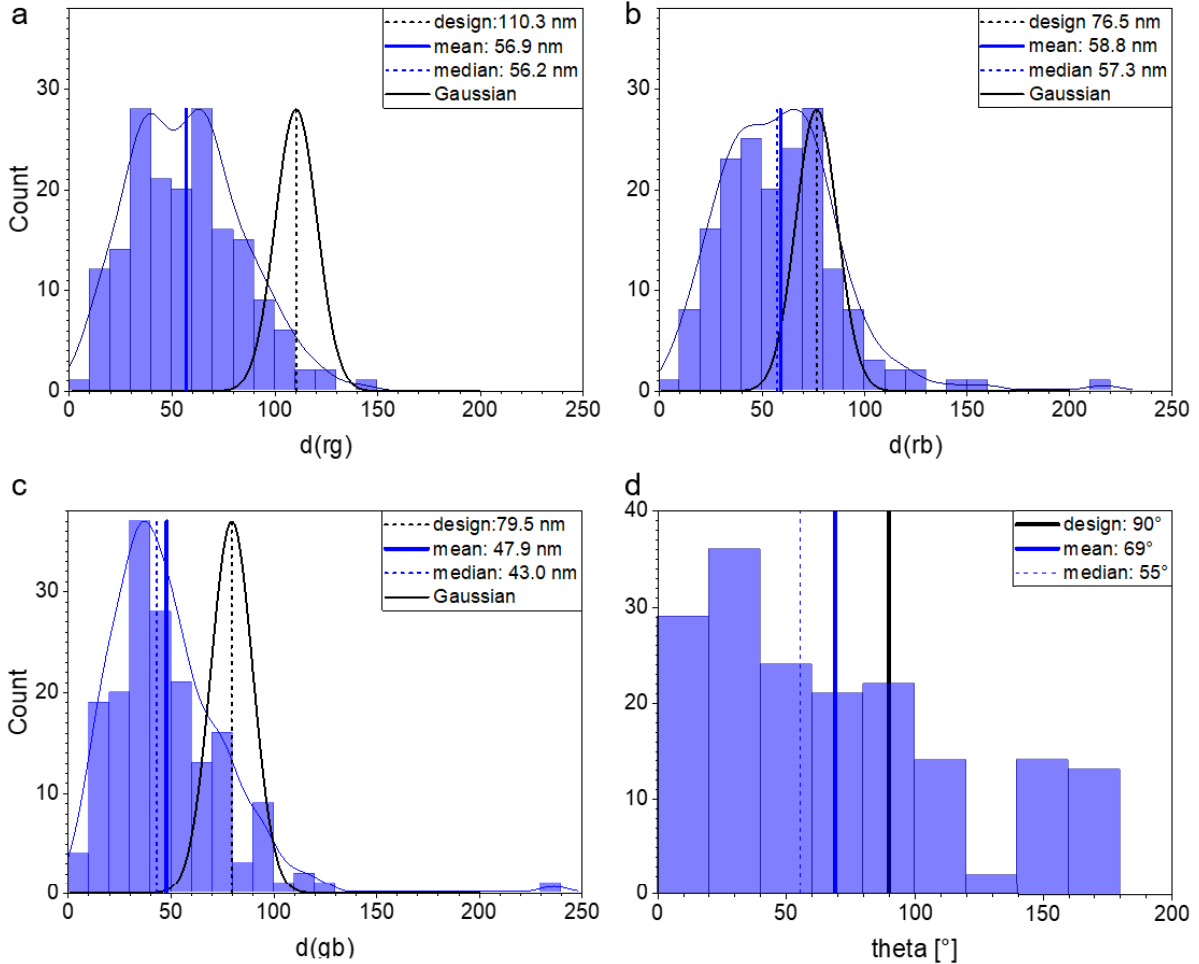


Figure 5.12: Distributions of the fluorophore distances red-green (rg), red-blue (rb) and green-blue (gb) as well as of the gbr angle θ for a noisy, design II tPad sample. Black dashed lines mark the values according to design, continuous and dashed blue lines mark the experimental mean and median, respectively. A Gaussian bell curve (black) illustrates the fluorophore distribution theoretically expected. The fluorophore distance distributions display kernel density fits (blue curves).

As for the sample of design I, the fluorophore distributions are broad, which reflects the fragmentation of the tPads. As for the design I sample, all distributions here display a mean and median below the expected values. Figure 5.12 d shows the distribution for θ and lists the mean and median. The angle θ is supposed to be 90° . As for the design I sample, the distribution is broad and displays values from $0-180^\circ$, with a stronger fraction in the range of higher angle values. Neither the mean nor the median lie close to the expected value, which represents the low amount of intact tPads in the sample. The proportions of tPads with fluorophore distances in the expected range are given in Table 5.9 a and b. In total, 53% of the tPads here display at least one, and 27% display at least two distance value within the expected ranges. These values lie in the same size range as for design I. Regarding the yield of tPads that display three fluorophore distances within design value $\pm 3 s_d$, their proportion increased compared to the sample of design I to 8.6%. Most probably that reflects that the range of valid distances is ± 30 nm here compared to ± 22 nm for the sample of design I tPads. The broadening stems from the larger mapping residue in this sample (see Figure 5.4 and Appendix Figure A.13). Overall, the tPads are not in a better

shape compared to the design I sample.

Table 5.9: Fluorophore distances in design II tPads labelled with all three fluorophores in the noisy sample. a) Absolute number and proportion of tPads with 1, 2 and 3 fluorophore distances within $\pm 3 s_d \approx \pm 30$ nm of the designed distance on 175 tPads. b) Absolute number and proportion of measured distances rb, rg, and gb within ± 30 nm of the designed distance in the 175 tPads.

a)	3	2	1	b)	rb	rg	gb
n	15	32	45	$n(exp)$	103	34	63
n_{rel} [%]	8.6	18.3	25.7	$n_{rel}(exp)$ [%]	58.9	19.4	36.0

Labelling. Figure 5.13 displays the labelling ratio for six fields of view for the noisy sample as it was done in Figure 5.10 for the standard sample. Table 5.10 summarises the cluster count for the 17130 clusters found after FP 1 as well as for the rgb clusters after FP 2 and 3, and FP 2-4.

Because in design II the fluorophores are incorporated into the tPad, binding failure or detachment should not play a role. In contrast to the standard sample, the green labelling was more successful. The distribution of the cluster types is less even throughout the sample than in the standard sample.

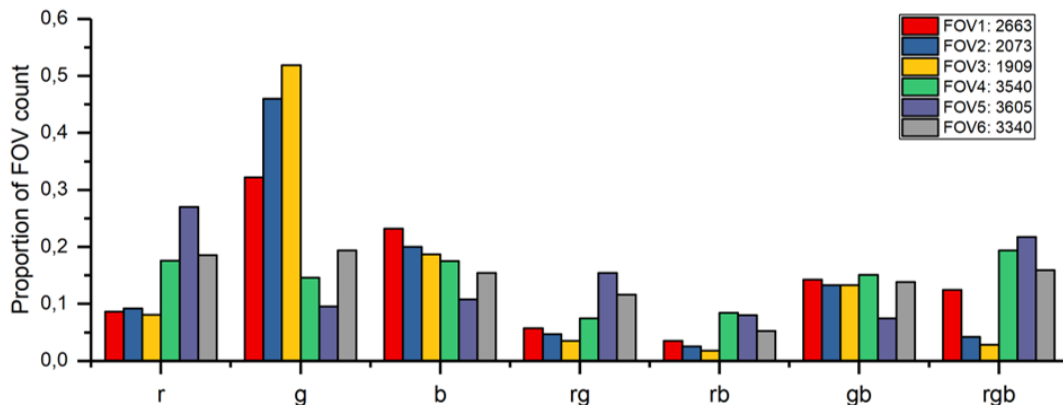


Figure 5.13: Labelling in the noisy, design II tPad sample. Ratio of the clusters in six fields of view (FOV) labelled with one to three fluorophores found after applying the colour threshold (FP 1). The cluster type (r, g, b, ...) is given in the x -axis.

Table 5.10: Cluster counts and proportions for the sum of all FOV of Figure 5.13 after the colour threshold (FP 1), and for the rgb clusters after additional size and shape filters (FP 2+3), or all filters (FP2-4). Again, most clusters contain one fluorophore. The user had to remove about 88 % of the rgb clusters due to ill tracking of at least one fluorophore position.

cluster	after FP 1							rgb after		
	total	r	g	b	rg	rb	gb	rgb	FP 2+3	FP2-4
count	17130	2789	4311	2912	1527	942	2176	2473	1440	175
%		16.3	25.2	17.0	8.9	5.5	12.7	14.4	8.4	1.0

Naturally, one would assume that an increase in fragmentation or not filtering the sample leads to an increase in the one- and two-colour cluster proportions. However, the ratio of one-colour : two-colour : three-colour clusters for the standard sample, 70 : 21 : 9, is similar to the ratio in the noisy sample, where it is 59 : 27 : 14. The fact that the increased proportion of origami fragments in this sample compared to the standard sample does not show can be because ill-structured tPads contribute to all kinds of clusters (Table 5.8). As for the design I, one can assume that there are fragments of tPads that contribute to the one- and two-colour clusters, and ruptured tPads that contribute to the three-colour clusters.

That there is no significant increase in the proportion of one-colour clusters indicates that the surface blocking is effective, and not many fluorophore staples, which do not contain an anchoring biotin, remain on the flow cell surface.

Overall, increasing signal noise by increasing the proportion of fragmented origami and not removing the fluorophore staples is not reflected in the labelling ratio. Thus, the method seems to exclude the noise well.

5.2.3 Reliability and robustness of the multicolour method

As discussed in the previous chapter, the structural characterisation of origami in this indirect method is the statistical evaluation of a set of target values. These statistics could fail to depict the state of the origami on the flow cell surface if they included non-origami or excluded origami. This has to be avoided by thoroughly choosing the clustering parameters and the filter parameters in the method workflow. In order to evaluate the robustness of the method in terms of reflecting the state of the origami on the flow cell surface, random co-localisations at different cluster densities and the influence of the parameter settings on the statistics are discussed in the following.

Random co-localisations depending on the cluster density

As stated in Section 5.2.2, random co-localisation refers to the effect that fluorophores are deposited on the flow cell surface in a way that they form two- or three-colour clusters that meet the filter criteria without being origami. In order to evaluate the chance of misinterpreting a random co-localisation as origami, mixed datasets were investigated. That is, the colour channels of three different fields of view were mixed. As there is no correlation between the signals, analysing these datasets according to the usual workflow (Figure 5.3) should ideally not yield two- or three-colour clusters. Table 5.11 summarises the findings. In datasets named “original”, all three colour channels are from the same field of view, i. e. they should contain two- and three-colour clusters.

Table 5.11: Random co-localisation for different cluster densities before applying filter parameters. In the sample name, “standard” refers to the experiment with design I tPads, while “noisy” refers to the experiment with design II tPads with strong background noise. “Original” indicates that all colour channels stem for the same FOV, while for “mixed” they originate from three different FOVs, a. f. means “after filtration”. Cluster density in clusters/ μm^2 , noisy mixed/standard mixed without unit, all other values in %.

tab:raco	cluster density	1-colour	2-colour	3-colour	3-colour a. f.
standard original	9.7	70.2	20.9	8.9	4.1
standard mixed	13.2	96.4	3.5	0.1	0.05
mixed/original*100	136.2	137.3	16.8	1.1	1.2
noisy original	63.1	58.4	27.1	14.4	1.0
noisy mixed	67.3	73.2	21.2	5.7	0.02
mixed/original*100	106.5	125.2	78.1	39.3	1.9
noisy mixed/standard mixed	5.1	0.8	6.0	60.0	0.4

First, random co-localisation is evaluated in the standard sample by comparing original and mixed datasets. The cluster density in the standard original dataset is slightly lower than in the standard mixed dataset, but both values are in the same size range. As it was expected, the proportion of one-colour clusters increases in the standard mixed dataset, while the proportions of two- and three-colour clusters decrease. However, two- and three-colour clusters were found as well. In order to quantify what percentage of the two- and three-colour clusters in the original dataset could stem from a coincidence, the ratio “mixed/original*100” in percent is given in the table as well. It was found that about 17% of the two-colour clusters found prior to applying the filters 2 and 3 could originate from random co-localisation. However, for the three-colour cluster, that same proportion is 1% only (Table 5.10). That is, random

co-localisation does not affect the number of three-colour clusters.

The second factor to compare is the original noisy dataset to the mixed noisy dataset. The cluster densities for the original and the mixed datasets are in the same size range again. While in the mixed dataset the proportion of one-colour clusters increased and the proportion of three-colour clusters decreased again, the number of two-colour clusters stayed in the same size range. Calculating the same ratios as for the standard sample, about 78 % of the two-colour clusters and 39 % of the three-colour clusters found prior to filtering could be attributed to random co-localisation. Here, the demand for further filtering is obvious. At the end of the filter routine, only 2 % of the three-colour clusters might not be origami. As for the standard sample, that is negligible.

Third, the mixed dataset of the noisy sample is compared to the mixed dataset of the standard sample. The cluster density for the noisy datasets is about five times the density of the standard datasets. Prior to filtering, this caused a sixfold increase in the proportion of two-colour-clusters from 3.5 % to 21.2 %. Amongst the three-colour clusters it caused an increase from 0.1 % to 5.7 %, which is about sixty times. As for the standard mixed dataset, filtering was able to practically eliminate the false findings amongst the three-colour clusters in the noisy mixed dataset. However, there is probably an upper threshold for the cluster density, beyond which filtration might not be capable to exclude random co-localisation.

Finally, the two original datasets are compared. While the cluster density in the noisy sample is 6.5 times the density in the standard sample, the density of three-colour clusters after filtration is only about 1.6 times that high. That is, in the same amount of clusters, only 1/4 of the number of intact tPads are found. That lines out with AFM data.

In all datasets the number of two-colour clusters is two to four times the number of three-colour clusters. In theory, analysing the fluorophore distributions amongst the two-colour clusters would yield further information on the labelling and fragmentation. However, as random co-localisation occurs at such high frequencies, filtration might not be able to compensate this. Thus, the length distributions for the two colour clusters are not presented or discussed for this origami.

The influence of the clustering parameters and the filter criteria

Choosing appropriate clustering and filter parameters has to balance finding all origami, eliminating signals not originating from origami, i. e. noise, as early as possible to make the routine fast, and avoiding biases in the results. To evaluate how parameter changes influence the resulting distribution, the gb fluorophore distance distributions generated from one field of view will be compared upon changing one parameter at a time. In order to evaluate whether a parameter change excludes origami as well, the number of intact structures found will be compared. Intact structures in this context are structures that display all fluorophore distances d within expected ranges ($d \pm 3 \cdot s_d$). Field of view 1 of the noisy sample serves as the FOV under study.

Table 5.12 sums up the settings and Figure 5.14 shows the gb distance distributions.

First, a reference gb distribution and a reference number of intact structures is determined (parameter settings “reference” in Table 5.12). This reference dataset displays the state of the tPads on the flow cell surface in a reasonably correct way. As a measure whether a parameter setting yields the same tPad characterisation as the reference dataset, the number of intact structures and the shapes of the distributions are compared. The numbers of intact origami are supposed to be equal, while the gb distributions should display similar shapes. Variations will occur here because the reference dataset rather allows noise in than that it excludes data that could be intact origami. Of the seven parameters (clustering parameter CIP 1-3 and filter parameter FP 1-4), the binning pixel size (CIP 2), the colour threshold (FP 1), the shape filter (FP 3) and the user filter (FP 4) will be evaluated. That is because they are supposedly the most influential. The size filter was kept at the range of 0-250 nm in all parameter

Table 5.12: Settings chosen to evaluate the influence of the clustering parameters and the filter criteria on the resulting fluorophore distance distribution. The name of the settings is given in the first column. For FP 2, the lower and upper boundaries in nm are given. For FP 3, the two possible types of the shape filter, eccentricity and standard deviation of a point cloud, are denoted as “ex” and “std”; for “ex”, lower and upper boundaries are given.

Setting	CP 1 2D binning pixel size [nm]	CP 2 event threshold for binary image	CP 3 size parameter of structural element	FP 1 colour thresholds for each colour channel	FP 2 size filter [nm]	FP 3 shape filter
reference	50	6	5	20	0/250	ex: 0.28/3.5
1	25	6	5	20	0/250	ex: 0.28/3.5
2	50	6	5	45	0/250	ex: 0.28/3.5
3	50	6	5	20	0/250	std 5 nm
4	50	6	5	20	0/250	std 10 nm
5	50	6	5	20	0/250	ex: 0.9/1.1
6	50	6	5	20	0/250	ex: 0.67/1.5

settings instead of varying it. That is because its influence on the distribution is known, which is cutting the resulting distributions at a chosen value.

The initial distribution displays three peaks (“FP4: unbiased” in Figure 5.14). The theoretical gb distance is 79.5 nm. The largest peak lies in the vicinity of that values, and probably contains intact tPads. Given the poor localisation of a considerable proportion of the fluorophores displayed in the probed field of view (Figure 5.11) and the fact that an intact tPad should be about 100 nm x 100 nm in size, non-tPad structures might be included in the two remaining peaks to a higher degree as in the first peak. The number of intact structures in this distribution was three.

Lowering the 2D binning pixel size to 25 nm has resulted in slightly less clusters found. The distribution displays the three peaks of the initial distribution as well, but the first peak has increased while the other two have shrunk. Furthermore, a fourth peak appears as a shoulder before the first. This large peak occurs probably because clusters formerly included in the second and third peak were split and count twice now. In addition to the cluster splitting, the second and third peak decrease because a proportion of the larger clusters is excluded as the area considered as one cluster is smaller than for the reference value. As the percentage of noise is probably higher amongst the larger clusters, decreasing their proportion in the distribution means that this clustering parameter can reduce noise effectively. Nevertheless, the new peak shoulder from the cluster splitting is an artefact. It might be pronounced for this sample, as the stretched outlines of many fluorophore point clouds predispose false cluster splitting. Apparently, there is a minimum binning pixel size, which is set by the size of the origami. Four intact structures were found instead of three as in the reference distribution. Probably, an artefact is introduced here as well. Overall, 25 nm must be considered below the lower limit where the state of the sample is reflected correctly.

Next, the colour threshold was more than doubled. As a result, considerably less structures were found and the distribution displays three flat peaks, roughly preserving the reference shape. The decrease reflects the labelling situation in the tPads. As no intact structure was found, the colour threshold it set too restrictive here. It apparently comprises a powerful filter tool.

For the reference distribution, the size and shape filters did not dismiss many clusters. The stricter settings for the shape filter chosen here result in a distribution as broad as the initial, but without pronounced peaks. The distribution also includes fewer values and only one of the intact structures was found. Apparently, the filter excludes structures effectively, but not noise only.

The shape filter eliminates clusters, i. e. point clouds, by comparing them to an ellipse whose axis ratios are defined by the shape filter settings (see Section 5.1.3). The closer the axis ratios are to 1, the stricter the filter demands a circular point cloud, which is the expected shape. However, the shape parameters used to calculate the axis ratios are a cluster’s projections on the x - and y -axis. That is, depending on their orientation on the sample surface, ill-shaped clusters might meet the filter criteria. As an alternative filter for future applications and as the a last parameter setting presented here, the absolute value of the

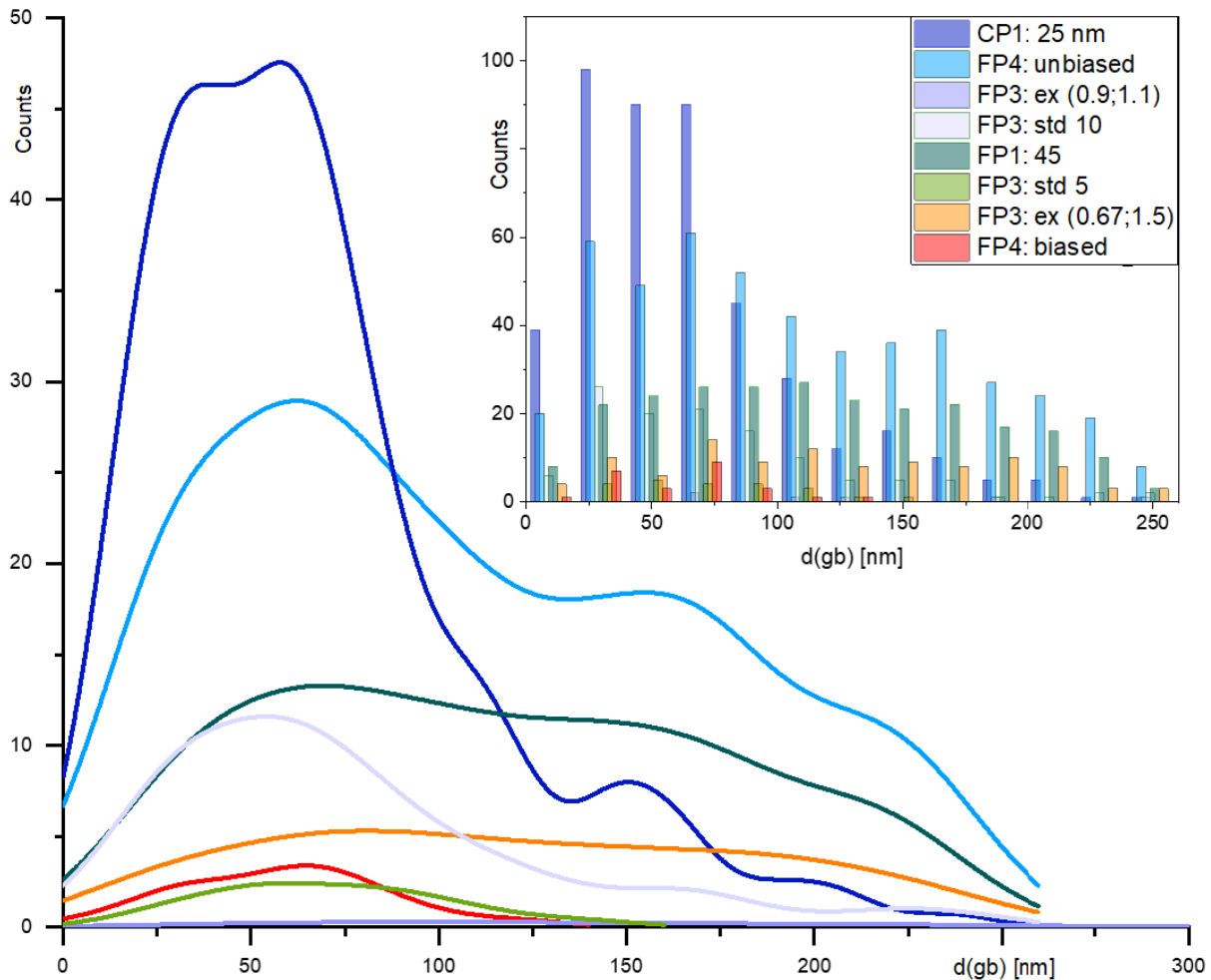


Figure 5.14: Influence of varying the method parameters. Distance distributions of $d(\text{gb})$ that result from using the settings given in Table 5.12.

standard deviation of a point cloud is investigated. In this sample, a standard deviation of 10 nm results in a distribution that keeps the shape of the initial one. The filter has discarded a considerable amount of values, but two of three intact structures are still found. This suggests that, while fine adjustment is still needed, the standard deviation seems a suitable filter tool.

Note that in all parameter settings discussed, the user filtered the remaining clusters appropriately in the final step. That is, they remove obviously faulty clusters. An example of a faulty cluster is given in the inset in Figure 5.11. Here, the green point cloud displays two centres, which could occur due to the moving of the tPad during the scan. It resulted in an unrepresentative mean position of the green fluorophore. However, the user filter is a powerful mean to bias the results. The distribution labelled as “FP4: biased” in Figure 5.14 resulted from the reference settings and the user allowing structures only that they considered as good. That is, a structure would have circular point clouds and display distance values close to the expected values in the tPad. As can be seen, the sample size decreased considerably and the shape of the distribution was not preserved. One intact structure was found. Clearly, this sample is prone to user biasing because of the strong background noise, which generates plenty of oddly shaped structures, which the user will remove.

In order to evaluate the influence of the user in the standard origami sample, Figure 5.15 displays the same distributions as discussed in Section 5.2.2 (see Figure 5.9 a - c) in orange, while the blue distributions were obtained without user filter application. As in the orange distributions the shapes are preserved, the user did not introduce a bias to the standard sample.

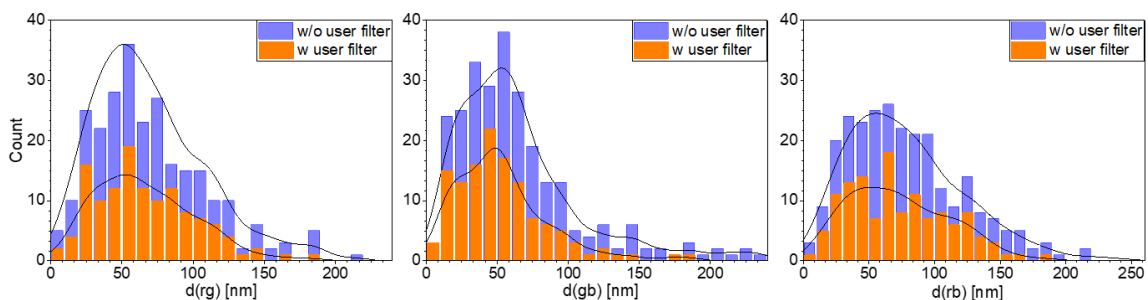


Figure 5.15: Influence of the user filter. Fluorophore distance distributions of the standard sample with (orange) and without (blue) applying the user filter. While the user reduces the total number of structures included, the shape of the distributions remain. Thus, if the user only removes faulty clusters, the result remains unbiased.

For the evaluation of the cluster, the routine presents a zoom-in on each cluster to the user, while it marks the cluster in the image of the FOV as well. For the user to filter reasonably, it is important to consult both images. For a run without the full FOV for consulting, the user approved only 10 instead of 20 three-colour clusters. For the standard sample, Table 5.7 suggests that the number of three-colour clusters is almost kept after the colour, size and shape filters, but it is more than halved after the user filter. A share of the dismissed structures might be tPads, however, the placements of the cluster centres did not represent the underlying structure well. Thus, the user filter was applied correctly and the remaining structures are the most representative for the tPads at the surface.

Overall, the distributions display comparable properties and find comparable numbers of intact structures, unless a bias is introduced by ill parameter choice. Hence, the method realistically and reliably displays the state of the origami on the flow cell surface if it is applied correctly. This includes choosing an appropriate cluster density as well as filter parameters that account for the origami characteristics.

5.3 Summary

Evaluation of the method. Overall, evaluating DNA origami based on the statistical distributions of characteristic target distances and angles between multiple distinct fluorophores has reflected the state of the origami on the flow cell surface in a reliable and true manner. Multicolour labelling has helped to locate origami as a fluorophore pattern and to create unambiguous target values to characterise the structural integrity. The fluorophore patterns created were chiral. Thus, the deposition side of the origami was determined as well, which was a new aspect in super-resolution microscopy-based evaluation of DNA origami.

A key part of the method is identifying the origami pattern in a noisy environment through cluster filtering. Of the three clustering parameters and the four filter parameters the routine provides, the binning pixel size, colour threshold, shape and user filter were varied to study their effect on the result. When setting the parameters within reasonable boundaries, the chance of including randomly co-localising fluorophores into the origami count was lowered to a negligible 1-2%. So far, the routine required the user as final filter to identify clusters that pass the other filters but do not represent an origami structure. This has seemingly left a considerable influence on the resulting fluorophore distribution to the user. However, if they only remove the obviously faulty clusters, the results will appear unbiased.

For any target distance, the registration error in combining positions from different colour channels has appeared as the main contributor to the loss in accuracy. While the registration error did not

interfere with the trueness of the average target value, in introduced an uncertainty of 10-15 nm to a single distance measurement. This value only considers the contribution of the registration error without the statistical localisation uncertainty of determining the fluorophore positions. The range is still considered precise^[379], but it limits the method in terms of evaluating single distance measurements. When including the uncertainty of the fluorophore localisation, the overall uncertainty of a distance measurement was determined in the range of 20-30 nm. Thus, the smallest distance of two fluorophores that can be determined, i. e. the resolution limit of the method with this setup, lies in that range.

Evaluation of the tPad designs. The tPads were found to readily anchor on the flow cell surface. In line with the yield in AFM, tPads appeared as a fragile origami. The broad fluorophore distance distributions, which displayed central values off the expected fluorophore distance, suggest tPads rupture, and that the fluorophore-bearing parts move relative to each other. For the designs I and II, just 4.1 % and 1.0 % of the tPads with all three fluorophores displayed all three target distances within three sample standard deviations around the expected value. In the cluster count, one- and two-colour clusters have also outnumbered three-colour clusters considerably, and less than a tenth of the structures found were labelled as desired. While the tPad fragmentation has contributed largely to the latter, the labelling rate of the origami was questionable as well. The labelling setup for the tPad employed one handle for attaching the dye and one or three dye molecules per fluorophore position that were present right after the synthesis. The fluorophore attachment did not seem to be the limiting factor here, but bleaching and probably the labelling quality of the fluorophore staples were.

That the tPads were fragile has impeded an attempt to improve the labelling through another tPad design. In the design II, the fluorophore staples carried three dye molecules of the same kind instead of one to counteract bleaching. In addition, they were incorporated into the tPad body during synthesis to prevent any detachment. The intensity count of the fluorophore signals tripled indeed as expected. However, in multiple repeat experiments, the percentage of structures labelled with all fluorophores has never increased, which was due to the disintegration of the tPads.

The disintegration has also prevented using the features of the design II pattern for further structure investigation. The triangular pattern with a 90° angle and the cathodes parallel to the outer tPad edges could have simplified the study of length changes depending on the salt concentration or yield determinations, for example.

Comparing multicolour SRM to AFM. AFM and the presented multicolour SRM method have agreed on the state of the investigated origami sample. In the SRM experiments of this work, the yield of intact tPads was determined as the proportion of three-colour clusters, for which all three target distances were found within three sample standard deviations around the expected value. This measure had the advantage that it excluded random co-localisations. As it excluded tPad fragments, it utilised a tPad subset similar to the one the AFM yield was based on. This allows comparing the qualitative results. While these results are similar for both methods, further work must be directed towards making the quantitative results comparable. For the tPad samples, the yield of intact structures in AFM has exceeded that of the SRM approach by an order of magnitude. On the one hand, this could have reflected a degradation of the tPads during the SRM experiment. The tPads could have been spoiled, e. g., due to flushing them into the flow cell, the enhanced roughness of the deposition surface or a difference in deposition behaviour on the functionalised flow cell surface compared to mica. Furthermore, 2D origami will stretch out on the atomically flat mica surface used in AFM. In the SRM approach, the origami was attached to the flow cell surface in four spots via biotin-anti-biotin links. The functionalisation of the flow cell surface with anti-biotin antibodies introduced a surface roughness of up to 5 nm^[383]. A 2D origami like the tPad could have crumpled here, so a structurally intact origami would have displayed unexpected fluorophore distances. As there is no comparable effect for the deposition on mica, this might

have introduced another bias, and might provide an explanation of the low yield. On the other hand, in the SRM approach, a single value was prone to a registration error in the range of at least ± 10 nm on average just from the mapping calibration, while in for AFM, this error was ± 4 nm (see Table 3.1). Thus, SRM was likely to overlook a part of the intact structures in the first place.

Apart from the labelling and mapping biases, the deposition behaviour of origami on the flow cell surface and on mica will be another point to clarify in future work. It is possible, for example, that the F127-blocking impeded the deposition of aggregates. In fact, clusters of multiple fluorophores suggesting aggregates as they were found in AFM images did not occur. Apparently, such clusters were either flushed out or dissolved.

In general, both methods have their strengths and weaknesses depending on the aim of the analysis. It is advantageous that AFM displays the origami directly instead of relying on labelling. If the latter is not reliable, which was the case in the experiments presented, it will quickly limit the significance of the SRM results.

However, any quantitative evaluation of the sample, such as the yield of intact structures or statistics on designated size values is more feasible, less time-consuming and less prone to human errors when inferred with SRM instead of AFM. That is because the contrast in SRM relies on different fluorescent signals, and thus, is sharper than the height contrast in AFM images. Furthermore, AFM imaging at this origami-weave depicting resolution is usually more time-consuming than SRM imaging.

Overall, the multicolour method has the chance to be as true and precise as AFM, while outperforming it regarding quantitative evaluations.

Chapter 6

Summary and Outlook

6.1 Thesis summary

The overall aim of this thesis was to promote quantitative structure evaluation in DNA origami-based nanofabrication. Two approaches towards this aim were taken:

- (i) introducing semi-automatic particle analysis in high-resolution AFM images based on the FindFoci^[6] plugin of ImageJ^[15] to evaluate the structure of novel hybrids from poly(3-tri(ethylene glycol)thiophene)-b-oligodeoxynucleotide block copolymers and the rectangular 2D origami pegboard “pad” with focus on the attachment yield and the placement of the BCP
- (ii) developing and testing a method that uses super-resolution fluorescence microscopy and the principles of single-molecule high-resolution co-localisation (SHREC)^[219] to evaluate the structural integrity and the deposition side of surface-deposited DNA origami frames “tPad”.

For both AFM and SRM in the context of DNA origami, these approaches were new, and in the proof-of-principle experiments, both methods allowed for extracting unbiased quantitative data for the structures under test. The AFM-based approach was suitable to determine the BCP attachment yield and the BCP distribution on the pad pegboard on an almost single-molecule level. The multicolour SRM approach has compiled the distributions of target values characteristic for the underlying tPad origami as a basis for evaluating the structural integrity and deposition side for a whole sample of several hundred structures at once.

In this chapter, the results presented in the different chapters will be summarised and discussed. In the course of this work, new findings regarding the formation of 2D origami and polymer-DNA origami hybrids have emerged as well. To line out with the aim of this work, these findings will only be reviewed here, and discussed in the summaries of the respective chapters.

Chapter 3 presents the design and synthesis of the two 2D origami pad and tPad. AFM imaging was used to evaluate the synthesis yield and the structure formation. For the cavity-bearing tPads, AFM imaging was also used as the control method for evaluating melting temperature, thermal stability, resilience to mechanical stress during filtration and stacking behaviour. For both 2D origami, the assembled structures have matched the design. While the pads have presented themselves as resilient origami template, the tPads have displayed both a lower synthesis yield and a lower mechanical stability. Therefore, the pads were used as templates in the hybrid formation discussed in Chapter 4, and the tPads as structure under test for the SRM-based structure evaluation in Chapter 5.

Chapter 4 presents the three-step assembly of a novel hybrid of the rectangular DNA origami pad and

1 : 1 diblock copolymers made from a poly(3-tri(ethylene glycol)thiophene) and an oligodeoxynucleotide (ODN). The first step was the synthesis of a water-soluble, amine-functionalised, regioregular head-to-tail P3(EO)₃T via *ex-situ*-initiated Kumada catalyst-transfer polycondensation^[172]. In the second step, the polymer block was coupled to ODN blocks via strain-promoted azide-alkyne click chemistry^[351]. According to the HPLC-based reaction kinetics study, this step has proceeded with a high yield. As DNA component, ODNs with the sliding sequences 18T and 10T, or a specific sequence 20N were used. In the third step, the different block copolymers were attached successfully to three types of pads via sticky-end ligation. The three pad types featured different patterns of sliding or specific handles complementary to the ODNs. For all pad types, the hybrid formation resulted in more than 90% of the pads having at least one BCP attached.

The semi-automatic, quantitative analysis of high-resolution AFM images using the image analysis tool FindFoci^[6] was employed to determine the attachment yield per handle and the positioning of the BCPs in relation to the underlying handle pattern. The analysis yielded a single block copolymer position with an uncertainty of 10-20%. Investigating a statistically relevant number of 44 to 107 block copolymers per pad type, and combining single types of positions into events such as occurrence “on a handle“, or “between two handles” yielded robust positioning results. While each handle was supposed to bind one BCP, 0.33 objects per handle were found at maximum. Apart from the sequence, the handle pattern was identified as an influential parameter for the BCP attachment yield. The yield has benefitted from installing next-neighbour handles at 6 nm distance in the pattern, while steric hindrance wielded by already attached objects could have possibly impeded the attachment at the same time. Furthermore, the attached objects tended to interact. Hints have appeared that π - π -stacking interactions have played a role in that regard.

Chapter 5 presents a novel method based on single-molecule high-resolution co-localisation (SHREC)^[219] super-resolution microscopy that can potentially evaluate the structural integrity, placement, deposition side and orientation of a bulk sample of surface-bound origami. It extracts this information from characteristic patterns of spectrally distinguishable fluorophores that the origami is labelled with. Within the pattern, the fluorophores create target values such as distances and angles. The methods determines the target values to evaluate them by comparing them to the theoretically expected vales. Chapter 5 presents proof-of-principle experiments that evaluate the structural integrity and the deposition side of the DNA origami “tPad”. First, the chapter discussed the quality of the mappings of the three colour channels with Tetraspeck beads as fiducial markers. For origami deposited without a directional preference as it was used in these studies, the mapping did not introduce a bias. However, it added a registration error in the range of ± 10 -15 nm to a fluorophore position. This is still considered precise^[379], but appeared as a large contribution to the uncertainty of the target value determination. The two experiments presented next have used tPads labelled with three distinguishable fluorophores (red, blue and green) as structures under test. While the first experiment used a standard, filtered origami solution, the second experiment used unfiltered tPads with excess fluorophore staples to deliberately create a strong fluorescent background. In both experiment, the method was able to locate tPads. The yield of tPads with all three fluorophore distances red-blue, red-green and green-blue within three standard deviations around the expected value was found to be 4.1% and 1.0%, respectively. The distributions of these target distances as well as of the target gbr angle θ were found to be broader than the registration uncertainty and origami-related statistical variations in the target values could account for. These findings have reflected the structural distortion of the tPad samples and indicated labelling insufficiencies. Furthermore, it was discussed that the method has reflected the state of the origami on the flow cell truly and robustly against human bias, when setting the clustering and filter parameters of the Matlab-based data-analysis routine correctly.

6.2 Discussion and future tasks

The AFM-based approach

The AFM-based approach used one of the most common analysis techniques in DNA nanotechnology to add to the sparsely investigated field of qualitative investigation of hybrids from DNA and organic nanomaterial on an almost single-molecule level. It tackled one of AFM's weak points, which is the time consuming, subjective, manual image analysis.

Quantitative analysis of the attachment yield and the placement of organic nanoobjects in DNA-based hybrids. Among the studies on hybrids from DNA origami and organic functional nanomaterial, the presented work is one of the limited number with in-depth quantitative analyses of the attachment yield and the object positioning.

A class of hybrids comparable to the investigated polymer-origami hybrids are hybrids from DNA origami and proteins. Part of the reports on protein-origami hybrids focus on single-molecule investigations, e. g., for force measurements^[384,385] or to study molecular motors^[386]. These do not need to address the overall hybridisation yield. Studies that discuss proof-of-principle hybrid formation usually provide a yield per attachment site. This is comparable to the work presented here, but usually, the studies rely on the manual analysis of few structures. The studies that are most comparable to the presented system, i. e. studies on the site-specific attachment of synthetic polymers to DNA origami, focus less on the attachment yield per binding site. For the enzyme-directed PANI synthesis on DNA origami, a structure formation yield was not discussed^[12] at all. Most studies provide the proportion of origami displaying at least one attached polymer^[13,14,328,352]. For the *in-situ* atom-transfer radical polymerisation of PEGMEMA¹ on distinct points and lines of a rectangular DNA origami, Tokura *et al.*^[328] have quantified the face-down and face-up deposition of the hybrid structures, but did not quantify the attachment yield. The average heights of the unbound or bound polymers were usually provided as well. Furthermore, several studies have quantified further properties of the assembled structure such as their nanomechanical properties and surface potential using KPFM^[13] or changes in the fluorescent behaviour^[12,14,352]. Evaluating the number of polymer molecules per handle, or how well their position corresponds to the template design, was not focused on. Knudsen *et al.*^[13] discuss the site-specific attachment qualitatively and suggest that more than one polymer molecule can bind to one origami pegboard, however, they do not attempt counting the molecules. In a consecutive study including the assembly of a polyfluorene-DNA polymer on the rectangular origami, Madsen *et al.*^[14] have coarsely classified the polymer binding to a rectangle using the categories “good” and “mediocre”, but again, they did not discuss the number of polymers per rectangle. For construction of a molecular electro-optical modulator from a DNA origami frame and oligomers of poly(phenylenevinylene) and polyaniline^[352], the authors claim a yield of 20 % for the target structure, but do not break down the yield for attaching each polymer on its own.

The basic information on the attachment yield per handle and the site-specificity of the attachment is likely to play a key role when polymers will be used in the current attempts of DNA nanotechnology to assemble functional structures. Thus, this work has presented a working approach for a relevant future topic.

While computational routines have been applied before to evaluate bare DNA origami (AFM^[139], 3D structure reconstruction in Cryo-EM^[387–389]) and the binding of inorganic nanomaterial to DNA origami (TEM^[80]), this work has applied it for the first time to soft and flexible organic nanomaterial on DNA origami. Introducing FindFoci^[6] has made the image analysis less prone to human bias. Thus it has ensured that results from multiple experiments are comparable and significant. However, this semi-automated approach still allows for subjectivity, which needs to be reduced further. A promising

¹poly(ethylene glycol) methyl ether methacrylate

approach would be employing a particle identification routine with quicker and more customised means to separate the signal of interest from the background, even if the height contrast is not incisive. Such routines are probably implemented in commercially available software for evaluating industrial cleanliness. Another approach close to this topic has reported on a potent machine-learning approach to evaluate cells^[390], which could provide another starting point for improving the computational image analysis. Another weak point AFM has to overcome to secure its spot in qualitative analysis in DNA nanotechnology is the long imaging times. Here, high-speed AFMs have emerged as a promising development that does not sacrifice image resolution. As proteins withstand the scanning conditions^[156,368,391], the method might be suitable for the investigation of hybrids of DNA nanostructures and synthetic polymers as well.

The SRM-based approach

The SHREC-based method presented here is one of the few attempts to use SRM for origami quality control. When this thesis was prepared, the single report in this field has utilised 3D DNA-PAINT to structurally characterise DNA polyhedra^[120]. In comparison to the AFM-based approach, automation of the SRM-based approach is more feasible. It can possibly process a larger number of samples as it quickly images a large number of structures and employs computer-based data analysis. That the presented approach does not provide a direct image of the whole structure is not a disadvantage as long as the probed values are fully expressible as a target value in the labelling pattern. Thus, a technique like this is a promising candidate for becoming a standard analysis method. However, the experimental protocol including the labelling setup and the mapping need further improvement to achieve a precision and trueness of the target value determination comparable to AFM and TEM.

Method improvements

Two key improvements to make are decreasing the registration error and improving the labelling. Decreasing the registration error will increase the precision of the method and make it suitable for single-molecule investigations as well. Furthermore, additional care must be taken to avoid significant bias in oriented samples. That is because the trueness of the method as presented here relies on the fact that the fluorophore distance vectors on origami occur in random relative orientation to the mapping residue vectors. At large numbers of origami, this leads to a symmetric distribution of the target values around the true value. In samples of oriented origami, the orientation of the fluorophore distance vectors is fixed. In order to avoid a bias increase in oriented samples, either the sum of all residue vectors in the field of view has to be zero (which can just occur by chance), or the single vectors must be negligibly small. To reduce the registration error, the results presented here suggest introducing the fiducial markers to every field of view with origami instead of determining one mapping function for all fields of view in an experiment. Instead of Tetraspeck beads, a smaller structure such as another origami can be used as fiducial marker to not overpower the fluorescence of the structures under test. Furthermore, the literature suggests several improvements. Pertsinidis *et al.*^[224] found it advantageous to image all fluorophore centroids on the same detector pixel, and that drift image registration will benefit from real-time closed-loop feedback loops. Furthermore, they have reported a better calibration of the mapping function with dye molecules than with beads. This supports the idea to use dye-labelled origami as fiducial markers. To improve the labelling rate, more than one fluorophore staple per position, DNA PAINT and/or quantum dots instead of organic dyes could be employed. While bleaching is inevitable², a DNA PAINT approach does not suffer from it due to the continuous exchange of the fluorophore at the imaged position. However, the multiple flushing steps can lead to less robust, prolonged experiments. Incorporating more than

²For example, for PALM the number of fluorophores that bleach before they can contribute to the data is $> 30\%$ ^[199].

one fluorophore staple into the design introduces the least changes to the presented protocol. It would probably not lower the trueness or precision of the method either. That is because up to four staples can be placed to protrude to the same origami side in a radius of about 6 nm, which is currently in the size range of the precision of a single fluorophore localisation in a registered multicolour image. Using quantum dots would provide a stable signal, but the labelling protocol has to be carefully engineered to provide a high yield. For studies on method improvement, using a more resilient origami than the tPad as structure under test is recommendable. That could be a 2D origami with closed surfaces like the pad, or a flat 3D origami as it was used, for example, in nanopore studies (reviewed by Bell and Kaiser^[392]).

Opportunities for further analyses

Evaluating placement and orientation. In addition to providing the fluorophore distance and the deposition side distributions, the method is capable of extracting the placement coordinates and the orientation for all origami in the sample as well. For that purpose, the coordinates of the fluorophores and the orientations of the fluorophore distance vectors will be evaluated as demonstrated for the fluorophore distances and the deposition side.

Yield determination and quantitative structure information. The quantitative measure for the state of the tPads on the flow cell surface used here is the number of tPads labelled with all three fluorophores that display all fluorophore distances within an expected range. A more general calculation of the yield would be the ratio of the number of intact tPads and the total number of tPads on the flow cell surface. The sample datasets here could not provide these values, because the labelling yield³ and the bleaching ratio⁴ remained unknown. In further experiments, the labelling yield could ideally be improved until being close to 100%, and taken as a constant. The bleaching ratio could be determined with PAGE or HPLC. In case of a patterned surface for deposition, a yield could also be calculated based on the absolute number of places that must be occupied.

With an improved labelling, the ratios of the cluster counts with a certain number of fluorophores, and the distributions of the target values could be analysed with regard to the origami structure, such as preferred rupture sites, or bending. Given sufficiently large sample sizes, fitting probability density functions to the distributions of the target values will aid with identifying structure-specific origami subsets.

Automation, other surfaces and objects under study. The SRM method is probably not limited to specific substrates like AFM and TEM are. Upon adjustment of the protocol, the method might be applied, e.g., to origami on silicon wafers, which can be advantageous with regard to future application in nanoelectronics and nanophotonics. Furthermore, the method is suitable for 2D and 3D origami. For 3D origami, just another fluorophore needs to be introduced.

It is already favourable for automation that a computational cluster analysis allows a fast and feasible quantification of the sample characteristics. Furthermore, it was demonstrated that properly adjusted clustering and filter parameters can eliminate non-origami from the analysed data effectively. In order to make the method completely independent from human bias, the user filter must be abolished. A moderate origami density on the flow cell surface is advisable in that regard. To further reduce noise, other or additional filters can be introduced. If this is not sufficient, the user filter might be kept initially as part of a machine learning processes, and might be abolished once the routine is precise enough.

Although discussed in this context, the method is not limited to origami but is suitable for other structures in that size range that can be labelled accordingly.

³ratio of labelled structures and total structures; per fluorophore

⁴ratio of staples with emitting fluorophores in fluorophore staples after treatment like in origami

The presented approaches have addressed the task of quality control for DNA-based nanostructure formation. Including the topic of quality control, sources agree that the techniques and protocols currently available are not sufficient to acquire a full characterisation of any complex DNA structure^[2,58,75]. Open questions can be as fundamental as accurately measuring the concentration of 100% correctly formed DNA nanostructures^[2] or studying origami assembly kinetics at the single molecule level^[2], and become as complex as structurally characterising DNA nanoobjects *in vivo*^[137].

The results of this work shall encourage the development of more potent analytical tools. Furthermore, this thesis has reported a novel approach to assembling hybrids from conjugated polymers and DNA origami, which can be used in the assembly of DNA-based nanophotonic and nanoelectronic structures.

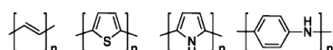
Appendix

Appendix A

Additional images

Introduction

1st generation

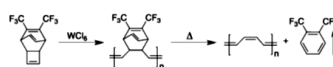


Infusible, insoluble, rigid-rod polymers:

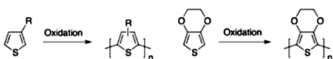
electrochemical polymerisation

2nd generation

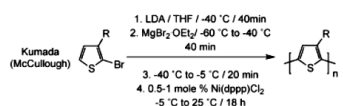
Polymers with better processability:



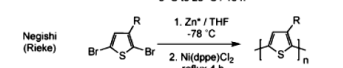
two-step synthesis of polyacetylene from a processable precursor



ROMP synthesis of polyacetylene; one-step oxidation synthesis of processable poly(3-alkylthiophene)s and poly(3,4-ethylenedioxythiophene)

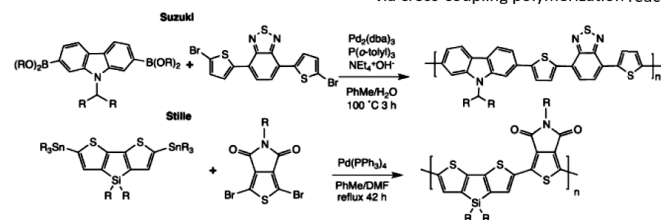


well-defined regioregular poly(3-alkylthiophene)s by metal-catalyzed polymerization methods (after simplification and optimisation this resulted in the Grignard metathesis method (GRIM))



3rd generation

Stable semiconducting (co)polymers with tunable electronic and optical properties via cross-coupling polymerization reactions



Outlook

Pd catalyzed Direct (hetero)arylation polymerisation (DHAP)

Figure A.1: Generations of conjugated polymers grouped according to progress in the synthesis procedures and material properties as suggested by Morin *et al.*^[8]. For each generation, representative examples are given. Adapted with permission from^[8]. Copyright 2016 Royal Society of Chemistry.

Construction and characterisation of 2D DNA origami

PAGE for investigating the hybridisation of the fluorophore handles and ODNs of design I tPads

In order to evaluate the hybridisation behaviour of the specific ODNs and handles involved in labelling design I tPads, the qualitative PA gel displayed in Appendix Figure A.2 was run. Counting from the left, the lanes 1, 3 and 5 contained just the fluorophore-bearing ODNs and the lanes 2,4 and 6 contained the tPad staples with the complementary handles. The lanes 7-9 contained 1:1 mixtures of all fluorophore ODNs and one handle, respectively. Each type of ssDNA was used at a 5 nM concentration. The mixtures were kept at room temperature (RT) for one day. The lanes 10-12 held the same mixtures kept at 45 °C to test the influence of an elevated temperature on the hybridisation. The concentration of a ssDNA species in the lanes 1-6 is not the same as in the lanes 7-12. Hence, the position of the bands are comparable, while their intensities are not. Among the mixtures in the lanes 7-12, the intensities are comparable as well.

The gel was imaged three times prior to staining using lasers and emission filters to image one fluorophore at a time. The images are given in Appendix Figure A.2 a to c. Compared to the bare ODNs and staples in the lanes 1-6, new bands occurred in the lanes 7-12. For each handle, the new band only appears in images that picture the fluorophore that was supposed to attach to this handle. Thus, the gel proves that the hybridisation takes place and proceeds specifically. The band intensities of the RT and the 45 °C appear to be the same, indicating that the chosen temperature does not influence the hybridisation. However, unbound fluorophore ODNs and handles (visualised in the stained gel in Appendix Figure A.2 d) are visible in all lanes as well. This indicates that the hybridisation does not proceed quantitatively. For fluorophore-labelled tPads of design I and design II visualised in agarose gels see Appendix Figure A.14.

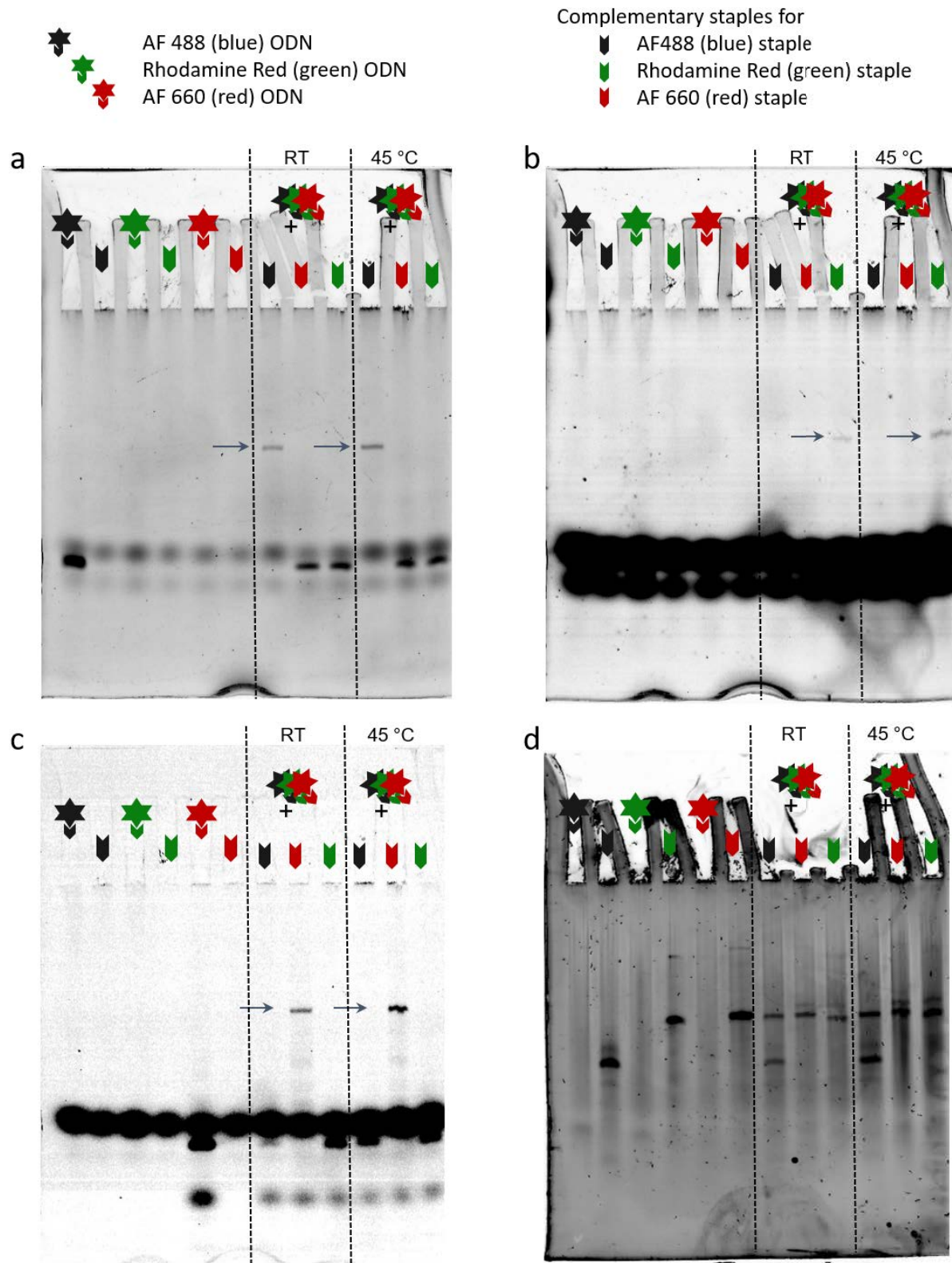


Figure A.2: Hybridisation of fluorophore-bearing ODNs and staples of design I tPads with the complementary handles at room temperature and 45 °C visualised with PA gel. Each of the first six lanes contains one type of the fluorophore-bearing ODNs or the staples with the handles. The samples in lane 7-12 contain all ODN types, but one handle type each. The gel was imaged prior to staining to visualise the positions of (a) Alexa Fluor 488, (b) Rhodamine Red, and (c) Alexa Fluor 660. Black arrows indicate the position of ODN-handle hybrids. As can be seen, each ODN binds its complementary handle selectively. (d) Image of the stained gel.

CanDo images of tPads and the pad

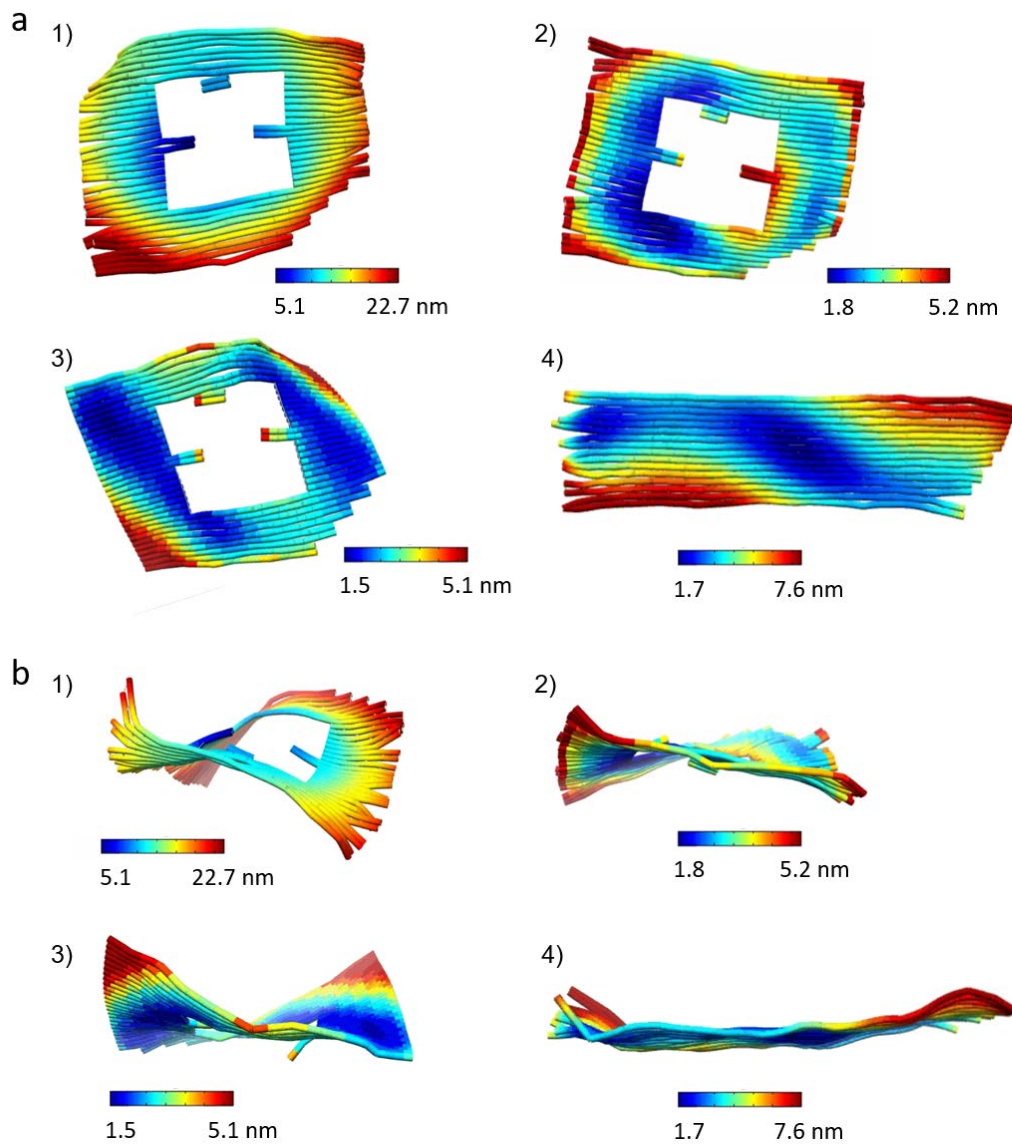


Figure A.3: Model images of origami in solution: a) front view and b) view from the top edge of 1) a non-twist-corrected u-staple tPad, 2) a twist-corrected u-staple tPad (not used in this work), 3) a non-twist-corrected z-staple tPad and 4) the twist-corrected pad. The images were generated using CanDo^[60,61].

Hybrids of P3(EO)₃T and pads

P3(EO)₃T and P3(EO)₃T-b-ODN synthesis scheme

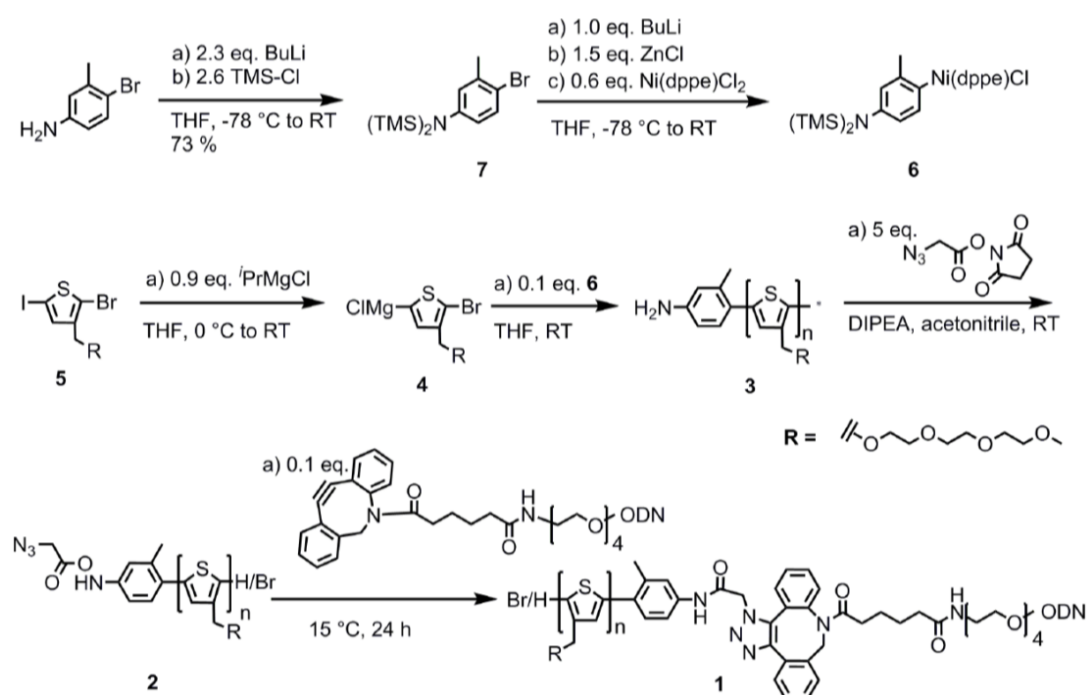


Figure A.4: Detailed reaction scheme of the synthesis route of an azide-functionalised P3(EO)₃T (poly(3-tri(ethylene glycol)thiophene); alternative name: poly(3-2,5,8,11-tetraoxadodecane thiophene)) and its coupling to a DBCO-functionalised ODN via strain-promoted azide-alkyne cycloaddition. (1) P3(EO)₃T-b-ODN, (2) azidoacetic NHS ester coupled to (3); (3) amine-functionalised poly(3-2,5,8,11-tetraoxadodecane thiophene) (amine-P3(EO)₃T); (4) Grignard reagent derived from (5); (5) precursor of the monomer 1-(2-bromo-5-iodothiophen-3-yl)-2,5,8,11-tetraoxadodecane; (6) (4-amino-2-methylphenyl)nickel(dppe)chloride; (7) N-(4-bromo-3-methylphenyl)-1,1,1-trimethyl-N-(trimethylsilyl)silanamine. Reproduced with permission from^[172]. Copyright 2017 American Chemical Society.

Pads with double-stranded handles

As discussed for each pad type in Section 4.1, the ability of the handles to hybridise with their complementary ODNs on the pad was tested. As most of the resulting structural features are delicate, a quantitative analysis as performed with the hybrids could not be conducted. Appendix Figure A.5 shows type I pads after adding 20N ODN. On the 14 handles of line I2 and the four handles of line I3 there are higher structures than on the pad body or the line I1 with 15A handles, which indicates staple attachment. Adding 8T ODNs to enhance the 15A handles in I1 did not result in visible structures. Appendix Figures A.6 and A.7a and b show type II and type III pads after adding 23T ODNs. Appendix Figure A.7 shows type III pads after adding 8T ODNs.

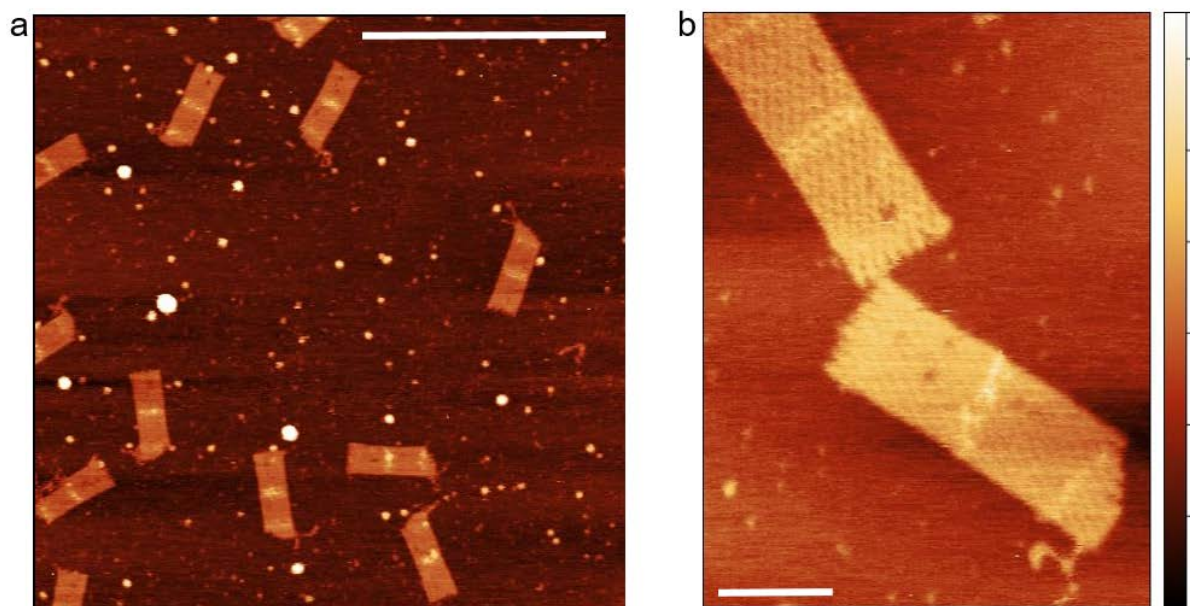


Figure A.5: Type I pads after adding 20N ODNs. Scale bar and height range: a) 400 nm, 0-8 nm; b) 50 nm, 0-6.5 nm.

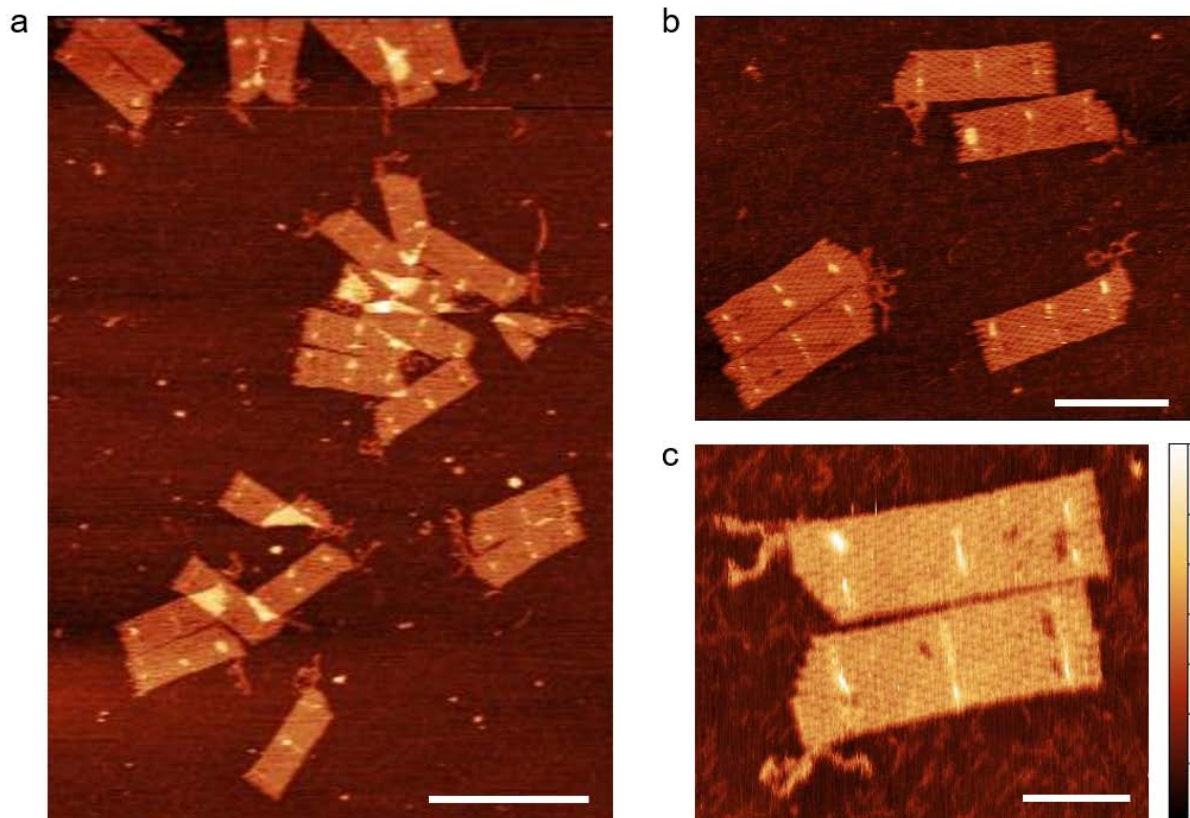


Figure A.6: Type II pads after adding 23T ODNs. Scale bar and height range: a) 200 nm, 0-8 nm; b) 100 nm, 0-6.4 nm; c) 50 nm, 0-5 nm.

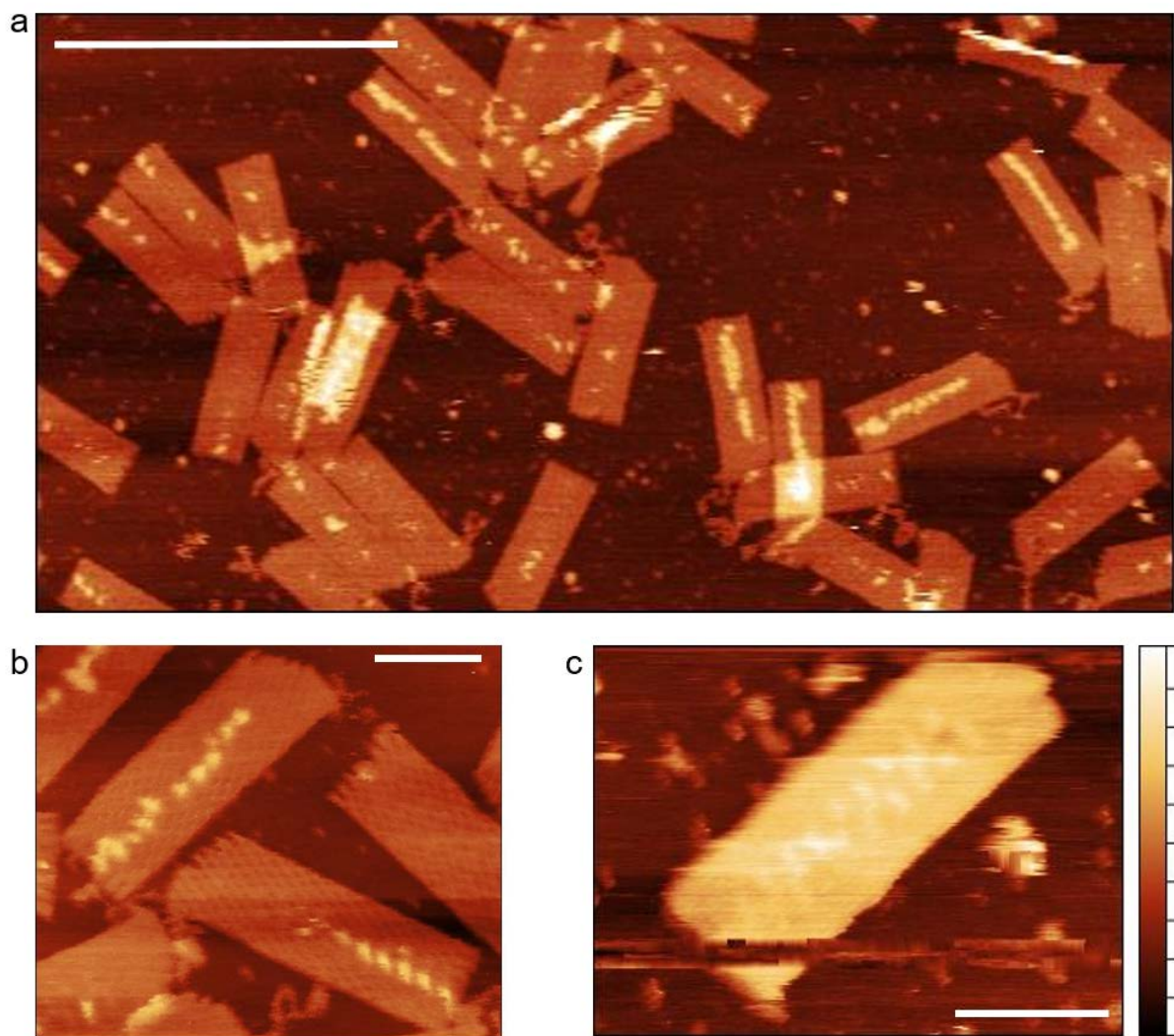


Figure A.7: Type III pads after adding a), b) 23T and c) 8T ODNs. Scale bar and height range: a) 300 nm, 0-8 nm; b) 50 nm, 0-8 nm; c) 50 nm, 0-5 nm.

FindFoci threshold setting

Employing the FindFoci routine, the threshold separating pad and bound objects was set at 140 % of the pad height. The value was determined from the pad height and the handle array height of type III pads with single-stranded handles as shown in Appendix Figure A.8, and applied for all pad types.

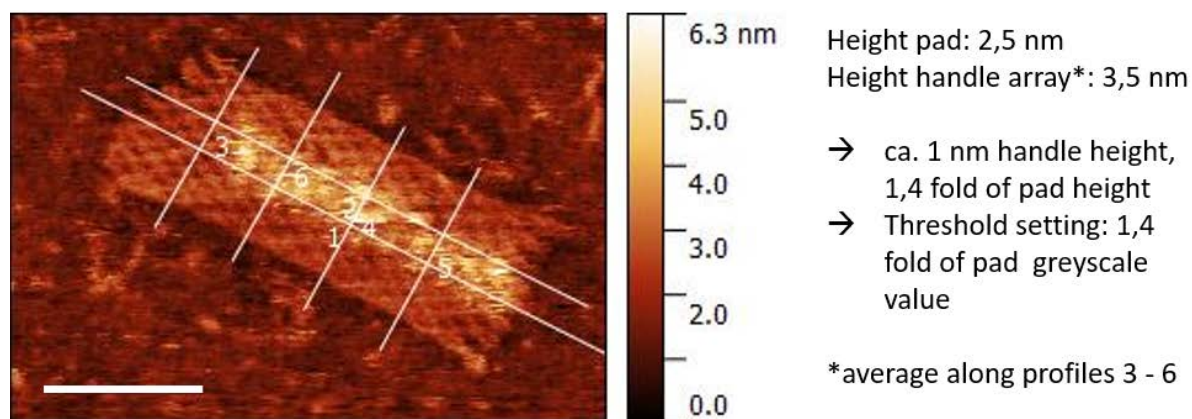


Figure A.8: Pad type III with single-stranded handles. The heights of the bare pad were determined at appropriate sections of the profiles 1 and 2, while the average height of the handle array was calculated from the height profiles 3-6.

Hybrids of PNIPAAm and pads

In the way a BCP was formed with P3(EO)₃T and an oligodeoxynucleotide, any water-soluble polymer can be used, and the resulting BCP can be placed on DNA origami. A proof of principle was done with commercially available PNIPAAm, as can be seen in Appendix Figure A.9.

PNIPAAm shows a lower critical solution temperature (LCST) phase transition, forming coils below 32 °C, and globules above that temperature. In order to observe it on origami, the sample shown in Appendix Figure A.9 was investigated with hot stage AFM in an initial experiment. While switching between 40 °C and 15 °C two times, the sample was robust to scanning. The bound block copolymers were visible at the lower temperature, disappeared at the higher temperature and appeared again at the lower temperature. Probably, the LCST phase transition was observed, however, the experiment has to be repeated to ensure the result.

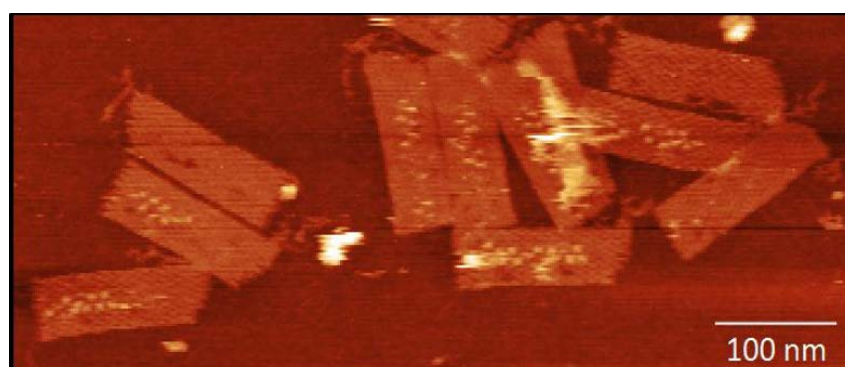


Figure A.9: Attachment of PNIPAAm-b-18T to the pad type III.

Equivalent diameter

The equivalent diameter d_{eq} is the diameter of a circle with the same area as the basal area of an object on a pad in the xy -plane determined with FindFoci. Together with the object height h , it provides an idea of the 3D shape of the origami-bound objects. Compared to the object heights (Figure 4.6), the distributions of the equivalent diameter in Appendix Figure A.10 are broader. One influential fact is probably that the tip-pressures varies amongst the images, which propagates into the variation of the lateral size to a larger extend than into the height. In addition, errors from the exaggeration of the lateral sizes in AFM imaging and the threshold setting in FindFoci can probably lead to an overestimation of the equivalent diameter. For the type I pads with 20N handles binding P3(EO)₃T-b-20N and type III pads with 8A handles binding P3(EO)₃T-b-10T, the average object height and diameter are very similar, while for type II pads with 15A handles and type III pads with 8A handles binding P3(EO)₃T-b-18T, d_{eq} exceeds h . Apparently, the longer link is more flexible, or susceptible to tip manipulation. Taking into account the variation introduced by the scanning process and the tip pressure, height and diameter appear similar, i. e. the objects appear globular-shaped.

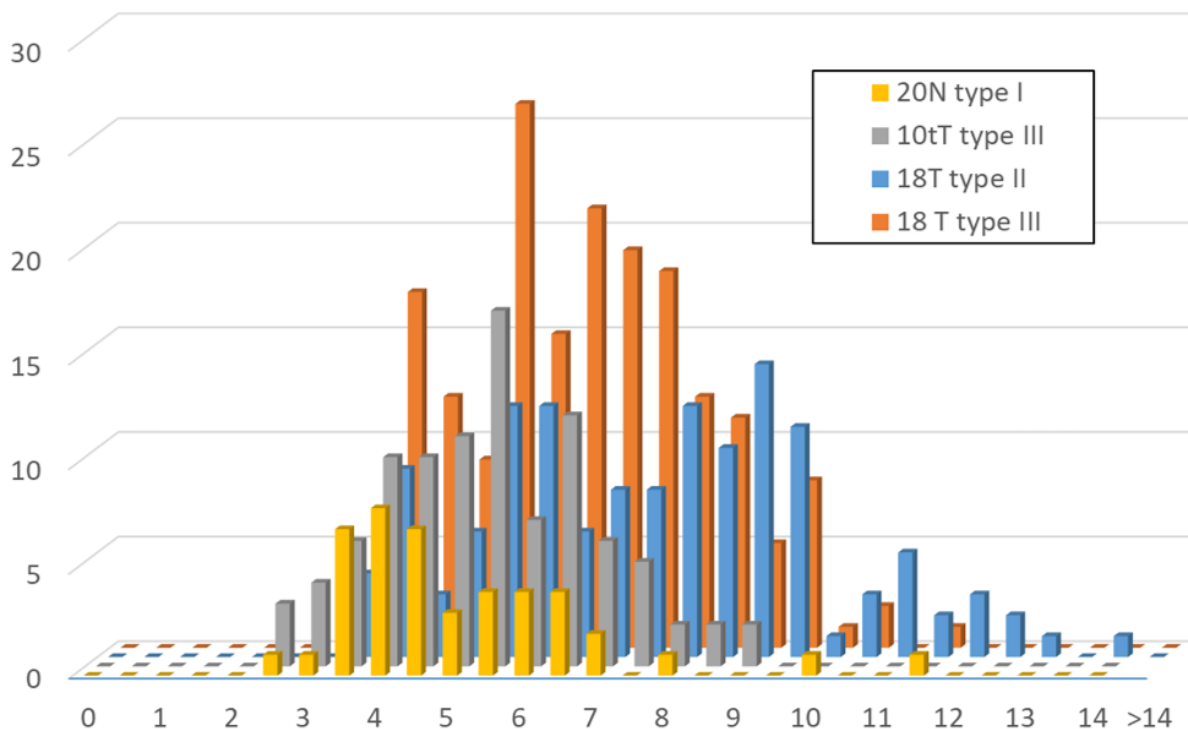


Figure A.10: Equivalent diameter of the objects bound to different pad types. The key lists the objects by ODN of the block copolymer and pad type they are bound to. The x -axis is scaled to reflect the BCP lengths as it was done in Figure 4.6.

Multicolour super-resolution microscopy

Matlab routine source code

A Matlab routine performs the steps 10 to 18 (orange in Figure 5.3). The source code is available upon request from the Diez Group, B CUBE, Technische Universität Dresden, Arnoldstr. 18, 01307 Dresden, Germany.

Absorption and emission spectra of the Atto dyes

The design II tPads were labelled using the dyes Atto 488, Atto 550 and Atto 647N that can be excited and detected selectively with appropriate lasers. Their absorption and emission spectra as well as the excitation lasers used are given in Appendix Figure A.11.

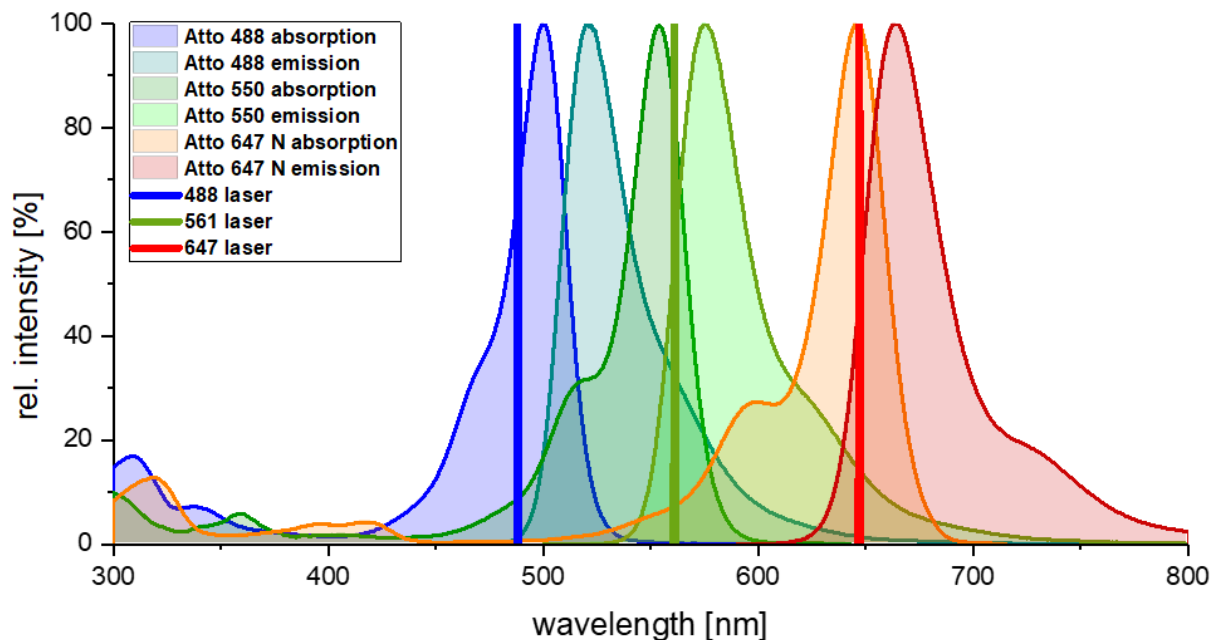


Figure A.11: Absorption and emission spectra for the three dyes Atto 488 (blue), Atto 550 (green) and Atto 647N (red). The three excitation spectra are overlapping to a small extend only, as are the emission spectra. This marker set is used in the tPad design II. The wavelengths of the lasers used for excitation are displayed as well.

Raw data processing

Appendix Figure A.12 displays a screenshot of a marker localisation matrix of one field of view as required for the cluster identification. The table is the result of tracking the fluorophore positions with ThunderSTORM^[232]. It includes all fluorophore positions in one colour channel in each of the k images (here named frames) taken per field of view. In addition to the x_i - and y_i -coordinates, it lists the uncertainties of the coordinates u_i . For the weighted least-squares fitting of the x_i - and y_i -coordinates, the uncertainties are calculated based on the Thompson-Larson-Webb-formula^[231] (see (1.2)).

id	frame	x [nm]	y [nm]	sigma [nm]	intensity [photon]	offset [photon]	bkgstd [photon]	chi ²	uncertainty [nm]
1	1	390,5778	7304,2885	68,7693	211,9624	73,2245	11,1905	492,1205	13,9187
2	1	391,3077	13832,0024	105,4613	274,5597	66,7403	7,0567	230,3508	16,5583
3	1	470,4962	45225,9387	122,1784	1299,9112	69,3881	12,3610	476,1881	8,3953
4	1	596,7774	44418,2335	133,9981	565,6034	72,4102	9,9179	366,2512	17,1881
5	1	670,2409	6033,9253	128,6118	314,5851	66,5711	9,1763	358,9959	25,4748
6	1	700,1874	31658,9053	129,5848	393,3869	71,5298	11,3847	458,7420	25,2277
7	1	698,6355	40784,6046	116,8814	284,4588	71,3484	9,8878	355,6326	24,9641
///	///	///	///	///	///	///	///	///	///
350	1	52830,2157	42942,9962	102,8869	366,4578	69,8828	12,9310	651,4106	19,6072
351	1	52793,2336	44778,3520	138,0400	568,9712	59,0261	8,9561	364,8651	16,6618
352	1	52820,4844	42953,7313	127,5248	512,4833	65,8570	12,5949	615,4143	20,8902
353	2	354,4856	13877,2421	119,5733	332,5762	65,0968	10,2866	417,5932	23,3050
354	2	321,8565	42485,5773	122,9729	1182,4484	67,1774	11,5127	426,4072	8,7586
355	2	483,3343	7269,1719	132,6795	390,7808	67,2604	8,7380	321,6369	21,2706
356	2	448,5192	45221,5921	109,9738	848,3947	70,4611	11,1918	509,8681	9,4192
357	2	541,2327	6163,1629	103,4181	256,8475	67,2037	9,4927	381,0482	21,2099
358	2	833,7081	38515,6817	134,0964	1157,2283	76,3616	13,1391	533,9073	11,3453
359	2	903,5996	29487,8244	135,6523	462,5383	72,1715	10,4773	426,6175	22,0282
...

Figure A.12: Screenshot of ThunderSTORM results of the marker localisation.

First mapping calibration

The first mapping calibration was derived from a field of view with 15 Tetraspeck beads. Appendix Figure A.13 displays the fluorophore distance distributions before and after the mapping as Figure 5.4 does for the second mapping. Like in the latter case, mapping decreases the width of the distributions considerably. However, fluorophore distances above 0 nm - which would indicate a perfect fluorophore registration - remain due to residual error.

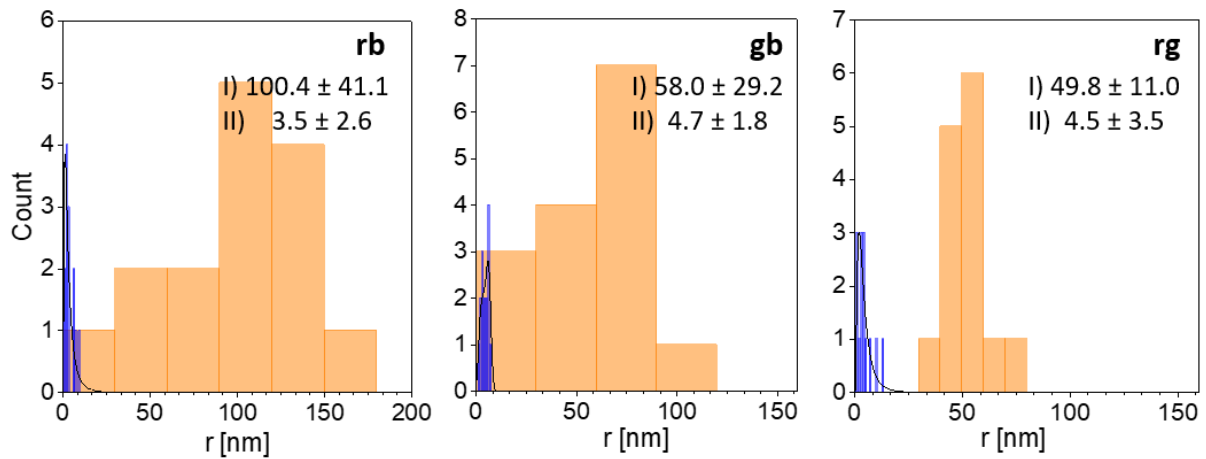
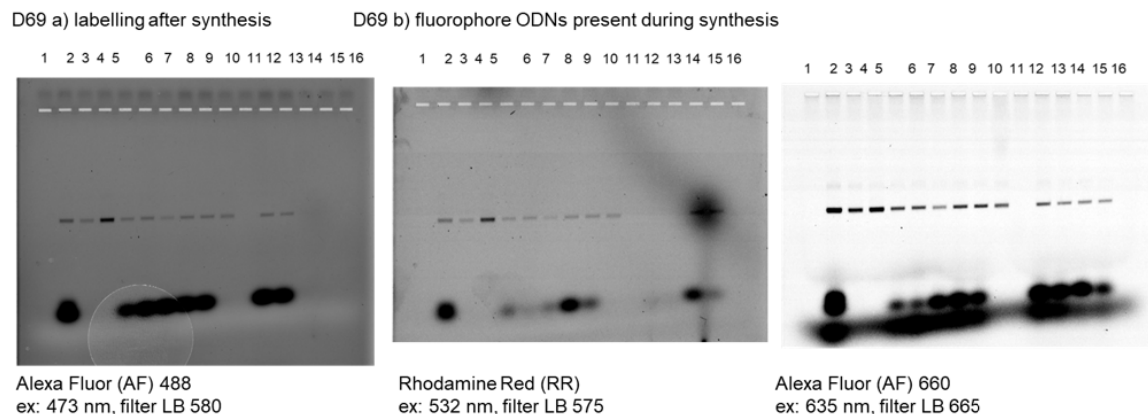


Figure A.13: Fluorophore distance distribution for the distances red-blue (rb), green-blue (gb) and red-green (rg) before (orange) and after (blue) mapping. The locations of the 15 Tetraspeck beads imaged during the standard origami experiment serve as fiducial marker dataset (first mapping). The insets state the means and standard deviations of the distribution before (I) and after (II) mapping in nm.

Fluorophore-labelled tPads of design I and design II visualised in agarose gels

a Design I tPads „D69“ imaged prior to staining:



1	3	4	5	6	2	15	7	8	9	10	11	12	13	14	16
log2	D69b unfil	D69b fil	D69b fns	after 1 h freezer: D69a fil + all dyes @ RT	D69 unfil 1:3 + all dyes: 1h @ RT	D69 unfil 1:3 + all dyes: 1h @ 45 °C	D69a fil + all dyes @ RT	D69a fil + all dyes @ 45 °C, 2h	D69b fil + all dyes @ 45 °C, 2h, filtered	D69a fil	D69a fil + AF488/A F660 @ RT 2h	D69a fil + AF488/A F660 @ 45 °C	D69a fil + AF488/R @ RT, 2h	D69a fil + AF488/RR @ 45 °C 2h	log2

log2:2-log DNA ladder, unfil:unfiltered, fil: filtrated, fns: freeze'n'squeeze, RT: room temperature. All lanes with loading dye.

b Design II tPads “D68” before and after staining. All lanes contain loading dye.

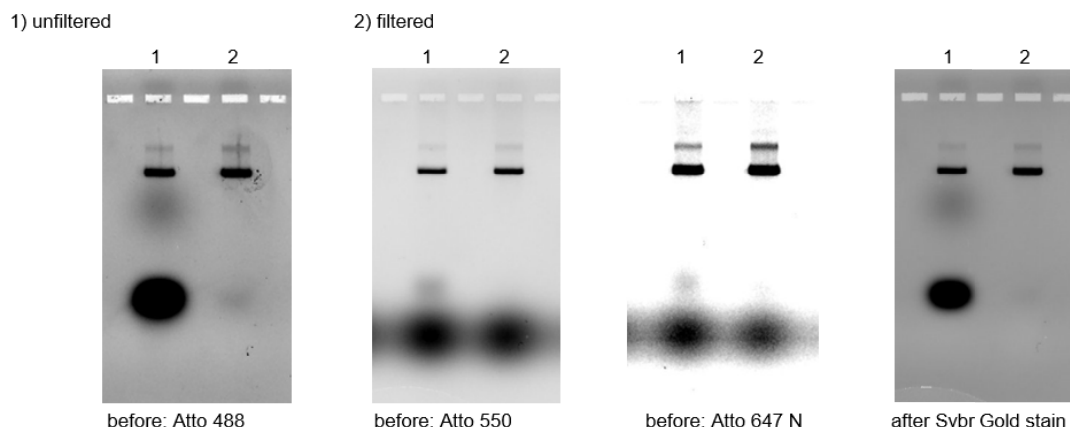


Figure A.14: Fluorophore-labelled tPads of (a) design I and (b) design II visualised in agarose gels. The tPads are clearly visible prior to staining through the fluorescent labelling. In all tPad samples, all types of fluorophores were incorporated. For design I tPads, there was no visible intensity difference between tPads labelled during or after the synthesis. In the filtered design II tPads, fluorophore staples did not remain, or remained barely. For the binding specificity of fluorophore-labelled ODNs and handles in design I tPads see Appendix Figure A.2.

Appendix B

EGNAS

The specific sequences of the 20N' handle and the blue, green and red handle (Table 3.2) were generated using EGNAS^[77] (version: 1158 Feb 14:22:34) according to the description provided by Kick *et al.*^[77]. The executable EGNAS file for Microsoft Windows operating systems was downloaded from the online supporting information^[77]. The data input for using EGNAS involves datasets for the forbidden and the included sequences¹, as well as the length of the target sequence, specifications of the GC content, whether GC ends are demanded or not, and further intra- and interstrand properties. The critons specified in the forbidden sequences include the homopolymeric runs AAAA, TTTT, GGG, CCC as discussed by Kick *et al.*^[77] and critons of four bases derived from the sequence of the staple that will be extended with the target sequence. The list of included sequences contains the M13mp18 scaffold sequence and the sequences of all staples of the origami. Table B.1 lists the forbidden sequences and other program specifications for each of the four handles. For the 20N' handle, only one sequence could be generated. That is because, initially, it was supposed to be attached to 20 tPad staples, which has enlarged the list of forbidden critons considerably. For the blue, green and red handle, ten sets of ten sequences each were generated, of which one was chosen randomly for each handle.

¹According to Kick *et al.*^[77], a dataset of neighbouring sequences can be provided as well, but was not considered in this work.

Table B.1: EGNAS input and forbidden sequences to generate the 20N' handle for BCP attachment and the blue, green and red handles for the fluorophore attachment.

EGNAS input	handle 20N'	blue	green	red
Sequence length	20 bases	20 bases	20 bases	20 bases
Length of basic sequences (criton length)	8 bases	8 bases	8 bases	8 bases
GC content from	9 till 11 bases	11 till 11 bases	11 till 11 bases	11 till 11 bases
Forbidden sliding length	8 bases	8 bases	8 bases	8 bases
Demand on GC ends	none	none	none	none
Forbidden stem length of hairpin structures	2 base pairs	2 base pairs	2 base pairs	2 base pairs
Maximum number of sequences to be generated per set	10	10	10	10
Maximum number of sets to be generated	10	10	10	10
Forbidden subsequences	AAAA CAGC TTAG CCAT TTTT GCAG TTTA TACT GGG TGCA AGGA TTAC CCC AGCT CAGG ATTA TCGT GAGC TCAG AATT CTCG CGAG ATCA GAAT GCTC TCGA AATC GGAA TGCT TTGC TAAT CGGA GTGC CTTC ATAA GCGG TGTG CCTT GATA GCGG CTGT CCCT TGAT TGGC ACTG ACCC ATGA ATGG CACT AACC AATG TATG ACAC AAAC AAAT ATAT AACA AAAA AAAA GGAA AAAC GAAA GTTA TGGA AAAA TTAT CGTT TTGG CGGC GTTA CCGT CTTC GCGG TGTT TCCG TCTT AGCG ATGT ATCC TTCT TAGC GATG TATC CTTC GTAG TGAT TTAT TCTT TGTA TTGA TTTA ATCT TTGT GTTG TTTT TATC TTTG AGTT GTTT TTAT CTTT CAGT TGTT CTTA TCTT ACAG CTGT ACTT CTCT AACA TCTG GTCG ACTC CAAC GTTT AGTC GACT AGGA TGTT AAGT GCGG CAGG CTGT CAAG ACGC TCAG ACTG GCAA TACG CTCA TACT CGCA TTAC TCTC GTAC TCGC GTTA CTCT GGTA TTCG CGTT ACTC AGGT ATTG ACGT TACT CAGG GATT TACG ATAC TCAG TGAT CTAC TATA CTCA ATGA GCTA TTAT GCTC AATG TGCT GTA TGCT TCTT TTGC CGTT AGTC TTCT ATTG AGAA TAGT TTTC TGTG CAGA GTAG GTTT GTGT CCAG GGTA CGTT TGTG GCCA AGGT CCGT TTGT GGCC GAGG TCCG GTTG TGGC GGAG TTCC AGTT TTGG AGGA ATTC AAGT ATTG AAGG GATT GAAG TATT TAAG AGAT CGAA GTAT CTAA AAGA GCGA GGTA TCTA TAAG AGCG AGGT TTCT TTAT TAGC TAGG ACTA ATTA ATAG TGTA TACT TATT AGGA TTGT ATAC TTAT CAGG TTTG GATA GTTA ACAG GTTT TGAT TGTT CACA TGTT ATGA ATGT ACAC ATGT AATG TATG CACA TATG AAAT CTAT ACAC ATAT TAAA GCTA CACA GATA TTAA TGCT GCAC AGAT ATTA TTGC AGCA TAGA CATT ATTG	AAAA TTTT GGG CCC TCGT CTCG GCTC TGCT GTGC TGTG CTGT ACTG CACT ACAC AACA AAAC AAAA CGGC GCGG AGCG TAGC GTAG TGTA TTGT TTTG CTTT TCTT CTCT ACTC GACT GCGG ACGC TACG TTAC GTTA CGTT ACGT TACG CTAC GCTA TGCT TTGC ATTG TGTG GTGT TGTG GTTG AGTT GTTG AAGT GAAG CGAA GCGA AGCG TAGC ATAG AGGA CAGG ACAG CACA ACAC CACA GCAC AGCA	AAAA TTTT GGG CCC TCGT CTCG GCTC TGCT GTGC TGTG CTGT ACTG CACT ACAC AACA AAAC AAAA CGGC GCGG AGCG TAGC GTAG TGTA TTGT TTTG CTTT TCTT CTCT ACTC GACT GCGG ACGC TACG TTAC GTTA CGTT ACGT TACG CTAC GCTA TGCT TTGC ATTG TGTG GTGT TGTG GTTG AGTT GTTG AAGT GAAG CGAA GCGA AGCG TAGC ATAG AGGA CAGG ACAG CACA ACAC CACA GCAC AGCA	AAAA TTTT GGG CCC TCGT CTCG GCTC TGCT GTGC TGTG CTGT ACTG CACT ACAC AACA AAAC AAAA CGGC GCGG AGCG TAGC GTAG TGTA TTGT TTTG CTTT TCTT CTCT ACTC GACT GCGG ACGC TACG TTAC GTTA CGTT ACGT TACG CTAC GCTA TGCT TTGC ATTG TGTG GTGT TGTG GTTG AGTT GTTG AAGT GAAG CGAA GCGA AGCG TAGC ATAG AGGA CAGG ACAG CACA ACAC CACA GCAC AGCA

Appendix C

DNA sequences

In the following, all DNA sequence are given in the usual 5' - 3' direction.

tPads

Sequences of the tPad body. The following body staples constitute the tPad bodies for studying the edge staple designs, the AuNP attachment and the multicolour super-resolution microscopy tPad designs I and II. T_M is the staple melting temperature. If for one of the tPad types, staples need to be replaced by the application-specific staples given in the following tables, this is noted in the last four columns of this table as follows.

Edge staples: z-staples and staples of the three attachments sites in the tPad cavity (holder) are indicated. The z-staples can be left out to yield non-stacking tPads, or be replaced by u-staples. The holder staples can be replaced to anchor, e. g., a three-arm strut.

AuNP: these staples are replaced by staples for AuNP attachment with same number.

Design I: staples yield fluorophore-bearing tPads according to design I.

Design II: staples yield fluorophore-bearing tPads according to design II.

No.	Sequence	T_M [°C]	edge staples	AuNP	Design I	Design II
1	CCGTCTATCAGGCGATGGCCCACTGGTCGAGG	87			AF488: 1 DI	
2	GAACGTGGACTCCAACGTCAAAGGCCTAAAGG	82				
3	GTTCCAGTTTGGAAACAAGAGTCCAGGGAAAAGC	81				
4	CAAAAGAATAGCCCGAGATAGGGTGAAGAAA	78				
5	TGGTTCGAAAATCGGCAAAATCCCTTATAAAT	76				
6	TTGCCCCAGCAGGCGAAAATCCTGTTGCGTTG	83				
7	TGAGAGAGTTGCAGCAAGCGTCCGAAAACCT	83				
8	GCAACAGCTGATTGCCCTTCACCGCGCCAAC	86				
9	TTTTTCTTTTCACCAAGTTGGGCGC	72	z			
10	TGCCGTAATCGTTAGAATCAGAGCTTAGACAG	78			left out	Atto 488: 10 bII
11	GAGCCCCCTTGCTTTGACGAGCACAGTGT	82		AuNP		
12	CGGCGAACCTTAATGCGCCGCTACAAAGAGTC	83		AuNP		
13	GCGAAAGGTCACGCTGCGCGTAAACGTAGCAAT	83		AuNP		
14	AATGAGTGTAAGTGTAAGCCTGCTGGCAAG	78				
15	CGCTCACTCACAATTCCACACAACCTTCGCTAT	80		AuNP		
16	GTCGTGCTAGCTGTTTCTGTGTGTGCTGCA	83		AuNP		
17	GCGCGGGGGGTACCGAGCTCGAAGGGTTTTC	89		AuNP	biotin: 17b	Atto 647N: 17 DII
18	CAGGGTGGGCATGCCTGCAGGTCGGGCCAGTG	90	z			
19	AACAGGAGAAATCAAGTTTTTTGACGTGAACCATCACCC	82	z			
20	TGCTTTCCAGCACTAAATCGGAACGCGAAAAA	78			additional: 19 DI	

No.	Sequence	T_M [°C]	edge staples	AuNP	Design I	Design II
21	TACTATGGGATTTAGAGCTTGACGCTATTTAA	75				
22	CCGCCGCGGTGGCGAGAAAGGAAGTGAGTGT	86				
23	TGTAGCGGAGCGGGCGCTAGGGCGGGGTGCCT	91				
24	CGGAAGCAAGCTAACTCACATTAATTTGATGG	77				
25	TATCCGCTGCCCGCTTTCAGTCGACGCTGGT	86				
26	CATGGTCAAGCTGCATTAATGAATCCTGGCCC	81				
27	GGATCCCCAGAGGCGGTTTGCCTATGAGACGG	86			left out	
28	GAACGGTACGCTCAATCGTCTGAAACACGACC	82				biotin: 28 bII
29	TATAATCAGAAAAACGCTCATGGAACAGAGA	75				
30	TGTCCATCCAGAACAATATTACCGTAAGAATA	75			biotin: 34b	
31	ACTTCTTTGAACTCAAACATCGGTGGCTATT	76				biotin: 35 bII
32	GGAAGGGCGCCATTTCAGGCTGCGCACTTGCT	87				
33	TACGCCAGTCTGGTGCCGAAACCTTCTCTGTA	83				
34	AGGCGATTGATCGCACTCCAGCCATGAGCGAG	85			additional: 35 DI	
35	CCAGTCACTGAGGGGACGACGACAGGAACAAA	83				
36	CCAAGCTTATGGGCGCATCGTAACGGTCACGT	83	z			
37	TTTACATTGCCGATTAAGGGATTGGGAGCTA	77	z			
38	CATTTTGACGCCAGAATCCTGAGAGTATAACG	78		AuNP	biotin: 38b	biotin: 38 bII
39	TGCAACAGGTGAGGCCACCGAGTAAGGGCGCG	87				biotin: 39 bII
40	GTAATATCACGCAAATTAACCGTTCACCACAC	77				
41	GAGTAGAAGATTAGTAATAACATCAACTGTTG	73		AuNP		
42	CGCCATTGATCGGTGCGGGCCTCATACGAGC	87				
43	GCACCGCTGCGGAAAGGGGATGAAATTGT	83				
44	CTCAGGAAAAGTTGGGTAACGCCATTTCGTAAT	78				
45	TGCCAGTTGACGTTGTAACGACACTCTAGA	78			left out	biotin: 45 bII
46	AGTAATAAAGGAGCACTAAACAACCTTGAGGATT	75			biotin: 46b	
47	TAGAACCAGGAATTGAGGAAGGTATTCGACA	78				
48	CGTGGCACATATCTGGTCAGTTGG	76				
49	AGTCTTTATTGCTGAACCTCAAATATCAAACC	75				
50	CATCGCCATAAAACAGAGGTGAGGAATCTAAA	75				
51	GCCAGCTTTAATTGCGCTCTGGCCAACCACCA	83				
52	TAACAACCATTTTTTAACCAATAATCGTAAA	71				
53	CGGCGGATAAAAATTCGCATTAATCCGGTTGA	78			biotin: 53b	fehlt
54	TGGTGTAGAATATTTAAATTGTAAGAAGATTG	71	z			
55	AGAGCCGTGGCAGATTCCACAGTCATGGATTA	81	z			
56	ATATCTTAAGGGACATTCTGGCCAATACCTA	76		AuNP		56 DII
57	CAGTTGAATTCTGACCTGAAAGCGCCAGCCAT	81				
58	CTCAATCAAGACAATATTTTTGAAACCTTGCTG	75				
59	GCATCACCATGCGCGAACTGATAGCCCTAAAA	81				
60	GCAGAAGATTA AAAATACCGAACGAGGCAAAG	77				
61	GGAACGCCATCAAAAATCATCAACATTAATGGCTTCCG	81				
62	AATCAGCTCGTCGGATTCTCCGTGGTATCGGC	83				
63	ATTTTGTTTGACCGTAATGGGATACGTGCATC	77			AF 660: 63 DI	63 DII
64	TAGAAGTAAAGAAACCACGAGAAGGATGATGG	77				
65	ACTCGTATAAGTTTGAAGTAACATTGTTTGGAT	73				
66	GAGAGCCAGCAGCAACAACAGTGCCACGCT		holder			
67	ACTAGCATGAATCGATGAACGGTATGAGAAAAG	77				
68	TAATCAGAGGTCATTGCGCTGAGAGAATATGAT	76				
69	TATAAGCAAGCTATTTTTGAGAGATAATGCCG	75	z			
70	TTATCATCCAATAGATAATACATTAATAGATT	68	z			
71	GCGGAACATTAGACTTTACAAAATATCTAAA	73		AuNP		
72	AATTTTAATAAATCCTTTGCCCGACAAATCAA	72				
73	ATTAACACCGCCTGATGAAACGGTCAGT		holder			
74	AAACAAGAGTCAATCATATGTACCTTTTGTTA	72				
75	GGCTATCAAAAGCCCCAAAACAGACGTTAAT	77				
76	CAATTCATAAATTGCGTAGATTTTCTACCTTTT	72				
77	TATACTFCAAAATATTTGACGTTCCGCTGA	75				
78	GCCGGAGATAAAGATTCAAAGGGCTCAGAGC	81				
79	ATTCAACATTTTAAATGCAATGCAAACATTA	71				79 bII
80	GAGAGGGTCGCAAGGATAAAAATTGAAGCCTT	78	z			
81	CGTCAGATATATCTCTGATTATCAGAGCGGAA	77	z			
82	AATAAAGACAATATAATCCTGATTATCATTTT	68		AuNP		
83	ACCATACTGAATAATGGAAGGGTACGTTATT	75				
84	TGTGTAGGCACTCAAATCACCATCTCTGGAGC	81				
85	CCTCATATGTTCTAGCTGATAAATTCTACAAA	73				
86	ACATCGGGTGATGAAACAAACATCCATTTGAA	76				
87	TTGCTTTGTTATTTCATTTCAATTACATAAATC	69				
88	ATAAAGCTAATTAAGCAATAAAGCCATTAGAT	77				
89	TGACCCGTAAATCATACAGGCAATGTTTAGC	71				
90	TATTTCAAATTTACTAATAGTAGTAAAAAGG	71	z			

No.	Sequence	T_M [°C]	edge staples	AuNP	Design I	Design II
91	AAAATTAAGAATATACAGTAACAGAGGTTTAA	69	z			
92	AAAGAAGAAGAAACAATAACGGATAAAACAGA	72		AuNP		
93	GAGGCGAAAATACCAAGTTACAAATAGAACCT	76				
94	ATTAGCAAAAATCGGTTGTACCAACTGAGTAA	75				
95	ACATCCAATAATACTTTTGGCGGATTTAGAAC	75				
96	TTACCTTTAACATAGCGATAGCTTTTTATCAA	72				
97	AATATATGCTATTAATTAATTTCTTTTAACC	67				
98	ACATTTCCGGTAGATTTAGTTTGGACTGATAAGA	73				
99	TATATTTTATATAACAGTTGATTCGCTTAATT	68				
100	TGGCATCAAACCTAAAGTACGGTGCATGTTTT	76	z			
101	ACGCTGAGTTACATTTAACAAATTTAAGAAAAC	72	z			
102	TCCTTGAATTTAATGGAAACAGTACCTGAGCA	76		AuNP		
103	AATCGTCGTGAGTGAATAACCTGATCGCGCA	80				
104	GCGAACGACAAATGGTCAATAACCGGCAAAAGA	80				
105	TTCATTCCCATTGGGGCGCGAGCTAGCATT	81				
106	AATCATAGACCGACCGTGTGATAACATAATTA	75				
107	TCCGGCTCATCTTCTGACCTAAATATGCGTT	78				
108	CTATATGTAAATGCTGGAAAACTTTTTCAAAT	71				
109	CAGGATTAGAGAGTACGCAAACTCCAACAGGT		holder			
110	GGTCATTTTAATTCGAGCTTCAAACCTCAAAT	75				
111	GCTGAATAAGGAAGCCCCGAAAGACAATGACCA	80				
112	AAATATGCGAAGCAAAGCGGATTGCTGACTAT	77	z			
113	TTAAATAAAAAGAGTCAATAGTGAAGATTAAG	69	z			
114	TTTGAATGTCTGAGAGACTACCTCCTTAGAA	76		AuNP		
115	GTTAATTTAGGTTGGGTTATATAACTTCTGTA	72				
116	AAGACAAAGAACGCGAATGCAAATCCAATCGC		holder			
117	GCGAACCAGACCGGAACTTTAATTGCTCCTTT	80				
118	TCGCGTTTTGCGGATGGCTTAGACCAATTCT	80				
119	AGATTAAGTAATGCTGTAGCTCAACTGGAAGT	76				
120	CTAGAAAAGCCAACATGTAATTTAATATAAAG	71				
121	ATACAAATGGGCTTAATTGAGAATTGTCCAGA	75				
122	GCTTTAAAATATTCATTGAATCCAGAGCAAC	75				
123	TAAATCAAGGATAGCGTCCAATACACGACGAT	77				
124	TATAGTCAGCCAGAGGGGTAATATTGCAAAA	77	z			
125	CATTTTCGGAATAAACACCGGAATATAAGGCG	77	z			
126	TTAACAACAGCCTGTTTAGTATCATTTAATGG	73		AuNP		
127	CAACAGTATCTTACCAGTATAAAGATATTTTA	71				
128	CGTCATAACAGTTCAGAAAACGAGTTCAAATA	75				
129	TTTAGACTAAATCAGGTCTTTACCCATCAAAA	73				
130	TACCGACAAGAAAAATAATATCCATAATCGG	75				
131	CGACGACACCTGTTTATCAACAATACGGGTAT	78				
132	ACTATCATATTACGAGGCATAGTAATTATAACC	73				
133	AAAAACCATCAACTAATGCAGATACTACGTTA	73				
134	GAAGTTTTGATTCATCAGTTGAGATTATTACA	72	z			
135	TTACGAGCAGCCAGTAATAAGAGAGGCAGAGG	81	z			
136	CCTGAACAAAAGGTAAAGTAATTCGCCATAT	76		AuNP		
137	AGAACGCGATAAACAACATGTTACCAACGCT	78				
138	CAAAAGGAAACCTCGTTTACCAGTGCGGAAT	80				
139	TACCACATAAATAGCGAGAGGCTTGTAATG	76				
140	CTGTCTTTCAATAGCAAGCAAATCCGCGAGGC	81				
141	TAAACCAATTTATTTTCATCGTAGGGGAGGTT	75				
142	AGTCAGGATTTAAGAAGCTGGCTCGGATATTC	77				
143	ATAAAACGCAACTTTAATCATTGTCTGCTCAT	73				
144	GGTAGAAAAGTAGTAAATTTGGGCTGAGAAACA	76	z			
145	AAGGCTTAATGTAGAAACCAATCAATCCTAAT	73	z			
146	ACCGCGCCCCTTATCATTCCAAGAAGATAAGT	80		AuNP		
147	AAGCCGTTGTACCGCACTCATCGAGCTAATGC	82				
148	TTATGCGACGTTGGGAAGAAAAATCATAACGC	77				
149	TTAATTTAACTAACGGAACAACATTTAGGAA	71				
150	GTTTTAGCAACGAGCGTCTTTCCACATATTAT	76				
151	TTGAAGCCGCTACAATTTTATCCTATTTTTTG	73				
152	ATFACCCAAATCTTGACAAGAACCAAAATCCGC	77				
153	TCAGTGAAGGCGCATAGGCTGGCTGAACGAGG	85				
154	CCAGAACGTGAAAAGAGGACAGATGCCGAACTGACCAACTT	85	z			
155	TTTGCCAGTCCGGTATTCCTAAGAAAAGATATAG	76	z			
156	CCAACGCTGAACCTCCCGACTTGCGAATCATT	82		AuNP		156 DII
157	TGCACCCATTAATCAAGATTAGTGAACAAGC	76				
158	TCAAGAGTAATCAACGTAACAAAAGGAATTACC	75				
159	ACAGACCATAAGGCTTGCCCTGACTGAGATGG	82				
160	TTATCCCATACCGAAGCCCTTTTTCCAGAAGG	80				

No.	Sequence	T_M [°C]	edge staples	AuNP	Design I	Design II
161	TTTAACGTAGCAAGAAACAATGAAGGAATACC	75				
162	AGCCTTTACAGAGAGACCCACAAGAATTGAGTTCCTTATT	81				
163	TTAGACGGAGGGTAATTGAGCGCTAAATACAT	77				
164	CAAGCGGATCTTTGACCCCGACCCCTGAAC	86				
165	ATCATCGCCGAAAGAGGCCAAAAGAGTTAAAGG	78				
166	GACCTGCTCGTAATGCCACTACGACAGCAGCG	85				
167	CGCAGACGCATGAGGAAGTTTCCA	76				
168	TAAGCAGATTACAAAATAAACAGCGAGCCTAA	75	z	AuNP		169 DII
169	AGCTATCTATCCAAAATAAGAAACGGAATCTTA	73				
170	ATAATAAGCAAAAATGAAAATAGCTGCTATTT	69				
171	AGAGATAAATAACATAAAAACAGGGAAGCGCA	75				
172	AAAGTCAGGAGAATTAACCTGAACAGATTATAC	73				
173	AAACACTCAAACAAGTACAACGGAGATTTGT	75				
174	ACCTAAACTGATAAATGTGTCTG	67				
175	GTAATAACCATGTTACTTAGCCGGACCTTCA	77				
176	AAAGACTTTTTGTCAATCATAAGGGAAAACGGTGT	76	z			
177	AAACCGAGAGGTAATATTGACGGACCGACTT	78				
178	CAAAAAGAAAAAGGGCGACATTCAACAAAATCA	75				Atto 550: 177 DII
179	ACGCAGTAAAAATTCATATGGTTTAGGCCGGA	77				
180	ACATAAAGACGGAAATAAGTTTATTAGCAGCAC	75			RR: 180 DI	
181	TTCCGTCGCATCGCCACGCATAAGAAACGCA	83			biotin: 183b	biotin: 181 bII
182	CCGCTTTTATACCGATAGTTGCGCTAAAGGAA	78				
183	AAAGACAGTTGCTTTCGAGGTGAATGAAAATC	76				
184	CATTAAAGTAGCCGAACAAAGTTAAAGAAAAG	73	z	AuNP		
185	GGGAGGGAGAAACGCAATAATAACATAGCAAT	77				
186	CAAAGACACTGGCATGATTAAGACTAAGCCCA	78				
187	ATCAATAGTGTAGCAAACGCTAGAAATATCAG	73				
188	AAGACACCGTGGCAACATATAAAACCGATATA	76				
189	ACAACAACTGAGGCTTGCAGGGAATACACTA	80				
190	ACAGCTTGGCGGGATCGTCACCCTAGGCACCA	86				
191	GTATCGGTTTTATCAGCCATCGGAACGAGGGTATTAAACGG	84				
192	TAATTGCAACGGCTACAGAGGCTTTGAGGACT	80	z		biotin: 193b	biotin 193: bII
193	GAGCCATTACCGGAACCGCCTCCCAGAGCCAC	87				
194	CCAGTAGCTCATAATCAAAAATCACCCACCCA	78				
195	AACGTCACTCATAGCCCCCTTATTGGTTGAGG	81				
196	CGTAATCAAGACTGTAGCCGTTTTTTCACAAA	77			left out	
197	GGAGTGAGTAAACAACCTTTCACAGTTTGCCT	77				
198	TTGCGAATTTAGTAAATGAATTTTAAACTACA	69				
199	TCCAAAAAACAGTCTAAAGTTTTCCCTCATAGTTAGCGT	79	z			
200	AAAGGCTCCAAAAGGAGCCTT	69	z			
201	GCCACCCTGTGAATTATCACCGTCAAATTATT	77	z			
202	GAGCCACCTGGGAATTAGAGCCAGCCGATTGA	83			biotin : 202b	biotin: 202 bII
203	CCATCTTTACCATTACCATTAGCAACCAGCGC	80				
204	ATTTTCGGCAATGAAACCATCGATTTGTACACA	76			additional: 204 DI	
205	TTAGCGTCGTAGCGACAGAATCAAGTTTCAGC	80				
206	GATTTTGCAATAGAAAGGAACAACCGACAATG	76				
207	TCCAGACGAATAATTTTTTCACGTTTTCTTAA	72			biotin: 207b	
208	CACCTCAAGTGCCCGTATAAACAATCTGTAA	78			biotin: 208b	
209	GAGCCGCCTAAGTTTAAACGGGGTACTCCTCA	82				
210	CAGGTCACTGGCTTTTGATGATACTTTGCTC	78				
211	CAATAAATCTGAATTTACCGTTCGAGAGGGTTGATATAA	78			211 DI	211 DII
212	AACACTGAGCCCAATAGGAACCCAAATGGAAA	78				
213	ACGCCTGTAGAGCCACCACCTCACCCCTC	87			biotin: 213b	
214	CCCCTGCCAGAACCGCCACCTCTCAGAGCC	90				
215	TGAGTAAACGAGCGCCACCAGAACCAGAACCA	85	z			215 DII
216	ACTGGTAAAGCCAGCATTGACAGGAAGCGTTTG	81				
217	GTCATAACAACGATTGGCCTTGATATCATCGGC	80				
218	GCGCAGTCTCCTCATTAAAGCCAGTGTACCGT	82				
219	GATAGCAAGTTTCGTCCACAGTACCTGTATGG	80				
220	CCGCCACCCTCAGCATTCCACAGACAGGTCGTCTT	87	z			
221	TATTTGCGAACCATTGTTAATGC	67	z			
222	ACATGAAAGTATAAGAGGCTGAGCAGTGCCT	78				
223	AGAGAAGGATTAGGATTAGCGGGGAGGAGTGT	81				
224	AGTACCAGCCGGATAAGTGCCTGCCAGTAAGC	83				
225	GTATAGCCCGAATAGGTGTATCA	72				225 DII
226	CCGTACTCAGGAGGTTTAGTACCGTTTTTCAGG	81				
227	AGAACC GCCACCTCAGAA	70				

u-staples. The following staples can replace the z-staples to yield u-staple tPads.

No.	Sequence
9	TTTTTCTTTTCACCAGTTGGGCGCCAGGGTGG
10	AAATCAAGTTTTTTGGACGTGAACCATCACCC
27	GCATGCCTGCAGGTCGGGCCAGTGCCAAGCTT
28	GCCGATTAAAGGGATTGGGAGCTAAACAGGAG
45	ATGGGCGCATCGTAACGGTCACGTTGGTGTAG
46	GGCAGATTCACCAGTCATGGATTATTTACATT
63	AATATTTAAATTGTAAGAAGATTGTATAAGCA
64	CAATAGATAATACATTAATAGATTAGAGCCGT
75	AGCTATTTTTGAGAGATAATGCCGGAGAGGGT
76	ATATTCCTGATTATCAGAGCGGAATTATCATC
85	CGCAAGGATAAAAATTGAAGCCTTTATTTCAA
86	GAATATACAGTAACAGAGGTTTAACGTCAGAT
95	ATTCTACTAATAGTAGTGAAAAGGTGGCATCA
96	TTACATTTAACAATTTAAGAAAACAAAATTAA
105	AACTAAAGTACGGTGTTCATGTTTTTAAATATGC
106	AAGAGTCAATAGTGAAAGATTAAGACGCTGAG
119	GAAGCAAAGCGGATTGCTGACTATTATAGTCA
120	GAATAAACACCGGAATATAAGGCGTTAAATAA
129	GCCAGAGGGGGTAATATTGCAAAAAGAAATTT
130	AGCCAGTAATAAGAGAGGCAGAGGCATTTTCG
139	GATTCATCAGTTGAGATTATTACAGGTAGAAA
140	ATGTAGAAAACCAATCAATCCTAATTTACGAGC
149	AGTAGTAAATTGGGCTGAGAAAACACCAGAACG
150	TCCGGTATTCTAAGAAAGATATAGAAGGCTTA
additional: 159u	TGAAAGAGGACAGATGCCGAACCTGACCAACTT
160	TTACAAAATAAACAGCGAGCCTAATTTGCCAG
177	TAGCCGAACAAAGTTAAAGAAAAGTAAGCAGA
additional 193u	GTGAATTATCACCGTCAAATTTATTCATTAAG
208	CAGAACCGCCACCCTCTCAGAGCCGCCACCCT
221	TATTTGCGAACCTATTGTTAATGCCCCCTGCC

AuNP staples. The following staples replace the basic staples for AuNP attachment.

No.	Sequence
11	GAGCCCCCTTGCTTTGACGAGCACAGTGTTTTTGACAAAAGCCGACCACCAAAG
12	CGGCGAACCTTAATGCGCCGCTACAAAAGAGTCGACAAAAGCCGACCACCAAAG
13	GCGAAAAGTCCAGCTGCGCGTAACGTAGCAATGACAAAAGCCGACCACCAAAG
15	CGCTCACTCACAATCCACACAACCTTCGCTATGACAAAAGCCGACCACCAAAG
16	GTCGTGCCTAGCTGTTTCCTGTGTGTGCTGCAGACAAAAGCCGACCACCAAAG
17	GCGCGGGGGGTACCGAGCTCGAAGGGTTTTTCGACAAAAGCCGACCACCAAAG
41	GAGTAGAAGATTAGTAATAACATCAACTGTTGGACAAAAGCCGACCACCAAAG
38	CATTTTGACGCCAGAATCCTGAGAGTATAACGGACAAAAGCCGACCACCAAAG
56	ATATCTTTAAGGGACATTCTGGCCAATACCTAGACAAAAGCCGACCACCAAAG
71	GCGGAACATTAGACTTTTACAAAACATATCTAAAGACAAAAGCCGACCACCAAAG
82	AATAAAGACAATATAATCCTGATTATCATTTTGACAAAAGCCGACCACCAAAG
92	AAAGAAGAAGAAAACAATAACGGATAAAAACAGAGACAAAAGCCGACCACCAAAG
102	TCCTTGAATTTAATGGAAACAGTACCTGAGCAGACAAAAGCCGACCACCAAAG
114	TTTGAATGTCTGAGAGACTACCTCCTTAGAAGACAAAAGCCGACCACCAAAG
126	TTAACAACAGCCTGTTTAGTATCATTTAATGGGACAAAAGCCGACCACCAAAG
136	CCTGAACAAAAGGTTAAAGTAATTCGCCATATGACAAAAGCCGACCACCAAAG
146	ACCGCGCCCCCTTATCATTCCAAGAAGATAAGTGACAAAAGCCGACCACCAAAG
156	CCAACGCTGAACCTCCCAGCTTGCGAATCATTGACAAAAGCCGACCACCAAAG
169	AGCTATCTATCCAAATAAGAAACGGAATCTTAGACAAAAGCCGACCACCAAAG
185	GGGAGGGAGAAAACGCAATAATAACATAGCAATGACAAAAGCCGACCACCAAAG

The ODNs bound to the AuNP are thiol-20N: 5'-HS-CTTTGGTGGTTCGGCTTTGTC-3'.

Fluorophore tPad design I. The following staples and fluorophore-labelled ODNs are specific of the design I tPad. Modifications are [BIO]: biotin, and the dyes AF488: Alexa Fluor 488, RR: Rhodamine Red, AF660: Alexa Fluor 660. The biotin staples include an ATTATTATT spacer. In the handle-bearing staples, the handle sequence is separated from the body staple sequence by an additional T base.

Name	Sequence
AF488: 1 DI	CCGTCTATCAGGCGATGGCCACTGGTCGAGGTGCCGTAATCGTTAGATGACTGCTGGATGACTACTGG
AF 660: 63 DI	ATTTTGTGTTGACCGTAATGGGATACGTGCATCTGCCAGTTGACGTTGTTGTGTAGTCCGTGTGTGTTGC
RR: 180 DI	ACATAAAGACGGAATAAGTTTTATTAGCAGCACCGTAATCAAGACTGTATCGCACACTCTCCACAACCTAC
19 DI	ATCAGAGCTTAGACAGGAACGGTACGCTCAATCGTCTGAAACACGACC
35 DI	AAAACGACACTCTAGAGGATCCCCAGAGGCGGTTTTCGTATGAGACGG
204DI	GCGCGTTTTTCACAAAACAATAAATCTGAATT
211 DI	TACCGTTCGAGAGGGTTGATATAA
AF488 ODN	[AF488]CCAGTAGTCATCCAGCAGTC
AF 660 ODN	[AF660]GCAACACACACGGACTACAC
RR ODN	[RR]GTAGTTGTGGAGAGTGTGCG
17b	[BIO]ATTATTATTAGCGCGGGGGGTACCGAGCTCGAAGGGTTTTTC
34b	[BIO]ATTATTATTAAGGCGATTGATCGCACTCCAGCCATGAGCGAG
38b	[BIO]ATTATTATTACATTTTGACGCCAGAATCCTGAGAGTATAACG
46b	[BIO]ATTATTATTAAGTAATAAAGGAGCACTAACAACCTTGAGGATT
53b	[BIO]ATTATTATTACGGCGGATAAAAATTCGCATTAATCCGGTTGA
183b	[BIO]ATTATTATTAAGACAGTTGCTTTCGAGGTGAATGAAAATC
193b	[BIO]ATTATTATTAGAGCCATTACCGGAACCGCCTCCCAGAGCCAC
202b	[BIO]ATTATTATTAGAGCCACCTGGGAATTAGAGCCAGCCGATTGA
207b	[BIO]ATTATTATTATCCAGACGAATAATTTTTTCACGTTTTCTTAA
208b	[BIO]ATTATTATTACACCCTCAAGTGCCCGTATAAACAATCTGAA
213b	[BIO]ATTATTATTAACGCCTGTAGAGCCACCACCCTCACCACCCTC

Fluorophore tPad design II. The following staples are specific of the design II tPad. Modifications are [BIOTEG]: biotin with triethylene glycol spacer, and the dyes Atto 488, Atto 550, Atto 647N. In the dye-bearing staples, the dyes are separated from each other and from the body staple sequence by a TCT spacer (purine bases avoided).

Name	Sequence
Atto550: 175	AAACCGAGAGGTAAATATTGACGGACCGACTTGAGCCATCT[ATTO550]TCT[ATTO550]TCT[ATTO550]
63 DII	ATTTTGTGTTGACCGTAATGGGATACGTGCATCTGCCAGTTGAGGGGAC
215 DII	TGAGTAACGAGCCGCCACCAGAACCGGAACCAGAGCCACCACCGGAACC
Atto647N: 17	GCGCGGGGGGTACCGAGCTCGAAGGGTTTTCCAGTCTCT[ATTO647N]TCT[ATTO647N]TCT[ATTO647N]
Atto488: 10	TGCCGTAATCGTTAGAATCAGAGCTTAGACAGGAACGGTCT[ATTO488]TCT[ATTO488]TCT[ATTO488]
56 DII	ATATCTTAAAGGGACATTCTGGCCAATACCTACATTTTGACGCTCAATC
193 bII	TTTGGGAATTAGAGCCAGCCGATTGATTCTTCTTCTT[BIOTEG]
38 bII	GTCTGAAACACGACCAGTAATAAAGGAGCACTAACAACCTTGAGGATTTTCTTCTTCTT[BIOTEG]
39 bII	TGCAACAGGTGAGGCCACCGAGTAAGGGCGCGTTCTTCTTCTT[BIOTEG]
35 bII	ACGACGTTGTAAAACGACACTCTAGATTCTTCTTCTT[BIOTEG]
202 bII	GCCTCCCAGAGCCACCACCCTCAAGTGCCCGTATAAACAATCTGAATTCTTCTTCTT[BIOTEG]
28 b II	TACGCCAGAATCCTGAGAGTATAACGTTCTTCTTCTT[BIOTEG]
45 bII	GACGACAGGAACAAACGGCGGATAAAAATTCGCATTAATCCGGTTGATTCTTCTTCTT[BIOTEG]
181 bII	TTCCGTGCGATCGCCACGCATAAGAAACGCATTCTTCTTCTT[BIOTEG]
79 bII	ATTCAACCATTTAAATGCAATGCAACATTATCTTCTTCTT[BIOTEG]

Pads

Sequences of the pad body. In the following, the pad body staples are given. In order to prepare pads with handles according to the pad types I-III, the staples marked in the last column need to be replaced by staples specific of that pad type, which are given in the following tables.

No.	Sequence	replaced in type
1	CCAACGTCTCGTGCCAGCTGCATTCGAGCCGG	
2	TAAGAGGAACGACGATAAAAAACCAACGAGAAA	
3	TAAAGCATAATCAACAGTTGAAAGACCTACCA	III
4	CCCTAAAAATTCGACAACCTCGTATTTGCGGAA	III
5	ATCGAGAACAAGCAAGGTTAACGTCAAAAATCCTGAACA	
6	AAATATATACATTTAACAATTTCAATCAATTA	
7	AATCTTACTTTTAGCGAACCTCCC	
8	CATTACCCAAGGGAACCGAACTGACATAACCG	
9	GTAGATTTTCAGGTTAACGTTATTTGCACGTAAAAACAGA	
10	CCTGTTTACAAGAAAAATAATA	
11	AAAAGAAACCCACAAGAATTGAGTTAAACAGC	
12	ACCAATGATCAGAGCCACCACCTTTAACGGG	
13	TGCACTCCAGCCAGCTAACTCACATTAGGTCATAAGAAT	II
14	TTGGCCTTTCACCGTCAACGACTATTCATA	
15	GATTTTTTCCGTTTTTATTTTCAT	
16	ATTCAGTGTAGCCGGAACGAGGCGCAGGGAGT	
17	AAGAGAATATAAAGTACCGAGTAATTTAGGCAGAGGCATT	
18	CCGTAACAAAGCGCAGTCTCTGAATCAGACGA	III
19	GATTAGTTGCTATTTTTGAAGCCTTAAATCAA	
20	CACCAGAAGTGTGAAATCCGCGACACCCTCA	
21	AGGTAAATGAGTAACATTATCATTAAATCCT	
22	GACTTGCGGGAGGTTTGCACCCAGCTACAATTTAAGAAAA	I; II
23	TAAGTTGGGTAACGCCCCTGCAGTCTCCTTCACC	
24	TCCCATCCTAATTTACCGGAATCATAATTACTACTTTTTTC	
25	ACCGCCACCTTGAGTAACAGTGCCCTCAGAAC	III
26	CAAATCAGATATAGAATTTGCCAGTTACAAAATAAGCCCA	
27	ATATATGTTGTAATGCTGATGCATACAAATT	
28	ATAAACACGAGCATGTAGAAACCA	
29	GTTAATAAAATCCTGAGAAAACCTGCACCGTG	II
30	GAAGGTTAAGAGCCAGCAGCAAATGGCAGATT	II; III
31	TAAGAACGCGAGGCGCAACGCTAACGAGCGATAGCAAT	
32	TCATATTAGGCGAATTATTCATTTTGAATT	
33	TAGACGGGCAGCGCCAAAGACAAACATTAAG	I; II
34	ATTTGGGGGCCATCAAAAATAATT	
35	GTCGAGAGGAAACATGAAAGTATTTTCATAAT	
36	CGCAAGACTTAATGGAAACAGTACTTACAAAA	
37	AGGAAGGGCGCGTAACCACCACACTTACCGCC	
38	GCTGTAGGCATCTGCCAGTTTG	
39	CAATACTGTAAGAATACGTGGCACCGAACG	III
40	CCATTCAGGCTGCGCATTCCACACAACATAAATGAATC	
41	AGCTTGCTACAACCATCGCCACGCCAACTTT	
42	GGCCAACCTCCACTATTAAGAACAAGTTTTT	
43	TCTGTCCAGACGACGATTGAGAATCGCCATATGAGACTAC	I; II
44	CCGCCTCACAGAATCAAGTTTGATGATTAA	
45	GGCATTTTCCGGTCATAGCCCC	
46	GCCAACATCAAAGGTAAAGTAAT	
47	ACCGAGGAAACACCAGAAGGAA	
48	CACCAGTCAATATCCAGAACAATACCGCCGCG	I; II; III
49	GATTAGCGGGGTTTTGTCAAGAGAAGGATTAG	
50	TTGGGAATGGAGGTTGAGGCAGGTTTACCGT	
51	CATATTATCGCGCCCAATAGCAAG	
52	CTTATFAGCGTTTGCCATCTTAAGAGGCT	
53	ACTTTTTAAAGAACGCGAGAAAAGAAAAAG	
54	TGAGACGCCCTTATAAATCAAATTAGAGCT	
55	GTCAGAAGTTGCAAAAAGAGTTTTAGCTGCTC	
56	TCCAGTAAACAAGCCCAATAGGAAAAGTAAATG	III
57	CTGGCGAAAGGGGACCGAGCTCGAATTCGTTACCAG	
58	TTGACCCCGATTTTAAAGAACTGAACATAATG	
59	ATGTTACTAATAAGGCTTGCCCTGAAATAGCG	
60	TTGGGGTAATCAGAGCGGGAGCCGTTGTAG	
61	CAATGACATTCGAGGTGAATTTCTTAAACAGCTTG	
62	TGCGTTGCATTACAGGTAGAAAGAAAATCTAC	II

No.	Sequence	replaced in type
63	AGGCCGATGAACCATCACCCAAATCGTGGACT	
64	CAGATACAACCTCCAACAGGTCAAATATAAT	
65	ATACATTTAGCAGAAGATAAAAACACTTCTGAC	III
66	AAAATACGCGTCTTTCCAGACGTTCCCATGTA	III
67	TAAACAGTCAAACGGCGGATTGA	
68	CAAAATCAGTAGCGCGTTTTTCATCGCAATAAT	
69	CAAAAGGGGTGCGTGAGGCTTGACAGCGGT	I; II
70	AACAAGAGGCGCGGGAGAGGCGGTTGTTATC	
71	TGGTTTTAAAACGGAGATTTGTATCGAGGGTAG	
72	CAACATTAATGTGAGTTTGACCATTAGATACCTATTATA	
73	AGTTTTGTTAATGCCACTACGAAGAAAACGAA	I; II; III
74	TATTTTGCATCACGCAAATTAATAAACAGG	III
75	ACCTTATGCCAGCGATTATACCAACTAAAGAC	
76	CATCAATATGCTTTGAATACCAAGATAAATCA	
77	GGCTTAACAATAAACAACATGT	
78	TTTTTCATTGTATGGGATTTTTGCTTCATTTTTC	III
79	TACTAATAGTAGTAGCATTATAGGAACCGCGAGCTGAAAAGGTAATGCTTT	
80	GGCAAAATGGCAACAGCTGATTGCAGAGGATC	I; II
81	AGAGGCAAAGGACGTTGGGAAGAATTCATCAG	I; II
82	TACAAACACATCGCCATTAATAATACAGACAA	III
83	ACAACATTGCTCACTGCCCGCTTTTGCCTAAT	
84	ATCAAGAGACAGATGAACGGTGTATGCGCCGA	
85	CATTGACATAGAGCCAGCAAAATCGAATAAGT	
86	TAACTATAGAGTGAATAACCTTGCAACGGATT	
87	GAAAGAGGTAATCTTGACAAGAACTGGATAGC	
88	AATTAATTTTTAGTTAATTTTCATCAAATAAGA	
89	CAATCATAAATCAACGTAACAAGCCAGAGG	II
90	CGGAAGCAATAACGCCAAAAGGAATGTGAATT	
91	GCAGCGAATAAAGGAATTGCGAATGGTTTAGT	III
92	ATAGGTGTGCCCCCTGCCTATTTCCACCGGAA	
93	GTCATAGCTTCGCTATTACGCCAG	
94	CATAGGCTGGCAATATTCATTG	
95	CAGTTAATATCACCGTACTCAGGAAATAATTT	
96	AACAACCTATATTAACACCGCCTGCAAAGGGAC	III
97	AAGTCAGATCACAATCAATAGAAATGAGCCAT	
98	TACGCCAGAACGAACTAACCAGGGTCTATGGA	
99	GTTGCTTTAAAGGGAGCCCCCGATAGAATAGC	
100	TGCCGTGAGCAACAGAGATAGAACCAGGTGAG	III
101	CGTAGGAATCATTACTTATCCCAATCCAAAATATCAG	
102	CACGCTGTCTAAAATATCTTTAGATTATAC	III
103	GCGGTGAGATAGATTAGAGCCGCTTGCGCAATT	III
104	CCTTTTACTAATGGAAGGGTTAGAGAATFGAG	I; II
105	CGCTCACAAACTGTTGGGAAGGGC	
106	ATATATTCAGCCTTTAATTTGTATCTAAGTGCC	
107	ATACCGATAGTCAGACCAGGCG	
108	CAAAAATCAGTAAAATGTTTAGACCCGGATATT	
109	CAACGGCTTTTCAGCGGAGTGAGACCTCAGAA	III
110	CCACCAGCCATTAGCAAGGCCGCAACATAT	
111	GAGTACCTTAGGAATACCACATTCGCTCATTA	
112	CAAGAACGGGTATTAACAGAGAGAATAACATAAGCGCAT	I; II
113	AGGGGACGACGACAGTTAGAGCTTAATTTGCTGGGATTAGA	
114	TCAGCTAATGCAGAACTATAAAGCCAACGCTCGGGTTATA	
115	TGCTGGGTACACGACCAGTAATAAACAGTGC	III
116	CAGTAGCGCCTCAGAGCCGCCACCCGTATAAA	
117	AATTTTCGAGGAAGTTTCCATTACTCATCT	III
118	TAAAGGCCTGAAAATCTCCAAAAAAGCCCGGA	
119	AGGGATAGGCGTCATACATGGCTTGCCCGCCAG	III
120	AACCACCGAGGATTTAGAAGTAAATTATCA	III
121	CTGGTGCCGGAAACCAAGTGTAAGCCTGGGGCCAGTCGG	
122	TAAAGTACCACGTTGGTGTAGATG	
123	TCGCGCAGCCTGATTATCAGATGAAATAGATA	
124	TTCTGAAATCGGGAGAAACAATTTCTGTAA	
125	GAACAACAGACAGCATCGGAACATCGCCCTG	III
126	TTGGGCGCGGGTTGAGTGTGTTTCACTAAATC	
127	CAAAGAAAAAAGAAGATGATGAAAGAAAAACAA	
128	GAGACTCCCTCAGTACCAGGCGGAGGTTTATC	
129	CGCCACCCAACCATCGATAGCAGCAGCAAACG	
130	TGCCCCAGCAGGCGAAAAATCCTGAGAGAGTTGCAGCAAGC	
131	CCGAGATACAGGGTGGTTTTTCTTTAATCATG	
132	CCGCCACCGTACTGGTAATAAGTTTCAGAGCCG	III
133	CTTAATGCGAAAGCCGGCGAACGTCGAAATC	II
134	TTGCCCGACTGTAGCATTCCGCGATAATGCAC	III
135	TCCTTGAAAAAATCATAGGTCTGATTAACAAC	
136	TATCAAAATCAGATGAATATACAGCCTTAGAA	
137	AACGGAATATAGCCGAACAAAGTT	

No.	Sequence	replaced in type
138	GATCGGTGCGGGCCTCTGTTTCCTGTGTGAAATTTGCGTA	
139	TTTCACGTGCTTTTTCGCGGATCGTCCTGCTCC	
140	CTACATTTTGACGCTCAAT	III
141	AAAAGTTTATTGACGGAAATTATTAGGGCGAC	II
142	TTTTTATACTCATAGTTAGCGTAAGTACAAAC	II; III
143	CTTACCAGGCGCCTGTTTATCAAC	
144	AATGGTCGTAGCCAGCTTTTCAT	
145	CTCGTTAGCGAGGTGCCGTAAGCCAGTTTGG	
146	TAAATTTAGATTGAGGGAGATCAACAAACGGA	
147	TTCAACAGACAGAGGCTTTGAGGAGCGCGAAA	III
148	GAGTCAATAGTGAATTTATCAACATAGCGATAGCTTAGAT	
149	TTATTTTGGGGTAATTGAGCGCTATAAGAAAC	
150	CAGCCTTTACCAAGTACCGCACTC	
151	AATCCCCCTCAGGCATCAATTC	
152	CAATATCTGGTCAGTTGGCACACCTTGCTGAACCTCAAAT	
153	TTGAGATTTTAAATTGCTCCTTTTGTATTTTGC	I; II
154	GTCCAATACAGAAAACGAGAATGAATATTTTC	
155	TGGTTTACAGAATTAACCTTAAATCATTTACGAGG	
156	CATAGTAATTCGAGCTTCAAAGCGTATGCAAC	
157	CGTCTGAACAACAGGAAAAACGCTCATG	
158	AATAGATAAGTCCTGAAGTATCATATGCGTTAAATCCAAT	
159	GTAAGCAGACCCAAAAGAAGTGGCCCTTTAGC	II
160	CAAAGTACTTTCAACTTTAATCATTTACGAGG	
161	TACAACGCACGTTATTAATCCTCATAAATTTT	II; III
162	GGGTAATAGGTCTTTACCCTGAATTTTCGCA	I; II
163	CACTACGTTAAAGGGATTTTAGACAGTAAAAAG	
164	ATTCAACCATGGTTTGAACAGGGAAAAATAC	II
165	AGCTATCATTACGCAGTATGTTACCGTAAT	
166	AAGCATAAGGCAAAGCGCCATTCG	
167	GAAACCTGAAAGGGCGAAAAACCGCGATGGCC	
168	ATTATTTCTGGTTGATATAAGTATAAAGGCTC	II
169	GGATGGCTATCGGCCTCAGGAAGA	
170	ATCAATAATCGGCTGTTGATAAATAAGGCGTTTTCTGACC	
171	TAGAAAATAGCAAGAAACAATGAATCTTTCCA	
172	AAACAGTTCTGCGGAATCGTCATATGACCTTC	
173	CACCATTAACCACCACCAGAGCCTTGATGAT	
174	CGTTTTAAGAGCAACACTATCATAGCTTGAGA	
175	GGAACCCTGACGAGCACGTATAACACATCACT	
176	AGCCATTGATGGATTATTTACATTGAAAAATC	III
177	GTCAGACTCCGGAACCAGAGCCACGGAAACCT	I; II
178	GTCAGTGCCCTCAGAACCGCCACATAGAAAG	III
179	ATTCTGGCTAGAAGAAGTCAAACCTGTACTATG	III
180	TACCAGTCAAGAATACACTAAAACAAACGGGT	
181	AGAGATAACGCAAAGACACCACGACCAGTAG	
182	CGACCGTGCTTTTCCTTATCATTC	
183	ACAGGAGTCTCAGAGCCACCACCCAAACAACCT	III
184	GAGCCTAAGGCTTATCCGGTATTC	
185	ATAAATTCGAGTAGTAAATTTGGACCCTCGT	
186	CTGAAAGCTCTTTGATTAGTAATAGTGCTTTTC	III
187	GTGAATTAGATATTCACAAACAAATTAAGCC	I; II
188	CCTGAGCACCACCAGAAGGAGCGGTTAGACTT	
189	ATAATAAGACATACATAAAGGTGGGAAAACGTC	
190	CTTTTTAACTATTAATTAATTTTCTAACAGTA	II
191	GGATTCTCCGTGGGAATGATTCCCAATTCGCAAAAAGAT	
192	GGCGCATCGTAACCGTCTCAACATGTTTTAAAAACCAGAC	
193	CGCGTCTGGCCTTCCATAAACCCTGTTTAGCTCCATAAAT	
194	GACTCCTTTTACCGAAGCCCTTTTTTATCCTG	
195	ATCGTCGCCTCCGGCTTAGGTTAACAGTAG	
196	GAGTGAGCTTTCCGGCACCGCTT	
197	CCGTAATGGGATAGGTGGTGTCTGGAAGTTTCAAATATCG	
198	TGACGGGGCCGCTACAGGGCGCATCGGCCT	
199	AGAATGGACTGAGTTTCGTCACCACGATCTAA	I; II; III
200	TCACGCTGAAGAAAGCGAAAGGAGCGGG	
201	GCGCTGGCAAGTGTAGCGG	III
202	TTACCAGAGCCCCGAAAGACTTCATTCCATA	
203	CCCGGGTATGTGCTGCAAGGCGAT	
204	AGACAGCCATCAGTGAGGCCACCGAGGAACGG	III
205	AGAGGCTTCAAAGCGGATTCATCGAACGAGT	
206	GCCAGTGCCAAGCTTGCATGAGGGTTTTCCAGTCAAGAC	
207	GCCTGGCCCTGTTTGTGATGGTGGTTGGCGAGAA	
208	CGCCTGATTAATCCTGATTGTTTGGGAGCACT	
209	AGATTTAGCGAGTAACAACCCGTC	
210	AGTCTGTCAATGGCTATTAGTCTTACTGATAG	III

Replacement staples of type I pads.

Line I1

No.	Sequence
104	CCTTTTACTAATGGAAGGGTTAGAGAATTGAGTTTTTTTTTTTTTTTT
43	TCTGTCCAGACGACGATTGAGAATCGCCATATGAGACTACTTTTTTTTTTTTT
80	GGCAAAATGGCAACAGCTGATTGCAGAGGATCTTTTTTTTTTTTTTTTT
48	CACCAGTCAATATCCAGAACAATACCGCCGCGTTTTTTTTTTTTTTTT

Line I2

No.	Sequence
112	CAAGAACGGGTATTAAACAGAGAGAATAACATAAGCGCATGACAAAGCCGACCACCAAAG
187	GTGAATTAGATATTCACAAACAAATTAAGCCGACAAAGCCGACCACCAAAG
33	TAGACGGGCAGCGCCAAAGACAAACATTAAGGACAAAGCCGACCACCAAAG
153	TTGAGATTTAATTGCTCCTTTTGATTTTTGCGACAAAGCCGACCACCAAAG
81	AGAGGCAAAGGACGTTGGGAAGAATTCATCAGGACAAAGCCGACCACCAAAG
73	AGTTTTGTTAATGCCACTACGAAGAAAACGAAGACAAAGCCGACCACCAAAG
199	AGAATGGACTGAGTTTCGTCAACCACGATCTAAGACAAAGCCGACCACCAAAG
29	GTTAATAAAAATCCTGAGAAAACCTGCACCGTGGACAAAGCCGACCACCAAAG
164	ATTCAACCATGGTTTGAACAGGGAATAACGACAAAGCCGACCACCAAAG
62	TGCGTTGCATTACAGGTAGAAAGAAAATCTACGACAAAGCCGACCACCAAAG
161	TACAACGCACGTTATTAATCCTCATAAATTTTGACAAAGCCGACCACCAAAG
142	TTTTTATACTCATAGTTAGCGTAAGTACAAACGACAAAGCCGACCACCAAAG
13	TCGCACTCCAGCCAGCTAACTCACATTAGGTCATAAGAATGACAAAGCCGACCACCAAAG
141	AAAAGTTTATTGACGGAAATTATTAGGGCGACGACAAAGCCGACCACCAAAG

Line I3

No.	Sequence
22	GACTTGCGGGAGGTTTGCACCCAGCTACAATTTAAGAAAAGACAAAGCCGACCACCAAAG
162	GGGTAATAGGTCTTTACCCCTGAATTTTCGACGACAAAGCCGACCACCAAAG
177	GTCAGACTCCGGAACCAGAGCCACGGAACCTGACAAAGCCGACCACCAAAG
69	CAAAAGGGGTGCTGAGGCTTGCAGACGGTGACAAAGCCGACCACCAAAG

Replacement staples of type II pads.

Line II1

No.	Sequence
104	CCTTTTACTAATGGAAGGGTTAGAGAATTGAGAAAAAAAAAAAAAAAAAAAA
43	TCTGTCCAGACGACGATTGAGAATCGCCATATGAGACTACAAAAAAAAAAAAAAAAAAAA
133	CTTAATGCGAAAGCCGGCGAACGTCGAAATCAAAAAAAAAAAAAAAAAAAAA
190	CTTTTTAACATTAATTAATTTTCTAACAGTAAAAAAAAAAAAAAAAAAAA
80	GGCAAAATGGCAACAGCTGATTGCAGAGGATCAAAAAAAAAAAAAAAAAAAAA
48	CACCAGTCAATATCCAGAACAATACCGCCGCAAAAAAAAAAAAAAAAAAAAA
30	GAAGGTTAAGAGCCAGCAGCAATGGCAGATTAAAAAAAAAAAAAAAAAAAAA

Line II2

No.	Sequence
112	CAAGAACGGGTATTAAACAGAGAGAATAACATAAGCGCATAAAAAAAAAAAAAAAAAAAA
187	GTGAATTAGATATTCACAAACAAATTAAGCCAAAAAAAAAAAAAAAAAAAA
33	TAGACGGGCAGCGCCAAAGACAAACATTAAGAAAAAAAAAAAAAAAAAAAA
153	TTGAGATTTAATTGCTCCTTTTGATTTTTGCAAAAAAAAAAAAAAAAAAAAA
81	AGAGGCAAAGGACGTTGGGAAGAATTCATCAGAAAAAAAAAAAAAAAAAAAA
73	AGTTTTGTTAATGCCACTACGAAGAAAACGAAAAAAAAAAAAAAAAAAAA
199	AGAATGGACTGAGTTTCGTCAACCACGATCTAAAAAAAAAAAAAAAAAAAA

Line II3	
No.	Sequence
89	CAATCATAAATCAACGTAACAAGCCAGAGGAAAAAAAAAAAAAAAAAAAA
22	GACTTGCGGGAGGTTTGCACCCAGCTACAATTTAAGAAAAAAAAAAAAAAAAAAAA
162	GGGTAATAGGTCTTTACCCTGAATTTTCGCAAAAAAAAAAAAAAAAAAAAA
159	GTAAGCAGACCCAAAAAGAACTGGCCCTTTAGCAAAAAAAAAAAAAAAAAAAAA
177	GTCAGACTCCGGAACCAGAGCCACGGAACCTAAAAAAAAAAAAAAAAAAAA
168	ATTATCTGGTTGATATAAGTATAAAGGCTCAAAAAAAAAAAAAAAAAAAAA
69	CAAAGGGGTCGCTGAGGCTTGCAGACGGTAAAAAAAAAAAAAAAAAAAA

Replacement staples of type III pads.

No.	Sequence
140	CTACATTTTGACGCTCAATAAAAAAAAA
100	TGCCTGAGCAACAGAGATAGAACCGAGGTGAGAAAAAAAAAAAA
39	CAATACTGTAAGAATACGTGGCACCGAACGAAAAAAAAAAAA
210	AGTCTGTCAATGGCTATTAGTCTTACTGATAGAAAAAAAAAAAA
142	TTTTTATACTCATAGTTAGCGTAAGTACAAACAAAAAAAAAAAA
66	AAAATACGCGTCTTTCCAGACGTTCCCATGTAAAAAAAAAAAA
78	TTTTTCATTGTATGGGATTTTGCTTCATTTTCAAAAAAAAAAAAA
109	CAACGGCTTTTCAGCGGAGTGAGACCTCAGAAAAAAAAAAAA
91	GCAGCGAATAAAGGAATTGCGAATGGTTTAGTAAAAAAAAAAAA
176	AGCCATTGATGGATTATTTACATTGAAAAATCAAAAAAAAAAAAA
115	TGCTGGTACACGACCAGTAATAAACAGTGCAAAAAAAAAAAAA
96	AACAACATATTAACACCGCCTGCAAAGGGACAAAAAAAAAAAA
65	ATACATTTAGCAGAAGATAAAAACACTTCTGACAAAAAAAAAAAA
82	TACAAACACATCGCCATTAATAATACAGACAAAAAAAAAAAA
134	TTGCCCGACTGTAGCATTCCGCGATAATGCACAAAAAAAAAAAA
199	AGAATGGACTGAGTTTCGTCACCCACGATCTAAAAAAAAAAAA
56	TCCAGTAACAAGCCCAATAGGAAAAGTAAATGAAAAAAAAAAAA
183	ACAGGAGTCTCAGAGCCACCACCCAAACAACCTAAAAAAAAAAAA
178	GTCAGTGCCCTCAGAACCGCCACATAGAAAGAAAAAAAAAAAA
30	GAAGGTTAAGAGCCAGCAGCAAATGGCAGATTAAAAAAAAAAAAA
179	ATTCCTGGCTAGAAGAACTCAAACCTGTAATGAAAAAAAAAAAA
186	CTGAAAGCTCTTTGATTAGTAATAGTGCTTTCAAAAAAAAAAAAA
74	TATTTTGCATCACGCAAATTAACATAACAGGAAAAAAAAAAAA
204	AGACAGCCATCAGTGAGGCCACCGAGGAACGGAAAAAAAAAAAA
73	AGTTTTGTAAATGCCACTACGAAGAAAACGAAAAAAAAAAAA
117	AATTTTCGAGGAAGTTTCCATTAATCATCTAAAAAAAAAAAA
147	TTCAACAGACAGAGGCTTTGAGGAGCGCGAAAAAAAAAAAA
125	GAACAACAGACAGCATCGGAACATCGCCTGAAAAAAAAAAAA
48	CACCAGTCAATATCCAGAACAATACCGCCGCGAAAAAAAAAAAA
103	GCGGTCAGATAGATTAGAGCCGTCTGGCAATTAAAAAAAAAAAAA
120	AACCACCGAGGATTTAGAAGTAAATATCAAAAAAAAAAAAA
4	CCCTAAAAATTCGACAACCTCGTATTTGCGGAAAAAAAAAAAA
161	TACAACGCACGTTATTAATCCTCATAAATTTTAAAAAAAAAAAA
18	CCGTAACAAAAGCGCAGTCTCTGAATCAGACGAAAAAAAAAAAA
119	AGGGATAGGCGTCATACATGGCTTGCCGCCAGAAAAAAAAAAAA
132	CCGCCACCGTACTGGTAATAAGTTTCAGAGCCGAAAAAAAAAAAA
25	ACCGCCACCTTGAGTAACAGTGCCCTCAGAACAACAAAAAAAAAAAA
3	TAAAGCATAATCAACAGTTGAAAGACCTACCAAAAAAAAAAAAA
102	CACGCTGTCTAAAATATCTTTAGATTATACAAAAAAAAAAAA
201	GCGCTGGCAAGTGTAGCGGAAAAAAAAAAAA

M13mp18

AATGCTACTACTATTAGTAGAATTGATGCCACCTTTTCAGCTCGCGCCCAATGAAAATATAGCTAAACAGGTTATTGACCATTTCGCAAAATGTATCTA
ATGGTCAAACATAACTCTACTCGTTTCGCAGAAATGGGAATCAACTGTTATATGGAATGAAACTCCAGACACCGTACTTTAGTTGCATATTTAAACATGT
TGAGCTAGACGATTATTCAGCAATTAAGCTCTAAGCCATCCGCAAAAATGACCTCTTATCAAAGGAGCAATTAAGGTTACTCTCTAATCTGACCTG
TTGGATTTTGGCTTCGGTTCGTTTCGTTTGAAGCTCGAATTAAGCCGATTAAGAGTCTTTCCGGCTTCCTCTTAATCTTTTGTAGCTAAACCCGCT
TTGCTTCTGACTATAATAGTCAGGGTAAAGACCTGATTTTGGATTATGGTCACTTCTCGTTTCTGAACTGTTTAAAGCAATTTGAGGGGATTCAATGAA
TATTTATGACGATTTCCGCGATTGGAGCGTATCCAGTCTAAACATTTTACTATTACCCTCTCGCAAAACTCTTTTGCAAAAGCCTCTCGCTATTTT
GGTTTTATCGTTCGTTGTAACAGGGTTATGATAGTGTTCCTTCTTAAAGTCTAAATGCAATTTCCCTTTTGGCGTTATGTATCTGCAATTTGATG
GTATTCCTAAATCTCAACTGATGAATCTTCTACCTGTAATAATGTTGTCCTGTTAGTTGCTTTTATTAACGTAGATTTTCTTCCCAACGCTCTGACTG
GTATAATGAGCCAGTTCTTAAATATCGCATAAGGTAATTCACAATGATTAAGTTAAATTAACCAATCTCAAGCCAAATTTACTCTGTTTTCGGTGT
CTCGTCAGGGCAAGCCTTATCTACTGAATGAGCAGCTTTGTACGTTGATTGGGTAATGAATATCCGTTCTTGTCAAGATTACTCTGTATGAAGTCA
GCCAGCCTATGCGCTGGTCTGTACACCGTTCATCTGTCTCTTTCAAAGTTGGTTCAGTTCCGTTCCCTTATGATTGACCGTCTGCGCTCGTCCGGCT
AAGTAACATGGAGCAGGTCGCGGATTTCGACACAATTTATCAGGCGATGATACAAAATCTCCGTTGTAATTTGTTTCGCGTTGGTATAATCGCTGGGGT
CAAGATGAGTGTTTAGTGTATCTTTTGGCTCTTTCGTTTAAAGTTGGTCCCTCGTAGTGGCATTACGATTTTACCCTTTAATGAAAATCTTCTC
ATGAAAAGCTTTTTCCTCAAAGCTCTGTAGCCTGTTGCTACCCCTGTTCCGATGCTGTTCTTCCGCTGCTGAGGGTACACCTCCGCAATTAAGCCTC
TTAATCCCTGCAAGCCTCAGGACCGCAATATATCGGTTATCGGTTGGGCGATGGTGTGTTGTCATTGTCGCGCAACTATCCGTTATCAAGCTGTTAAGAA
ATTACCTCGAAGCAAGCTGATAAACCAGTAAATTAAGGCTCCTTTTGGAGCTTTTTCAGCGTGAATAAATTTATTTATTCGCAAT
TCCTTTAGTTGTTCCCTTACTTCTACTCCGCTGAAACTGTTGAAAGTTGTTTAAAGCAAAATCCCATACAGAAAATTTATTTACTAACGCTGGAAAGAC
GACAAAATTTAGTCTGTTACCTAACTATGAGGGCTGTCTGTGAAATGCTACAGGCGTTGTAATTTGACTGGTACGAGAACTCAGTGTACGGTACAT
GGTTTCCTATTGGGCTTGTATTCCTGAAATGAGGTTGGTCCCTGAGGTTGGCGCTTCGAGGTTGGCGTTTCGAGGGTGGCGTTTCGAGGTTGGCGTT
TGAGTACGGTGTATACCTTATTCGGGCTATACTTATATCAACCTCTCGACGGCACTTATCCGCTGGTACTGAGCAAAACCCGCTAATCTAATCTCT
TCTTTGAGGAGTCTCAGCCTTAAATCTTTCATGTTTTCAGATAATAGTTTCCGAAATAGGCAGGGGCAATTAAGTGTATATACGGGCACTGTTACTC
AAGGCACTGAGCCCTGTAACCTTATACCGATACACTCTGTATCATCAAAAGCCATGTATGACGCTTACTGGAACGTTAAATTCAGAGCTGCGCTTT
CCATTTGCGCTTTAATGAGGATTTAATTTGTTTGTGAATATCAAGGCAATTCGTTGACTCGCTCAACCTCTCTGTAATGCTGGCGGGCTCTGGTGGT
GGTTTCGTTGGGGCTCTGAGGTTGGTGGCTCTGAGGGTGGCGCTTCGAGGTTGGCGCTTCGAGGAGCGGTTCCGGTGGTGGTTCGGTTCGGT
ATTTGATTTGAAAAGTGGCAACGCTAATAAGGGGCTATGACCGAAAATCCGATGAAAACCGCTACAGTCTGACGCTAAAGGCAAACTGATTC
TGTGCTACTGATTACCGTGTATCTGATGTTTTCATTGGTACGTTTCCGCTGACTTGTAAATGTAATGTTGCTACTGTTGTTTTCGGTCTAAT
TCCCAATGGCTCAAGTGGTACGGTGTATAATTCACCTTAAATGAATAATTTCCGCTCAATTTTACCTTCCCTCCCTCAATCGGTTGAATGTCGCCCT
TTGCTTTTGGCGCTGTAACCATATGAATTTTCTATTGATTGTAACAAAATAAATTTTCCGTTGGTGTCTTTGGTTCCTTTATATGTTGCCACCTT
TATGATGTTTCTACTGTTTTCAGCTATCGTAAATAAGGAGTTTCGTAACACCGCTTCGCTTTCGAGGTTTCGTTTGGTATTCGTTTATGTTGCTG
TCTTCTGGTAACTTGTTCGCTACTCTGTTACTTTCTTAAAGGGCTTCGGTAAAGATAGCTATTGCTATTTTCAATGTTTCTGCTCTAATTTGG
GCTTAACCTAATTTCTGTTGTTTCTCTGATATAGCGCTCAATTTACCTCTGACTTGTGTTTTCAGGGTGTTCAGTTAATGTTTTCGGTCTAATGCTG
CCCTGTTTATATGTTTCTCTCTGTAAAGGCTGCTATTTTCAATTTTACGTTAAACAAAATCGTTTCTTATTTGGATTGGGATAAATAATATGGCT
GTTTATTTTGAATGCAAAATTAGGCTCTGGAAGACGCTCGTTAGCGTTGGTAAGATTTCAGGATAAAATTTAGCTGGGTGCAAAATAGCAACTAATC
TTGATTTAAGGCTTCAAAACCTCCCGCAAGTCCGGAGGTTTCGCTAAACCGCTTCGCTTTCAGAAATCCCGTTCTTGAATACCGGATAAGCTTCTATAT
TATGGCGCGCTAATGATTCTCAGTAAATAAAGGCTTCGTTGTTCTCGATGAGTGGGTTACTGGTTAATACCCGTTCTTGGAAATGATAAG
GAAAGACAGCCGATTTGTTGTTTCTCATGTTTCTCATGTTTACGCTGTAATTTAGGATGTTTTCGTTTTCAGGGTGTTCAGTTAATGTTTTCGCT
GTTTCTGATTAGCTGAACATGTTGTTTATGTCGTCGTCGACAGAATTACTTTACCTTTTGTGCGTACTTTATATCTCTTATTTACTGGCTCGAAAAT
GCCTCTGCTAAATACATGTTGGCGTTGTTAAATATGGCGATTTCIAATTAAGCCCTACTGTTGAGCGTTGGCTTTATACCTGGTAAGAATTTGTATAAC
CATATGATACTAAACAGGCTTTTCTAGTAAATATGATTCCGCTGTTTATTTCTTAAATTAACCGCTTATTTATCACACCGTTCGTTTCAAAACCTTAA
ATTTAGGTCAGAAAGTAAATTAACATAAATAATTTGAAAAATTTCTCGCTTCTTTGCTTTCGCGATTGGATTGCAATCAGCATTTACATATAGTTA
TATAACCAACCTAAGCGGAGTTTAAAGGTTAGTCTCTCAGACTTATGTTTTCGATAAATTAACCTTCTCAGCGCTTAAATCTAAGCTATGCTAT
CGCTATGTTTCAAGGATTTCAAGGAAAATTAATAATAGCGACGATTTACAGGAAGCAAGGTTATTTACTCACATATATGATTTATGATGTTTCCCA
TAAAAAAGGTAATTAATGAAATGTTAAATGTAATTAATTTGTTTTCGTTGATGTTTTCATCATCTTCTTTTGTCTCAGGTAATGAAATGAATA
ATTCCGCTCTGCGCGATTTTGTAACCTTGGTATTCAAGCAATAGCGCAATCCGTTATTTGTTTTCGCGATGTAAGGTTACTGTTTACTGTAATTCATC
TGACGTTAAACCTGAAAATCTACGCAATTTCTTTATTTCTGTTTACGTCGAAATAATTTTGATATGGTAGGTTCTAACCTTCCATTTATTCAGAAAT
AATCCAAAATCAGGATTTATATTGATGAATTCAGCATCATGATAATCAGGAATATGATAAATCCGCTCCTCTGGTGGTTTCTTTGTTTCGCGAAA
ATGATAATGTTACTCAAACCTTTAAATTAATAACGTTTCGGGCAAGGATTTAATACGAGTTGTCGAATGTTTGTAAAGTCTAATACTTCTAATCTCTC
AAATGATTAATCTATTGACGGCTCTAATCTATTAGTTGTTAGTGTCTTAAAGATATTTAGATAAACCCTTCTCAATTCCTTCAACTGTTGATTGGCA
ACTGACCAGATATTGATTGAGGGTTTGTATTTGAGGTTTCAGCAAGGTGATGCTTTAGATTTTTCATTTGCTGCTGGCTCTCAGCGTGGCACTGTTGACG
CGGTTGTTAATACTGACCGCTCACCTCTGTTTATCTTCTGCTGGTGGTTCGTTTCGCTTATTTAATGGCGATGTTTAAAGGCTATCAGTTCCGCGATT
AAAGACTAATAGCCATTTCAAAAATATTGCTGTGCCAGTATCTTACGCTTACAGGTCAGAGGGTTCTATCTCTGTTGGCCAGAATGTCCTTTTAT
ACTGGTCTGTGACTGGTGAATCTGCCAATGTAATAATCCATTTACAGCAGATTGAGCGTCAAATGTAGGATTTCCATGAGCGTTTTCCTGTTGCAA
TGGCTGGCGGTAATTTGTTCTGGATATTACCAGCAAGCGGATAGTTGAGTCTTCTACTCAGGCAAGTGTATTACTAATCAAAAGAAAGTATTGCG
TACAACGGTAAATTTGCGTGTATGGACAGACTCTTTTACTCGGTGGCTCAGTATTATAAAAACACTTCTCAGGATTTGCGGTACCCTTCTGCTTAAA
ATCCCTTAAATCCGCTCCTGTTTACTCCCGCTCTGATTCTAACAGGAAAGCAAGCTTATACGTTGCTCGTCAAAGCAACATAGTACGCGCTGTAGC
GGCGAATTAAGCGCGGGGTTGTTGGTTACGCGCAGCGTACCGTACACTTCCAGCGCCCTAGCGCCGCTCTTTTCGCTTCTTCCCTTCCCTTTTC
TCGCCAGTTTCGCGGCTTCCCGCTCAAAGCTCAAATCGGGGCTCCCTTTAGGTTTCGATTTAGTGTCTTACGGCACCTCGACCCCAAAAACCTGTA
TTTGGGTTGATGTTTACGTTAGTGGCCATCGCCCTGATAGAGGTTTTCGCGCTTTGACGTTGGAGTCCAGCTTCTTAAATAGTGGACTCTTGTTCCTCA
ACTGGAACAACACTCAACCTATCTCGGGCTATTTCTTTGATTATAAGGATTTTGGCGATTTCGGAACCACATCAACAGGATTTTCGCTGCTGGG
GCAAAACAGCTGGACCGCTTGTGCAACTCTCTCAGGGCCAGGCGGTGAAGGGCAATCAGCTGTTGCCGCTCTACTGGTGAAGAAAACCCACCTG
CGCCCAATACGCAAAACCGCTTCCCGCGCGGTTGGCGATTCTAATAATGACAGCTGGCAGCAGAGTTTCCCGACTGGAAGCGGCGAGTGGCGCAAC
GCAATTAATGTAGTTAGCTCACTCATTAGGCACCCAGGCTTTACACTTATGCTTCCGCTCGTATGTTGTGGAATTTGAGCGGATAACAAATTTTC
ACACAGGAACAGCTATGACCATGATTACGAATTCGAGCTCGTACCCGGGATCTCTAGAGTCGACCTGAGGCAATGCAAGCTTGGCACTGGCGCTG
TTTTACAACGTCGTGACTGGGAAAACCTGGCGTTACCCAATTAATCGCTTTCAGCAGATCCCTTTCGCGAGCTGGCGTAATAGCGAAGAGCGCCG
CACCATCGCCCTTCCCAACAGTTGCGCAGCTGAATGGCAATGGCGCTTTTCCGCTGTTTCCGGCACCAAGCGGTGGCGAAAGCTGGCTGGTGGAGTGC
GATCTCTCGTAGGGCGGATCTGTCGTTCCCTCAAACCTGGCAGATGACCGGTTACGATGCGCCATCTACACCAACGTGACCTATCCCATTTACGGTCA
ATCCGCGTTTGTTCACGAGAAATCCGACGGTGTGTTACTCGCTCACATTTAATGTTGATGAAAGCTGGCTACAGGAAGGCCAGACCGAATTTTTT
TGATGGCTTCCATTTGTTAAAAAATGAGCTGATTTAACAATAATTAATGCGAATTTAACAATAATTAACGTTTAAATTTAATTTGCTTATA
CAATCTTCTGTTTGGGCTTTCTGATTTACACCGGGTACATGATTGACATGCTGATTTTACGATTTACCGTTACATGCTTCTGTTTGTGCTC
CAGACTCTCAGGCAATGACCTGATAGCTTTGATGATCTCTCAAAAATAGCTACCCCTCCGGCATTAAATTTACGCTAGAACCGTTGAAATCATATTT
GATGGTATTGACTGCTCCGGCTTTCTCACCTTTTGAATCTTTACCTACACATTTACTCAGGCATTGCAATTTAAATATATAGAGGTTCTAAAATTT
TTTTATCTCGTTGAAATAAAGCTTCTCCCGCAAAAGTATTACAGGTTCAATAGTTTTCGTTACAAACCGATTTAGCTTTATGCTGAGGCTTTATT
GCTTAATTTTCGTTAATGCTTGCCTGATGATTTTGGATTT

Appendix D

List of abbreviations

A	Adenine
a.u.	Arbitrary unit
AFM	Atomic force microscopy
APS	Ammonium persulfate
AuNP, AuNR	Gold nanoparticle, gold nanorod
b	Base
BCP	Block copolymer
bp	Base pair
C	Cytosine
CP	Conjugated polymer
cryo-EM	cryogenic electron microscopy
Da	Dalton
DBCO	Dibenzocyclooctyne
DDS	Dichloro-dimethyl silane
DNA	Deoxyribonucleic acid
ds	Double-stranded
EDTA	Ethylenediaminetetraacetic acid
EGNAS	Exhaustive Generation of Nucleic Acid Sequences software
FRET	Förster resonance energy transfer
fps	frames per second
G	Guanine
HPLC	High-pressure liquid chromatography
HPSF	High-purity salt free purification
HS-AFM	High-speed AFM
KCTP	Kumada catalyst-transfer polycondensation
LCST	Lower critical solution temperature
MWCO	Molecular weight cut-off
NA	Numerical aperture
nt	Nucleotide
NP	Nanoparticle
ODN	Oligodeoxynucleotide
P3(EO)3T-b-ODN	poly(3-tri(ethylene glycol)thiophene)-block-oligodeoxynucleotide
PAGE	Polyacrylamide gel electrophoresis
PAINT	Point accumulation for imaging in nanoscale topography
PALM	Photoactivated localisation microscopy
PNIPAAm	Poly(<i>N</i> -isopropylacrylamide)
PSF	Point spread function
QD	Quantum dot
rcf	Relative centrifugal force
RP-HPLC	Reversed-phase HPLC
rpm	Rounds per minute
SERS	Surface-enhanced Raman scattering
SHREC	Single-molecule high-resolution co-localisation
SIM	Structured illumination microscopy
SMLM	Single-molecule localisation microscopy
SPAAC	Strain-promoted azide-alkyne cycloaddition
SRM	super-resolution microscopy
ssDNA	single-stranded DNA
STED	Stimulated emission depletion

STORM	Stochastic optical reconstruction microscopy
T	Thymine
TAE	Trizma-acetic acid-EDTA buffer
TE	Trizma-EDTA buffer
TEAA	Triethylammonium acetate buffer
TEM	Transmission electron microscopy
TEMED	<i>N,N,N',N'</i> -tetramethylethane-1,2-diamine
TIRF	Total internal reflection fluorescence
UV/VIS	Ultraviolet-visible
2D, 3D	two-dimensional, three-dimensional

Bibliography

- [1] David Schor. *10 nm lithography process*. WikiChip Semiconductor and Computer Engineering. May 20, 2018. URL: https://en.wikichip.org/wiki/10_nm_lithography_process (visited on 05/30/2018).
- [2] Divita Mathur and Igor L. Medintz. “Analyzing DNA Nanotechnology: A Call to Arms For The Analytical Chemistry Community”. In: *Analytical Chemistry* 89.5 (Mar. 7, 2017), pp. 2646–2663. ISSN: 0003-2700. DOI: 10.1021/acs.analchem.6b04033. URL: <https://doi.org/10.1021/acs.analchem.6b04033> (visited on 03/25/2018).
- [3] Sumedh P. Surwade, Shichao Zhao, and Haitao Liu. “Molecular Lithography through DNA-Mediated Etching and Masking of SiO₂”. In: *Journal of the American Chemical Society* 133.31 (Aug. 10, 2011), pp. 11868–11871. ISSN: 0002-7863, 1520-5126. DOI: 10.1021/ja2038886. URL: <http://pubs.acs.org/doi/abs/10.1021/ja2038886> (visited on 11/09/2015).
- [4] Sumedh P. Surwade et al. “Nanoscale Growth and Patterning of Inorganic Oxides Using DNA Nanostructure Templates”. In: *Journal of the American Chemical Society* 135.18 (May 8, 2013), pp. 6778–6781. ISSN: 0002-7863, 1520-5126. DOI: 10.1021/ja401785h. URL: <http://pubs.acs.org/doi/abs/10.1021/ja401785h> (visited on 04/05/2016).
- [5] Cheikh Tidiane Diagne et al. “DNA Origami Mask for Sub-Ten-Nanometer Lithography”. In: *ACS Nano* 10.7 (July 26, 2016), pp. 6458–6463. ISSN: 1936-0851. DOI: 10.1021/acsnano.6b00413. URL: <http://dx.doi.org/10.1021/acsnano.6b00413> (visited on 09/13/2016).
- [6] Alex D. Herbert, Antony M. Carr, and Eva Hoffmann. “FindFoci: A Focus Detection Algorithm with Automated Parameter Training That Closely Matches Human Assignments, Reduces Human Inconsistencies and Increases Speed of Analysis”. In: *PLOS ONE* 9.12 (Dec. 5, 2014), e114749. ISSN: 1932-6203. DOI: 10.1371/journal.pone.0114749. URL: <http://journals.plos.org/plosone/article?id=10.1371/journal.pone.0114749> (visited on 06/02/2016).
- [7] Henning Sirringhaus. “25th Anniversary Article: Organic Field-Effect Transistors: The Path Beyond Amorphous Silicon”. In: *Advanced Materials* 26.9 (Mar. 1, 2014), pp. 1319–1335. ISSN: 1521-4095. DOI: 10.1002/adma.201304346. URL: <http://onlinelibrary.wiley.com/doi/10.1002/adma.201304346/abstract> (visited on 01/04/2017).
- [8] Pierre-Olivier Morin, Thomas Bura, and Mario Leclerc. “Realizing the full potential of conjugated polymers: innovation in polymer synthesis”. In: *Materials Horizons* 3.1 (2016), pp. 11–20. DOI: 10.1039/C5MH00164A. URL: <http://pubs.rsc.org/en/Content/ArticleLanding/2016/MH/C5MH00164A> (visited on 01/16/2018).
- [9] Joseph S. Chang, Antonio F. Facchetti, and Robert Reuss. “A Circuits and Systems Perspective of Organic/Printed Electronics: Review, Challenges, and Contemporary and Emerging Design Approaches”. In: *IEEE Journal on Emerging and Selected Topics in Circuits and Systems* 7.1 (Mar. 2017), pp. 7–26. ISSN: 2156-3357, 2156-3365. DOI: 10.1109/JETCAS.2017.2673863. URL: <http://ieeexplore.ieee.org/document/7875098/> (visited on 01/14/2018).
- [10] John E. Anthony. “Organic electronics: Addressing challenges”. In: *Nature Materials* 13.8 (Aug. 2014), pp. 773–775. ISSN: 14761122. DOI: 10.1038/nmat4034. URL: <http://search.ebscohost>.

- com/login.aspx?direct=true&db=a9h&AN=97162102&site=ehost-live (visited on 01/04/2017).
- [11] Tim Erdmann. “High Charge Carrier Mobility Polymers for Organic Transistors”. PhD thesis. Dresden: TU Dresden, Feb. 3, 2017. 267 pp.
- [12] Zhen-Gang Wang, Qing Liu, and Baoquan Ding. “Shape-Controlled Nanofabrication of Conducting Polymer on Planar DNA Templates”. In: *Chemistry of Materials* 26.11 (June 10, 2014), pp. 3364–3367. ISSN: 0897-4756, 1520-5002. DOI: 10.1021/cm501445u. URL: <http://pubs.acs.org/doi/abs/10.1021/cm501445u> (visited on 05/13/2015).
- [13] Jakob Bach Knudsen et al. “Routing of individual polymers in designed patterns”. In: *Nature Nanotechnology* 10.10 (Oct. 2015), pp. 892–898. ISSN: 1748-3387. DOI: 10.1038/nnano.2015.190. URL: <http://www.nature.com/nnano/journal/v10/n10/full/nnano.2015.190.html> (visited on 11/14/2015).
- [14] Mikael Madsen et al. “Preparation, Single-Molecule Manipulation, and Energy Transfer Investigation of a Polyfluorene- graft -DNA polymer”. In: *Chemistry - A European Journal* 23.44 (Aug. 4, 2017), pp. 10511–10515. ISSN: 09476539. DOI: 10.1002/chem.201702780. URL: <http://doi.wiley.com/10.1002/chem.201702780> (visited on 07/15/2018).
- [15] Caroline A. Schneider, Wayne S. Rasband, and Kevin W. Eliceiri. “NIH Image to ImageJ: 25 years of image analysis”. In: *Nature Methods* 9.7 (July 2012), pp. 671–675. ISSN: 1548-7091. DOI: 10.1038/nmeth.2089. URL: <http://www.nature.com/nmeth/journal/v9/n7/full/nmeth.2089.html> (visited on 06/02/2016).
- [16] J. D. Watson and F. H. C. Crick. “Molecular Structure of Nucleic Acids: A Structure for Deoxyribose Nucleic Acid”. In: *Nature* 171.4356 (Apr. 1953), pp. 737–738. ISSN: 1476-4687. DOI: 10.1038/171737a0. URL: <https://www.nature.com/articles/171737a0> (visited on 05/11/2018).
- [17] Julius Marmur and Paul Doty. “Thermal renaturation of deoxyribonucleic acids”. In: *Journal of molecular biology* 3.5 (1961), pp. 585–594. URL: <http://www.sciencedirect.com/science/article/pii/S0022283661800235> (visited on 03/10/2017).
- [18] Judith G. ; Voet Voet. *Biochemistry*. 4th ed. Hoboken, NJ: Wiley, 2011. XXV, 1428, I-53 S. : zahlr. Ill. und graph. Darst. ISBN: 978-0-470-91745-9 978-0-470-57095-1. URL: <http://swbplus.bsz-bw.de/bsz336937601cov.htm>.
- [19] S. G. Delcourt and R. D. Blake. “Stacking energies in DNA.” In: *Journal of Biological Chemistry* 266.23 (Aug. 15, 1991), pp. 15160–15169. ISSN: 0021-9258, 1083-351X. URL: <http://www.jbc.org/content/266/23/15160> (visited on 06/23/2018).
- [20] Richard A. Friedman and Barry Honig. “The electrostatic contribution to DNA base-stacking interactions”. In: *Biopolymers* 32.2 (Feb. 1992), pp. 145–159. ISSN: 1097-0282. DOI: 10.1002/bip.360320205. URL: <https://onlinelibrary.wiley.com/doi/abs/10.1002/bip.360320205> (visited on 06/20/2018).
- [21] R A Friedman and B Honig. “A free energy analysis of nucleic acid base stacking in aqueous solution.” In: *Biophysical Journal* 69.4 (Oct. 1995), pp. 1528–1535. ISSN: 0006-3495. URL: <https://www.ncbi.nlm.nih.gov/pmc/articles/PMC1236383/> (visited on 06/20/2018).
- [22] Annamaria Fiethen et al. “Stacking Energies for Average B-DNA Structures from the Combined Density Functional Theory and Symmetry-Adapted Perturbation Theory Approach”. In: *Journal of the American Chemical Society* 130.6 (Feb. 1, 2008), pp. 1802–1803. ISSN: 0002-7863. DOI: 10.1021/ja076781m. URL: <https://doi.org/10.1021/ja076781m> (visited on 06/23/2018).
- [23] Robin Holliday. “A mechanism for gene conversion in fungi”. In: *Genetics Research* 5.2 (July 1964), pp. 282–304. ISSN: 1469-5073, 0016-6723. DOI: 10.1017/S0016672300001233. URL: <https://www.cambridge.org/core/journals/genetics-research/article/mechanism-for-gene-conversion-in-fungi/E11586A6605C2A54C648BACEABECF954#> (visited on 07/29/2018).

- [24] Nadrian C. Seeman. “Nucleic acid junctions and lattices”. In: *Journal of Theoretical Biology* 99.2 (Nov. 21, 1982), pp. 237–247. ISSN: 0022-5193. DOI: 10.1016/0022-5193(82)90002-9. URL: <http://www.sciencedirect.com/science/article/pii/0022519382900029> (visited on 12/28/2016).
- [25] Neville Kallenbach, Rong-Ine Ma, and Nadrian C. Seeman. “An immobile nucleic acid junction constructed from oligonucleotides”. In: *Nature* 305 (Aug. 11, 1983), pp. 829–831. URL: <http://www.nature.com/nature/journal/v305/n5937/pdf/305829a0.pdf> (visited on 11/26/2015).
- [26] Junghuei Chen and Nadrian C. Seeman. “Synthesis from DNA of a molecule with the connectivity of a cube”. In: *Nature* 350.6319 (Apr. 18, 1991), pp. 631–633. ISSN: 0028-0836. DOI: 10.1038/350631a0. URL: <http://www.nature.com/nature/journal/v350/n6319/abs/350631a0.html> (visited on 12/28/2016).
- [27] Stephanie S. Simmel, Philipp C. Nickels, and Tim Liedl. “Wireframe and Tensegrity DNA Nanostructures”. In: *Accounts of Chemical Research* 47.6 (June 17, 2014), pp. 1691–1699. ISSN: 0001-4842. DOI: 10.1021/ar400319n. URL: <http://dx.doi.org/10.1021/ar400319n> (visited on 09/06/2016).
- [28] Nadrian C. Seeman. “Macromolecular Design, Nucleic Acid Junctions, and Crystal Formation”. In: *Journal of Biomolecular Structure and Dynamics* 3.1 (Aug. 1, 1985), pp. 11–34. ISSN: 0739-1102. DOI: 10.1080/07391102.1985.10508395. URL: <https://doi.org/10.1080/07391102.1985.10508395> (visited on 06/02/2018).
- [29] Tsu Ju Fu and Nadrian C. Seeman. “DNA double-crossover molecules”. In: *Biochemistry* 32.13 (Apr. 1, 1993), pp. 3211–3220. ISSN: 0006-2960. DOI: 10.1021/bi00064a003. URL: <https://doi.org/10.1021/bi00064a003> (visited on 06/02/2018).
- [30] Thomas H. LaBean et al. “Construction, Analysis, Ligation, and Self-Assembly of DNA Triple Crossover Complexes”. In: *Journal of the American Chemical Society* 122.9 (Mar. 1, 2000), pp. 1848–1860. ISSN: 0002-7863. DOI: 10.1021/ja993393e. URL: <https://doi.org/10.1021/ja993393e> (visited on 06/02/2018).
- [31] Zhiyong Shen et al. “Paranemic Crossover DNA: A Generalized Holliday Structure with Applications in Nanotechnology”. In: *Journal of the American Chemical Society* 126.6 (Feb. 1, 2004), pp. 1666–1674. ISSN: 0002-7863. DOI: 10.1021/ja038381e. URL: <https://doi.org/10.1021/ja038381e> (visited on 06/02/2018).
- [32] Yoel P. Ohayon et al. “Topological Linkage of DNA Tiles Bonded by Paranemic Cohesion”. In: *ACS Nano* 9.10 (Oct. 27, 2015), pp. 10296–10303. ISSN: 1936-0851. DOI: 10.1021/acsnano.5b04333. URL: <https://doi.org/10.1021/acsnano.5b04333> (visited on 06/02/2018).
- [33] Yoel P. Ohayon et al. “Covalent Linkage of One-Dimensional DNA Arrays Bonded by Paranemic Cohesion”. In: *ACS Nano* 9.10 (Oct. 27, 2015), pp. 10304–10312. ISSN: 1936-0851. DOI: 10.1021/acsnano.5b04335. URL: <https://doi.org/10.1021/acsnano.5b04335> (visited on 06/02/2018).
- [34] Arun Richard Chandrasekaran. “Programmable DNA scaffolds for spatially-ordered protein assembly”. In: *Nanoscale* 8.8 (2016), pp. 4436–4446. ISSN: 2040-3364, 2040-3372. DOI: 10.1039/C5NR08685J. URL: <http://xlink.rsc.org/?DOI=C5NR08685J> (visited on 09/06/2016).
- [35] Dage Liu et al. “Tensegrity: Construction of Rigid DNA Triangles with Flexible Four-Arm DNA Junctions”. In: *Journal of the American Chemical Society* 126.8 (Mar. 3, 2004), pp. 2324–2325. ISSN: 0002-7863. DOI: 10.1021/ja031754r. URL: <https://doi.org/10.1021/ja031754r> (visited on 06/02/2018).
- [36] Jianping Zheng et al. “From molecular to macroscopic via the rational design of a self-assembled 3D DNA crystal”. In: *Nature* 461.7260 (Sept. 3, 2009), pp. 74–77. ISSN: 0028-0836. DOI: 10.1038/nature08274. URL: <http://www.nature.com/nature/journal/v461/n7260/abs/nature08274.html> (visited on 12/30/2016).
- [37] Ruojie Sha et al. “Self-Assembled DNA Crystals: The Impact on Resolution of 5-Phosphates and the DNA Source”. In: *Nano Letters* 13.2 (Feb. 13, 2013), pp. 793–797. ISSN: 1530-6984. DOI: 10.1021/nl304550c. URL: <https://doi.org/10.1021/nl304550c> (visited on 06/02/2018).

- [38] Jiemin Zhao et al. “Post-Assembly Stabilization of Rationally Designed DNA Crystals”. In: *Angewandte Chemie International Edition* 54.34 (2015), pp. 9936–9939. ISSN: 1521-3773. DOI: 10.1002/anie.201503610. URL: <https://onlinelibrary.wiley.com/doi/abs/10.1002/anie.201503610> (visited on 06/02/2018).
- [39] Xiao Wang et al. “An Organic Semiconductor Organized into 3D DNA Arrays by “Bottom-up” Rational Design”. In: *Angewandte Chemie International Edition* 56.23 (2017), pp. 6445–6448. ISSN: 1521-3773. DOI: 10.1002/anie.201700462. URL: <https://onlinelibrary.wiley.com/doi/abs/10.1002/anie.201700462> (visited on 06/02/2018).
- [40] William M. Shih, Joel D. Quispe, and Gerald F. Joyce. “A 1.7-kilobase single-stranded DNA that folds into a nanoscale octahedron”. In: *Nature* 427.6975 (Feb. 12, 2004), pp. 618–621. ISSN: 0028-0836. DOI: 10.1038/nature02307. URL: <http://www.nature.com/nature/journal/v427/n6975/full/nature02307.html> (visited on 09/21/2016).
- [41] Bryan Wei, Mingjie Dai, and Peng Yin. “Complex shapes self-assembled from single-stranded DNA tiles”. In: *Nature* 485.7400 (May 30, 2012), pp. 623–626. ISSN: 0028-0836, 1476-4687. DOI: 10.1038/nature11075. URL: <http://www.nature.com/doi/10.1038/nature11075> (visited on 06/18/2015).
- [42] Yonggang Ke et al. “Three-Dimensional Structures Self-Assembled from DNA Bricks”. In: *Science* 338.6111 (Nov. 30, 2012), pp. 1177–1183. ISSN: 0036-8075, 1095-9203. DOI: 10.1126/science.1227268. URL: <http://science.sciencemag.org/content/338/6111/1177> (visited on 12/28/2016).
- [43] Kiyohiko Kawai and Tetsuro Majima. “Effect of hydrogen bonding on the photo-oxidation of DNA”. In: *Journal of Photochemistry and Photobiology C: Photochemistry Reviews* 3.1 (June 21, 2002), pp. 53–66. ISSN: 1389-5567. DOI: 10.1016/S1389-5567(02)00005-9. URL: <http://www.sciencedirect.com/science/article/pii/S1389556702000059> (visited on 06/25/2018).
- [44] Jakob Bach Knudsen. “Integration of Conjugated Polymers in DNA Nanostructures”. PhD thesis. Aarhus University, Denmark, 2014. URL: http://pure.au.dk/portal/files/82320107/Jakob_Bach_Knudsen_PhD_Thesis.pdf (visited on 05/13/2015).
- [45] Paul W. K. Rothemund. “Folding DNA to create nanoscale shapes and patterns”. In: *Nature* 440.7082 (Mar. 16, 2006), pp. 297–302. ISSN: 0028-0836, 1476-4679. DOI: 10.1038/nature04586. URL: <http://www.nature.com/doi/10.1038/nature04586> (visited on 03/23/2015).
- [46] Andreas Kociński et al. “Isothermal DNA origami folding: avoiding denaturing conditions for one-pot, hybrid-component annealing”. In: *Nanoscale* 7.5 (2015), pp. 2102–2106. ISSN: 2040-3364, 2040-3372. DOI: 10.1039/C4NR04176C. URL: <http://xlink.rsc.org/?DOI=C4NR04176C> (visited on 10/09/2016).
- [47] Wooli Bae et al. “Programmed folding of DNA origami structures through single-molecule force control”. In: *Nature Communications* 5 (Dec. 3, 2014), p. 5654. ISSN: 2041-1723. DOI: 10.1038/ncomms6654. URL: <http://www.nature.com/doi/10.1038/ncomms6654> (visited on 10/09/2016).
- [48] Lulu Qian et al. “Analogic China map constructed by DNA”. In: *Chinese Science Bulletin* 51.24 (Dec. 1, 2006), pp. 2973–2976. ISSN: 1001-6538, 1861-9541. DOI: 10.1007/s11434-006-2223-9. URL: <http://link.springer.com/article/10.1007/s11434-006-2223-9> (visited on 12/30/2016).
- [49] Ebbe S. Andersen et al. “Self-assembly of a nanoscale DNA box with a controllable lid”. In: *Nature* 459.7243 (May 7, 2009), pp. 73–76. ISSN: 0028-0836. DOI: 10.1038/nature07971. URL: <http://www.nature.com/nature/journal/v459/n7243/full/nature07971.html> (visited on 09/30/2016).
- [50] Shawn M. Douglas et al. “Self-assembly of DNA into nanoscale three-dimensional shapes”. In: *Nature* 459.7245 (May 21, 2009), pp. 414–418. ISSN: 0028-0836. DOI: 10.1038/nature08016. URL:

- <http://www.nature.com/nature/journal/v459/n7245/full/nature08016.html> (visited on 02/02/2016).
- [51] Hendrik Dietz, Shawn M. Douglas, and William M. Shih. “Folding DNA into Twisted and Curved Nanoscale Shapes”. In: *Science (New York, N.Y.)* 325.5941 (Aug. 7, 2009), pp. 725–730. ISSN: 0036-8075. DOI: 10.1126/science.1174251. URL: <https://www.ncbi.nlm.nih.gov/pmc/articles/PMC2737683/> (visited on 03/24/2018).
- [52] Dongran Han et al. “DNA origami with complex curvatures in three-dimensional space”. In: *Science (New York, N.Y.)* 332.6027 (Apr. 15, 2011), pp. 342–346. ISSN: 1095-9203. DOI: 10.1126/science.1202998.
- [53] Fei Zhang et al. “Complex wireframe DNA origami nanostructures with multi-arm junction vertices”. In: *Nature Nanotechnology* 10.9 (July 20, 2015), pp. 779–784. ISSN: 1748-3387, 1748-3395. DOI: 10.1038/nnano.2015.162. URL: <http://www.nature.com/doi/10.1038/nnano.2015.162> (visited on 09/03/2015).
- [54] Erik Benson et al. “DNA rendering of polyhedral meshes at the nanoscale”. In: *Nature* 523.7561 (July 23, 2015), pp. 441–444. ISSN: 0028-0836. DOI: 10.1038/nature14586. URL: <http://www.nature.com/nature/journal/v523/n7561/abs/nature14586.html> (visited on 01/07/2016).
- [55] Michael Matthies, Nayan P. Agarwal, and Thorsten L. Schmidt. “Design and Synthesis of Triangulated DNA Origami Trusses”. In: *Nano Letters* 16.3 (Mar. 9, 2016), pp. 2108–2113. ISSN: 1530-6984, 1530-6992. DOI: 10.1021/acs.nanolett.6b00381. URL: <http://pubs.acs.org/doi/abs/10.1021/acs.nanolett.6b00381> (visited on 05/18/2016).
- [56] Nayan P. Agarwal et al. “Structural Transformation of Wireframe DNA Origami via DNA Polymerase Assisted Gap-Filling”. In: *ACS Nano* 12.3 (Mar. 27, 2018), pp. 2546–2553. ISSN: 1936-0851. DOI: 10.1021/acs.nano.7b08345. URL: <https://doi.org/10.1021/acs.nano.7b08345> (visited on 06/20/2018).
- [57] Veikko Linko and Mauri A. Kostiainen. “Automated design of DNA origami”. In: *Nature Biotechnology* 34.8 (Aug. 2016), pp. 826–827. ISSN: 1087-0156. DOI: 10.1038/nbt.3647. URL: <http://www.nature.com/nbt/journal/v34/n8/full/nbt.3647.html> (visited on 09/19/2016).
- [58] P. Lourdu Xavier and Arun Richard Chandrasekaran. “DNA-based construction at the nanoscale: emerging trends and applications”. In: *Nanotechnology* 29.6 (Jan. 10, 2018), p. 062001. ISSN: 0957-4484. DOI: 10.1088/1361-6528/aaa120. URL: <http://iopscience.iop.org/article/10.1088/1361-6528/aaa120/meta> (visited on 01/24/2018).
- [59] Shawn M. Douglas et al. “Rapid prototyping of 3D DNA-origami shapes with caDNAno”. In: *Nucleic Acids Research* 37.15 (Aug. 2009), pp. 5001–5006. ISSN: 0305-1048. DOI: 10.1093/nar/gkp436. URL: <http://www.ncbi.nlm.nih.gov/pmc/articles/PMC2731887/> (visited on 06/12/2016).
- [60] Carlos Ernesto Castro et al. “A primer to scaffolded DNA origami”. In: *Nature Methods* 8.3 (Mar. 2011), pp. 221–229. ISSN: 1548-7091. DOI: 10.1038/nmeth.1570. URL: <http://www.nature.com/nmeth/journal/v8/n3/full/nmeth.1570.html> (visited on 09/21/2016).
- [61] Do-Nyun Kim et al. “Quantitative prediction of 3D solution shape and flexibility of nucleic acid nanostructures”. In: *Nucleic Acids Research* 40.7 (Apr. 2012), pp. 2862–2868. ISSN: 1362-4962. DOI: 10.1093/nar/gkr1173.
- [62] Rémi Veneziano et al. “Designer nanoscale DNA assemblies programmed from the top down”. In: *Science* 352.6293 (June 24, 2016), pp. 1534–1534. ISSN: 0036-8075, 1095-9203. DOI: 10.1126/science.aaf4388. URL: <http://science.sciencemag.org/content/352/6293/1534> (visited on 03/24/2018).
- [63] Nadrian C Seeman. “Interactive design and manipulation of macro-molecular architecture utilizing nucleic acid junctions”. In: *Journal of Molecular Graphics* 3.2 (June 1, 1985), pp. 34–39. ISSN: 0263-7855. DOI: 10.1016/0263-7855(85)80001-1. URL: <http://www.sciencedirect.com/science/article/pii/0263785585800011> (visited on 04/03/2018).

- [64] Nadrian C. Seeman. “De Novo Design of Sequences for Nucleic Acid Structural Engineering”. In: *Journal of Biomolecular Structure and Dynamics* 8.3 (Dec. 1, 1990), pp. 573–581. ISSN: 0739-1102. DOI: 10.1080/07391102.1990.10507829. URL: <https://doi.org/10.1080/07391102.1990.10507829> (visited on 04/03/2018).
- [65] Bryan Wei, Zhengyu Wang, and Yongli Mi. “Uniquimer: A de Novo DNA Sequence Generation Computer Software for DNA Self-assembly”. In: *DNA Computing*. Ed. by Chengde Mao and Takashi Yokomori. Berlin, Heidelberg: Springer Berlin Heidelberg, 2006, pp. 266–273. ISBN: 978-3-540-68423-7.
- [66] Jeffrey J. Birac et al. “Architecture with GIDEON, A Program for Design in Structural DNA Nanotechnology”. In: *Journal of molecular graphics & modelling* 25.4 (Dec. 2006), pp. 470–480. ISSN: 1093-3263. DOI: 10.1016/j.jmgm.2006.03.005. URL: <https://www.ncbi.nlm.nih.gov/pmc/articles/PMC3465968/> (visited on 04/03/2018).
- [67] Sean Williams et al. “Tiamat: A Three-Dimensional Editing Tool for Complex DNA Structures”. In: *DNA Computing*. Ed. by Ashish Goel, Friedrich C. Simmel, and Petr Sosik. Vol. 5347. Berlin, Heidelberg: Springer Berlin Heidelberg, 2009, pp. 90–101. ISBN: 978-3-642-03075-8 978-3-642-03076-5. DOI: 10.1007/978-3-642-03076-5_8. URL: http://link.springer.com/10.1007/978-3-642-03076-5_8 (visited on 04/03/2018).
- [68] Jinhao Zhu et al. “UNIQUIMER 3D, a software system for structural DNA nanotechnology design, analysis and evaluation”. In: *Nucleic Acids Research* 37.7 (Apr. 2009), pp. 2164–2175. ISSN: 1362-4962. DOI: 10.1093/nar/gkp005.
- [69] Fan Hong et al. “DNA Origami: Scaffolds for Creating Higher Order Structures”. In: *Chemical Reviews* 117.20 (Oct. 25, 2017), pp. 12584–12640. ISSN: 0009-2665. DOI: 10.1021/acs.chemrev.6b00825. URL: <http://dx.doi.org/10.1021/acs.chemrev.6b00825> (visited on 01/24/2018).
- [70] Ingo H. Stein et al. “Single-Molecule FRET Ruler Based on Rigid DNA Origami Blocks”. In: *ChemPhysChem* 12.3 (Feb. 25, 2011), pp. 689–695. ISSN: 1439-7641. DOI: 10.1002/cphc.201000781. URL: <http://onlinelibrary.wiley.com/doi/10.1002/cphc.201000781/abstract> (visited on 09/09/2016).
- [71] Na Wu and Itamar Willner. “pH-Stimulated Reconfiguration and Structural Isomerization of Origami Dimer and Trimer Systems”. In: *Nano Letters* (Sept. 2, 2016). ISSN: 1530-6984. DOI: 10.1021/acs.nanolett.6b03418. URL: <http://dx.doi.org/10.1021/acs.nanolett.6b03418> (visited on 09/18/2016).
- [72] S. L. Beaucage and M. H. Caruthers. “Deoxynucleoside phosphoramidites—A new class of key intermediates for deoxypolynucleotide synthesis”. In: *Tetrahedron Letters* 22.20 (Jan. 1, 1981), pp. 1859–1862. ISSN: 0040-4039. DOI: 10.1016/S0040-4039(01)90461-7. URL: <http://www.sciencedirect.com/science/article/pii/S0040403901904617> (visited on 06/02/2018).
- [73] M. H. Caruthers et al. “Chemical synthesis of deoxyoligonucleotides by the phosphoramidite method”. In: *Methods in Enzymology*. Vol. 154. Recombinant DNA Part E. Academic Press, Jan. 1, 1987, pp. 287–313. DOI: 10.1016/0076-6879(87)54081-2. URL: <http://www.sciencedirect.com/science/article/pii/0076687987540812> (visited on 06/02/2018).
- [74] Serge L. Beaucage and Radhakrishnan P. Iyer. “Advances in the Synthesis of Oligonucleotides by the Phosphoramidite Approach”. In: *Tetrahedron* 48.12 (Mar. 20, 1992), pp. 2223–2311. ISSN: 0040-4020. DOI: 10.1016/S0040-4020(01)88752-4. URL: <http://www.sciencedirect.com/science/article/pii/S0040402001887524> (visited on 06/02/2018).
- [75] Kai Liu et al. “Nucleic Acid Chemistry in the Organic Phase: From Functionalized Oligonucleotides to DNA Side Chain Polymers”. In: *Journal of the American Chemical Society* 136.40 (Oct. 8, 2014), pp. 14255–14262. ISSN: 0002-7863, 1520-5126. DOI: 10.1021/ja5080486. URL: <http://pubs.acs.org/doi/abs/10.1021/ja5080486> (visited on 03/24/2015).
- [76] Barbara Saccà and Christof M. Niemeyer. “DNA Origami: The Art of Folding DNA”. In: *Angewandte Chemie International Edition* 51.1 (Jan. 2, 2012), pp. 58–66. ISSN: 14337851. DOI:

- 10.1002/anie.201105846. URL: <http://doi.wiley.com/10.1002/anie.201105846> (visited on 09/08/2016).
- [77] Alfred Kick, Martin Bönsch, and Michael Mertig. “EGNAS: an exhaustive DNA sequence design algorithm”. In: *BMC Bioinformatics* 13 (2012), p. 138. ISSN: 1471-2105. DOI: 10.1186/1471-2105-13-138. URL: <http://dx.doi.org/10.1186/1471-2105-13-138> (visited on 09/08/2016).
- [78] Baoquan Ding et al. “Gold Nanoparticle Self-Similar Chain Structure Organized by DNA Origami”. In: *Journal of the American Chemical Society* 132.10 (Mar. 17, 2010), pp. 3248–3249. ISSN: 0002-7863, 1520-5126. DOI: 10.1021/ja9101198. URL: <http://pubs.acs.org/doi/abs/10.1021/ja9101198> (visited on 10/12/2015).
- [79] Anton Kuzyk et al. “DNA-based self-assembly of chiral plasmonic nanostructures with tailored optical response”. In: *Nature* 483.7389 (Mar. 14, 2012), pp. 311–314. ISSN: 0028-0836, 1476-4687. DOI: 10.1038/nature10889. URL: <http://www.nature.com/doifinder/10.1038/nature10889> (visited on 10/26/2015).
- [80] Fatih N. Gür et al. “Toward Self-Assembled Plasmonic Devices: High-Yield Arrangement of Gold Nanoparticles on DNA Origami Templates”. In: *ACS Nano* (May 12, 2016). ISSN: 1936-0851, 1936-086X. DOI: 10.1021/acsnano.6b01537. URL: <http://pubs.acs.org/doi/abs/10.1021/acsnano.6b01537> (visited on 05/18/2016).
- [81] Anirban Samanta et al. “Fluorescence Quenching of Quantum Dots by Gold Nanoparticles: A Potential Long Range Spectroscopic Ruler”. In: *Nano Letters* 14.9 (Sept. 10, 2014), pp. 5052–5057. ISSN: 1530-6984, 1530-6992. DOI: 10.1021/nl501709s. URL: <http://pubs.acs.org/doi/abs/10.1021/nl501709s> (visited on 03/30/2015).
- [82] Barbara Saccà et al. “Orthogonal Protein Decoration of DNA Origami”. In: *Angewandte Chemie International Edition* 49.49 (Dec. 3, 2010), pp. 9378–9383. ISSN: 1521-3773. DOI: 10.1002/anie.201005931. URL: <http://onlinelibrary.wiley.com/doi/10.1002/anie.201005931/abstract> (visited on 09/21/2016).
- [83] Wei Li et al. “Controlled Nucleation and Growth of DNA Tile Arrays within Prescribed DNA Origami Frames and Their Dynamics”. In: *Journal of the American Chemical Society* 136.10 (Mar. 12, 2014), pp. 3724–3727. ISSN: 0002-7863, 1520-5126. DOI: 10.1021/ja411446q. URL: <http://pubs.acs.org/doi/abs/10.1021/ja411446q> (visited on 03/30/2015).
- [84] S. P. Surwade et al. “Nanoscale patterning of self-assembled monolayers using DNA nanostructure templates”. In: *Chem. Commun.* 52.8 (2016), pp. 1677–1680. ISSN: 1359-7345, 1364-548X. DOI: 10.1039/C5CC08183A. URL: <http://xlink.rsc.org/?DOI=C5CC08183A> (visited on 09/19/2016).
- [85] Boxuan Shen et al. “Custom-shaped metal nanostructures based on DNA origami silhouettes”. In: *Nanoscale* 7.26 (2015), pp. 11267–11272. ISSN: 2040-3364, 2040-3372. DOI: 10.1039/C5NR02300A. URL: <http://xlink.rsc.org/?DOI=C5NR02300A> (visited on 01/07/2016).
- [86] Feng Zhou et al. “Mechanistic Study of the Nanoscale Negative-Tone Pattern Transfer from DNA Nanostructures to SiO₂”. In: *Chemistry of Materials* 27.5 (Mar. 10, 2015), pp. 1692–1698. ISSN: 0897-4756, 1520-5002. DOI: 10.1021/cm5044914. URL: <http://pubs.acs.org/doi/abs/10.1021/cm5044914> (visited on 04/05/2016).
- [87] Mengzhen Zhao et al. “Cavity-Type DNA Origami-Based Plasmonic Nanostructures for Raman Enhancement”. In: *ACS Applied Materials & Interfaces* 9.26 (July 5, 2017), pp. 21942–21948. ISSN: 1944-8244, 1944-8252. DOI: 10.1021/acsmi.7b05959. URL: <http://pubs.acs.org/doi/10.1021/acsmi.7b05959> (visited on 01/06/2018).
- [88] Akinori Kuzuya, Kentaro Numajiri, and Makoto Komiyama. “Accommodation of a Single Protein Guest in Nanometer-Scale Wells Embedded in a “DNA Nanotape””. In: *Angewandte Chemie International Edition* 47.18 (Apr. 21, 2008), pp. 3400–3402. ISSN: 1521-3773. DOI: 10.1002/anie.200800028. URL: <http://onlinelibrary.wiley.com/doi/10.1002/anie.200800028/abstract> (visited on 09/21/2016).

- [89] Akinori Kuzuya et al. “Precisely programmed and robust 2D streptavidin nanoarrays by using periodical nanometer-scale wells embedded in DNA origami assembly”. In: *Chembiochem: A European Journal of Chemical Biology* 10.11 (July 20, 2009), pp. 1811–1815. ISSN: 1439-7633. DOI: 10.1002/cbic.200900229.
- [90] Akinori Kuzuya et al. “Programmed Nanopatterning of Organic/Inorganic Nanoparticles Using Nanometer-Scale Wells Embedded in a DNA Origami Scaffold”. In: *Small* 6.23 (Dec. 6, 2010), pp. 2664–2667. ISSN: 1613-6829. DOI: 10.1002/smll.201001484. URL: <http://onlinelibrary.wiley.com/doi/10.1002/smll.201001484/abstract> (visited on 09/22/2016).
- [91] Takahiro Yamazaki et al. “Orthogonal enzyme arrays on a DNA origami scaffold bearing size-tunable wells”. In: *Nanoscale* 6.15 (June 30, 2014), p. 9122. ISSN: 2040-3364, 2040-3372. DOI: 10.1039/C4NR01598C. URL: <http://xlink.rsc.org/?DOI=C4NR01598C> (visited on 09/21/2016).
- [92] Masayuki Endo and Hiroshi Sugiyama. “Single-Molecule Imaging of Dynamic Motions of Biomolecules in DNA Origami Nanostructures Using High-Speed Atomic Force Microscopy”. In: *Accounts of Chemical Research* 47.6 (June 17, 2014), pp. 1645–1653. ISSN: 0001-4842. DOI: 10.1021/ar400299m. URL: <http://dx.doi.org/10.1021/ar400299m> (visited on 09/06/2016).
- [93] Xibo Shen et al. “Three-Dimensional Plasmonic Chiral Tetramers Assembled by DNA Origami”. In: *Nano Letters* 13.5 (May 8, 2013), pp. 2128–2133. ISSN: 1530-6984, 1530-6992. DOI: 10.1021/nl400538y. URL: <http://pubs.acs.org/doi/abs/10.1021/nl400538y> (visited on 10/26/2015).
- [94] Guoliang Ke et al. “Directional Regulation of Enzyme Pathways through the Control of Substrate Channeling on a DNA Origami Scaffold”. In: *Angewandte Chemie International Edition* 55.26 (June 20, 2016), pp. 7483–7486. ISSN: 1521-3773. DOI: 10.1002/anie.201603183. URL: <http://onlinelibrary.wiley.com/doi/10.1002/anie.201603183/abstract> (visited on 09/15/2016).
- [95] Anirban Samanta, Zhengtao Deng, and Yan Liu. “Infrared emitting quantum dots: DNA conjugation and DNA origami directed self-assembly”. In: *Nanoscale* 6.9 (2014), p. 4486. ISSN: 2040-3364, 2040-3372. DOI: 10.1039/c3nr06578b. URL: <http://xlink.rsc.org/?DOI=c3nr06578b> (visited on 03/30/2015).
- [96] Jie Chao et al. “DNA-based plasmonic nanostructures”. In: *Materials Today* 18.6 (July 2015), pp. 326–335. ISSN: 1369-7021. DOI: 10.1016/j.mattod.2015.01.018. URL: <http://www.sciencedirect.com/science/article/pii/S136970211500019X> (visited on 09/08/2016).
- [97] L. Wang and G. Arrabito. “Hybrid, multiplexed, functional DNA nanotechnology for bioanalysis”. In: *The Analyst* 140.17 (2015), pp. 5821–5848. ISSN: 0003-2654, 1364-5528. DOI: 10.1039/C5AN00861A. URL: <http://xlink.rsc.org/?DOI=C5AN00861A> (visited on 09/21/2016).
- [98] Chao Zhou, Xiaoyang Duan, and Na Liu. “DNA-Nanotechnology-Enabled Chiral Plasmonics: From Static to Dynamic”. In: *Accounts of Chemical Research* 50.12 (Dec. 19, 2017), pp. 2906–2914. ISSN: 0001-4842. DOI: 10.1021/acs.accounts.7b00389. URL: <http://dx.doi.org/10.1021/acs.accounts.7b00389> (visited on 01/28/2018).
- [99] Thomas Schlichthaerle et al. “DNA nanotechnology and fluorescence applications”. In: *Current Opinion in Biotechnology* 39 (June 2016), pp. 41–47. ISSN: 09581669. DOI: 10.1016/j.copbio.2015.12.014. URL: <http://linkinghub.elsevier.com/retrieve/pii/S0958166915001779> (visited on 04/05/2016).
- [100] Gideon I. Livshits et al. “Long-range charge transport in single G-quadruplex DNA molecules”. In: *Nature Nanotechnology* 9.12 (Dec. 2014), pp. 1040–1046. ISSN: 1748-3395. DOI: 10.1038/nnano.2014.246. URL: <https://www.nature.com/articles/nnano.2014.246> (visited on 03/25/2018).
- [101] Michael Mertig et al. “DNA as a Selective Metallization Template”. In: *Nano Letters* 2.8 (Aug. 1, 2002), pp. 841–844. ISSN: 1530-6984. DOI: 10.1021/nl025612r. URL: <https://doi.org/10.1021/nl025612r> (visited on 06/20/2018).
- [102] Albert M. Hung et al. “Large-area spatially ordered arrays of gold nanoparticles directed by lithographically confined DNA origami”. In: *Nature Nanotechnology* 5.2 (Feb. 2010), pp. 121–126.

- ISSN: 1748-3387, 1748-3395. DOI: 10.1038/nnano.2009.450. URL: <http://www.nature.com/doifinder/10.1038/nnano.2009.450> (visited on 10/26/2015).
- [103] Anthony C. Pearson et al. "DNA Origami Metallized Site Specifically to Form Electrically Conductive Nanowires". In: *The Journal of Physical Chemistry B* 116.35 (Sept. 6, 2012), pp. 10551–10560. ISSN: 1520-6106. DOI: 10.1021/jp302316p. URL: <http://dx.doi.org/10.1021/jp302316p> (visited on 09/19/2016).
- [104] Yanli Geng et al. "Electrically Conductive Gold- and Copper-Metallized DNA Origami Nanostructures". In: *Langmuir* 29.10 (Mar. 12, 2013), pp. 3482–3490. ISSN: 0743-7463. DOI: 10.1021/la305155u. URL: <http://dx.doi.org/10.1021/la305155u> (visited on 09/19/2016).
- [105] Bezu Teschome et al. "Temperature-dependent charge transport through individually contacted DNA origami-based Au nanowires". In: *Langmuir* (Sept. 14, 2016). ISSN: 0743-7463. DOI: 10.1021/acs.langmuir.6b01961. URL: <http://dx.doi.org/10.1021/acs.langmuir.6b01961> (visited on 09/18/2016).
- [106] Hareem T. Maune et al. "Self-assembly of carbon nanotubes into two-dimensional geometries using DNA origami templates". In: *Nature Nanotechnology* 5.1 (Jan. 2010), pp. 61–66. ISSN: 1748-3387. DOI: 10.1038/nnano.2009.311. URL: <http://www.nature.com/nnano/journal/v5/n1/full/nnano.2009.311.html> (visited on 05/14/2015).
- [107] Robert Schreiber et al. "Ordering Gold Nanoparticles with DNA Origami Nanoflowers". In: *ACS Nano* 10.8 (Aug. 23, 2016), pp. 7303–7306. ISSN: 1936-0851. DOI: 10.1021/acsnano.6b03076. URL: <http://dx.doi.org/10.1021/acsnano.6b03076> (visited on 09/01/2016).
- [108] Xibo Shen et al. "Rolling Up Gold Nanoparticle-Dressed DNA Origami into Three-Dimensional Plasmonic Chiral Nanostructures". In: *Journal of the American Chemical Society* 134.1 (Jan. 11, 2012), pp. 146–149. ISSN: 0002-7863, 1520-5126. DOI: 10.1021/ja209861x. URL: <http://pubs.acs.org/doi/abs/10.1021/ja209861x> (visited on 10/26/2015).
- [109] Ye Tian et al. "Lattice engineering through nanoparticle-DNA frameworks". In: *Nature Materials* 15.6 (2016), pp. 654–661. ISSN: 1476-1122. DOI: 10.1038/nmat4571.
- [110] Zhong Chen et al. "Strong Chiroptical Activities in Gold Nanorod Dimers Assembled Using DNA Origami Templates". In: *ACS Photonics* 2.3 (Mar. 18, 2015), pp. 392–397. DOI: 10.1021/ph500434f. URL: <http://dx.doi.org/10.1021/ph500434f> (visited on 09/09/2016).
- [111] Xiang Lan et al. "Bifacial DNA Origami-Directed Discrete, Three-Dimensional, Anisotropic Plasmonic Nanoarchitectures with Tailored Optical Chirality". In: *Journal of the American Chemical Society* 135.31 (Aug. 7, 2013), pp. 11441–11444. ISSN: 0002-7863, 1520-5126. DOI: 10.1021/ja404354c. URL: <http://pubs.acs.org/doi/abs/10.1021/ja404354c> (visited on 11/07/2015).
- [112] Xiang Lan et al. "Au Nanorod Helical Superstructures with Designed Chirality". In: *Journal of the American Chemical Society* 137.1 (Jan. 14, 2015), pp. 457–462. ISSN: 0002-7863. DOI: 10.1021/ja511333q. URL: <https://doi.org/10.1021/ja511333q> (visited on 06/20/2018).
- [113] Anton Kuzyk et al. "Reconfigurable 3D plasmonic metamolecules". In: *Nature Materials* 13.9 (Sept. 2014), pp. 862–866. ISSN: 1476-1122. DOI: 10.1038/nmat4031. URL: <http://www.nature.com/nmat/journal/v13/n9/full/nmat4031.html> (visited on 02/20/2017).
- [114] Maximilian J. Urban et al. "Optically Resolving the Dynamic Walking of a Plasmonic Walker Couple". In: *Nano Letters* 15.12 (Dec. 9, 2015), pp. 8392–8396. ISSN: 1530-6984. DOI: 10.1021/acs.nanolett.5b04270. URL: <https://doi.org/10.1021/acs.nanolett.5b04270> (visited on 06/20/2018).
- [115] Vivek V. Thacker et al. "DNA origami based assembly of gold nanoparticle dimers for surface-enhanced Raman scattering". In: *Nature Communications* 5 (Mar. 13, 2014). ISSN: 2041-1723. DOI: 10.1038/ncomms4448. URL: <http://www.nature.com/doifinder/10.1038/ncomms4448> (visited on 09/09/2016).

- [116] Paul Kühler et al. “Plasmonic DNA-Origami Nanoantennas for Surface-Enhanced Raman Spectroscopy”. In: *Nano Letters* 14.5 (May 14, 2014), pp. 2914–2919. ISSN: 1530-6984, 1530-6992. DOI: 10.1021/nl5009635. URL: <http://pubs.acs.org/doi/abs/10.1021/nl5009635> (visited on 11/14/2015).
- [117] Christian Heck et al. “Gold Nanolenses Self-Assembled by DNA Origami”. In: *ACS Photonics* 4.5 (May 17, 2017), pp. 1123–1130. DOI: 10.1021/acsp Photonics.6b00946. URL: <https://doi.org/10.1021/acsp Photonics.6b00946> (visited on 03/25/2018).
- [118] Bing Liu et al. “A Gold-Nanoparticle-Based SERS Reporter that Rolls on DNA Origami Templates”. In: *ChemNanoMat* 3.10 (2017), pp. 760–763. ISSN: 2199-692X. DOI: 10.1002/cnma.201700165. URL: <https://onlinelibrary.wiley.com/doi/abs/10.1002/cnma.201700165> (visited on 06/20/2018).
- [119] G. P. Acuna et al. “Fluorescence Enhancement at Docking Sites of DNA-Directed Self-Assembled Nanoantennas”. In: *Science* 338.6106 (Oct. 26, 2012), pp. 506–510. ISSN: 0036-8075, 1095-9203. DOI: 10.1126/science.1228638. URL: <http://science.sciencemag.org/content/338/6106/506> (visited on 06/20/2018).
- [120] Ryosuke Inuma et al. “Polyhedra self-assembled from DNA tripods and characterized with 3D DNA-PAINT”. In: *science* 344.6179 (2014), pp. 65–69. URL: <http://www.sciencemag.org/content/344/6179/65.short> (visited on 08/27/2015).
- [121] Alexandria N. Marchi et al. “Toward Larger DNA Origami”. In: *Nano Letters* 14.10 (Oct. 8, 2014), pp. 5740–5747. ISSN: 1530-6984. DOI: 10.1021/nl502626s. URL: <http://dx.doi.org/10.1021/nl502626s> (visited on 11/14/2015).
- [122] Arun Richard Chandrasekaran, Muthuirulan Pushpanathan, and Ken Halvorsen. “Evolution of DNA origami scaffolds”. In: *Materials Letters* 170 (May 1, 2016), pp. 221–224. ISSN: 0167-577X. DOI: 10.1016/j.matlet.2016.01.161. URL: <http://www.sciencedirect.com/science/article/pii/S0167577X16301422> (visited on 06/20/2018).
- [123] Masayuki Endo et al. “Two-dimensional DNA origami assemblies using a four-way connector”. In: *Chemical Communications* 47.11 (2011), p. 3213. ISSN: 1359-7345, 1364-548X. DOI: 10.1039/c0cc05306f. URL: <http://xlink.rsc.org/?DOI=c0cc05306f> (visited on 11/09/2015).
- [124] Arivazhagan Rajendran et al. “Programmed Two-Dimensional Self-Assembly of Multiple DNA Origami Jigsaw Pieces”. In: *ACS Nano* 5.1 (Jan. 25, 2011), pp. 665–671. ISSN: 1936-0851. DOI: 10.1021/nn1031627. URL: <http://dx.doi.org/10.1021/nn1031627> (visited on 09/09/2016).
- [125] Zhao Zhao, Hao Yan, and Yan Liu. “A Route to Scale Up DNA Origami Using DNA Tiles as Folding Staples”. In: *Angewandte Chemie International Edition* 49.8 (Feb. 15, 2010), pp. 1414–1417. ISSN: 1521-3773. DOI: 10.1002/anie.200906225. URL: <http://onlinelibrary.wiley.com/doi/10.1002/anie.200906225/abstract> (visited on 09/21/2016).
- [126] Zhao Zhao, Yan Liu, and Hao Yan. “Organizing DNA Origami Tiles into Larger Structures Using Preformed Scaffold Frames”. In: *Nano Letters* 11.7 (July 13, 2011), pp. 2997–3002. ISSN: 1530-6984. DOI: 10.1021/nl201603a. URL: <http://dx.doi.org/10.1021/nl201603a> (visited on 09/21/2016).
- [127] Thomas Gerling et al. “Dynamic DNA devices and assemblies formed by shape-complementary, non-base pairing 3D components”. In: *Science* 347.6229 (Mar. 27, 2015), pp. 1446–1452. ISSN: 0036-8075, 1095-9203. DOI: 10.1126/science.aaa5372. URL: <http://science.sciencemag.org/content/347/6229/1446> (visited on 10/09/2016).
- [128] Aleksander Czogalla et al. “Amphipathic DNA Origami Nanoparticles to Scaffold and Deform Lipid Membrane Vesicles”. In: *Angewandte Chemie International Edition* 54.22 (May 26, 2015), pp. 6501–6505. ISSN: 14337851. DOI: 10.1002/anie.201501173. URL: <http://doi.wiley.com/10.1002/anie.201501173> (visited on 03/25/2018).
- [129] Sungwook Woo and Paul W. K. Rothemund. “Programmable molecular recognition based on the geometry of DNA nanostructures”. In: *Nature Chemistry* 3.8 (July 10, 2011), pp. 620–627. ISSN:

- 1755-4330, 1755-4349. DOI: 10.1038/nchem.1070. URL: <http://www.nature.com/doi/10.1038/nchem.1070> (visited on 03/02/2016).
- [130] Jaeseung Hahn et al. “Addressing the Instability of DNA Nanostructures in Tissue Culture”. In: *ACS Nano* 8.9 (Sept. 23, 2014), pp. 8765–8775. ISSN: 1936-0851. DOI: 10.1021/nn503513p. URL: <http://dx.doi.org/10.1021/nn503513p> (visited on 07/29/2017).
- [131] Zaixing Jiang et al. “Serum-induced degradation of 3D DNA box origami observed with high-speed atomic force microscopy”. In: *Nano Research* 8.7 (July 2015), pp. 2170–2178. ISSN: 1998-0124, 1998-0000. DOI: 10.1007/s12274-015-0724-z. URL: <http://link.springer.com/10.1007/s12274-015-0724-z> (visited on 07/31/2017).
- [132] Dianming Wang et al. “Stability study of tubular DNA origami in the presence of protein crystallisation buffer”. In: *RSC Adv.* 5.72 (2015), pp. 58734–58737. ISSN: 2046-2069. DOI: 10.1039/C5RA12159K. URL: <http://xlink.rsc.org/?DOI=C5RA12159K> (visited on 05/17/2016).
- [133] Saminathan Ramakrishnan et al. “Structural stability of DNA origami nanostructures in the presence of chaotropic agents”. In: *Nanoscale* 8.19 (2016), pp. 10398–10405. ISSN: 2040-3364, 2040-3372. DOI: 10.1039/C6NR00835F. URL: <http://xlink.rsc.org/?DOI=C6NR00835F> (visited on 05/18/2016).
- [134] Hyojeong Kim et al. “Stability of DNA Origami Nanostructure under Diverse Chemical Environments”. In: *Chemistry of Materials* 26.18 (Sept. 23, 2014), pp. 5265–5273. ISSN: 0897-4756. DOI: 10.1021/cm5019663. URL: <http://dx.doi.org/10.1021/cm5019663> (visited on 09/19/2016).
- [135] Risheng Wang, Colin Nuckolls, and Shalom J. Wind. “Assembly of Heterogeneous Functional Nanomaterials on DNA Origami Scaffolds”. In: *Angewandte Chemie International Edition* 51.45 (Nov. 5, 2012), pp. 11325–11327. ISSN: 1521-3773. DOI: 10.1002/anie.201206389. URL: <http://onlinelibrary.wiley.com/doi/10.1002/anie.201206389/abstract> (visited on 09/19/2016).
- [136] Shawn M. Douglas, Ido Bachelet, and George M. Church. “A Logic-Gated Nanorobot for Targeted Transport of Molecular Payloads”. In: *Science* 335.6070 (Feb. 17, 2012), pp. 831–834. ISSN: 0036-8075, 1095-9203. DOI: 10.1126/science.1214081. URL: <http://science.sciencemag.org/content/335/6070/831> (visited on 10/04/2016).
- [137] Anders H. Okholm and Jørgen Kjems. “DNA nanovehicles and the biological barriers”. In: *Advanced Drug Delivery Reviews*. Biologically-inspired drug delivery systems 106 (Nov. 15, 2016), pp. 183–191. ISSN: 0169-409X. DOI: 10.1016/j.addr.2016.05.024. URL: <http://www.sciencedirect.com/science/article/pii/S0169409X16301843> (visited on 07/31/2017).
- [138] Jie Song et al. “Direct Visualization of Transient Thermal Response of a DNA Origami”. In: *Journal of the American Chemical Society* 134.24 (June 20, 2012), pp. 9844–9847. ISSN: 0002-7863, 1520-5126. DOI: 10.1021/ja3017939. URL: <http://pubs.acs.org/doi/abs/10.1021/ja3017939> (visited on 11/09/2015).
- [139] Jonathan Lee Tin Wah et al. “Observing and Controlling the Folding Pathway of DNA Origami at the Nanoscale”. In: *ACS Nano* 10.2 (Feb. 23, 2016), pp. 1978–1987. ISSN: 1936-0851. DOI: 10.1021/acsnano.5b05972. URL: <http://dx.doi.org/10.1021/acsnano.5b05972> (visited on 09/19/2016).
- [140] J. M. Arbona, J. Elezgaray, and J. P. Aimé. “Modelling the folding of DNA origami”. In: *EPL (Europhysics Letters)* 100.2 (2012), p. 28006. ISSN: 0295-5075. DOI: 10.1209/0295-5075/100/28006. URL: <http://stacks.iop.org/0295-5075/100/i=2/a=28006> (visited on 10/08/2016).
- [141] Frits Dannenberg et al. “Modelling DNA origami self-assembly at the domain level”. In: *The Journal of Chemical Physics* 143.16 (Oct. 28, 2015), p. 165102. ISSN: 0021-9606, 1089-7690. DOI: 10.1063/1.4933426. URL: <http://scitation.aip.org/content/aip/journal/jcp/143/16/10.1063/1.4933426> (visited on 09/12/2016).
- [142] Anastasia Shapiro et al. “Cooperativity-based modeling of heterotypic DNA nanostructure assembly”. In: *Nucleic Acids Research* 43.13 (July 27, 2015), pp. 6587–6595. ISSN: 0305-1048,

- 1362-4962. DOI: 10.1093/nar/gkv602. URL: <http://nar.oxfordjournals.org/lookup/doi/10.1093/nar/gkv602> (visited on 01/07/2016).
- [143] Jean-Philippe J. Sobczak et al. “Rapid Folding of DNA into Nanoscale Shapes at Constant Temperature”. In: *Science* 338.6113 (Dec. 14, 2012), pp. 1458–1461. ISSN: 0036-8075, 1095-9203. DOI: 10.1126/science.1229919. URL: <http://science.sciencemag.org/content/338/6113/1458> (visited on 10/08/2016).
- [144] Katherine E. Dunn et al. “Guiding the folding pathway of DNA origami”. In: *Nature* 525.7567 (Sept. 3, 2015), pp. 82–86. ISSN: 0028-0836. DOI: 10.1038/nature14860. URL: <http://www.nature.com/nature/journal/v525/n7567/full/nature14860.html> (visited on 01/07/2016).
- [145] A. E. Marras et al. “Directing folding pathways for multi-component DNA origami nanostructures with complex topology”. In: *New Journal of Physics* 18.5 (2016), p. 055005. ISSN: 1367-2630. DOI: 10.1088/1367-2630/18/5/055005. URL: <http://stacks.iop.org/1367-2630/18/i=5/a=055005> (visited on 10/08/2016).
- [146] Jie Song et al. “Isothermal Hybridization Kinetics of DNA Assembly of Two-Dimensional DNA Origami”. In: *Small* 9.17 (Sept. 9, 2013), pp. 2954–2959. ISSN: 1613-6829. DOI: 10.1002/sml1.201202861. URL: <http://onlinelibrary.wiley.com/doi/10.1002/sml1.201202861/abstract> (visited on 10/08/2016).
- [147] Xixi Wei et al. “Mapping the Thermal Behavior of DNA Origami Nanostructures”. In: *Journal of the American Chemical Society* 135.16 (Apr. 24, 2013), pp. 6165–6176. ISSN: 0002-7863. DOI: 10.1021/ja4000728. URL: <http://dx.doi.org/10.1021/ja4000728> (visited on 09/19/2016).
- [148] Jacob M. Majikes, Jessica A. Nash, and Thomas H. LaBean. “Competitive annealing of multiple DNA origami: formation of chimeric origami”. In: *New Journal of Physics* 18.11 (2016), p. 115001. ISSN: 1367-2630. DOI: 10.1088/1367-2630/18/11/115001. URL: <http://stacks.iop.org/1367-2630/18/i=11/a=115001> (visited on 02/21/2017).
- [149] Jean-Michel Arbona, Jean-Pierre Aimé, and Juan Elezgaray. “Cooperativity in the annealing of DNA origamis”. In: *Journal of Chemical Physics* 138.1 (Jan. 7, 2013), pp. 015105–015105–10. ISSN: 00219606. DOI: 10.1063/1.4773405. URL: <http://search.ebscohost.com/login.aspx?direct=true&db=a9h&AN=84631005&site=ehost-live> (visited on 09/19/2016).
- [150] Xixi Wei, Jeanette Nangreave, and Yan Liu. “Uncovering the Self-Assembly of DNA Nanostructures by Thermodynamics and Kinetics”. In: *Accounts of Chemical Research* 47.6 (June 17, 2014), pp. 1861–1870. ISSN: 0001-4842, 1520-4898. DOI: 10.1021/ar5000665. URL: <http://pubs.acs.org/doi/abs/10.1021/ar5000665> (visited on 03/30/2015).
- [151] Jean-Michel Arbona, Jean-Pierre Aimé, and Juan Elezgaray. “Folding of DNA origamis”. In: *Frontiers in Life Science* 6.1 (June 1, 2012), pp. 11–18. ISSN: 2155-3769. DOI: 10.1080/21553769.2013.768556. URL: <http://dx.doi.org/10.1080/21553769.2013.768556> (visited on 10/09/2016).
- [152] Barbara Saccà, Rebecca Meyer, and Christof M. Niemeyer. “Temperature-dependent FRET spectroscopy for the high-throughput analysis of self-assembled DNA nanostructures in real time”. In: *Nature Protocols* 4.3 (Feb. 2009), pp. 271–285. ISSN: 1754-2189. DOI: 10.1038/nprot.2008.220. URL: <http://www.nature.com/nprot/journal/v4/n3/full/nprot.2008.220.html> (visited on 03/10/2017).
- [153] Erik Winfree et al. “Design and self-assembly of two-dimensional DNA crystals”. In: *Nature* 394.6693 (Aug. 6, 1998), pp. 539–544. ISSN: 0028-0836. DOI: 10.1038/28998. URL: <http://www.nature.com/nature/journal/v394/n6693/abs/394539a0.html> (visited on 12/28/2016).
- [154] Yu He et al. “Hierarchical self-assembly of DNA into symmetric supramolecular polyhedra”. In: *Nature* 452.7184 (Mar. 13, 2008), pp. 198–201. ISSN: 0028-0836. DOI: 10.1038/nature06597. URL: <http://www.nature.com/nature/journal/v452/n7184/full/nature06597.html> (visited on 09/21/2016).

- [155] Akinori Kuzuya et al. “Nanomechanical DNA origami ‘single-molecule beacons’ directly imaged by atomic force microscopy”. In: *Nature Communications* 2 (Aug. 23, 2011), p. 449. DOI: 10.1038/ncomms1452. URL: <http://www.nature.com/ncomms/journal/v2/n8/full/ncomms1452.html> (visited on 09/19/2016).
- [156] Masayuki Endo et al. “Regulation of DNA Methylation Using Different Tensions of Double Strands Constructed in a Defined DNA Nanostructure”. In: *Journal of the American Chemical Society* 132.5 (Feb. 10, 2010), pp. 1592–1597. ISSN: 0002-7863, 1520-5126. DOI: 10.1021/ja907649w. URL: <http://pubs.acs.org/doi/abs/10.1021/ja907649w> (visited on 09/22/2016).
- [157] Divita Mathur and Eric R. Henderson. “Programmable DNA Nanosystem for Molecular Interrogation”. In: *Scientific Reports* 6 (June 7, 2016), p. 27413. ISSN: 2045-2322. DOI: 10.1038/srep27413. URL: <https://www.nature.com/articles/srep27413> (visited on 07/20/2018).
- [158] Philipp C. Nickels et al. “DNA Origami Seesaws as Comparative Binding Assay”. In: *ChemBioChem* 17.12 (June 16, 2016), pp. 1093–1096. ISSN: 1439-7633. DOI: 10.1002/cbic.201600059. URL: <http://onlinelibrary.wiley.com/doi/10.1002/cbic.201600059/abstract> (visited on 09/19/2016).
- [159] Lars Opherden et al. “Paramagnetic Decoration of DNA Origami Nanostructures by Eu³⁺ Coordination”. In: *Langmuir* 30.27 (July 15, 2014), pp. 8152–8159. ISSN: 0743-7463. DOI: 10.1021/la501112a. URL: <http://dx.doi.org/10.1021/la501112a> (visited on 09/21/2016).
- [160] J. Prinz et al. “DNA origami based Au-Ag-core-shell nanoparticle dimers with single-molecule SERS sensitivity”. In: *Nanoscale* 8.10 (2016), pp. 5612–5620. ISSN: 2040-3364, 2040-3372. DOI: 10.1039/C5NR08674D. URL: <http://xlink.rsc.org/?DOI=C5NR08674D> (visited on 09/19/2016).
- [161] Verena J. Schüller et al. “Cellular Immunostimulation by CpG-Sequence-Coated DNA Origami Structures”. In: *ACS Nano* 5.12 (Dec. 27, 2011), pp. 9696–9702. ISSN: 1936-0851. DOI: 10.1021/nn203161y. URL: <https://doi.org/10.1021/nn203161y> (visited on 07/20/2018).
- [162] Guillermo P. Acuna et al. “Distance Dependence of Single-Fluorophore Quenching by Gold Nanoparticles Studied on DNA Origami”. In: *ACS Nano* 6.4 (Apr. 24, 2012), pp. 3189–3195. ISSN: 1936-0851, 1936-086X. DOI: 10.1021/nn2050483. URL: <http://pubs.acs.org/doi/abs/10.1021/nn2050483> (visited on 04/20/2016).
- [163] Enrico Pibiri et al. “Single-Molecule Positioning in Zeromode Waveguides by DNA Origami Nanoadapters”. In: *Nano Letters* 14.6 (June 11, 2014), pp. 3499–3503. ISSN: 1530-6984, 1530-6992. DOI: 10.1021/nl501064b. URL: <http://pubs.acs.org/doi/abs/10.1021/nl501064b> (visited on 11/14/2015).
- [164] Russell P. Goodman et al. “Reconfigurable, braced, three-dimensional DNA nanostructures”. In: *Nature Nanotechnology* 3.2 (Feb. 2008), pp. 93–96. ISSN: 1748-3395. DOI: 10.1038/nnano.2008.3. URL: <https://www.nature.com/articles/nnano.2008.3> (visited on 07/20/2018).
- [165] Barbara Saccà et al. “High-Throughput, Real-Time Monitoring of the Self-Assembly of DNA Nanostructures by FRET Spectroscopy”. In: *Angewandte Chemie International Edition* 47.11 (2008), pp. 2135–2137. ISSN: 1521-3773. DOI: 10.1002/anie.200704836. URL: <https://www.onlinelibrary.wiley.com/doi/abs/10.1002/anie.200704836> (visited on 07/20/2018).
- [166] Jonathan R. Burns et al. “Lipid-Bilayer-Spanning DNA Nanopores with a Bifunctional Porphyrin Anchor”. In: *Angewandte Chemie International Edition* 52.46 (2013), pp. 12069–12072. ISSN: 1521-3773. DOI: 10.1002/anie.201305765. URL: <https://onlinelibrary.wiley.com/doi/abs/10.1002/anie.201305765> (visited on 07/20/2018).
- [167] Yonggang Ke et al. “Scaffolded DNA Origami of a DNA Tetrahedron Molecular Container”. In: *Nano Letters* 9.6 (June 10, 2009), pp. 2445–2447. ISSN: 1530-6984. DOI: 10.1021/nl901165f. URL: <http://dx.doi.org/10.1021/nl901165f> (visited on 09/19/2016).
- [168] Akinori Kuzuya and Makoto Komiyama. “Design and construction of a box-shaped 3D-DNA origami”. In: *Chemical Communications* 0.28 (July 8, 2009), pp. 4182–4184. ISSN: 1364-548X. DOI:

- 10.1039/B907800B. URL: <https://pubs.rsc.org/en/content/articlelanding/2009/cc/b907800b> (visited on 07/20/2018).
- [169] Linda K. Bruetzel et al. “Conformational Changes and Flexibility of DNA Devices Observed by Small-Angle X-ray Scattering”. In: *Nano Letters* 16.8 (Aug. 10, 2016), pp. 4871–4879. ISSN: 1530-6984. DOI: 10.1021/acs.nanolett.6b01338. URL: <http://dx.doi.org/10.1021/acs.nanolett.6b01338> (visited on 01/23/2018).
- [170] Jaswinder Sharma et al. “Toward reliable gold nanoparticle patterning on self-assembled DNA nanoscaffold”. In: *Journal of the American Chemical Society* 130.25 (2008), pp. 7820–7821. URL: <http://pubs.acs.org/doi/abs/10.1021/ja802853r> (visited on 11/09/2015).
- [171] Gaetan Bellot et al. “Recovery of intact DNA nanostructures after agarose gel-based separation”. In: *Nature methods* 8.3 (2011), pp. 192–194. (Visited on 08/26/2015).
- [172] Johanna Zessin et al. “Tunable Fluorescence of a Semiconducting Polythiophene Positioned on DNA Origami”. In: *Nano Letters* (July 26, 2017). ISSN: 1530-6984. DOI: 10.1021/acs.nanolett.7b02623. URL: <http://dx.doi.org/10.1021/acs.nanolett.7b02623> (visited on 07/31/2017).
- [173] Tosan Omabegho, Ruojie Sha, and Nadrian C. Seeman. “A Bipedal DNA Brownian Motor with Coordinated Legs”. In: *Science* 324.5923 (Apr. 3, 2009), pp. 67–71. ISSN: 0036-8075, 1095-9203. DOI: 10.1126/science.1170336. URL: <http://science.sciencemag.org/content/324/5923/67> (visited on 03/09/2018).
- [174] G. Binnig, C. F. Quate, and Ch. Gerber. “Atomic Force Microscope”. In: *Physical Review Letters* 56.9 (Mar. 3, 1986), pp. 930–933. DOI: 10.1103/PhysRevLett.56.930. URL: <https://link.aps.org/doi/10.1103/PhysRevLett.56.930> (visited on 03/03/2018).
- [175] Germán Luque-Caballero et al. “Atomic force microscopy as a tool to study the adsorption of DNA onto lipid interfaces”. In: *Microscopy Research and Technique* (Mar. 1, 2016), n/a–n/a. ISSN: 1097-0029. DOI: 10.1002/jemt.22654. URL: <http://onlinelibrary.wiley.com/doi/10.1002/jemt.22654/abstract> (visited on 09/19/2016).
- [176] R. Campos et al. “Electronically addressable nanomechanical switching of i-motif DNA origami assembled on basal plane HOPG”. In: *Chem. Commun.* 51.74 (2015), pp. 14111–14114. ISSN: 1359-7345, 1364-548X. DOI: 10.1039/C5CC04678E. URL: <http://xlink.rsc.org/?DOI=C5CC04678E> (visited on 01/07/2016).
- [177] Xiaoning Zhang et al. “DNA origami deposition on native and passivated molybdenum disulfide substrates”. In: *Beilstein Journal of Nanotechnology* 5 (Apr. 22, 2014), pp. 501–506. ISSN: 2190-4286. DOI: 10.3762/bjnano.5.58. URL: <http://www.beilstein-journals.org/bjnano/content/5/1/58> (visited on 09/19/2016).
- [178] J. Vesenka et al. “Substrate preparation for reliable imaging of DNA molecules with the scanning force microscope”. In: *Ultramicroscopy* 42-44 (July 1, 1992), pp. 1243–1249. ISSN: 0304-3991. DOI: 10.1016/0304-3991(92)90430-R. URL: <http://www.sciencedirect.com/science/article/pii/030439919290430R> (visited on 03/03/2018).
- [179] David Pastré et al. “Adsorption of DNA to Mica Mediated by Divalent Counterions: A Theoretical and Experimental Study”. In: *Biophysical Journal* 85.4 (Oct. 2003), pp. 2507–2518. ISSN: 0006-3495. DOI: 10.1016/S0006-3495(03)74673-6. URL: <http://www.sciencedirect.com/science/article/pii/S0006349503746736> (visited on 10/08/2016).
- [180] Andrew J. Lee et al. “Tuning the translational freedom of DNA for high speed AFM”. In: *Nano Research* 8.6 (July 11, 2015), pp. 1811–1821. ISSN: 1998-0124, 1998-0000. DOI: 10.1007/s12274-014-0681-y. URL: <http://link.springer.com/article/10.1007/s12274-014-0681-y> (visited on 09/09/2016).
- [181] Arivazhagan Rajendran, Masayuki Endo, and Hiroshi Sugiyama. “Single-Molecule Analysis Using DNA Origami”. In: *Angewandte Chemie International Edition* 51.4 (Jan. 23, 2012), pp. 874–890. ISSN: 1521-3773. DOI: 10.1002/anie.201102113. URL: <http://onlinelibrary.wiley.com/doi/10.1002/anie.201102113/abstract> (visited on 09/06/2016).

- [182] Niels V. Voigt et al. “Single-molecule chemical reactions on DNA origami”. In: *Nature Nanotechnology* 5.3 (Mar. 2010), pp. 200–203. ISSN: 1748-3387. DOI: 10.1038/nnano.2010.5. URL: <http://www.nature.com/nnano/journal/v5/n3/abs/nnano.2010.5.html> (visited on 05/14/2015).
- [183] Toshio Ando. “High-speed atomic force microscopy coming of age”. In: *Nanotechnology* 23.6 (2012), p. 062001. ISSN: 0957-4484. DOI: 10.1088/0957-4484/23/6/062001. URL: <http://stacks.iop.org/0957-4484/23/i=6/a=062001> (visited on 09/09/2016).
- [184] Arivazhagan Rajendran, Masayuki Endo, and Hiroshi Sugiyama. “State-of-the-Art High-Speed Atomic Force Microscopy for Investigation of Single-Molecular Dynamics of Proteins”. In: *Chemical Reviews* 114.2 (Jan. 22, 2014), pp. 1493–1520. ISSN: 0009-2665. DOI: 10.1021/cr300253x. URL: <http://dx.doi.org/10.1021/cr300253x> (visited on 09/06/2016).
- [185] Yosuke Takeuchi et al. “Single-molecule observations of RNA-RNA kissing interactions in a DNA nanostructure”. In: *Biomaterials Science* 4.1 (2016), pp. 130–135. DOI: 10.1039/C5BM00274E. URL: <http://pubs.rsc.org/en/Content/ArticleLanding/2016/BM/C5BM00274E> (visited on 01/07/2016).
- [186] Shelley FJ Wickham et al. “Direct observation of stepwise movement of a synthetic molecular transporter”. In: *Nature nanotechnology* 6.3 (2011), pp. 166–169. URL: <http://www.nature.com/nnano/journal/v6/n3/abs/nnano.2010.284.html> (visited on 10/13/2016).
- [187] Tsai Chin Wu, Masudur Rahman, and Michael L. Norton. “From Nonfinite to Finite 1D Arrays of Origami Tiles”. In: *Accounts of Chemical Research* 47.6 (June 17, 2014), pp. 1750–1758. ISSN: 0001-4842. DOI: 10.1021/ar400330y. URL: <http://dx.doi.org/10.1021/ar400330y> (visited on 09/06/2016).
- [188] Shelley FJ Wickham et al. “A DNA-based molecular motor that can navigate a network of tracks”. In: *Nature nanotechnology* 7.3 (2012), pp. 169–173. URL: <http://www.nature.com/nnano/journal/v7/n3/abs/nnano.2011.253.html> (visited on 10/13/2016).
- [189] Jinglin Fu et al. “Multi-enzyme complexes on DNA scaffolds capable of substrate channelling with an artificial swinging arm”. In: *Nature Nanotechnology* 9.7 (May 25, 2014), pp. 531–536. ISSN: 1748-3387, 1748-3395. DOI: 10.1038/nnano.2014.100. URL: <http://www.nature.com/doi/10.1038/nnano.2014.100> (visited on 03/30/2015).
- [190] Ingo H. Stein, Christian Steinhauer, and Philip Tinnefeld. “Single-Molecule Four-Color FRET Visualizes Energy-Transfer Paths on DNA Origami”. In: *Journal of the American Chemical Society* 133.12 (Mar. 30, 2011), pp. 4193–4195. ISSN: 0002-7863. DOI: 10.1021/ja1105464. URL: <http://dx.doi.org/10.1021/ja1105464> (visited on 09/19/2016).
- [191] Theodor Förster. “Zwischenmolekulare Energiewanderung und Fluoreszenz”. In: *Annalen der Physik* 437.1 (Jan. 1, 1948), pp. 55–75. ISSN: 1521-3889. DOI: 10.1002/andp.19484370105. URL: <http://onlinelibrary.wiley.com/doi/10.1002/andp.19484370105/abstract> (visited on 03/10/2018).
- [192] John Zenk, Chanon Tuntivate, and Rebecca Schulman. “Kinetics and Thermodynamics of Watson-Crick Base Pairing Driven DNA Origami Dimerization”. In: *Journal of the American Chemical Society* 138.10 (Mar. 16, 2016), pp. 3346–3354. ISSN: 0002-7863. DOI: 10.1021/jacs.5b10502. URL: <http://dx.doi.org/10.1021/jacs.5b10502> (visited on 09/09/2016).
- [193] Miran Liber et al. “A Bipedal DNA Motor that Travels Back and Forth between Two DNA Origami Tiles”. In: *Small* 11.5 (Feb. 1, 2015), pp. 568–575. ISSN: 1613-6829. DOI: 10.1002/smll.201402028. URL: <http://onlinelibrary.wiley.com/doi/10.1002/smll.201402028/abstract> (visited on 09/21/2016).
- [194] Ernst Abbe. “Beiträge zur Theorie des Mikroskops und der mikroskopischen Wahrnehmung”. In: *Archiv für mikroskopische Anatomie* 9.1 (Dec. 1, 1873), pp. 413–418. ISSN: 0176-7364. DOI: 10.1007/BF02956173. URL: <https://link.springer.com/article/10.1007/BF02956173> (visited on 06/20/2018).

- [195] John William Strutt Lord Rayleigh Sec. R. S. “On the theory of optical images, with special reference to the microscope”. In: *The London, Edinburgh, and Dublin Philosophical Magazine and Journal of Science* 42.255 (Aug. 1, 1896), pp. 167–195. ISSN: 1941-5982. DOI: 10.1080/14786449608620902. URL: <https://doi.org/10.1080/14786449608620902> (visited on 06/20/2018).
- [196] Norman Bobroff. “Position measurement with a resolution and noise-limited instrument”. In: *Review of Scientific Instruments* 57.6 (June 1, 1986), pp. 1152–1157. ISSN: 0034-6748. DOI: 10.1063/1.1138619. URL: <https://aip.scitation.org/doi/abs/10.1063/1.1138619> (visited on 03/15/2018).
- [197] Stefan W. Hell and Jan Wichmann. “Breaking the diffraction resolution limit by stimulated emission: stimulated-emission-depletion fluorescence microscopy”. In: *Optics Letters* 19.11 (June 1, 1994), p. 780. ISSN: 0146-9592, 1539-4794. DOI: 10.1364/OL.19.000780. URL: <https://www.osapublishing.org/ol/abstract.cfm?uri=ol-19-11-780> (visited on 10/23/2015).
- [198] M. G. Gustafsson. “Surpassing the lateral resolution limit by a factor of two using structured illumination microscopy”. In: *Journal of Microscopy* 198 (Pt 2 May 2000), pp. 82–87. ISSN: 0022-2720.
- [199] Eric Betzig et al. “Imaging Intracellular Fluorescent Proteins at Nanometer Resolution”. In: *Science* 313.5793 (Sept. 15, 2006), pp. 1642–1645. ISSN: 0036-8075, 1095-9203. DOI: 10.1126/science.1127344. URL: <http://science.sciencemag.org/content/313/5793/1642> (visited on 10/02/2016).
- [200] Samuel T. Hess, Thanu P.K. Girirajan, and Michael D. Mason. “Ultra-High Resolution Imaging by Fluorescence Photoactivation Localization Microscopy”. In: *Biophysical Journal* 91.11 (Dec. 2006), pp. 4258–4272. ISSN: 00063495. DOI: 10.1529/biophysj.106.091116. URL: <http://linkinghub.elsevier.com/retrieve/pii/S0006349506721403> (visited on 04/17/2016).
- [201] Michael J Rust, Mark Bates, and Xiaowei Zhuang. “Sub-diffraction-limit imaging by stochastic optical reconstruction microscopy (STORM)”. In: *Nature Methods* 3.10 (Oct. 2006), pp. 793–796. ISSN: 1548-7091, 1548-7105. DOI: 10.1038/nmeth929. URL: <http://www.nature.com/doi/10.1038/nmeth929> (visited on 10/23/2015).
- [202] Mike Heilemann et al. “Subdiffraction-Resolution Fluorescence Imaging with Conventional Fluorescent Probes”. In: *Angewandte Chemie International Edition* 47.33 (Aug. 4, 2008), pp. 6172–6176. ISSN: 1521-3773. DOI: 10.1002/anie.200802376. URL: <http://onlinelibrary.wiley.com/doi/10.1002/anie.200802376/abstract> (visited on 03/10/2018).
- [203] Christian Steinhauer et al. “Superresolution Microscopy on the Basis of Engineered Dark States”. In: *Journal of the American Chemical Society* 130.50 (Dec. 17, 2008), pp. 16840–16841. ISSN: 0002-7863. DOI: 10.1021/ja806590m. URL: <https://doi.org/10.1021/ja806590m> (visited on 03/10/2018).
- [204] Christian Steinhauer et al. “DNA Origami as a Nanoscopic Ruler for Super-Resolution Microscopy”. In: *Angewandte Chemie International Edition* 48.47 (Nov. 9, 2009), pp. 8870–8873. ISSN: 1521-3773. DOI: 10.1002/anie.200903308. URL: <http://onlinelibrary.wiley.com/doi/10.1002/anie.200903308/abstract> (visited on 05/14/2015).
- [205] Samet Kocabey et al. “Membrane-Assisted Growth of DNA Origami Nanostructure Arrays”. In: *ACS Nano* 9.4 (Apr. 28, 2015), pp. 3530–3539. ISSN: 1936-0851, 1936-086X. DOI: 10.1021/acsnano.5b00161. URL: <http://pubs.acs.org/doi/abs/10.1021/acsnano.5b00161> (visited on 08/11/2015).
- [206] Jürgen J. Schmied et al. “DNA Origami Nanopillars as Standards for Three-Dimensional Superresolution Microscopy”. In: *Nano Letters* 13.2 (Feb. 13, 2013), pp. 781–785. ISSN: 1530-6984, 1530-6992. DOI: 10.1021/nl304492y. URL: <http://pubs.acs.org/doi/abs/10.1021/nl304492y> (visited on 10/22/2015).

- [207] Mingjie Dai, Ralf Jungmann, and Peng Yin. “Optical imaging of individual biomolecules in densely packed clusters”. In: *Nature Nanotechnology* 11.9 (July 4, 2016), pp. 798–807. ISSN: 1748-3387, 1748-3395. DOI: 10.1038/nnano.2016.95. URL: <http://www.nature.com/doifinder/10.1038/nnano.2016.95> (visited on 09/25/2016).
- [208] Ke Xu, Hazen P. Babcock, and Xiaowei Zhuang. “Dual-objective STORM reveals three-dimensional filament organization in the actin cytoskeleton”. In: *Nature Methods* 9.2 (Feb. 2012), pp. 185–188. ISSN: 1548-7105. DOI: 10.1038/nmeth.1841. URL: <https://www.nature.com/articles/nmeth.1841> (visited on 06/20/2018).
- [209] Mario Raab et al. “Using DNA origami nanorulers as traceable distance measurement standards and nanoscopic benchmark structures”. In: *Scientific Reports* 8.1 (Jan. 29, 2018), p. 1780. ISSN: 2045-2322. DOI: 10.1038/s41598-018-19905-x. URL: <https://www.nature.com/articles/s41598-018-19905-x> (visited on 03/09/2018).
- [210] Jürgen J. Schmied et al. “Fluorescence and super-resolution standards based on DNA origami”. In: *Nature methods* 9.12 (2012), pp. 1133–1134. URL: <http://www.nature.com/articles/nmeth.2254> (visited on 10/22/2015).
- [211] Joran Deschamps, Markus Mund, and Jonas Ries. “3D superresolution microscopy by supercritical angle detection”. In: *Optics Express* 22.23 (Nov. 17, 2014), p. 29081. ISSN: 1094-4087. DOI: 10.1364/OE.22.029081. URL: <https://www.osapublishing.org/oe/abstract.cfm?uri=oe-22-23-29081> (visited on 06/02/2018).
- [212] Charlotte Kaplan et al. “Absolute Arrangement of Subunits in Cytoskeletal Septin Filaments in Cells Measured by Fluorescence Microscopy”. In: *Nano Letters* 15.6 (June 10, 2015), pp. 3859–3864. ISSN: 1530-6984, 1530-6992. DOI: 10.1021/acs.nanolett.5b00693. URL: <http://pubs.acs.org/doi/abs/10.1021/acs.nanolett.5b00693> (visited on 11/14/2015).
- [213] Chenxiang Lin et al. “Submicrometre geometrically encoded fluorescent barcodes self-assembled from DNA”. In: *Nature Chemistry* 4.10 (Sept. 24, 2012), pp. 832–839. ISSN: 1755-4330, 1755-4349. DOI: 10.1038/nchem.1451. URL: <http://www.nature.com/doifinder/10.1038/nchem.1451> (visited on 08/11/2015).
- [214] Jürgen J. Schmied et al. “DNA origami-based standards for quantitative fluorescence microscopy”. In: *Nature Protocols* 9.6 (June 2014), pp. 1367–1391. ISSN: 1750-2799. DOI: 10.1038/nprot.2014.079. URL: <https://www.nature.com/articles/nprot.2014.079> (visited on 06/02/2018).
- [215] Ralf Jungmann et al. “Single-Molecule Kinetics and Super-Resolution Microscopy by Fluorescence Imaging of Transient Binding on DNA Origami”. In: *Nano Letters* 10.11 (Nov. 10, 2010), pp. 4756–4761. ISSN: 1530-6984. DOI: 10.1021/nl103427w. URL: <http://dx.doi.org/10.1021/nl103427w> (visited on 09/19/2016).
- [216] A. Sharonov and R. M. Hochstrasser. “Wide-field subdiffraction imaging by accumulated binding of diffusing probes”. In: *Proceedings of the National Academy of Sciences* 103.50 (Dec. 12, 2006), pp. 18911–18916. ISSN: 0027-8424, 1091-6490. DOI: 10.1073/pnas.0609643104. URL: <http://www.pnas.org/cgi/doi/10.1073/pnas.0609643104> (visited on 04/17/2016).
- [217] Alexander Johnson-Buck et al. “Multifactorial Modulation of Binding and Dissociation Kinetics on Two-Dimensional DNA Nanostructures”. In: *Nano Letters* 13.6 (June 12, 2013), pp. 2754–2759. ISSN: 1530-6984, 1530-6992. DOI: 10.1021/nl400976s. URL: <http://pubs.acs.org/doi/abs/10.1021/nl400976s> (visited on 04/05/2016).
- [218] Mario Raab et al. “Fluorescence Microscopy with 6 nm Resolution on DNA Origami”. In: *ChemPhysChem* 15.12 (Aug. 25, 2014), pp. 2431–2435. ISSN: 1439-7641. DOI: 10.1002/cphc.201402179. URL: <http://onlinelibrary.wiley.com/doi/10.1002/cphc.201402179/abstract> (visited on 10/22/2015).
- [219] L. Stirling Churchman et al. “Single molecule high-resolution colocalization of Cy3 and Cy5 attached to macromolecules measures intramolecular distances through time”. In: *Proceedings of the National Academy of Sciences of the United States of America* 102.5 (Jan. 2, 2005),

- pp. 1419–1423. ISSN: 0027-8424, 1091-6490. DOI: 10.1073/pnas.0409487102. URL: <http://www.pnas.org/content/102/5/1419> (visited on 08/22/2017).
- [220] Kim I. Mortensen et al. “Optimized measurements of separations and angles between intra-molecular fluorescent markers”. In: *Nature Communications* 0 (Oct. 16, 2015). ISSN: 2041-1723. DOI: 10.1038/ncomms9621. URL: <http://www.ncbi.nlm.nih.gov/pmc/articles/PMC4634324/> (visited on 08/22/2017).
- [221] Paolo Annibale et al. “Identification of the factors affecting co-localization precision for quantitative multicolor localization microscopy”. In: *Optical Nanoscopy* 1.1 (Dec. 1, 2012), p. 9. ISSN: 2192-2853. DOI: 10.1186/2192-2853-1-9. URL: <https://link.springer.com/article/10.1186/2192-2853-1-9> (visited on 08/21/2017).
- [222] Miklos Erdelyi et al. “Correcting chromatic offset in multicolor super-resolution localization microscopy”. In: *Optics Express* 21.9 (May 6, 2013), pp. 10978–10988. ISSN: 1094-4087. DOI: 10.1364/OE.21.010978. URL: <https://www.osapublishing.org/abstract.cfm?uri=oe-21-9-10978> (visited on 08/21/2017).
- [223] K. I. Mortensen et al. “How to Measure Separations and Angles Between Intramolecular Fluorescent Markers”. In: *Methods in Enzymology. Single-Molecule Enzymology: Fluorescence-Based and High-Throughput Methods* 581 (Jan. 1, 2016), pp. 147–185. ISSN: 0076-6879. DOI: 10.1016/bs.mie.2016.08.020. URL: <http://www.sciencedirect.com/science/article/pii/S0076687916302671> (visited on 08/22/2017).
- [224] Alexandros Pertsinidis, Yunxiang Zhang, and Steven Chu. “Subnanometre single-molecule localization, registration and distance measurements”. In: *Nature* 466.7306 (July 29, 2010), pp. 647–651. ISSN: 0028-0836. DOI: 10.1038/nature09163. URL: <https://www.nature.com/nature/journal/v466/n7306/full/nature09163.html> (visited on 08/21/2017).
- [225] ISO 5725-1:1994(en). *Accuracy (trueness and precision) of measurement methods and results — Part 1: General principles and definitions*. Tech. rep. Geneva, CH: International Organization for Standardization, 1994.
- [226] Bo Zhang, Josiane Zerubia, and Jean-Christophe Olivo-Marin. “Gaussian approximations of fluorescence microscope point-spread function models”. In: *Applied Optics* 46.10 (Apr. 1, 2007), pp. 1819–1829. ISSN: 2155-3165. DOI: 10.1364/AO.46.001819. URL: <https://www.osapublishing.org/ao/abstract.cfm?uri=ao-46-10-1819> (visited on 03/11/2018).
- [227] Hendrik Deschout et al. “Precisely and accurately localizing single emitters in fluorescence microscopy”. In: *Nature Methods* 11.3 (Feb. 27, 2014), pp. 253–266. ISSN: 1548-7091, 1548-7105. DOI: 10.1038/nmeth.2843. URL: <http://www.nature.com/doifinder/10.1038/nmeth.2843> (visited on 10/22/2015).
- [228] Pavel Frantsuzov et al. “Universal emission intermittency in quantum dots, nanorods and nanowires”. In: *Nature Physics* 4.7 (July 2008), pp. 519–522. ISSN: 1745-2481. DOI: 10.1038/nphys1001. URL: <https://www.nature.com/articles/nphys1001> (visited on 04/15/2018).
- [229] Fernando D. Stefani, Jacob P. Hoogenboom, and Eli Barkai. “Beyond quantum jumps: Blinking nanoscale light emitters”. In: *Physics Today* 62.2 (Feb. 1, 2009), pp. 34–39. ISSN: 0031-9228. DOI: 10.1063/1.3086100. URL: <https://physicstoday.scitation.org/doi/10.1063/1.3086100> (visited on 04/15/2018).
- [230] Alex Small and Shane Stahlheber. “Fluorophore localization algorithms for super-resolution microscopy”. In: *Nature Methods* 11.3 (Mar. 2014), pp. 267–279. ISSN: 1548-7091. DOI: 10.1038/nmeth.2844. URL: <http://www.nature.com/nmeth/journal/v11/n3/abs/nmeth.2844.html?foxtrotcallback=true> (visited on 08/21/2017).
- [231] Russell E. Thompson, Daniel R. Larson, and Watt W. Webb. “Precise Nanometer Localization Analysis for Individual Fluorescent Probes”. In: *Biophysical Journal* 82.5 (May 2002), pp. 2775–2783. ISSN: 0006-3495. DOI: 10.1016/S0006-3495(02)75618-X. URL: <http://www.sciencedirect.com/science/article/pii/S000634950275618X> (visited on 05/11/2017).

- [232] Martin Ovesný et al. “ThunderSTORM: a comprehensive ImageJ plug-in for PALM and STORM data analysis and super-resolution imaging”. In: *Bioinformatics (Oxford, England)* 30.16 (Aug. 15, 2014), pp. 2389–2390. ISSN: 1367-4811. DOI: 10.1093/bioinformatics/btu202.
- [233] E. J. Ambrose. “A Surface Contact Microscope for the study of Cell Movements”. In: *Nature* 178.4543 (Nov. 24, 1956), pp. 1194–1194. ISSN: 0028-0836. DOI: 10.1038/1781194a0. URL: <http://www.nature.com/nature/journal/v178/n4543/abs/1781194a0.html> (visited on 11/22/2016).
- [234] D. Axelrod. “Cell-substrate contacts illuminated by total internal reflection fluorescence.” In: *The Journal of Cell Biology* 89.1 (Apr. 1, 1981), pp. 141–145. ISSN: 0021-9525, 1540-8140. DOI: 10.1083/jcb.89.1.141. URL: <http://jcb.rupress.org/content/89/1/141> (visited on 11/22/2016).
- [235] Michael J. Mlodzianoski et al. “Sample drift correction in 3D fluorescence photoactivation localization microscopy”. In: *Optics Express* 19.16 (Aug. 1, 2011), pp. 15009–15019. ISSN: 1094-4087.
- [236] Bo Huang et al. “Three-dimensional super-resolution imaging by stochastic optical reconstruction microscopy”. In: *Science (New York, N.Y.)* 319.5864 (Feb. 8, 2008), pp. 810–813. ISSN: 1095-9203. DOI: 10.1126/science.1153529.
- [237] Bo Huang et al. “Whole-cell 3D STORM reveals interactions between cellular structures with nanometer-scale resolution”. In: *Nature Methods* 5.12 (Dec. 2008), pp. 1047–1052. ISSN: 1548-7105. DOI: 10.1038/nmeth.1274. URL: <https://www.nature.com/articles/nmeth.1274> (visited on 06/20/2018).
- [238] E. A. K. Cohen and R. J. Ober. “Measurement errors in fluorescence microscopy image registration”. In: *2012 Conference Record of the Forty Sixth Asilomar Conference on Signals, Systems and Computers (ASILOMAR)*. 2012 Conference Record of the Forty Sixth Asilomar Conference on Signals, Systems and Computers (ASILOMAR). Nov. 2012, pp. 1602–1606. DOI: 10.1109/ACSSC.2012.6489300.
- [239] Ardeshir Goshtasby. “Image Registration by Local Approximation Methods”. In: *Image Vision Comput.* 6.4 (Nov. 1988), pp. 255–261. ISSN: 0262-8856. DOI: 10.1016/0262-8856(88)90016-9. URL: [http://dx.doi.org/10.1016/0262-8856\(88\)90016-9](http://dx.doi.org/10.1016/0262-8856(88)90016-9) (visited on 03/16/2018).
- [240] L. Stirling Churchman and James A. Spudich. “Colocalization of Fluorescent Probes: Accurate and Precise Registration with Nanometer Resolution”. In: *Cold Spring Harbor Protocols* 2012.2 (Jan. 2, 2012), pdb.top067918. ISSN: 1940-3402, 1559-6095. DOI: 10.1101/pdb.top067918. URL: <http://cshprotocols.cshlp.org/content/2012/2/pdb.top067918> (visited on 08/22/2017).
- [241] Takeo Ito, Hideki Shirakawa, and Sakuji Ikeda. “Simultaneous polymerization and formation of polyacetylene film on the surface of concentrated soluble Ziegler-type catalyst solution”. In: *Journal of Polymer Science: Polymer Chemistry Edition* 12.1 (Jan. 1974), pp. 11–20. ISSN: 1542-9369. DOI: 10.1002/pol.1974.170120102. URL: <https://onlinelibrary.wiley.com/doi/abs/10.1002/pol.1974.170120102> (visited on 06/23/2018).
- [242] Hideki Shirakawa et al. “Synthesis of electrically conducting organic polymers: halogen derivatives of polyacetylene, (CH)_x”. In: *Journal of the Chemical Society, Chemical Communications* 0.16 (Jan. 1, 1977), pp. 578–580. ISSN: 0022-4936. DOI: 10.1039/C39770000578. URL: <http://pubs.rsc.org/en/content/articlelanding/1977/c3/c39770000578> (visited on 06/23/2018).
- [243] C. K. Chiang et al. “Electrical Conductivity in Doped Polyacetylene”. In: *Physical Review Letters* 39.17 (Oct. 24, 1977), pp. 1098–1101. DOI: 10.1103/PhysRevLett.39.1098. URL: <https://link.aps.org/doi/10.1103/PhysRevLett.39.1098> (visited on 06/23/2018).
- [244] C. K. Chiang et al. “Synthesis of highly conducting films of derivatives of polyacetylene, (CH)_x”. In: *Journal of the American Chemical Society* 100.3 (Feb. 1, 1978), pp. 1013–1015. ISSN: 0002-7863. DOI: 10.1021/ja00471a081. URL: <https://doi.org/10.1021/ja00471a081> (visited on 06/23/2018).

- [245] Jianguo Mei and Zhenan Bao. “Side Chain Engineering in Solution-Processable Conjugated Polymers”. In: *Chemistry of Materials* 26.1 (Jan. 14, 2014), pp. 604–615. ISSN: 0897-4756. DOI: 10.1021/cm4020805. URL: <http://dx.doi.org/10.1021/cm4020805> (visited on 01/14/2018).
- [246] R. E. Peierls. *Quantum Theory of Solids*. Oxford Classic Texts in the Physical Sciences. Oxford, New York: Oxford University Press, Feb. 1, 2001. 238 pp. ISBN: 978-0-19-850781-9.
- [247] Nils Wiberg. *Lehrbuch der Anorganischen Chemie*. 102nd compl. rev. ed. Berlin, Boston: De Gruyter, 2008. ISBN: 978-3-11-017770-1. DOI: 10.1515/9783110177701. URL: <https://www.degruyter.com/viewbooktoc/product/19732> (visited on 06/20/2018).
- [248] Frauke Rininsland et al. “Metal ion-mediated polymer superquenching for highly sensitive detection of kinase and phosphatase activities”. In: *Proceedings of the National Academy of Sciences* 101.43 (Oct. 26, 2004), pp. 15295–15300. ISSN: 0027-8424, 1091-6490. DOI: 10.1073/pnas.0406832101. URL: <http://www.pnas.org/content/101/43/15295> (visited on 06/23/2018).
- [249] Samuel W. Thomas, Guy D. Joly, and Timothy M. Swager. “Chemical Sensors Based on Amplifying Fluorescent Conjugated Polymers”. In: *Chemical Reviews* 107.4 (Apr. 1, 2007), pp. 1339–1386. ISSN: 0009-2665. DOI: 10.1021/cr0501339. URL: <https://doi.org/10.1021/cr0501339> (visited on 06/23/2018).
- [250] Xuli Feng et al. “Water-soluble fluorescent conjugated polymers and their interactions with biomacromolecules for sensitive biosensors”. In: *Chemical Society Reviews* 39.7 (July 2010), pp. 2411–2419. ISSN: 1460-4744. DOI: 10.1039/b909065g.
- [251] Md. Mahbubur Rahman et al. “Electrochemical DNA Hybridization Sensors Based on Conducting Polymers”. In: *Sensors (Basel, Switzerland)* 15.2 (Feb. 5, 2015), pp. 3801–3829. ISSN: 1424-8220. DOI: 10.3390/s150203801. URL: <https://www.ncbi.nlm.nih.gov/pmc/articles/PMC4367386/> (visited on 06/23/2018).
- [252] Richard D. McCullough and Renae D. Lowe. “Enhanced electrical conductivity in regioselectively synthesized poly(3-alkylthiophenes)”. In: *Journal of the Chemical Society, Chemical Communications* 0.1 (Jan. 1, 1992), pp. 70–72. ISSN: 0022-4936. DOI: 10.1039/C39920000070. URL: <http://pubs.rsc.org/en/content/articlelanding/1992/c3/c39920000070> (visited on 02/25/2018).
- [253] Rodrigo Noriega et al. “A general relationship between disorder, aggregation and charge transport in conjugated polymers”. In: *Nature Materials* 12.11 (Nov. 2013), pp. 1038–1044. ISSN: 1476-1122. DOI: 10.1038/nmat3722. URL: <http://www.nature.com/nmat/journal/v12/n11/full/nmat3722.html> (visited on 01/04/2017).
- [254] Mario Leclerc, Francisco Martinez Diaz, and Gerhard Wegner. “Structural analysis of poly(3-alkylthiophene)s”. In: *Die Makromolekulare Chemie* 190.12 (Dec. 1, 1989), pp. 3105–3116. ISSN: 0025-116X. DOI: 10.1002/macp.1989.021901208. URL: <http://onlinelibrary.wiley.com/doi/10.1002/macp.1989.021901208/abstract> (visited on 02/25/2018).
- [255] Zachary B. Henson, Klaus Müllen, and Guillermo C. Bazan. “Design strategies for organic semiconductors beyond the molecular formula”. In: *Nature Chemistry* 4.9 (Sept. 2012), pp. 699–704. ISSN: 1755-4349. DOI: 10.1038/nchem.1422. URL: <https://www.nature.com/articles/nchem.1422> (visited on 07/20/2018).
- [256] R. J. Kline et al. “Controlling the Field-Effect Mobility of Regioregular Polythiophene by Changing the Molecular Weight”. In: *Advanced Materials* 15.18 (2003), pp. 1519–1522. ISSN: 1521-4095. DOI: 10.1002/adma.200305275. URL: <https://onlinelibrary.wiley.com/doi/abs/10.1002/adma.200305275> (visited on 07/20/2018).
- [257] Pavel Schilinsky et al. “Influence of the Molecular Weight of Poly(3-hexylthiophene) on the Performance of Bulk Heterojunction Solar Cells”. In: *Chemistry of Materials* 17.8 (Apr. 1, 2005), pp. 2175–2180. ISSN: 0897-4756. DOI: 10.1021/cm047811c. URL: <https://doi.org/10.1021/cm047811c> (visited on 07/20/2018).

- [258] Nanjia Zhou et al. “All-Polymer Solar Cell Performance Optimized via Systematic Molecular Weight Tuning of Both Donor and Acceptor Polymers”. In: *Journal of the American Chemical Society* 138.4 (Feb. 3, 2016), pp. 1240–1251. ISSN: 0002-7863. DOI: 10.1021/jacs.5b10735. URL: <https://doi.org/10.1021/jacs.5b10735> (visited on 07/20/2018).
- [259] Raja Shahid Ashraf et al. “The Influence of Polymer Purification on Photovoltaic Device Performance of a Series of Indacenodithiophene Donor Polymers”. In: *Advanced Materials* 25.14 (2013), pp. 2029–2034. ISSN: 1521-4095. DOI: 10.1002/adma.201300027. URL: <https://onlinelibrary.wiley.com/doi/abs/10.1002/adma.201300027> (visited on 07/20/2018).
- [260] Luyao Lu et al. “Mechanistic Studies of Effect of Dispersity on the Photovoltaic Performance of PTB7 Polymer Solar Cells”. In: *Chemistry of Materials* 27.2 (Jan. 27, 2015), pp. 537–543. ISSN: 0897-4756. DOI: 10.1021/cm5042953. URL: <https://doi.org/10.1021/cm5042953> (visited on 07/20/2018).
- [261] Y. Kim et al. “Effect of the End Group of Regioregular Poly(3-hexylthiophene) Polymers on the Performance of Polymer/Fullerene Solar Cells”. In: *The Journal of Physical Chemistry C* 111.23 (June 1, 2007), pp. 8137–8141. ISSN: 1932-7447. DOI: 10.1021/jp072306z. URL: <https://doi.org/10.1021/jp072306z> (visited on 07/20/2018).
- [262] M. Jeffries-EL, G. Sauvé, and R. D. McCullough. “In-Situ End-Group Functionalization of Regioregular Poly(3-alkylthiophene) Using the Grignard Metathesis Polymerization Method”. In: *Advanced Materials* 16.12 (June 29, 2004), pp. 1017–1019. ISSN: 1521-4095. DOI: 10.1002/adma.200400137. URL: <https://www.onlinelibrary.wiley.com/doi/abs/10.1002/adma.200400137> (visited on 06/23/2018).
- [263] Jin Kuen Park et al. “End-Capping Effect of a Narrow Bandgap Conjugated Polymer on Bulk Heterojunction Solar Cells”. In: *Advanced Materials* 23.21 (2011), pp. 2430–2435. ISSN: 1521-4095. DOI: 10.1002/adma.201004629. URL: <https://onlinelibrary.wiley.com/doi/abs/10.1002/adma.201004629> (visited on 07/20/2018).
- [264] Volodymyr Senkovskyy et al. “Conductive Polymer Brushes of Regioregular Head-to-Tail Poly(3-alkylthiophenes) via Catalyst-Transfer Surface-Initiated Polycondensation”. In: *Journal of the American Chemical Society* 129.20 (May 1, 2007), pp. 6626–6632. ISSN: 0002-7863. DOI: 10.1021/ja0710306. URL: <https://doi.org/10.1021/ja0710306> (visited on 07/20/2018).
- [265] Hongbo Li, Carin C. C. Johansson Seechurn, and Thomas J. Colacot. “Development of Preformed Pd Catalysts for Cross-Coupling Reactions, Beyond the 2010 Nobel Prize”. In: *ACS Catalysis* 2.6 (June 1, 2012), pp. 1147–1164. DOI: 10.1021/cs300082f. URL: <https://doi.org/10.1021/cs300082f> (visited on 07/20/2018).
- [266] Fu-She Han. “Transition-metal-catalyzed Suzuki-Miyaura cross-coupling reactions: a remarkable advance from palladium to nickel catalysts”. In: *Chemical Society Reviews* 42.12 (May 28, 2013), pp. 5270–5298. ISSN: 1460-4744. DOI: 10.1039/C3CS35521G. URL: <https://pubs.rsc.org/en/content/articlelanding/2013/cs/c3cs35521g> (visited on 07/20/2018).
- [267] Yen-Ju Cheng, Sheng-Hsiung Yang, and Chain-Shu Hsu. “Synthesis of Conjugated Polymers for Organic Solar Cell Applications”. In: *Chemical Reviews* 109.11 (Nov. 11, 2009), pp. 5868–5923. ISSN: 0009-2665. DOI: 10.1021/cr900182s. URL: <http://dx.doi.org/10.1021/cr900182s> (visited on 01/21/2018).
- [268] Bridget Carsten et al. “Stille Polycondensation for Synthesis of Functional Materials”. In: *Chemical Reviews* 111.3 (Mar. 9, 2011), pp. 1493–1528. ISSN: 0009-2665. DOI: 10.1021/cr100320w. URL: <http://dx.doi.org/10.1021/cr100320w> (visited on 01/21/2018).
- [269] Payam Payamyar et al. “Two-dimensional polymers: concepts and perspectives”. In: *Chemical Communications* 52.1 (2016), pp. 18–34. DOI: 10.1039/C5CC07381B. URL: <http://pubs.rsc.org/en/Content/ArticleLanding/2016/CC/C5CC07381B> (visited on 04/07/2018).
- [270] Anton Kiriy, Volodymyr Senkovskyy, and Michael Sommer. “Kumada Catalyst-Transfer Polycondensation: Mechanism, Opportunities, and Challenges”. In: *Macromolecular Rapid*

- Communications* 32.19 (Oct. 4, 2011), pp. 1503–1517. ISSN: 10221336. DOI: 10.1002/marc.201100316. URL: <http://doi.wiley.com/10.1002/marc.201100316> (visited on 06/07/2016).
- [271] Melissa P. Aplan and Enrique D. Gomez. “Recent Developments in Chain-Growth Polymerizations of Conjugated Polymers”. In: *Industrial & Engineering Chemistry Research* 56.28 (July 19, 2017), pp. 7888–7901. ISSN: 0888-5885. DOI: 10.1021/acs.iecr.7b01030. URL: <http://dx.doi.org/10.1021/acs.iecr.7b01030> (visited on 01/16/2018).
- [272] Sandip Das et al. “Water soluble polythiophenes: preparation and applications”. In: 5.26 (Feb. 17, 2015), pp. 20160–20177. ISSN: 2046-2069. DOI: 10.1039/C4RA16496B. URL: <http://pubs.rsc.org/en/content/articlelanding/2015/ra/c4ra16496b> (visited on 01/16/2017).
- [273] D. Tyler McQuade, Anthony E. Pullen, and Timothy M. Swager. “Conjugated Polymer-Based Chemical Sensors”. In: *Chemical Reviews* 100.7 (July 1, 2000), pp. 2537–2574. ISSN: 0009-2665. DOI: 10.1021/cr9801014. URL: <https://doi.org/10.1021/cr9801014> (visited on 06/23/2018).
- [274] Peter S. Heeger and Alan J. Heeger. “Making sense of polymer-based biosensors”. In: *Proceedings of the National Academy of Sciences* 96.22 (Oct. 26, 1999), pp. 12219–12221. ISSN: 0027-8424, 1091-6490. DOI: 10.1073/pnas.96.22.12219. URL: <http://www.pnas.org/content/96/22/12219> (visited on 06/23/2018).
- [275] Paul E. Shaw, Arvydas Ruseckas, and Ifor D. W. Samuel. “Exciton Diffusion Measurements in Poly(3-hexylthiophene)”. In: *Advanced Materials* 20.18 (2008), pp. 3516–3520. ISSN: 1521-4095. DOI: 10.1002/adma.200800982. URL: <https://onlinelibrary.wiley.com/doi/abs/10.1002/adma.200800982> (visited on 06/23/2018).
- [276] Maryam Hatamzadeh, Mehdi Jaymand, and Bakhshali Massoumi. “Graft copolymerization of thiophene onto polystyrene synthesized via nitroxide-mediated polymerization and its polymer - clay nanocomposite”. In: *Polymer International* 63.3 (2013), pp. 402–412. ISSN: 1097-0126. DOI: 10.1002/pi.4513. URL: <https://onlinelibrary.wiley.com/doi/abs/10.1002/pi.4513> (visited on 06/23/2018).
- [277] Tuba Gözet, Ahmet M. Önal, and Jale Hacaloglu. “Investigation of the Effect of Dopant on Characteristics of Poly(3-methyl thiophene) via Pyrolysis Mass Spectrometry”. In: *Journal of Macromolecular Science, Part A* 44.3 (Mar. 1, 2007), pp. 259–263. ISSN: 1060-1325. DOI: 10.1080/10601320601077104. URL: <https://doi.org/10.1080/10601320601077104> (visited on 06/23/2018).
- [278] Vanessa C. Gonçalves and Débora T. Balogh. “Synthesis and characterization of a dye-functionalized polythiophene with different chromic properties”. In: *European Polymer Journal* 42.12 (Dec. 1, 2006), pp. 3303–3310. ISSN: 0014-3057. DOI: 10.1016/j.eurpolymj.2006.08.020. URL: <http://www.sciencedirect.com/science/article/pii/S0014305706002928> (visited on 06/23/2018).
- [279] Suren A. Gevorgyan and Frederik C. Krebs. “Bulk Heterojunctions Based on Native Polythiophene”. In: *Chemistry of Materials* 20.13 (July 1, 2008), pp. 4386–4390. ISSN: 0897-4756. DOI: 10.1021/cm800431s. URL: <https://doi.org/10.1021/cm800431s> (visited on 06/23/2018).
- [280] Ha Na Kim et al. “Recent progress on polymer-based fluorescent and colorimetric chemosensors”. In: *Chemical Society Reviews* 40.1 (Dec. 15, 2010), pp. 79–93. ISSN: 1460-4744. DOI: 10.1039/C0CS00058B. URL: <http://pubs.rsc.org/en/content/articlelanding/2011/cs/c0cs00058b> (visited on 06/23/2018).
- [281] Xingfen Liu, Quli Fan, and Wei Huang. “DNA biosensors based on water-soluble conjugated polymers”. In: *Biosensors and Bioelectronics* 26.5 (Jan. 15, 2011), pp. 2154–2164. ISSN: 0956-5663. DOI: 10.1016/j.bios.2010.09.025. URL: <http://www.sciencedirect.com/science/article/pii/S0956566310006391> (visited on 06/23/2018).
- [282] Xiang Li et al. “Conducting polymers in environmental analysis”. In: *TrAC Trends in Analytical Chemistry. New Materials in Analytical Chemistry* 39 (Oct. 1, 2012), pp. 163–179. ISSN: 0165-9936.

- DOI: 10.1016/j.trac.2012.06.003. URL: <http://www.sciencedirect.com/science/article/pii/S0165993612001938> (visited on 06/23/2018).
- [283] Hsing-Ju Wang et al. "Synthesis and photovoltaic properties of two-dimensional conjugated polythiophene derivatives presenting conjugated triphenylamine/thiophene moieties". In: *Polymer* 53.19 (Aug. 31, 2012), pp. 4091–4103. ISSN: 0032-3861. DOI: 10.1016/j.polymer.2012.07.010. URL: <http://www.sciencedirect.com/science/article/pii/S0032386112005770> (visited on 06/23/2018).
- [284] Luigi Angiolini et al. "Side chain porphyrin moiety linked to polymer-fullerene composite solar cell". In: *Reactive and Functional Polymers* 73.9 (Sept. 1, 2013), pp. 1198–1206. ISSN: 1381-5148. DOI: 10.1016/j.reactfunctpolym.2013.05.007. URL: <http://www.sciencedirect.com/science/article/pii/S1381514813001181> (visited on 06/23/2018).
- [285] Youngkyoo Kim et al. "A strong regioregularity effect in self-organizing conjugated polymer films and high-efficiency polythiophene:fullerene solar cells". In: *Nature Materials* 5.3 (Mar. 2006), pp. 197–203. ISSN: 1476-4660. DOI: 10.1038/nmat1574. URL: <https://www.nature.com/articles/nmat1574> (visited on 06/23/2018).
- [286] Ming Shao et al. "A water-soluble polythiophene for organic field-effect transistors". In: *Polymer Chemistry* 4.20 (2013), p. 5270. ISSN: 1759-9954, 1759-9962. DOI: 10.1039/c2py21020g. URL: <http://xlink.rsc.org/?DOI=c2py21020g> (visited on 05/26/2016).
- [287] Henning Sirringhaus, Nir Tessler, and Richard H. Friend. "Integrated Optoelectronic Devices Based on Conjugated Polymers". In: *Science* 280.5370 (June 12, 1998), pp. 1741–1744. ISSN: 0036-8075, 1095-9203. DOI: 10.1126/science.280.5370.1741. URL: <http://science.sciencemag.org/content/280/5370/1741> (visited on 06/23/2018).
- [288] Natalie Stutzmann, Richard H. Friend, and Henning Sirringhaus. "Self-Aligned, Vertical-Channel, Polymer Field-Effect Transistors". In: *Science* 299.5614 (Mar. 21, 2003), pp. 1881–1884. ISSN: 0036-8075, 1095-9203. DOI: 10.1126/science.1081279. URL: <http://science.sciencemag.org/content/299/5614/1881> (visited on 06/23/2018).
- [289] Sung Kwang Ahn et al. "Synthesis and characterization of novel crosslinkable poly(propylenedioxythiophene) derivative as a buffer layer for organic light-emitting diode applications". In: *Macromolecular Research* 20.5 (May 1, 2012), pp. 459–464. ISSN: 1598-5032, 2092-7673. DOI: 10.1007/s13233-012-0115-1. URL: <https://link.springer.com/article/10.1007/s13233-012-0115-1> (visited on 06/23/2018).
- [290] J. H. Burroughes et al. "Light-emitting diodes based on conjugated polymers". In: *Nature* 347.6293 (Oct. 1990), pp. 539–541. ISSN: 1476-4687. DOI: 10.1038/347539a0. URL: <https://www.nature.com/articles/347539a0> (visited on 06/23/2018).
- [291] Jie Shen, Kousuke Tsuchiya, and Kenji Ogino. "Synthesis and characterization of highly fluorescent polythiophene derivatives containing polystyrene sidearms". In: *Journal of Polymer Science Part A: Polymer Chemistry* 46.3 (Feb. 1, 2008), pp. 1003–1013. ISSN: 1099-0518. DOI: 10.1002/pola.22443. URL: <http://onlinelibrary.wiley.com/doi/10.1002/pola.22443/abstract> (visited on 01/20/2016).
- [292] A.D. Bendrea, L. Cianga, and I. Cianga. "Review Paper: Progress in the Field of Conducting Polymers for Tissue Engineering Applications". In: *J. Biomater. Appl.* 26 (2011), pp. 1–84.
- [293] Leon A. P. Kane-Maguire and Gordon G. Wallace. "Chiral conducting polymers". In: *Chemical Society Reviews* 39.7 (June 22, 2010), pp. 2545–2576. ISSN: 1460-4744. DOI: 10.1039/B908001P. URL: <http://pubs.rsc.org/en/content/articlelanding/2010/cs/b908001p> (visited on 06/23/2018).
- [294] Kohsuke Kawabata, Masaki Takeguchi, and Hiromasa Goto. "Optical Activity of Heteroaromatic Conjugated Polymer Films Prepared by Asymmetric Electrochemical Polymerization in Cholesteric Liquid Crystals: Structural Function for Chiral Induction". In: *Macromolecules* 46.6

- (Mar. 26, 2013), pp. 2078–2091. ISSN: 0024-9297. DOI: 10.1021/ma400302j. URL: <https://doi.org/10.1021/ma400302j> (visited on 06/23/2018).
- [295] S. Kowalski et al. “Direct arylation polycondensation as simplified alternative for the synthesis of conjugated (co)polymers”. In: *Progress in Polymer Science*. Topical issue on Conductive Polymers 38.12 (Dec. 1, 2013), pp. 1805–1814. ISSN: 0079-6700. DOI: 10.1016/j.progpolymsci.2013.04.006. URL: <http://www.sciencedirect.com/science/article/pii/S0079670013000403> (visited on 06/23/2018).
- [296] Marc Sevignon et al. “New synthetic method for the polymerization of alkylthiophenes”. In: *Tetrahedron Letters* 40.32 (Aug. 6, 1999), pp. 5873–5876. ISSN: 0040-4039. DOI: 10.1016/S0040-4039(99)01164-8. URL: <http://www.sciencedirect.com/science/article/pii/S0040403999011648> (visited on 06/23/2018).
- [297] E. N. Rodlovskaya et al. “Achievements in the synthesis of thiophene-containing polymers”. In: *Polymer Science Series C* 48.1 (July 1, 2006), pp. 58–84. ISSN: 1811-2382, 1555-614X. DOI: 10.1134/S1811238206010048. URL: <https://link.springer.com/article/10.1134/S1811238206010048> (visited on 06/23/2018).
- [298] Eftychia Grana et al. “Synthesis and molecular characterization of polythiophene and polystyrene copolymers: Simultaneous preparation of diblock and miktoarm copolymers”. In: *European Polymer Journal* 49.5 (May 1, 2013), pp. 1089–1097. ISSN: 0014-3057. DOI: 10.1016/j.eurpolymj.2013.01.011. URL: <http://www.sciencedirect.com/science/article/pii/S0014305713000293> (visited on 06/23/2018).
- [299] Parimal Routh, Sandip Das, and Arun K. Nandi. “Polythiophene -g-poly(dimethylaminoethyl methacrylate) stabilized Au nanoparticles and its morphology tuning by RNA with variation of electronic properties”. In: *RSC Advances* 2.30 (Oct. 29, 2012), pp. 11295–11305. ISSN: 2046-2069. DOI: 10.1039/C2RA21413J. URL: <http://pubs.rsc.org/en/content/articlelanding/2012/ra/c2ra21413j> (visited on 06/23/2018).
- [300] N. Chanunpanich et al. “Grafting polythiophene on polyethylene surfaces”. In: *Polymer International* 52.1 (2003), pp. 172–178. ISSN: 1097-0126. DOI: 10.1002/pi.1016. URL: <https://onlinelibrary.wiley.com/doi/abs/10.1002/pi.1016> (visited on 06/23/2018).
- [301] Christian Müller et al. “Crystalline -crystalline poly(3-hexylthiophene)-polyethylene diblock copolymers: Solidification from the melt”. In: *Polymer* 49.18 (Aug. 26, 2008), pp. 3973–3978. ISSN: 0032-3861. DOI: 10.1016/j.polymer.2008.07.006. URL: <http://www.sciencedirect.com/science/article/pii/S0032386108005636> (visited on 06/23/2018).
- [302] Kyung Tae Kim and Won Ho Jo. “Synthesis of poly(3-hexylthiophene)-graft-poly(t-butyl acrylate-co-acrylic acid) and its role of compatibilizer for enhancement of mechanical and electrical properties of Nylon 66/multi-walled carbon nanotube composites”. In: *Composites Science and Technology*. Smart Composites and Nanocomposites Special Issue with Regular Papers 69.13 (Oct. 1, 2009), pp. 2205–2211. ISSN: 0266-3538. DOI: 10.1016/j.compscitech.2009.06.013. URL: <http://www.sciencedirect.com/science/article/pii/S026635380900222X> (visited on 06/23/2018).
- [303] Ki Hong Kim and Won Ho Jo. “Polythiophene -graft-PMMA as a dispersing agent for multi-walled carbon nanotubes in organic solvent”. In: *Macromolecular Research* 16.8 (Dec. 1, 2008), pp. 749–752. ISSN: 1598-5032, 2092-7673. DOI: 10.1007/BF03218591. URL: <https://link.springer.com/article/10.1007/BF03218591> (visited on 06/23/2018).
- [304] Malika Jeffries-El, Geneviève Sauvé, and Richard D. McCullough. “Facile Synthesis of End-Functionalized Regioregular Poly(3-alkylthiophene)s via Modified Grignard Metathesis Reaction”. In: *Macromolecules* 38.25 (Dec. 2005), pp. 10346–10352. ISSN: 0024-9297, 1520-5835. DOI: 10.1021/ma051096q. URL: <http://pubs.acs.org/doi/abs/10.1021/ma051096q> (visited on 09/09/2016).

- [305] Brent S. Gaylord, Alan J. Heeger, and Guillermo C. Bazan. “DNA Hybridization Detection with Water-Soluble Conjugated Polymers and Chromophore-Labeled Single-Stranded DNA”. In: *Journal of the American Chemical Society* 125.4 (Jan. 1, 2003), pp. 896–900. ISSN: 0002-7863. DOI: 10.1021/ja027152+. URL: <https://doi.org/10.1021/ja027152+> (visited on 06/23/2018).
- [306] J. M. Pringle et al. “The influence of the monomer and the ionic liquid on the electrochemical preparation of polythiophene”. In: *Polymer* 46.7 (Mar. 10, 2005), pp. 2047–2058. ISSN: 0032-3861. DOI: 10.1016/j.polymer.2005.01.034. URL: <http://www.sciencedirect.com/science/article/pii/S0032386105000765> (visited on 06/23/2018).
- [307] F. Yilmaz et al. “Controlled Synthesis of Block Copolymers Containing Side Chain Thiophene Units and Their Use in Electrocopolymerization with Thiophene and Pyrrole”. In: *Journal of Macromolecular Science, Part A* 41.4 (Dec. 31, 2004), pp. 401–418. ISSN: 1060-1325. DOI: 10.1081/MA-120028475. URL: <https://doi.org/10.1081/MA-120028475> (visited on 06/23/2018).
- [308] M. D. Levi and D. Aurbach. “A short review on the strategy towards development of -conjugated polymers with highly reversible p- and n-doping”. In: *Journal of Power Sources* 180.2 (June 1, 2008), pp. 902–908. ISSN: 0378-7753. DOI: 10.1016/j.jpowsour.2007.08.080. URL: <http://www.sciencedirect.com/science/article/pii/S0378775307016436> (visited on 06/23/2018).
- [309] Ryo Miyakoshi, Akihiro Yokoyama, and Tsutomu Yokozawa. “Development of catalyst-transfer condensation polymerization. Synthesis of -conjugated polymers with controlled molecular weight and low polydispersity”. In: *Journal of Polymer Science Part A: Polymer Chemistry* 46.3 (2007), pp. 753–765. ISSN: 1099-0518. DOI: 10.1002/pola.22389. URL: <https://onlinelibrary.wiley.com/doi/abs/10.1002/pola.22389> (visited on 06/23/2018).
- [310] Joji Ohshita et al. “Synthesis of silicon-bridged polythiophene derivatives and their applications to EL device materials”. In: *Journal of Polymer Science Part A: Polymer Chemistry* 45.20 (2012), pp. 4588–4596. ISSN: 1099-0518. DOI: 10.1002/pola.22196. URL: <https://onlinelibrary.wiley.com/doi/abs/10.1002/pola.22196> (visited on 06/23/2018).
- [311] Shunsuke Tamba et al. “Synthesis of -conjugated poly(thienylenearylene)s with nickel-catalyzed C-H functionalization polycondensation”. In: *Polymer Journal* 44.12 (Dec. 2012), pp. 1209–1213. ISSN: 1349-0540. DOI: 10.1038/pj.2012.89. URL: <https://www.nature.com/articles/pj201289> (visited on 06/23/2018).
- [312] Tian An Chen and Reuben D. Rieke. “The first regioregular head-to-tail poly(3-hexylthiophene-2,5-diyl) and a regiorandom isopolymer: nickel versus palladium catalysis of 2(5)-bromo-5(2)-(bromozincio)-3-hexylthiophene polymerization”. In: *Journal of the American Chemical Society* 114.25 (Dec. 1, 1992), pp. 10087–10088. ISSN: 0002-7863. DOI: 10.1021/ja00051a066. URL: <https://doi.org/10.1021/ja00051a066> (visited on 02/25/2018).
- [313] Akihiro Yokoyama, Ryo Miyakoshi, and Tsutomu Yokozawa. “Chain-Growth Polymerization for Poly(3-hexylthiophene) with a Defined Molecular Weight and a Low Polydispersity”. In: *Macromolecules* 37.4 (Feb. 1, 2004), pp. 1169–1171. ISSN: 0024-9297. DOI: 10.1021/ma035396o. URL: <https://doi.org/10.1021/ma035396o> (visited on 02/25/2018).
- [314] Ge Qu, Justin J. Kwok, and Ying Diao. “Flow-Directed Crystallization for Printed Electronics”. In: *Accounts of Chemical Research* 49.12 (Dec. 20, 2016), pp. 2756–2764. ISSN: 0001-4842. DOI: 10.1021/acs.accounts.6b00445. URL: <http://dx.doi.org/10.1021/acs.accounts.6b00445> (visited on 01/04/2017).
- [315] Antonio Facchetti. “-Conjugated Polymers for Organic Electronics and Photovoltaic Cell Applications”. In: *Chemistry of Materials* 23.3 (Feb. 8, 2011), pp. 733–758. ISSN: 0897-4756. DOI: 10.1021/cm102419z. URL: <https://doi.org/10.1021/cm102419z> (visited on 06/23/2018).
- [316] Akinori Saeki et al. “Comprehensive Approach to Intrinsic Charge Carrier Mobility in Conjugated Organic Molecules, Macromolecules, and Supramolecular Architectures”. In: *Accounts of Chemical Research* 45.8 (Aug. 21, 2012), pp. 1193–1202. ISSN: 0001-4842. DOI: 10.1021/ar200283b. URL: <https://doi.org/10.1021/ar200283b> (visited on 06/23/2018).

- [317] Sarah Holliday, Jenny E. Donaghey, and Iain McCulloch. “Advances in Charge Carrier Mobilities of Semiconducting Polymers Used in Organic Transistors”. In: *Chemistry of Materials* 26.1 (Jan. 14, 2014), pp. 647–663. ISSN: 0897-4756. DOI: 10.1021/cm402421p. URL: <https://doi.org/10.1021/cm402421p> (visited on 06/23/2018).
- [318] Hsin-Rong Tseng et al. “High-mobility field-effect transistors fabricated with macroscopic aligned semiconducting polymers”. In: *Advanced Materials (Deerfield Beach, Fla.)* 26.19 (May 21, 2014), pp. 2993–2998. ISSN: 1521-4095. DOI: 10.1002/adma.201305084.
- [319] Hagen Klauk. *Organic Electronics II: More Materials and Applications*. Google-Books-ID: qjsBuDZSDY0C. John Wiley & Sons, Mar. 26, 2012. 443 pp. ISBN: 978-3-527-32647-1.
- [320] Yoann Olivier et al. “25th Anniversary Article: High-Mobility Hole and Electron Transport Conjugated Polymers: How Structure Defines Function”. In: *Advanced Materials* 26.14 (Apr. 1, 2014), pp. 2119–2136. ISSN: 1521-4095. DOI: 10.1002/adma.201305809. URL: <http://onlinelibrary.wiley.com/doi/10.1002/adma.201305809/abstract> (visited on 01/04/2017).
- [321] Zhao-Yang Zhang and Tao Li. “Single-chain and monolayered conjugated polymers for molecular electronics”. In: *Chinese Chemical Letters* 27.8 (Aug. 2016), pp. 1209–1222. ISSN: 1001-8417. DOI: 10.1016/j.ccllet.2016.05.031. URL: <http://www.sciencedirect.com/science/article/pii/S1001841716301541> (visited on 10/13/2016).
- [322] Robert M. Metzger. “Unimolecular Electronics”. In: *Chemical Reviews* 115.11 (June 10, 2015), pp. 5056–5115. ISSN: 0009-2665. DOI: 10.1021/cr500459d. URL: <http://dx.doi.org/10.1021/cr500459d> (visited on 10/13/2016).
- [323] Gaël Reece et al. “Electroluminescence of a Polythiophene Molecular Wire Suspended between a Metallic Surface and the Tip of a Scanning Tunneling Microscope”. In: *Physical Review Letters* 112.4 (Jan. 28, 2014), p. 047403. DOI: 10.1103/PhysRevLett.112.047403. URL: <https://link.aps.org/doi/10.1103/PhysRevLett.112.047403> (visited on 02/22/2018).
- [324] H. X. He et al. “Discrete conductance switching in conducting polymer wires”. In: *Physical Review B* 68.4 (July 3, 2003), p. 045302. DOI: 10.1103/PhysRevB.68.045302. URL: <https://link.aps.org/doi/10.1103/PhysRevB.68.045302> (visited on 06/23/2018).
- [325] Leif Lafferentz et al. “Conductance of a Single Conjugated Polymer as a Continuous Function of Its Length.” In: *Science (Washington, DC, United States)* 323 (Copyright (C) 2015 American Chemical Society (ACS). All Rights Reserved. 2009), pp. 1193–1197. ISSN: 0036-8075. DOI: 10.1126/science.1168255.
- [326] Seong Ho Choi and C. Daniel Frisbie. “Enhanced Hopping Conductivity in Low Band Gap Donor-Acceptor Molecular Wires Up to 20 nm in Length”. In: *Journal of the American Chemical Society* 132.45 (Nov. 17, 2010), pp. 16191–16201. ISSN: 0002-7863. DOI: 10.1021/ja1060142. URL: <https://doi.org/10.1021/ja1060142> (visited on 07/20/2018).
- [327] Joon Sung Lee et al. “Local Scanning Probe Polymerization of an Organic Monolayer Covalently Grafted on Silicon”. In: *Langmuir* 28.40 (Oct. 9, 2012), pp. 14496–14501. ISSN: 0743-7463. DOI: 10.1021/la302526t. URL: <https://doi.org/10.1021/la302526t> (visited on 06/23/2018).
- [328] Yu Tokura et al. “Bottom-Up Fabrication of Nanopatterned Polymers on DNA Origami by In Situ Atom-Transfer Radical Polymerization”. In: *Angewandte Chemie International Edition* 55.19 (May 4, 2016), pp. 5692–5697. ISSN: 1521-3773. DOI: 10.1002/anie.201511761. URL: <http://onlinelibrary.wiley.com/doi/10.1002/anie.201511761/abstract> (visited on 09/18/2016).
- [329] Hui Peng et al. “Conducting polymers for electrochemical DNA sensing”. In: *Biomaterials* 30.11 (Apr. 2009), pp. 2132–2148. ISSN: 01429612. DOI: 10.1016/j.biomaterials.2008.12.065. URL: <http://linkinghub.elsevier.com/retrieve/pii/S0142961208010545> (visited on 11/10/2015).
- [330] Ramaswamy Nagarajan et al. “Manipulating DNA Conformation Using Intertwined Conducting Polymer Chains”. In: *Macromolecules* 34.12 (June 1, 2001), pp. 3921–3927. ISSN: 0024-9297. DOI: 10.1021/ma0021287. URL: <https://doi.org/10.1021/ma0021287> (visited on 06/23/2018).

- [331] Yufeng Ma et al. "Polyaniline Nanowires on Si Surfaces Fabricated with DNA Templates". In: *Journal of the American Chemical Society* 126.22 (June 1, 2004), pp. 7097–7101. ISSN: 0002-7863. DOI: 10.1021/ja039621t. URL: <https://doi.org/10.1021/ja039621t> (visited on 06/23/2018).
- [332] Patrick Nickels et al. "Polyaniline nanowire synthesis templated by DNA". In: *Nanotechnology* 15.11 (2004), p. 1524. ISSN: 0957-4484. DOI: 10.1088/0957-4484/15/11/026. URL: <http://stacks.iop.org/0957-4484/15/i=11/a=026> (visited on 06/23/2018).
- [333] Liqin Dong et al. "Synthesis, Manipulation and Conductivity of Supramolecular Polymer Nanowires". In: *Chemistry - A European Journal* 13.3 (2007), pp. 822–828. ISSN: 1521-3765. DOI: 10.1002/chem.200601320. URL: <https://onlinelibrary.wiley.com/doi/abs/10.1002/chem.200601320> (visited on 06/23/2018).
- [334] S. Pruneanu et al. "Self-assembly of DNA-templated polypyrrole nanowires: Spontaneous formation of conductive nanoropes". In: *Advanced Functional Materials* (2008). DOI: 10.1002/adfm.200701336. URL: <https://eprint.ncl.ac.uk/77224> (visited on 06/23/2018).
- [335] Jennifer Hannant et al. "Modification of DNA-templated conductive polymer nanowires via click chemistry". In: *Chemical Communications* 46.32 (Aug. 3, 2010), pp. 5870–5872. ISSN: 1364-548X. DOI: 10.1039/C0CC00693A. URL: <http://pubs.rsc.org/en/content/articlelanding/2010/cc/c0cc00693a> (visited on 06/23/2018).
- [336] Reda Hassanien et al. "Preparation and Characterization of Conductive and Photoluminescent DNA-Templated Polyindole Nanowires". In: *ACS Nano* 4.4 (Apr. 27, 2010), pp. 2149–2159. ISSN: 1936-0851. DOI: 10.1021/nn9014533. URL: <https://doi.org/10.1021/nn9014533> (visited on 06/23/2018).
- [337] Scott M. D. Watson et al. "Synthesis, Characterisation and Electrical Properties of Supramolecular DNA-Templated Polymer Nanowires of 2,5-(Bis-2-thienyl)-pyrrole". In: *Chemistry - A European Journal* 18.38 (2012), pp. 12008–12019. ISSN: 1521-3765. DOI: 10.1002/chem.201201495. URL: <https://onlinelibrary.wiley.com/doi/abs/10.1002/chem.201201495> (visited on 06/23/2018).
- [338] Erez Braun and Kinneret Keren. "From DNA to transistors". In: *Advances in Physics* 53.4 (June 1, 2004), pp. 441–496. ISSN: 0001-8732. DOI: 10.1080/00018730412331294688. URL: <https://doi.org/10.1080/00018730412331294688> (visited on 06/23/2018).
- [339] J. Richter et al. "Nanoscale Palladium Metallization of DNA". In: *Advanced Materials* 12.7 (2000), pp. 507–510. ISSN: 1521-4095. DOI: 10.1002/(SICI)1521-4095(200004)12:7<507::AID-ADMA507>3.0.CO;2-G. URL: <https://onlinelibrary.wiley.com/doi/abs/10.1002/%28SICI%291521-4095%28200004%2912%3A7%3C507%3A%3AAID-ADMA507%3E3.0.CO%3B2-G> (visited on 06/23/2018).
- [340] Pik Kwan Lo and Hanadi F. Sleiman. "Nucleobase-Templated Polymerization: Copying the Chain Length and Polydispersity of Living Polymers into Conjugated Polymers". In: *Journal of the American Chemical Society* 131.12 (Apr. 2009), pp. 4182–4183. ISSN: 0002-7863, 1520-5126. DOI: 10.1021/ja809613n. URL: <http://pubs.acs.org/doi/abs/10.1021/ja809613n> (visited on 11/10/2015).
- [341] Amanda C. Kamps et al. "Self-Assembly of DNA-Coupled Semiconducting Block Copolymers". In: *Macromolecules* 47.11 (June 10, 2014), pp. 3720–3726. ISSN: 0024-9297, 1520-5835. DOI: 10.1021/ma500509u. URL: <http://pubs.acs.org/doi/abs/10.1021/ma500509u> (visited on 04/01/2015).
- [342] Zhi Li et al. "Reversible and Chemically Programmable Micelle Assembly with DNA Block-Copolymer Amphiphiles". In: *Nano Letters* 4.6 (June 1, 2004), pp. 1055–1058. ISSN: 1530-6984. DOI: 10.1021/nl049628o. URL: <https://doi.org/10.1021/nl049628o> (visited on 06/23/2018).
- [343] Fikri E. Alemdaroglu and Andreas Herrmann. "DNA meets synthetic polymers? highly versatile hybrid materials". In: *Organic & Biomolecular Chemistry* 5.9 (2007), p. 1311. ISSN: 1477-0520,

- 1477-0539. DOI: 10.1039/b617941j. URL: <http://xlink.rsc.org/?DOI=b617941j> (visited on 11/10/2015).
- [344] Minseok Kwak and Andreas Herrmann. “Nucleic Acid/Organic Polymer Hybrid Materials: Synthesis, Superstructures, and Applications”. In: *Angewandte Chemie International Edition* 49.46 (Nov. 8, 2010), pp. 8574–8587. ISSN: 14337851. DOI: 10.1002/anie.200906820. URL: <http://doi.wiley.com/10.1002/anie.200906820> (visited on 11/10/2015).
- [345] Minseok Kwak et al. “DNA Block Copolymer Doing It All: From Selection to Self-Assembly of Semiconducting Carbon Nanotubes”. In: *Angewandte Chemie International Edition* 50.14 (Mar. 1, 2011), pp. 3206–3210. ISSN: 1521-3773. DOI: 10.1002/anie.201007098. URL: <https://onlinelibrary.wiley.com/doi/abs/10.1002/anie.201007098> (visited on 07/20/2018).
- [346] K. Lee, L. K. Povlich, and J. Kim. “Label-Free and Self-Signal Amplifying Molecular DNA Sensors Based on Bioconjugated Polyelectrolytes”. In: *Advanced Functional Materials* 17.14 (Aug. 28, 2007), pp. 2580–2587. ISSN: 1616-3028. DOI: 10.1002/adfm.200700218. URL: <https://www.onlinelibrary.wiley.com/doi/abs/10.1002/adfm.200700218> (visited on 06/23/2018).
- [347] Christopher K. McLaughlin et al. “Three-Dimensional Organization of Block Copolymers on “DNA-Minimal” Scaffolds”. In: *Journal of the American Chemical Society* 134.9 (Mar. 7, 2012), pp. 4280–4286. ISSN: 0002-7863. DOI: 10.1021/ja210313p. URL: <http://dx.doi.org/10.1021/ja210313p> (visited on 03/12/2017).
- [348] Motoi Oishi et al. “Supramolecular Assemblies for the Cytoplasmic Delivery of Antisense Oligodeoxynucleotide: Polyion Complex (PIC) Micelles Based on Poly(ethylene glycol)-SS-Oligodeoxynucleotide Conjugate”. In: *Biomacromolecules* 6.5 (Sept. 1, 2005), pp. 2449–2454. ISSN: 1525-7797. DOI: 10.1021/bm0503701. URL: <https://doi.org/10.1021/bm0503701> (visited on 06/23/2018).
- [349] Motoi Oishi et al. “Smart Polyion Complex Micelles for Targeted Intracellular Delivery of PEGylated Antisense Oligonucleotides Containing Acid-Labile Linkages”. In: *ChemBioChem* 6.4 (Apr. 6, 2005), pp. 718–725. ISSN: 1439-7633. DOI: 10.1002/cbic.200400334. URL: <https://onlinelibrary.wiley.com/doi/abs/10.1002/cbic.200400334> (visited on 06/23/2018).
- [350] Ping Chen et al. “DNA-Grafted Polypeptide Molecular Bottlebrush Prepared via Ring-Opening Polymerization and Click Chemistry”. In: *Macromolecules* 45.24 (Dec. 21, 2012), pp. 9579–9584. ISSN: 0024-9297. DOI: 10.1021/ma302233m. URL: <https://doi.org/10.1021/ma302233m> (visited on 06/23/2018).
- [351] Nicholas J. Agard, Jennifer A. Prescher, and Carolyn R. Bertozzi. “A Strain-Promoted [3 + 2] Azide-Alkyne Cycloaddition for Covalent Modification of Biomolecules in Living Systems”. In: *Journal of the American Chemical Society* 126.46 (Nov. 1, 2004), pp. 15046–15047. ISSN: 0002-7863. DOI: 10.1021/ja044996f. URL: <https://doi.org/10.1021/ja044996f> (visited on 06/23/2018).
- [352] Xiao Wang et al. “Construction of a DNA Origami Based Molecular Electro-optical Modulator”. In: *Nano Letters* 18.3 (Mar. 14, 2018), pp. 2112–2115. ISSN: 1530-6984. DOI: 10.1021/acs.nanolett.8b00332. URL: <https://doi.org/10.1021/acs.nanolett.8b00332> (visited on 06/30/2018).
- [353] S. Karg et al. “Electrical and optical characterization of poly(phenylene-vinylene) light emitting diodes”. In: *Synthetic Metals* 54.1 (Mar. 1, 1993), pp. 427–433. ISSN: 0379-6779. DOI: 10.1016/0379-6779(93)91088-J. URL: <http://www.sciencedirect.com/science/article/pii/037967799391088J> (visited on 07/29/2018).
- [354] R. N. Marks et al. “The photovoltaic response in poly(p-phenylene vinylene) thin-film devices”. In: *Journal of Physics: Condensed Matter* 6.7 (1994), p. 1379. ISSN: 0953-8984. DOI: 10.1088/0953-8984/6/7/009. URL: <http://stacks.iop.org/0953-8984/6/i=7/a=009> (visited on 07/29/2018).
- [355] H. Antoniadis et al. “Photovoltaic and photoconductive properties of aluminum/poly(p-phenylene vinylene) interfaces”. In: *Synthetic Metals* 62.3 (Feb. 1, 1994), pp. 265–271. ISSN: 0379-6779. DOI: 10.1016/0379-6779(94)90215-1. URL: <http://www.sciencedirect.com/science/article/pii/0379677994902151> (visited on 07/29/2018).

- [356] J. De Mey. “Colloidal Gold Probes in Immunocytochemistry”. In: *Immunocytochemistry*. Ed. by Julia M. Polak and Susan Van Noorden. Butterworth-Heinemann, Jan. 1, 1983, pp. 82–112. ISBN: 978-0-7236-0669-7. DOI: 10.1016/B978-0-7236-0669-7.50013-1. URL: <http://www.sciencedirect.com/science/article/pii/B9780723606697500131> (visited on 07/05/2018).
- [357] Weihai Ni et al. “Tailoring Longitudinal Surface Plasmon Wavelengths, Scattering and Absorption Cross Sections of Gold Nanorods”. In: *ACS Nano* 2.4 (Apr. 1, 2008), pp. 677–686. ISSN: 1936-0851. DOI: 10.1021/nn7003603. URL: <https://doi.org/10.1021/nn7003603> (visited on 07/05/2018).
- [358] Taishi Zhang et al. “Single-Particle Spectroscopic Study on Fluorescence Enhancement by Plasmon Coupled Gold Nanorod Dimers Assembled on DNA Origami”. In: *The Journal of Physical Chemistry Letters* (May 13, 2015), pp. 2043–2049. ISSN: 1948-7185. DOI: 10.1021/acs.jpcllett.5b00747. URL: <http://dx.doi.org/10.1021/acs.jpcllett.5b00747> (visited on 05/19/2015).
- [359] Anja Henning-Knechtel et al. “Dielectrophoresis of gold nanoparticles conjugated to DNA origami structures”. In: *Beilstein Journal of Nanotechnology* 7 (July 1, 2016), pp. 948–956. ISSN: 2190-4286. DOI: 10.3762/bjnano.7.87. URL: <https://www.ncbi.nlm.nih.gov/pmc/articles/PMC4979641/> (visited on 07/03/2018).
- [360] Suchetan Pal et al. “DNA Directed Self-Assembly of Anisotropic Plasmonic Nanostructures”. In: *Journal of the American Chemical Society* 133.44 (Nov. 9, 2011), pp. 17606–17609. ISSN: 0002-7863. DOI: 10.1021/ja207898r. URL: <https://doi.org/10.1021/ja207898r> (visited on 08/05/2018).
- [361] Volodymyr Senkovskyy et al. “Convenient Route To Initiate Kumada Catalyst-Transfer Polycondensation Using Ni(dppe)Cl₂ or Ni(dppp)Cl₂ and Sterically Hindered Grignard Compounds”. In: *Macromolecules* 43.23 (Dec. 14, 2010), pp. 10157–10161. ISSN: 0024-9297. DOI: 10.1021/ma1024889. URL: <https://doi.org/10.1021/ma1024889> (visited on 07/09/2018).
- [362] Isao Adachi et al. “Synthesis of Well-Defined Polythiophene with Oxyethylene Side Chain: Effect of Phosphine Ligands on Catalyst-Transfer Polycondensation”. In: *Macromolecules* 39.23 (Nov. 1, 2006), pp. 7793–7795. ISSN: 0024-9297. DOI: 10.1021/ma061809k. URL: <http://dx.doi.org/10.1021/ma061809k> (visited on 12/29/2016).
- [363] Alex D. Herbert. *IMAGEJ FINDFOCI Plugins*. FindFoci. Nov. 18, 2014. URL: <http://www.sussex.ac.uk/gdsc/intranet/microscopy/UserSupport/AnalysisProtocol/imagej/findfoci> (visited on 03/22/2016).
- [364] David Nečas and Petr Klapetek. “Gwyddion: an open-source software for SPM data analysis”. In: *Central European Journal of Physics* 10 (Feb. 1, 2012), pp. 181–188. ISSN: 1895-1082. DOI: 10.2478/s11534-011-0096-2. URL: <http://adsabs.harvard.edu/abs/2012CEJPh..10..181N> (visited on 04/28/2016).
- [365] Johannes Schindelin et al. “Fiji: an open-source platform for biological-image analysis”. In: *Nature Methods* 9.7 (July 2012), pp. 676–682. ISSN: 1548-7091. DOI: 10.1038/nmeth.2019. URL: <http://www.nature.com/nmeth/journal/v9/n7/full/nmeth.2019.html> (visited on 04/28/2016).
- [366] H H Ku. “Notes on the use of propagation of error formulas”. In: *Journal of Research of the National Bureau of Standards. Section C: Engineering and Instrumentation* 70C.4 (Oct. 1966), p. 263. ISSN: 0022-4316. DOI: <https://dx.doi.org/10.6028/jres.070C.025>. URL: <http://nistdigitalarchives.contentdm.oclc.org/cdm/ref/collection/p16009coll6/id/99848>.
- [367] Franziska Fischer, Anja Henning-Knechtel, and Michael Mertig. “Investigating the aggregation behaviour of DNA origami frames”. In: *Physica Status Solidi A* (2015).
- [368] Masayuki Endo et al. “A Versatile DNA Nanochip for Direct Analysis of DNA Base-Excision Repair”. In: *Angewandte Chemie International Edition* 49.49 (Dec. 3, 2010), pp. 9412–9416. ISSN: 14337851. DOI: 10.1002/anie.201003604. URL: <http://doi.wiley.com/10.1002/anie.201003604> (visited on 09/08/2016).
- [369] Masayuki Endo et al. “Single-Molecule Manipulation of the Duplex Formation and Dissociation at the G-Quadruplex/i-Motif Site in the DNA Nanostructure”. In: *ACS Nano* 9.10 (Oct. 27, 2015),

- pp. 9922–9929. ISSN: 1936-0851. DOI: 10.1021/acsnano.5b03413. URL: <http://dx.doi.org/10.1021/acsnano.5b03413>.
- [370] Peter Markiewicz and M. Cynthia Goh. “Atomic force microscopy probe tip visualization and improvement of images using a simple deconvolution procedure”. In: *Langmuir* 10.1 (Jan. 1, 1994), pp. 5–7. ISSN: 0743-7463. DOI: 10.1021/la00013a002. URL: <https://doi.org/10.1021/la00013a002> (visited on 06/24/2018).
- [371] Gerald S. Manning. “The Persistence Length of DNA Is Reached from the Persistence Length of Its Null Isomer through an Internal Electrostatic Stretching Force”. In: *Biophysical Journal* 91.10 (Nov. 2006), pp. 3607–3616. ISSN: 00063495. DOI: 10.1529/biophysj.106.089029. URL: <http://linkinghub.elsevier.com/retrieve/pii/S0006349506720732> (visited on 06/26/2018).
- [372] Sriram Kosuri and George M Church. “Large-scale de novo DNA synthesis: technologies and applications”. In: *Nature Methods* 11.5 (May 2014), pp. 499–507. ISSN: 1548-7091, 1548-7105. DOI: 10.1038/nmeth.2918. URL: <http://www.nature.com/articles/nmeth.2918> (visited on 06/27/2018).
- [373] Merck. *Oligonucleotide Purification*. June 27, 2018. URL: <https://www.sigmaaldrich.com/technical-documents/articles/biology/best-purification.html> (visited on 06/27/2018).
- [374] Sherri Rinker et al. “Self-assembled DNA nanostructures for distance-dependent multivalent ligand-protein binding”. In: *Nature Nanotechnology* 3.7 (July 2008), pp. 418–422. ISSN: 1748-3387. DOI: 10.1038/nnano.2008.164. URL: <http://www.nature.com/nnano/journal/v3/n7/full/nnano.2008.164.html> (visited on 03/07/2017).
- [375] Bernard Tinland et al. “Persistence Length of Single-Stranded DNA”. In: (1997), p. 3.
- [376] M. C. Murphy et al. “Probing single-stranded DNA conformational flexibility using fluorescence spectroscopy”. In: *Biophysical Journal* 86.4 (Apr. 2004), pp. 2530–2537. ISSN: 0006-3495. DOI: 10.1016/S0006-3495(04)74308-8.
- [377] Na Wu et al. “Molecular Threading and Tunable Molecular Recognition on DNA Origami Nanostructures”. In: *Journal of the American Chemical Society* 135.33 (Aug. 21, 2013), pp. 12172–12175. ISSN: 0002-7863. DOI: 10.1021/ja403863a. URL: <http://dx.doi.org/10.1021/ja403863a> (visited on 09/21/2016).
- [378] *fitgeotrans*. MathWorks. June 15, 2018. URL: <https://www.mathworks.com/help/images/ref/fitgeotrans.html> (visited on 05/15/2018).
- [379] Ben J. Glasgow. “Conventional fluorescence microscopy below the diffraction limit with simultaneous capture of two fluorophores in DNA origami”. In: vol. 9714. 2016, pp. 971411–971411–8. DOI: 10.1117/12.2211074. URL: <http://dx.doi.org/10.1117/12.2211074> (visited on 09/25/2016).
- [380] Ronald L. ; Andrews Phillips. *Mathematical techniques for engineers and scientists* /. Vol. 118. SPIE Press monograph ; 118. Bellingham, Wash. <1000 20th St. Bellingham WA 98225-6705 USA>: SPIE, 2003. 1 online resource (xv, 797 p. : ill.) ISBN: 978-0-8194-7829-0 978-0-8194-4506-3. URL: <http://dx.doi.org/10.1117/3.467443>.
- [381] Anna Maria Popescu. *What is the distribution of the euclidean distance between two random points in 2d space?* Stack Overflow. Mar. 27, 2012. URL: <https://stats.stackexchange.com/questions/25358/what-is-the-distribution-of-the-euclidean-distance-between-two-random-points-in?noredirect=1&lq=1> (visited on 03/17/2017).
- [382] Alan Kvanli, Robert Pavur, and Kellie Keeling. *Concise Managerial Statistics*. Google-Books-ID: h6CQ1J0gwNgC. Cengage Learning, Mar. 18, 2005. 657 pp. ISBN: 978-0-324-22388-0.
- [383] Bharat Bhushan. *Scanning Probe Microscopy in Nanoscience and Nanotechnology*. Google-Books-ID: EW8_AAAAQBAJ. Springer Science & Business Media, Jan. 22, 2010. 975 pp. ISBN: 978-3-642-03535-7.
- [384] Philipp C. Nickels et al. “Molecular force spectroscopy with a DNA origami-based nanoscopic force clamp”. In: *Science* 354.6310 (Oct. 21, 2016), pp. 305–307. ISSN: 0036-8075, 1095-9203. DOI:

- 10.1126/science.aah5974. URL: <http://science.sciencemag.org/content/354/6310/305> (visited on 02/26/2017).
- [385] Jenny V. Le et al. “Probing Nucleosome Stability with a DNA Origami Nanocaliper”. In: *ACS Nano* 10.7 (July 26, 2016), pp. 7073–7084. ISSN: 1936-0851. DOI: 10.1021/acsnano.6b03218. URL: <http://dx.doi.org/10.1021/acsnano.6b03218> (visited on 09/15/2016).
- [386] Ija Jusuk et al. “Super-Resolution Imaging Conditions for enhanced Yellow Fluorescent Protein (eYFP) Demonstrated on DNA Origami Nanorulers”. In: *Scientific Reports* 5 (Sept. 16, 2015), p. 14075. ISSN: 2045-2322. DOI: 10.1038/srep14075. URL: <http://www.nature.com/articles/srep14075> (visited on 03/02/2016).
- [387] Yonggang Ke et al. “Multilayer DNA Origami Packed on a Square Lattice”. In: *Journal of the American Chemical Society* 131.43 (Nov. 4, 2009), pp. 15903–15908. ISSN: 0002-7863. DOI: 10.1021/ja906381y. URL: <http://dx.doi.org/10.1021/ja906381y> (visited on 09/19/2016).
- [388] Takayuki Kato et al. “High-Resolution Structural Analysis of a DNA Nanostructure by cryoEM”. In: *Nano Letters* 9.7 (July 8, 2009), pp. 2747–2750. ISSN: 1530-6984. DOI: 10.1021/nl901265n. URL: <http://dx.doi.org/10.1021/nl901265n> (visited on 10/11/2016).
- [389] X.-c. Bai et al. “Cryo-EM structure of a 3D DNA-origami object”. In: *Proceedings of the National Academy of Sciences* 109.49 (Dec. 4, 2012), pp. 20012–20017. ISSN: 0027-8424, 1091-6490. DOI: 10.1073/pnas.1215713109. URL: <http://www.pnas.org/cgi/doi/10.1073/pnas.1215713109> (visited on 04/18/2016).
- [390] Andrey Kan. “Machine learning applications in cell image analysis”. In: *Immunology and Cell Biology* 95.6 (July 2017), pp. 525–530. ISSN: 1440-1711. DOI: 10.1038/icb.2017.16. URL: <https://www.nature.com/articles/icb201716> (visited on 08/07/2018).
- [391] Yuki Suzuki et al. “DNA Origami Based Visualization System for Studying Site-Specific Recombination Events”. In: *Journal of the American Chemical Society* 136.1 (Jan. 8, 2014), pp. 211–218. ISSN: 0002-7863. DOI: 10.1021/ja408656y. URL: <http://pubs.acs.org/doi/abs/10.1021/ja408656y> (visited on 09/19/2016).
- [392] Nicholas A.W. Bell and Ulrich F. Keyser. “Nanopores formed by DNA origami: A review”. In: *FEBS Letters* 588.19 (Oct. 1, 2014), pp. 3564–3570. ISSN: 1873-3468. DOI: 10.1016/j.febslet.2014.06.013. URL: <http://onlinelibrary.wiley.com/doi/10.1016/j.febslet.2014.06.013/abstract> (visited on 09/08/2016).

List of Figures

1.1	Structure formation in DNA nanotechnology.	10
1.2	Forming a double-stranded DNA link with specific and sliding sequences.	12
1.3	2D origami with continuous surfaces and cavities for various applications.	13
1.4	Atomic force microscopy (AFM).	18
1.5	Super-resolution microscopy principles.	21
1.6	Conductance in conjugated polymers.	27
1.7	Mechanisms of metal-catalysed polymerisations.	28
1.8	Regioregular, water-soluble poly(3-tri(ethylene glycol)thiophene) (P3(EO) ₃ T) with amine starting groups via <i>ex situ</i> initiated KCTP used in this work for the deposition on DNA origami.	29
1.9	Representative metal/molecule/metal junctions for molecular electronics investigations.	31
1.10	Strain-promoted azide-alkyne cycloaddition (SPAAC).	33
1.11	Hybrid formation from DNA origami and organic semiconductors.	34
2.1	Schematic of FindFoci peak assessment algorithm.	43
2.2	Schemes of a flow cell with three channels.	46
3.1	CaDNAno-based design scheme of the pad origami.	52
3.2	CaDNAno-based design schemes of the tPad origami.	54
3.3	Structure evaluation with high-resolution liquid AFM.	55
3.4	Overview AFM images of correctly synthesised pads and tPads.	57
3.5	tPad heatmap and distribution of the staple melting temperature for the 223 tPad body staples for z-staple tPads.	58
3.6	Annealing temperature screening for the tPad.	59
3.7	Thermal stability of tPads (a) in solution and (b) deposited on a mica surface.	62
3.8	Intact origami after filtration in benchtop centrifuges at different rotational speeds with centrifugal filters of the companies Amicon and Pall with a molecular weight cut-off of 100 kDa.	64
3.9	Aggregate formation of tPads due to base stacking.	65
3.10	Arranging different gold nanoobjects on the pad and tPad to test the origamis' pegboard qualities.	69
4.1	Block copolymer synthesis from an azide-functionalised poly(3-tri(ethylene glycol)thiophene and a commercially available dibenzocyclooctyne-functionalised oligodeoxynucleotide.	74
4.2	HPLC and PAGE of the block copolymer formation via SPAAC click reaction.	76
4.3	Design sketches of the three pad types.	78
4.4	Hybrid formation with 0-3 M NaCl in the assembly buffer.	80
4.5	Hybrid formation from pads type I-III and corresponding block copolymers.	81

4.6	Object heights for 456 objects on 47 pads of all types.	84
4.7	High-resolution AFM images of hybrids of the pad type I and P3(EO) ₃ T-b-20N.	84
4.8	Hybrid formation from pad type II and P3(EO) ₃ T-b-18T.	87
4.9	Sequence-guided attachment to a modified pad type II.	89
4.10	Hybrid formation from the type III pad and either P3(EO) ₃ T-b-10T or P3(EO) ₃ T-b-18T.	90
4.11	Limits of the BCP localisation accuracy.	94
5.1	Labelling a 2D structure with spectrally distinguishable fluorophores for structural evaluation and position determination.	98
5.2	The two tPad designs with the fluorescent markers.	99
5.3	Method procedure for the multi-colour SRM characterisation of surface-bound origami.	101
5.4	Mapping calibration and colour-offset residue with Tetraspeck beads as the sample.	105
5.5	Scheme to describe the uncertainty in the fluorophore distance determination introduced by the colour-offset residue vector.	107
5.6	Numerical examples of two distance distributions for $d(\text{gb})$ to illustrate their broadening due to the colour offset.	108
5.7	Model to derive the distribution of the fluorophore distances.	111
5.8	Zoom into a typical three-colour image of surface-deposited design I tPads.	114
5.9	Distributions of the fluorophore distances red-green, red-blue and green-blue as well as of the gbr angle θ for a standard, design I tPad sample.	115
5.10	Labelling in the standard, design I tPad sample. Ratio of the clusters in six fields of view labelled with one to three fluorophores found after applying the colour threshold (FP 1).	118
5.11	Zoom of a typical field of view of a noisy design II sample.	121
5.12	Distributions of the fluorophore distances red-green, red-blue and green-blue as well as of the gbr angle θ for a noisy, design II tPad sample.	122
5.13	Labelling in the noisy, design II tPad sample. Ratio of the clusters in six fields of view labelled with one to three fluorophores found after applying the colour threshold (FP 1).	123
5.14	Influence of varying the method parameters.	127
5.15	Fluorophore distance distributions of the standard sample with and without applying the user filter.	128
A.1	Generations of conjugated polymers grouped according to progress in the synthesis procedures and material properties.	139
A.2	Hybridisation of fluorophore-bearing ODNs and staples of design I tPads with the complementary handles at room temperature and 45 °C visualised with PA gel.	141
A.3	Model images of origami in solution generated with CanDo.	142
A.4	Detailed reaction scheme of the synthesis route of an azide-functionalised P3(EO) ₃ T and its coupling to a DBCO-functionalised ODN via strain-promoted azide-alkyne cycloaddition.	143
A.5	Type I pads after adding 20N ODNs.	144
A.6	Type II pads after adding 23T ODNs.	144
A.7	Type III pads after adding 23T and 8T ODNs.	145
A.8	Pad type III with single-stranded handles.	146
A.9	Attachment of PNIPAAm-b-18T to the pad type III.	146
A.10	Equivalent diameter of the objects bound to different pad types.	147
A.11	Absorption and emission spectra for the three dyes Atto 488, Atto 550 and Atto 647 N.	148
A.12	Screenshot of ThunderSTORM results of the marker localisation.	149
A.13	Fluorophore distance distribution for the distances red-blue, green-blue and red-green before and after mapping.	149
A.14	Fluorophore-labelled tPads of design I and design II visualised in agarose gels.	150

List of Tables

1.1	Overview of representative characterisation techniques for DNA origami.	16
2.1	Constant-rate synthesis for pad origami (≈ 5 h).	38
2.2	Constant-rate synthesis (≈ 11 h).	38
2.3	Constant-temperature synthesis to determine the assembly temperature T_A (≈ 1.5 h).	38
2.4	Two-rate synthesis for the fluorophore-bearing tPads (≈ 7 h).	38
2.5	Solvent gradient for block copolymer purification with RP-HPLC.	39
2.6	Preparation of 12 % polyacrylamide gels.	41
2.7	Antibody buffer.	45
2.8	Blocking buffer.	45
2.9	Flushing buffer.	46
2.10	Anti-fade buffer.	46
2.11	Filter cubes for imaging the blue (488 nm), green (561 nm) and red (647 nm) channel.	47
3.1	Dimensions of the tPad scanned with AFM in air and liquid.	56
3.2	Sequences of the handles and oligodeoxynucleotides used as links for nanoobject attachment to the pad and the tPad.	66
4.1	Summary of pattern features and experimental results for hybrids from the pad types I-III.	82
4.2	Occupation of the hybrids of type III pads and P3(EO) ₃ T-b-18T as well as P3(EO) ₃ T-b-10T.	91
5.1	Fluorophore distances red-blue, red-green and green-blue according to design and mean distances \bar{d} from AFM images for design I and design II tPads.	100
5.2	Settings for the clustering parameters CP and filter parameters FP for the experiments presented.	104
5.3	Mean residues and sample standard deviations for applying a colour-offset file to a field of view it was not derived from (test errors).	107
5.4	Statistics of numerical example distributions of $d(\text{gb})$ derived with the first and second mapping.	109
5.5	Total fluorophore distance uncertainties s_d for the distance $d(\text{gb})$ of the two experiments with tPads calculated according to (5.16).	113
5.6	Fluorophore distances in design I tPads labelled with all three fluorophores.	116
5.7	Cluster counts and proportions for the sum of all FOVs of Figure 5.10, and for the rgb clusters after applying the size (FP 2), shape (FP 3) and user filter (FP 4).	118
5.8	Overview over structure subsets that can contribute to the colour cluster types.	119
5.9	Fluorophore distances in design II tPads labelled with all three fluorophores in the noisy sample.	123
5.10	Cluster counts and proportions for the sum of all FOVs of Figure 5.13, and for the rgb clusters after applying the size (FP 2), shape (FP 3) and user filter (FP 4).	123
5.11	Random co-localisation for different cluster densities before applying filter parameters.	124

5.12 Settings chosen to evaluate the influence of the clustering parameters and the filter criteria on the resulting fluorophore distance distribution.	126
B.1 EGNAS input and forbidden sequences to generate the 20N' handle for BCP attachment and the blue, green and red handles for the fluorophore attachment.	152

Acknowledgements

I cordially thank my supervisor Prof. Michael Mertig and my co-supervisor Prof. Manfred Stamm for the opportunity to work in this exciting, interdisciplinary field, for allowing me to develop my scientific skills and to work independently, but always having time for me to discuss. Furthermore, I express my gratitude for their patience with me at all levels of these doctorate studies.

It is my pleasure to thank all former and current members of the Mertig Group, Mathias, Johanna, Evgeni, Elli, Linda, Andreas, Katrin, Nora, Anja Blüher, Anja Henning-Knechtel, Beate (I could go on here) for the help and discussions, but also for creating the unique atmosphere, barbeques on the office balcony and countless other memories. Thanks to Dr. Andreas Heerwig for letting me use the pad origami he designed. Special thanks and my deepest respect go to Johanna Zessin for all the work she has put into the polymer synthesis, and the hybrid formation. Thank you also Johanna, for proof-reading some of this thesis, I look forward to returning the favour. I also cordially thank Dr. Mathias Lakatos for taking on most of the proof-reading work and providing the much needed outside perspective in the writing process.

I sincerely thank Dr. Anton Kiriy and Dr. Roman Tkatchov for sharing their vast knowledge and expertise regarding the synthesis of state-of-the-art conjugated polymers. Thanks also to my “tribe” at the IPF, Yevhen, Olga, Alice, Aruni, (again, that is not all) and my dear friend Anne Freitag, for support and sharing some good laughs around PhD seminars and workshops.

I extend my sincerest thanks to Prof. Stefan Diez, Dr. Friedrich W. Schwarz and the Diez Group for welcoming me in their lab and sharing their profound expertise in super-resolution microscopy with me. I very much thank Dr. Friedrich Schwarz and Dr. Philip Gröger for providing the Matlab routine for the analysis of the super-resolution data.

Many thanks also to Dr. Thorsten-Lars Schmidt for allowing us to use his HPLC and gel documentation system. A warm thank you also to the members of the Schmidt Group: Michael Matthies for the discussions around AFM, and Fatih, Simon, Najan, to just name a few, for adding to a creative atmosphere in our Lab Container.

Herzlich bedanke ich mich bei meiner Familie und insbesondere bei meiner Mutter. Ohne deine Geduld und Unterstützung durch alle Höhen und Tiefen der letzten 30 Jahre hätte ich dies hier nicht erreicht. Ich denke, Papi freut sich mit uns.

I also cheerfully thank my dear friends Roberto Riovanto and Martijn Griek for travelling with me to many places between Greece and Iceland, creating memories and being occasionally close, but always there.

Erklärung

Hiermit versichere ich, dass ich die vorliegende Arbeit ohne unzulässige Hilfe Dritter und ohne Benutzung anderer als der angegebenen Hilfsmittel angefertigt habe; die aus fremden Quellen direkt oder indirekt übernommenen Gedanken sind als solche kenntlich gemacht. Die Arbeit wurde bisher weder im Inland noch im Ausland in gleicher oder ähnlicher Form einer anderen Prüfungsbehörde vorgelegt.

Diese Dissertation wurde im Zeitraum vom Januar 2013 bis August 2018 unter wissenschaftlicher Betreuung von Prof. Michael Mertig am Lehrstuhl für Physikalische Chemie Mess- und Sensortechnik der TU Dresden im cfaed - Center for Advancing Electronics Dresden, TU Dresden, angefertigt.

Es haben keine früheren erfolglosen Promotionsverfahren stattgefunden.

Ich erkenne die Promotionsordnung der Fakultät Mathematik und Naturwissenschaften der Technischen Universität Dresden vom 23.02.2011 in zum Abgabzeitpunkt zuletzt geänderter Fassung in vollem Umfang an.

Dresden, 09.08.2018

Franziska Fischer